**Distribution Agreement**

In presenting this thesis or dissertation as a partial fulfillment of the requirements for an advanced degree from Emory University, I hereby grant to Emory University and its agents the non-exclusive license to archive, make accessible, and display my thesis or dissertation in whole or in part in all forms of media, now or hereafter known, including display on the world wide web. I understand that I may select some access restrictions as part of the online submission of this thesis or dissertation. I retain all ownership rights to the copyright of the thesis or dissertation. I also retain the right to use in future works (such as articles or books) all or part of this thesis or dissertation.

Signature:

_____ _____

Yuesong Hu Date

**Engineering DNA as a molecular tool to investigate T cell mechanical signaling**

By

Yuesong Hu

Doctor of Philosophy

Chemistry

---

Khalid Salaita

Advisor

---

Yonggang Ke

Committee Member

---

Brian Dyer

Committee Member

Accepted:

---

Kimberly Jacob Arriola, Ph.D, MPH

Dean of the James T. Laney School of Graduate Studies

---

Date

**Engineering DNA as a molecular tool to investigate T cell mechanical signaling**

By

Yuesong Hu

B.S., Lanzhou University, 2017

Advisor: Khalid Salaita, Ph.D.

An abstract of
A dissertation submitted to the Faculty of the
James T. Laney School of Graduate Studies of Emory University
in partial fulfillment of the requirements for the degree of
Doctor of Philosophy
in Chemistry
2023

Abstract

**Engineering DNA as a molecular tool to investigate T cell mechanical signaling**

By

Yuesong Hu

The initiation of the T cell immune response occurs when T cell receptors (TCR) recognize foreign antigens presented by target cells. The remarkable sensitivity and specificity of this process have been a subject of wonder for decades. This dissertation sheds new light on this phenomenon by revealing that immunoreceptors on the surface of T cells are subjected to mechanical forces, which play a vital role in promoting signaling during TCR-antigen interactions. Chapter 1 of the dissertation serves as an introduction, discussing T cell recognition, recently proposed mechanosensor model to explain the near-perfect sensitivity, and the utilization of DNA-based force sensors to visualize mechanotransduction. Chapter 2 presents a microparticle force sensor, designed to overcome the limitations of current force measurement tools. This technique enables the study of receptor forces on cellular-sized particle surface with a high-throughput readout using flow cytometry. Chapter 3 introduces a programmable DNA origami-based force sensor. This highly adaptable sensor can be incorporated into supported lipid bilayers and target cell membranes, facilitating the investigation of the magnitude and sources of TCR forces at dynamic physiological membrane junctions. Chapter 4 explores the mechanics of another T cell immunoreceptor, Lymphocyte function-associated antigen 1 (LFA-1), and demonstrates its role in antigen discrimination and cytotoxic degranulation. Finally, Chapter 5 provides a comprehensive summary of the dissertation's findings and discuss potential future research directions in the emerging field of mechanoimmunology.

**Engineering DNA as a molecular tool to investigate T cell mechanical signaling**

By

Yuesong Hu

B.S., Lanzhou University, 2017

Advisor: Khalid Salaita, Ph.D.

A dissertation submitted to the Faculty of the
James T. Laney School of Graduate Studies of Emory University
in partial fulfillment of the requirements for the degree of
Doctor of Philosophy
in Chemistry
2023

**Acknowledgement**

First, I would like to thank my PhD advisor, Khalid Salaita for his support and mentorship throughout of my PhD journey. Under his guidance, I grew up into an independent researcher, acquiring valuable research and presentation skills that have greatly contributed to my professional growth. Khalid's mentorship extends beyond just advising on my dissertation; he genuinely cares about the future achievements of his students. As an international student with limited access to fellowships, Khalid consistently forwarded me fellowship opportunities such as NCI F99/K00 and provided valuable assistance during the application process. Furthermore, recognizing my passion for immunology, Khalid facilitated numerous collaborations with other research labs, easing my transition into the field for my postdoctoral work. I also extend my appreciation to my committee members, Dr. Yonggang Ke and Dr. Brian Dyer, for their invaluable advice, which greatly contributed to the progress of my research.

I also would like to express gratitude to my mentors. My undergraduate background was focused on organic synthesis, I lacked experience in imaging, surface work, and cellular research. Victor Ma, my initial mentor, not only taught all these essential skills but also played a pivotal role in shaping and advancing my ideas. Furthermore, my second mentor, Rong Ma, provided invaluable support for my projects and engaged in insightful discussions every time I faced challenges.

I also want to thank my collaborators including Dr. Morgan Huse, Dr. Cheng Zhu, Dr. Byron Au-Yeung, and Dr. Renhao Li, Dr. Mitchell Wang and Dr. Joel Eggert. Working with them greatly broaden my knowledge in the field of immunology and mechanobiology. They also offered lots of help on my own projects. This dissertation could not be finished without their important inputs.

I would also express my gratitude to my closest friends, Selma, Yuxin, Aysha, Arventh, Zongshuo, Zhenjie, and Zhenzhe, who have consistently been there for me, whenever I needed someone to talk to or hang out with. Their presence has been a source of solace during the challenging moments of my PhD journey. Additionally, I want to extend my thanks to the entire Salaita lab for their support throughout my doctoral studies, including Hiroaki, Alex, Hanquan, Joshhua, Roxanne, Aaron, Jiahui, Jing, Alisina, Kim, Anna, Brandan, Allison, Yixiao, Radhika, Rachel, Jessica, Dale, Maia, Vageesha, Rachel, Thomas, Steven, Sarah, Yusha, Tharindu, Shuhong, Krista, Jhordan, Hus, Joseph, Luona, Tianyi, Edgar, Mark, Bakai, Wenxiao, and Coco.

Last, I would thank my parents. My parents have consistently offered their support for every decision I've made and have always been proud of me. I'm also grateful to my sister, who has taken on the role of looking after the family while I've been overseas.

## Table of Contents

## List of Figures

## List of tables

## List of Movies

## List of Abbreviations

| Abbreviation | Full Name |
|---|---|
| pN | piconewton |
| TCR | T cell receptor |
| LFA-1 | lymphocyte function-associated antigen 1 |
| pMHC | peptide major histocompatibility complex |
| ICAM-1 | intercellular adhesion molecule 1 |
| CME | clathrin mediated endocytosis |
| SMAC | supermolecular activation cluster |
| IS | immunological synapse |
| AFM | atomic force microscopy |
| TFM | traction force microscopy |
| TGT | tension gauge tether |
| BFP | biomembrane force probe |
| SLB | supported lipid bilayer |
| MFM | molecular force microscopy |
| FLIM | fluorescence lifetime imaging microscopy |

| | |
|---|---|
| WLC | worm-like-chain |
| GFP | green fluorescent protein |
| MTP | molecular tension probe |
| MTS | molecular tension sensor |
| MFM | molecular force microscopy |
| DNA-PAINT | DNA-Points Accumulation for Imaging in Nanoscale Topography |
| MTFM | molecular tension fluorescence microscopy |
| ELISA | enzyme-linked immunoassay |
| PCR | polymerase chain reaction |
| RCA | rolling circle amplification |
| RICM | reflection interference contrast microscopy |
| TIRF | total internal reflection fluorescence |
| MCR | mechanically induced catalytic amplification reaction |
| FISH | fluorescence in situ hybridization |
| HCR | hybridization chain reaction |

| | |
|---|---|
| HPLC | high-performance liquid chromatography |
| SPR | surface plasmon resonance |
| BCR | B cell receptor |
| CRISPR | clustered regularly interspaced short palindromic repeats |
| Cas | CRISPR-associated proteins |
| μTS | microparticle tension sensor |
| gRNA | guide RNA |
| DOTS | DNA origami tension sensor |
| ZAP70 | Zeta-chain-associated protein kinase 70 |
| Lck | lymphocyte-specific protein tyrosine kinase |
| LAT | linker for activation of T cells |
| Arp 2/3 | actin Related Protein 2/3 complex |
| Nck | non-catalytic region of tyrosine kinase |
| WASp | Wiskott–Aldrich syndrome protein |
| PI3K | phosphoinositide-3 kinase |
| PIP3 | phosphatidylinositol (3,4,5)-trisphosphate |

| | |
|---|---|
| PIP2 | phosphatidylinositol (4,5)-bisphosphate |
| ATP | Adenosine triphosphate |
| $IC_{50}$ | half maximal inhibitory concentration |
| RT | room temperature |
| PDMS | polydimethylsiloxane |
| APC | antigen presenting cells |
| APTES | (3-Aminopropyl) triethoxysilane |
| S/N | signal to noise ratio |
| FRET | fluorescence Resonance Energy Transfer |
| BHQ2 | black hole quencher 2 |
| PEG | polyethylene glycol |
| S.E.M. | standard error of the mean |
| S.D. | standard deviation |
| SSLB | spherical supported lipid bilayer |
| OVA | ovalbumin |
| CTL | cytotoxic T lymphocyte |
| ADP | adenosine 5‘-diphosphate |
| PD1 | programmed cell death receptor 1 |

| | |
|---|---|
| PDL1 | programmed cell death ligand 1 |
| SMCC | succinimidyl 4-(N-maleimidomethyl)cyclohexane-1-carboxylate |
| TCEP | Tris (2-carboxyethyl) phosphine |
| cSMAC | central supramolecular activation cluster |
| ITAM | immunoreceptor tyrosine-based activation motifs |
| LatB | Latrunculin B |
| BSA | Bovine serum albumin |
| ECM | Extracellular matrix |
| CCD | Electron multiplying charge coupled device |
| FACS | Fluorescence-activated cell sorting |
| FBS | Fetal bovine serum |

# Chapter 1. Mechanical regulation of T cell recognition

Partially adapted from Hu. Y; Duan, Y.; Salaita, K. DNA nanotechnology for investigating mechanical forces in the immune system. *Angew. Chemie. Int. Ed.,* **2023** e202302967 DOI: 10.1002/anie.202302967 Adapted with permission.

## 1.1 Introduction

One important class of biological signaling is juxtacrine signaling, which involves binding of a ligand and receptor at the junction between two cells that physically touch.[1] Juxtacrine signaling is particularly important in the context of the cytotoxic immune response. Upon encountering target cells, the T cell receptor (TCR) on the surface of T cells engages with foreign peptides that are displayed by major histocompatibility complexes (MHCs) and typically found on the surface of the target cell. In conjunction with additional receptor-ligand pairs, including lymphocyte function-associated antigen 1 (LFA-1) and Intercellular adhesion molecule-1 (ICAM-1), as well as CD28 and CD80/86, TCR-pMHC interaction facilitates the juxtaposition of the T cell and the target cell, ultimately culminating in the formation of a specialized interface referred to as the immune synapse (IS) (**Figure 1.1**).[2, 3, 4] TCR-pMHC binding induce signaling pathways, ultimately activating T cells to secrete cytotoxic chemicals to the IS, which further enters the target cell and induces apoptosis. Notably, T cell immune response is dependent on the binding affinity of TCR-pMHC and exhibits remarkable specificity, with T cells being activated by a single foreign pMHC while remaining quiescent even when confronted with hundreds of thousands of self pMHCs.[5, 6]

At the IS, receptor-ligand complexes are subjected to mechanical cues generated by the movement of the two cells, membrane dynamics, and the cytoskeleton contraction.[7] Cells possess the remarkable capacity to detect, integrate, and convert these mechanical signals into biochemical cues, a phenomenon known as "mechanotransduction."[8] Several studies over the past decade converge on the idea that TCR avidity is influenced by the mechanical forces and immune cell signaling is mediated at least in part by mechanotransduction, yet the molecular mechanism underlying this remains unclear.[9, 10]

This chapter will start with an introduction of T cell recognition, followed by a comprehensive discussion on how mechanical forces contribute to the remarkable specificity of T cell recognition at the molecular level of TCR-pMHC complexes. Subsequently, the chapter will provide an overview of the existing molecular tools used to investigate cell molecular forces, with a specific emphasis on DNA-based force probes.

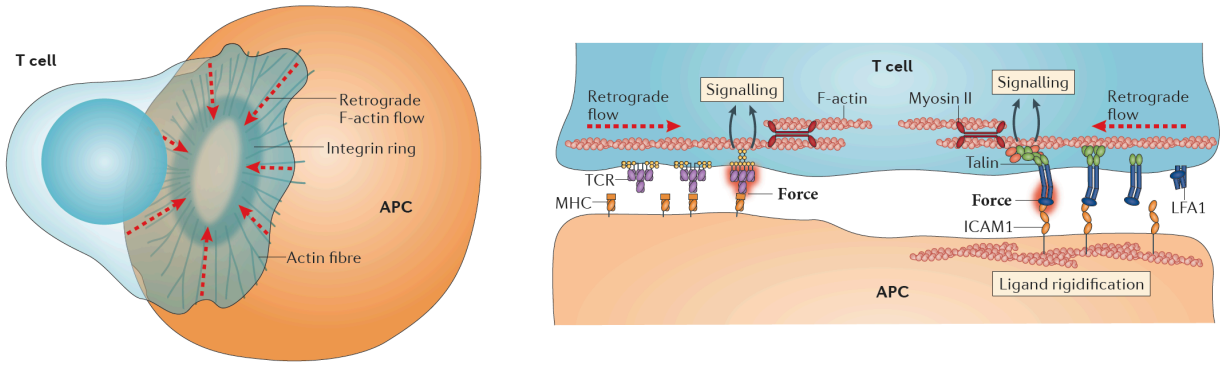


**Figure 1.1: Juxtacrine signaling and mechanotransduction at the immune synapse.** Reprinted from ref. 2 with permission.

## 1.2 Mechanical forces regulate T cell recognition

### 1.2.1 T cell recognition and TCR signaling

In recent years, an abundance of research has highlighted the influence of mechanical cues from the surrounding environment on T cell activities. For instance, T cells display diverse patterns of migration, activation, and proliferation when exposed to surfaces with varying stiffness levels.[11, 12] Given that T cells perceive and respond to their surrounding environment primarily through receptor-ligand pairs. My dissertation work started with the hypothesis that TCR-pMHC bonds at the IS experience mechanical forces, and these forces, in turn, are proposed to regulate T cell signaling, facilitating the discrimination between stimulatory and non-stimulatory antigens and ultimately augmenting the sensitivity of T cell recognition.

T cell recognition starts at the TCR signaling (**Figure 1.2**).[13] When the TCR recognizes and binds to pMHC on the target cell membrane, the co-receptor CD8 simultaneously binds to MHC and cluster with TCR. Within the intracellular domains of CD8, there is a binding site for the SRC family protein tyrosine kinase known as Lck, which can phosphorylate the immunoreceptor tyrosine-based activation motifs (ITAMs) present in the cytoplasmic domains of both the TCR ζ chain and CD3 subunits. Phosphorylation of ITAM by Lck leads to recruitment of the protein tyrosine kinase Zap70 to the TCR, which then gets phosphorylated and activated by Lck. Activated ZAP70 recruits and phosphorylate another signaling protein-linker for activation of T cells (LAT). Phosphorylated LAT provides docking sites for adaptor molecules including PLC-γ1, Grb2, and Gads, allowing the nucleation of multiple signaling complexes on LAT such as SLP70, VAV1 and SOS1. PLCγ can cleave phosphatidylinositol-4,5-bisphosphate (PIP2) in the plasma membrane to generate the secondary messengers - inositol-1,4,5-triphosphate (IP3) and Diacylglycerol (DAG). IP3 diffuses through the cytoplasm and interacts with IP3 receptors on the endoplasmic reticulum, causing the release of calcium, which through the effects of calcineurin, activates and promotes the nuclear translocation of Nuclear Factor of Activated T cells (NFAT), which, together with co-stimulatory receptor and cytokine receptor signals, orchestrate multiple T cell responses, including proliferation, migration, cytokine production and effector functions.

Within this thesis, my primary focus lies on cytotoxic T cells or CD8+ T cells. These cytotoxic T cells traverse the body, employing their TCRs to search for foreign pMHC displayed on the surface of cancer cell or virally infected cells. The interaction of TCRs with antigens triggers TCR signaling, subsequently activating the T cell to release perforin and granzyme to induce apoptosis of the target cell.[14, 15] Antigens consist of foreign peptides that are transported to the surface of the target cell and exhibited by MHC molecules, commonly referred to as pMHC. It is important to

note that the surface of target cells also presents 100,000 self pMHC complexes.[16] These self pMHC can weakly bind to TCRs but lack the capability to trigger TCR signaling. In contrast, even as few as 1–10 foreign pMHC molecules amidst a vast sea of thousands of self-peptide MHC molecules can elicit T cell activation.[17] This observation underscores the extraordinary specificity and extreme sensitivity inherent in T cell recognition. This heightened sensitivity is intricately linked to the disparity in affinity between self and foreign pMHC molecules for the TCR. Even subtle differences in affinity can have a profound impact on their stimulatory capacity. Modest reductions in affinity ranging from three to fivefold, completely eradicated T cell responses, despite increasing the peptide concentration by as much as 100,000-fold.[18]

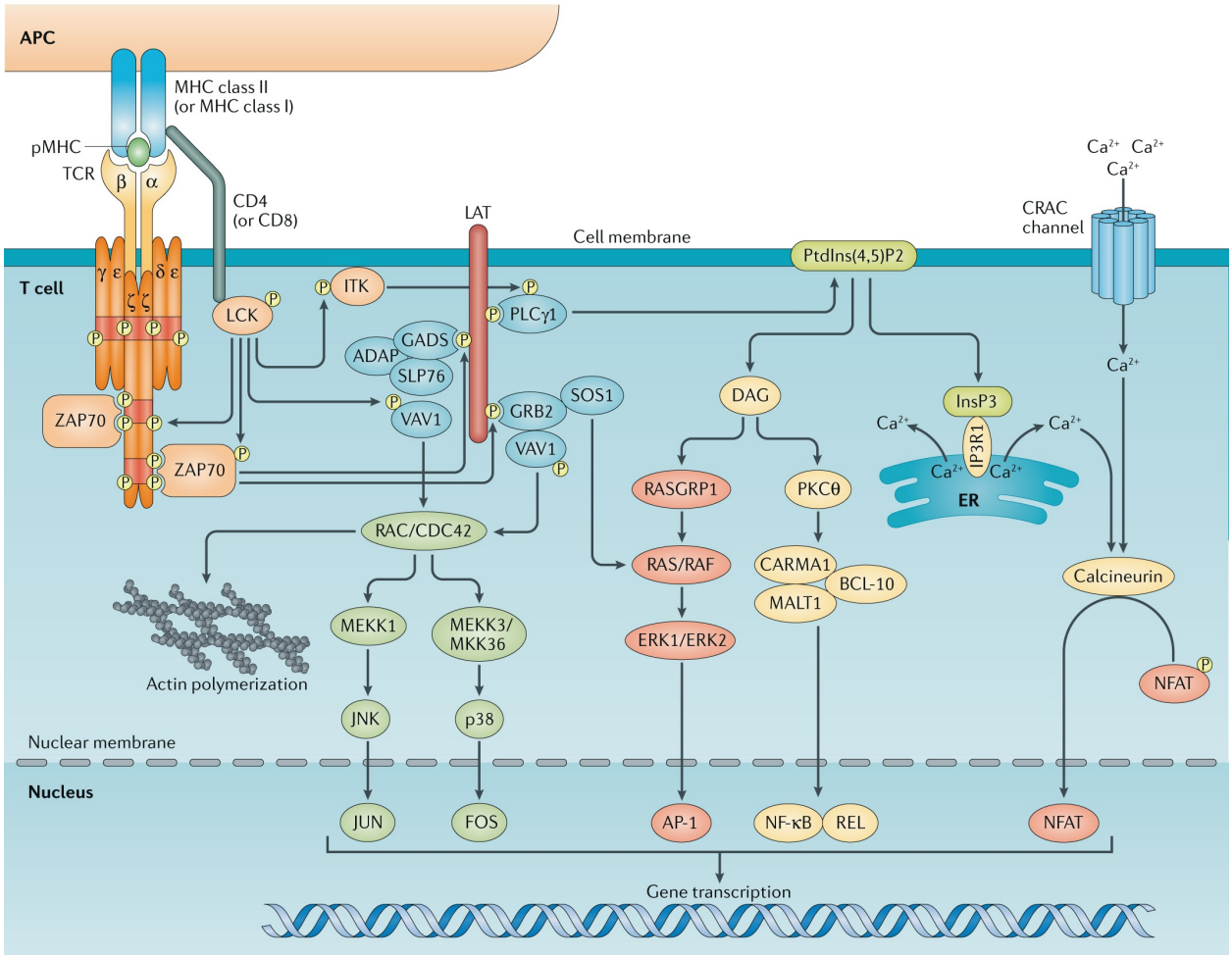


**Figure 1.2. TCR signaling pathways.** Reprinted from Ref. 13 with permission.

### 1.2.2 TCR-pMHC bond lifetime is crucial to TCR signaling

One promising model for elucidating the ultrasensitivity of TCR signaling is the kinetic proof-reading model.[19, 20] As previously mentioned, the TCR signaling pathway primarily involves a phosphorylation cascade of signaling proteins. According to the kinetic proof-reading model, this phosphorylation cascade is reversible because signaling proteins can disassociate from their docking sites or get dephosphorylated by phosphatase enzymes.[21, 22] As a result, for the entire cycle of reversible phosphorylation cascade to complete to trigger TCR signaling, the interaction between TCR and pMHC must persist for a sufficient duration. Failure to do so would result in signaling proteins reverting to their original states, ultimately leading to the non-activation of T cells. Antagonist or self-pMHCs with low binding affinity to the TCR are unable to activate T cells because their low affinity implies a high off rate ($k_{off}$), offering a short TCR-pMHC lifetime.[23]

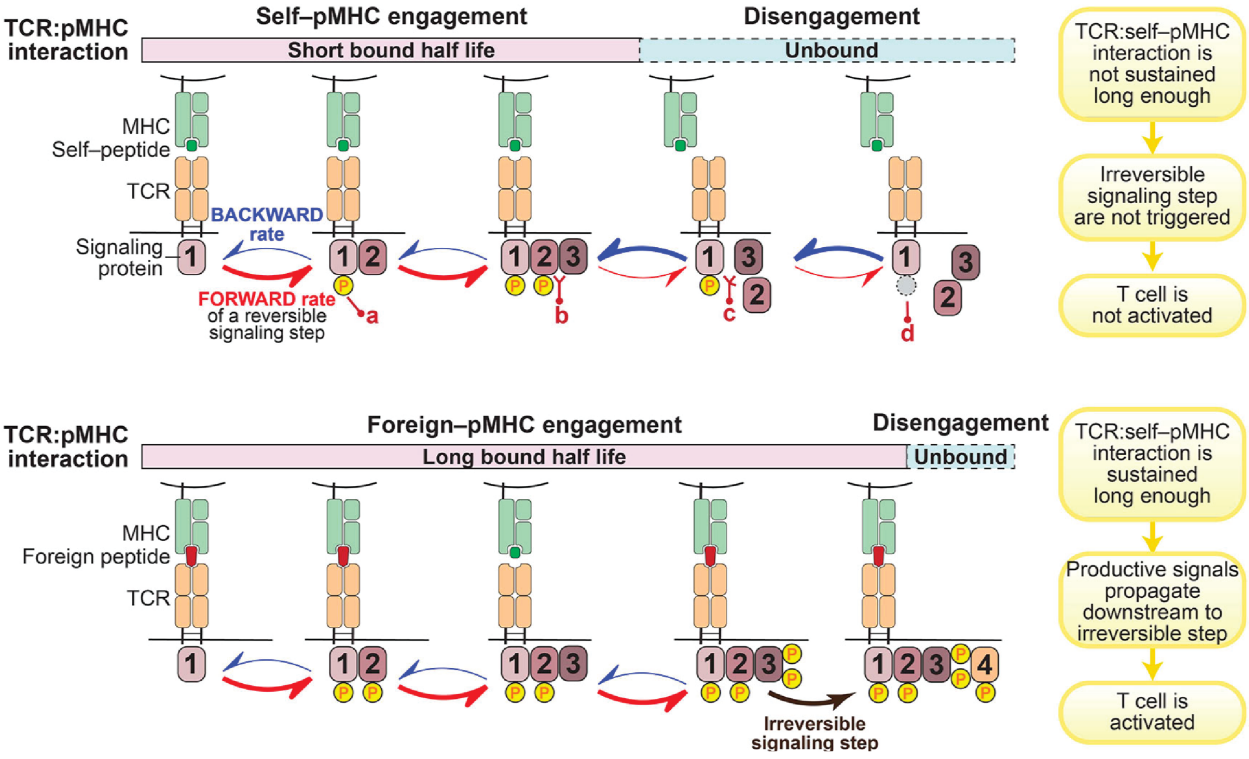

**Figure 1.3. Illustration of kinetic proofreading model.** TCR-pMHC engagement triggers a series of biochemical signaling steps, which eventually lead to activation of T cells. The series of biochemical signaling steps are reversible, allowing for TCR-pMHC disengagement to quickly restore signaling intermediates back to the initial resting stage. Self-pMHC binds to TCR with a short dwell time and therefore is not capable of triggering all signal steps to activate T cell. Reprinted from ref. 20 with permission.

This model effectively accounts for the majority of situations except certain discoveries showing that low-affinity antigens can still provoke a T cell response, leading to autoimmunity, while conversely, high-affinity antigens are unable to achieve this outcome. To address this knowledge gap, Chen et al. introduced the mechanosensor model. According to this model, TCR-pMHC interactions occurring at dynamic junctions between T cells and target cells are likely subject to mechanical forces.[24, 25, 26] These mechanical forces can induce changes in the conformation of the TCR-pMHC complex, thereby influencing the kinetics of TCR-pMHC binding. Interestingly, different TCR-antigen interactions respond differently to applied force, exhibiting either "catch bond" or "slip bond" behaviors (**Figure 1.4 a-b**). Slip bonds are a common bond type observed in nature, where force tends to be disruptive and destabilizing. When subjected to force, the binding between two entities is compromised, resulting in rapid dissociation or reduced bond lifetime. In contrast, "catch bond" represents a counterintuitive bond type in which the bond becomes stronger in the presence of force with an increased bond lifetime. This is like a hook, the more force applied, the stronger the binding becomes until the force surpasses a certain threshold, leading to dissociation.

With that being stated, when the TCR-antigen interaction follows a slip bond behavior, it results in a reduced bond lifetime under the influence of force, making it less likely for the phosphorylation cascade to reach completion. Consequently, this scenario does not lead to T cell

activation or a T cell response. In contrast, when the TCR-antigen interaction exhibits a catch bond behavior, the application of force enhances its lifetime, ensuring that the dwell time is sufficient for the TCR signaling process to complete, thereby activating the T cell. Numerous research groups, including Lang, Reinherz, Cheng, and Evavold, have demonstrated this phenomenon using techniques like single-molecule spectroscopy, such as optical tweezers and biomembrane force probes (BFP), to apply force to the TCR-antigen bonds and investigate their mechanosensing mechanisms (**Figure 1.4c**).[24, 27, 28, 29] For example, Cheng et al. found the force applied to TCR-agonist pMHC increased its bond lifetime and peaked at around 10 piconewtons (pN). In contrast, antagonist pMHCs exhibit slip bonds with the TCR under force (**Figure 1.4d-f**), where bond lifetimes consistently decreased with increasing force, failing to elicit T cell activation.[24]

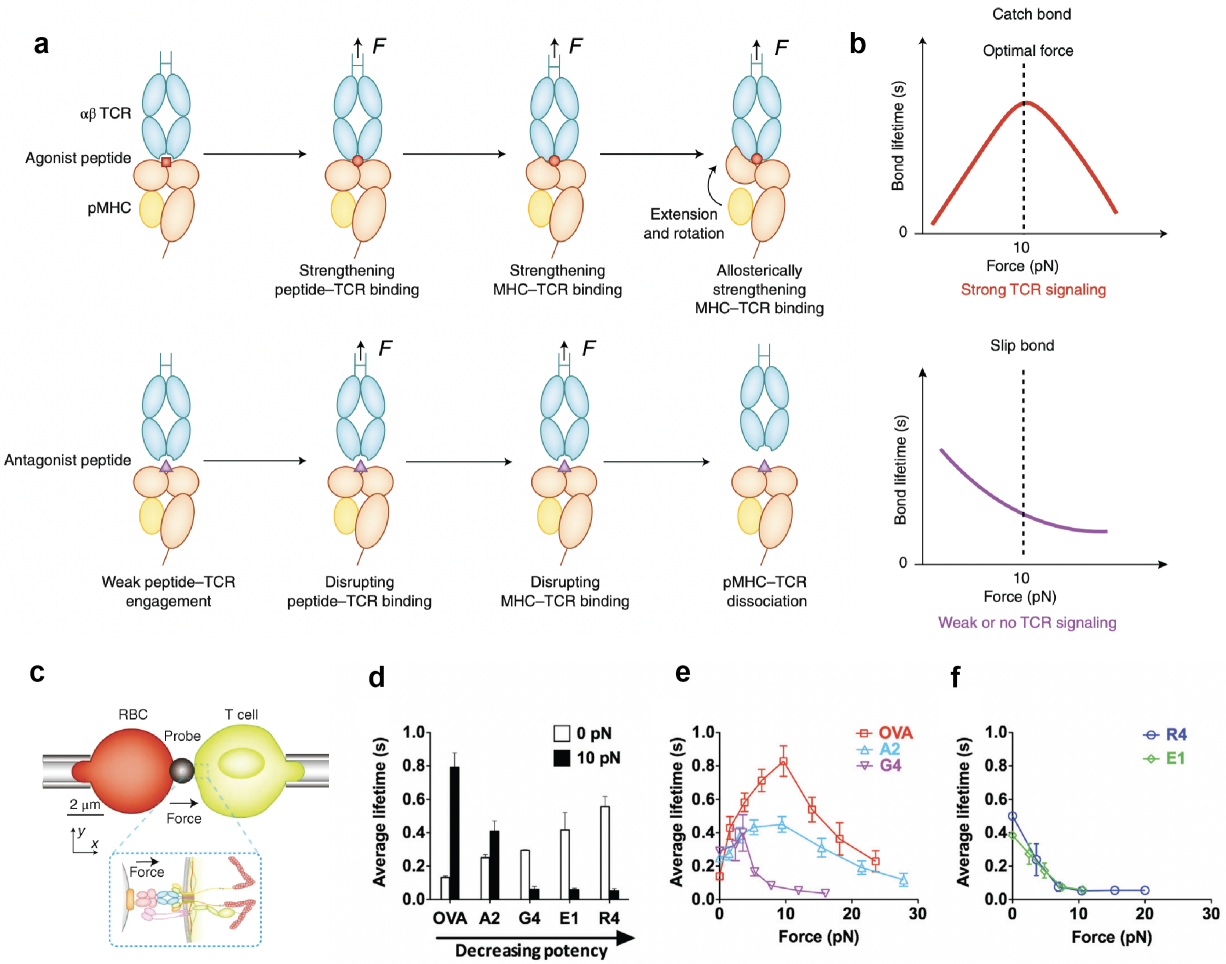

**Figure 1.4. TCR-antigen bonds exhibit catch-bond or slip bond behavior under force. a** Mechanical force transmitted to TCR-pMHC complex strengthens the binding affinity of TCR-agonist pMHC and decreases that of TCR-antagonist. This is accomplished by force induced conformation change. **b** With the force increasing, the bond lifetime of TCR-agonist pMHC first increases and then decreases, showing a catch bond behavior. In contrast, force monotonically shortens the bond lifetime of TCR-antagonist, exhibiting a slip bond behavior. **c** Schematic of biomembrane force probe assay used to apply force to TCR-pMHC bonds and track bond lifetime change under force. Probe bead between RBC and T cell is coated with pMHC ligands to engage TCR on the T cell. **d** Lifetimes of different TCR-pMHC bonds at 0 (white) and 10 (black) pN force. OVA peptide is agonist peptide. A2, G2, E1, R4 represent mutated peptide with decreasing potency. **e-f** Lifetime versus force curves showed that TCRs exhibited catch bond behavior when interacting with progressively weaker agonists OVA, A2, and G4 (**e**) but slip-only bonds with antagonists R4 and E1 (**f**). Reprinted from ref. 24 and 25 with permission.

Returning to the proof-reading model, it asserts that the duration of the TCR-antigen bond plays a crucial role in TCR signaling. The reason it falls short in explaining low affinity but high activation situations is because these TCR-pMHC affinities are characterized in solution through surface plasmon resonance (SPR) assay (referred to as 3D affinity). However, TCR-pMHC binding takes place within the immune synapse and should be evaluated in a 2D context.[30] Furthermore, in this 2D environment, TCR-pMHC complex could experience mechanical forces, which as aforementioned can exert influence on the affinity and change its bond lifetime. The influence of force on bond lifetime is independent of the 3D affinity as some low-affinity interactions can display catch bond behavior under force, whereas certain high-affinity antigens may exhibit slip bond behavior.[31] That explains why low affinity antigen can still activate T cells because mechanical force could increase the lifetime of its interaction with TCR, aligning with the principles of the proof-reading model and thus triggering T cell signaling.[32, 33]

In line with this theory, recent work by Garcia and Evavold mutated an amino acid on the TCR, obtaining a collection of TCR variants with varying affinities for the HIV antigen. They found that the stimulatory power of these TCR is poorly correlated with their affinities to antigen measured

in solution (**Figure 1.5a**,**b**).[31] Instead, it is closely associated with its bond type and peak lifetime under force (**Figure 1.5c, d**). These findings provide substantial support for the idea that the TCR functions as a mechanosensor, leveraging mechanical force to discriminate foreign antigen which provides a sufficient bond lifetime to trigger downstream TCR signaling.

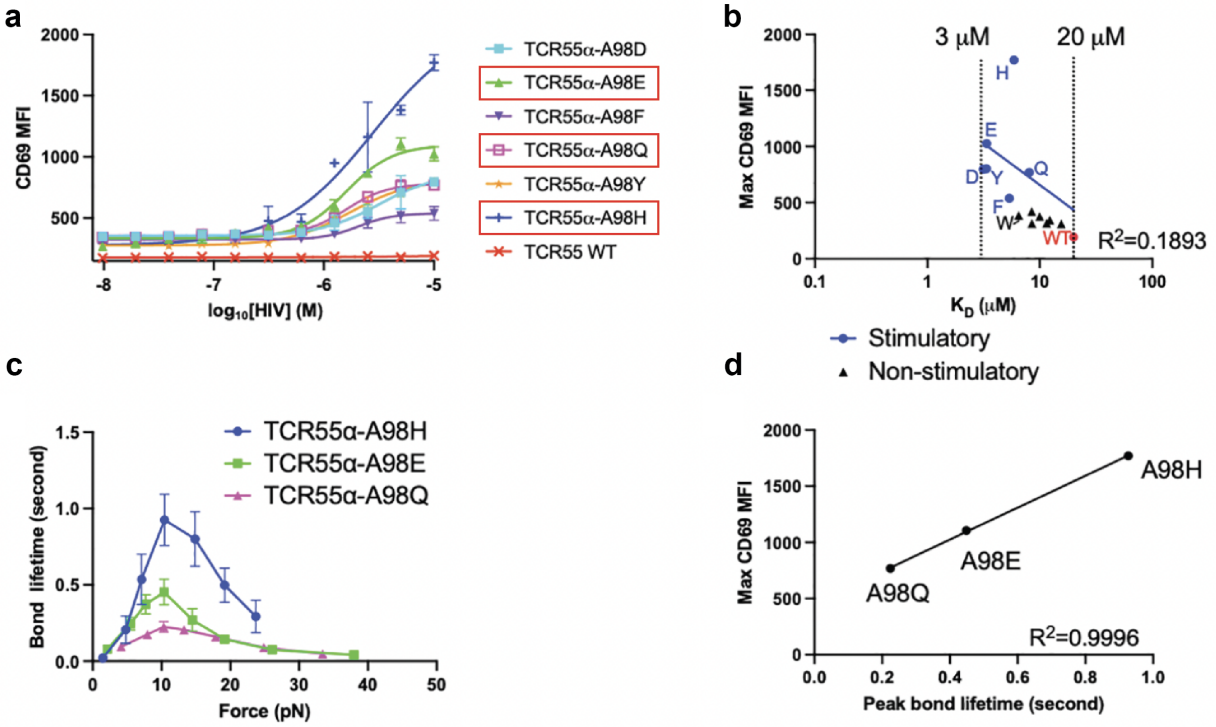


**Figure 1.5. TCR-pMHC peak lifetime is correlated with potency. a** TCR55a-A98 was mutated to D, E, F, Q, Y, and H and used to transduce T cells with WT TCR55b. T cells were stimulated with target cells pulsed with peptide antigens. T cells were than stained with anti-CD69 to determine the stimulatory power (potency) of different TCR-pMHC complexes. **b** Mean anti-CD69 versus 3D affinity between TCR and pMHC. The linear correlation analysis was performed for the TCRs (blue). $R^2$=0.1893 indicates a poor correlation. **c** Biomembrane force probe experiment measured lifetimes of different TCR-pMHC complexes under force. **d** Mean anti-CD69 versus peak lifetime of TCR-pMHC bond. $R^2$=0.9996 indicates a good correlation. Reprinted from ref. 31 with permission.

### 1.2.3 TCR mechanosensor model (conformation change)

If we consider the catch-bond-based mechanosensor model to be valid, two key assumptions must hold true. Firstly, mechanical force has the potential to alter the conformation of TCR-agonist pMHC in a way that enhances its binding affinity, thus increasing the bond lifetime. Secondly, TCR-pMHC complexes should experience force within the immune synapse formed between T cells and target cells.

Regarding the first assumption, over the past few decades, considerable progress has been made in deciphering the conformation of TCR-pMHC complexes. Techniques such as X-ray crystallography and NMR have provided detailed insights.[34, 35, 36] More recently, cryogenic electron microscopy studies have enhanced the physiological relevance of these findings by incorporating CD3 units and lipid bilayers into the analysis.[37, 38, 39] However, these conformational studies were conducted in the absence of mechanical force. Additionally, these studies typically overlook the cytoplasmic tail of the TCR zeta chain, which plays a role in coupling the TCR to the cytoskeleton for transmitting force.[40] At present, there is no TCR-pMHC structural data under force, primarily due to the difficulties involved in integrating mechanical force into existing structural analysis methods.

However, through steered molecular dynamics (SMD) simulations, Wu et al. identified conformation change in pMHC of the TCR-pMHC complex when subjected to mechanical forces (**Figure 1.6a, b**).[41] Force-induced conformation changes result in the formation of additional hydrogen bonds between pMHC and TCR, thereby enhancing binding affinity and prolonging bond lifetimes (**Figure 1.6c**). Importantly, this structural modification is observed exclusively in the case of agonist pMHC and not in antagonists. To experimentally confirm these findings, they

mutated amino acids on TCR or pMHC responsible for hydrogen bond formation. Subsequently, they employed BFP to pull mutated TCR-pMHC complexes (**Figure 1.6d**). They found that the catch bond behavior for mutated TCR-pMHC complexes was less pronounced, accompanied by a decrease in the peak lifetime (**Figure 1.6e**). This was correlated with their stimulatory power change (**Figure 1.6f**). Interestingly, this study primarily centered on examining the structural changes in the pMHC under mechanical force and claimed no obvious change was observed in TCR. In contrast, other investigations by Reinherz and Lang focused on the TCR's perspective.[27] They employed optical tweezers to pull TCR-pMHC complexes and observed a conformational transition spanning a range of 8 to 15 nm (**Figure 1.6h**), similar to what was observed in SMD simulations. They demonstrated significant involvement of the CβFG loop of TCR in this transition, as its removal led to much earlier transitions (**Figure 1.6i**). Furthermore, stabilizing the CβFG loop with antibody eliminated the transition and significantly increased bond lifetimes (**Figure 1.6i** and **j**). However, the exact mechanism by which the FG loop regulates the TCR's conformational change remains unclear. Considering the proximity of the CD3εγ subunits to the CβFG loop, they hypothesized that when TCR-pMHC experiences forces, the FG loop on TCR could function as a "lever" to disturb CD3εγ, which can in turn stabilize the FG loop or expose ITAM domain (**Figure 1.6k**).[16] Exposing ITAM might not directly extend bond lifetimes, but it could still enhance TCR signaling by facilitating Lck phosphorylation. Likewise, mechanical force can also pull positively charged ζ-chains move away from the negatively charged membrane, making the ITAM ζ-chains accessible to Lck.[42, 43]

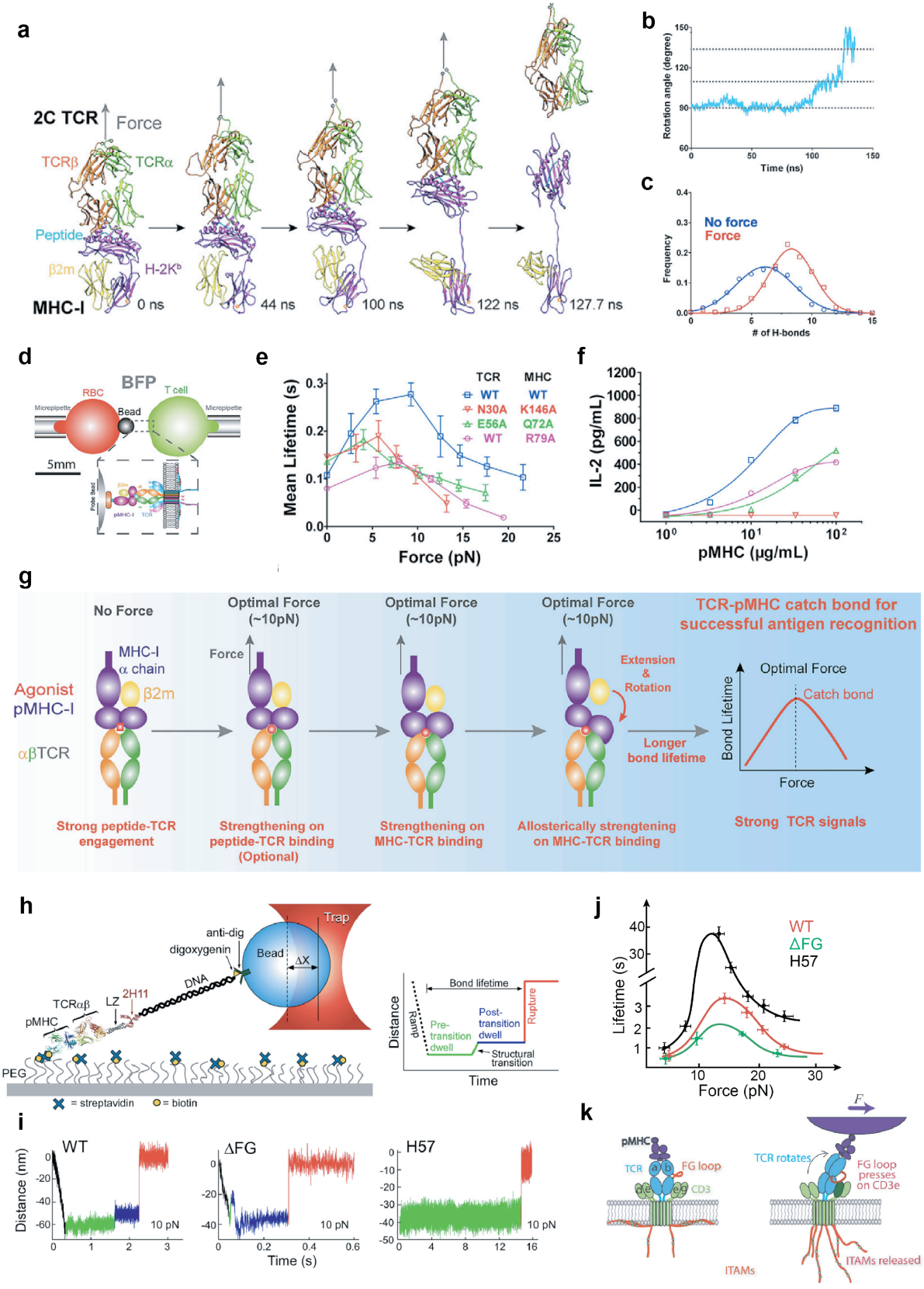
a
2C TCR
Force
TCRβ
TCRα
Peptide
β2m
H-2Kᵇ
MHC-I
0 ns
44 ns
100 ns
122 ns
127.7 ns
b
Rotation angle (degree)
Time (ns)
c
No force
Force
Frequency
# of H-bonds
d
BFP
RBC
T cell
Micropipette
Bead
5mm
e
Mean Lifetime (s)
Force (pN)
TCR MHC
WT WT
N30A K146A
E56A Q72A
WT R79A
f
IL-2 (pg/mL)
pMHC (μg/mL)
g
No Force
Optimal Force (~10pN)
Optimal Force (~10pN)
Optimal Force (~10pN)
TCR-pMHC catch bond for successful antigen recognition
MHC-I α chain
β2m
Agonist pMHC-I
αβTCR
Force
Extension & Rotation
Longer bond lifetime
Optimal Force
Catch bond
Bond Lifetime
Force
Strong peptide-TCR engagement
Strengthening on peptide-TCR binding (Optional)
Strengthening on MHC-TCR binding
Allosterically strengtening on MHC-TCR binding
Strong TCR signals
h
Trap
anti-dig
digoxygenin
Bead
ΔX
DNA
TCRαβ
LZ
2H11
pMHC
PEG
= streptavidin
= biotin
Distance
Bond lifetime
Rupture
Pre-transition dwell
Post-transition dwell
Structural transition
Time
i
WT
ΔFG
H57
Distance (nm)
10 pN
Time (s)
j
WT
ΔFG
H57
Lifetime (s)
Force (pN)
k
F
pMHC
TCR
FG loop
CD3
TCR rotates
FG loop presses on CD3ε
ITAMs
ITAMs released

**Figure 1.6. Mechanical force induces conformation change of TCR-pMHC complexes. a** Sequential snapshot of SMD simulations of the dissociation of peptide-MHC under force. **b** Time courses of the angle between the peptide and the direction of force in SMD simulations. **c** The distributions of H-bond numbers between TCR and pMHC for the peptide in the presence (red square) or absence (blue circle) of force. **d** Schematics of the BFP experiments. **e** Bond lifetimes of WT and mutated TCR-pMHC complexes measured by BFP under different magnitude of force. **f** IL-2 production of hybridoma cells stimulated under WT or mutated TCR-pMHC interactions. **g** Model explaining mechanically induced conformation change on pMHC molecule prolongs the bond lifetime. **h** Schematic of optical tweezer is used to pull TCR-pMHC complex at specific level of force to induce and track conformation transitions while measuring the bond lifetime. Distance versus lifetime plot on a left shows a loading profile. Increase in distance indicates conformation change of TCR-pMHC complex (black) or rupture of complex (red). **i** Traces of TCR-pMHC complexes under 10 pN force. WT TCR-pMHC trace shows a typical transition and rupture. ΔFG traces typically transition early. H57 Fab traces typically show no transition and dwell for longer periods before rupture. **j** Force versus bond lifetime plots for different TCR-pMHC complexes. (Plot is regenerated based on the results of the original paper, error bars on the plot are meaningless) Catch bonds peak at∼15 pN for WT and shift to lower force for ΔFG with significant reduction in bond lifetime. H57 stabilized the FG loop exhibiting dramatic amplification of catch bond lifetimes. **k** Model explaining mechanically induced conformation change on TCR, with FG loop involved, prolongs the bond lifetime. Reprinted from Ref 27, 41 and 43 with permission.

In summary, both SMD analysis and single molecule force spectroscopy experiments have provided evidence that mechanical force can induce conformational changes in TCR-pMHC complexes. SMD analysis has further revealed that these conformational changes can facilitate increased hydrogen bond interactions between pMHC and TCR, thereby enhancing binding affinity and prolonging bond lifetimes. Additionally, it has been observed that the FG loop within the TCR plays a regulatory role in these conformational changes, contributing to the extension of bond lifetimes under mechanical force. Furthermore, multiple studies suggest that mechanical force can bypass the TCR-pMHC complexes and directly induce structural changes in the CD3 and ζ chains. These changes lead to the exposure of ITAM domains, facilitating Lck phosphorylation, and ultimately facilitating TCR signaling.

### 1.2.3 TCR mechanosensor model (mechanical force)

Regarding the second assumption, the aforementioned single molecule force spectroscopy studies indicate that TCR-pMHC binding and TCR signaling are responsive to mechanical forces. However, it's important to note that these experiments were conducted on isolated TCR-pMHC complexes or T cells engaging only a small number of antigens. Furthermore, the force exerted on the TCR-pMHC bonds in these experiments was not generated internally from T cell itself but rather externally applied using single molecule instruments. The question that remains unanswered is when engaging antigens on the target cell membrane., whether T cell itself generates forces to TCR-antigen bonds to amplify TCR signaling.

Previous research has indicated that cells have the ability to apply force to their surroundings through cytoskeleton rearrangement.[44] The cytoskeleton consists of F-actin and myosin. F-actin is a polymer that forms through the controlled polymerization of individual actin subunits (**Fig 1.7a**).[45, 46, 47] When filament growth is directed towards the cell's plasma membrane, it results in pushing force approximately 1-2 pN per polymerizing filament.[48, 49] Simultaneously, polymerized actin can interact with Myo-II, which then moves along it in an ATP-dependent manner (**Fig 1.7b**). This motor activity of myosin leads to actomyosin contractility, generating a force of 3-5 pN.[50, 51] These forces can be transduced to immunoreceptors because they are coupled to the cytoskeleton. For example, TCR is associated with cytoskeleton through positively charged motifs positioned within the ζ intracytoplasmic region of TCR or by recruiting actin nucleation regulators such as Arp2/3 and WASP.[40, 52, 53] Other immunoreceptors like LFA-1 receptors achieve a connection with F-actin through adaptor proteins, such as talin, which possess binding sites for both the receptor and F-actin.[54] In such scenarios, the mechanical forces generated by the dynamic cytoskeletal

processes can transmit to the receptors on the cell membrane and subsequently to the bonds between receptors and their ligands. It's crucial to acknowledge that at the immune synapse, where cell-cell junctions are exceptionally dynamic, receptor-ligand bonds can also experience forces independent of cytoskeleton. This is due to the highly variable sizes of these interactions. For instance, TCR-antigen and CD28-CD80/86 bonds are roughly 15 nm in size, while the LFA-1-ICAM-1 bond spans approximately 40 nm (**Fig 1.7c**).[4, 55, 56] Furthermore, components like phosphatases and the glycocalyx on the T cell surface can extend beyond 45 nm. The size mismatches among these proteins can give rise to repulsive forces, which are exerted on smaller complexes like TCR-antigen (**Fig 1.7d**). Part of my thesis will demonstrated this hypothesis.

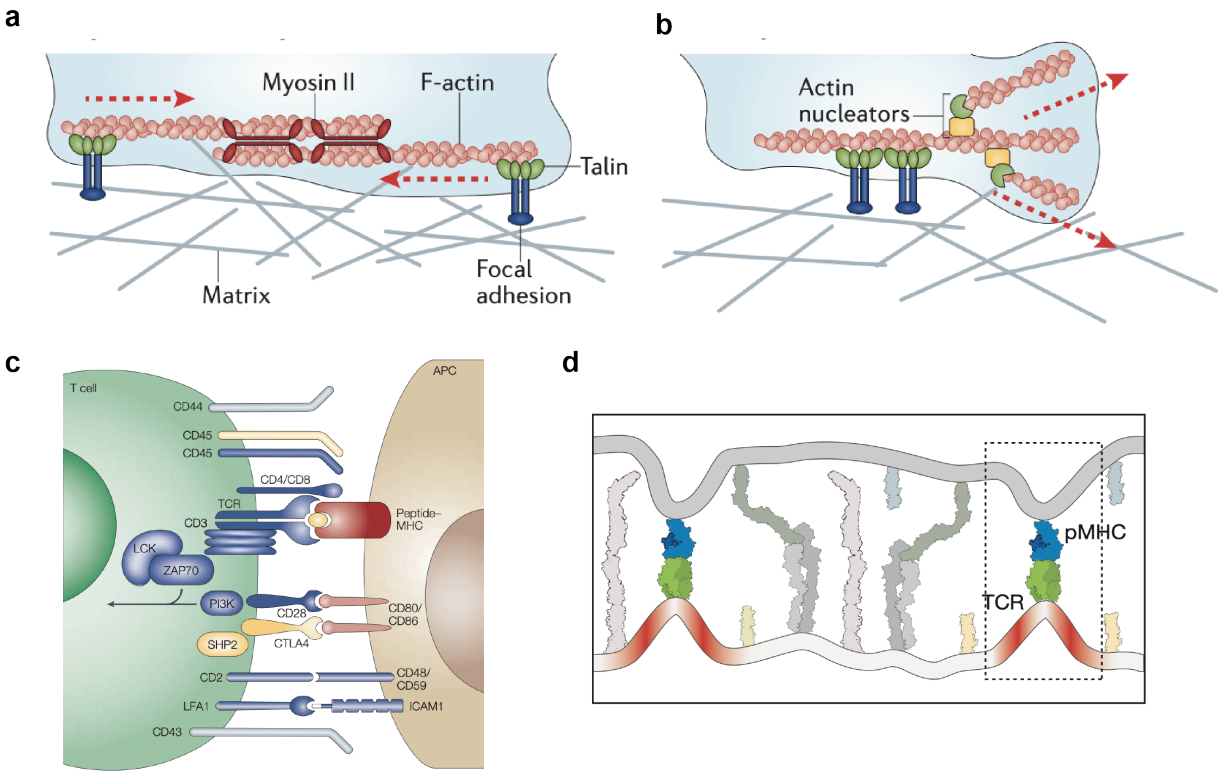


**Figure 1.7. Potential sources of mechanical forces. a** F-actin polymerization leads to protrusion which generate force to the receptors. **b** Myosin motion along the F-actin generate contraction force which transduce to receptors through F-actin. **c** Scheme showing different receptor-ligand pairs and phosphatase at the immune synapse. **d** Scheme showing that proteins at the immune

synapse have different sizes, thus imposing strain to small complexes such as TCR-pMHC. Reprinted from ref 2, 4, and 56 with permission.

Even though prior works suggest that T cell can exert force, but the exact magnitude of force experienced by individual TCR-antigen bonds remain unknown. Additionally, even if force is transmitted to TCR-pMHC bonds, it remains uncertain whether this force is a critical factor in TCR signaling and the subsequent immune response of T cells. Recent research has even suggested that the stimulatory power of the TCR is not necessarily linked to its mechanical properties and has raised the possibility that mechanical force might instead impair antigen discrimination.[57] There is a clear and promising need to develop force sensors capable of measuring the forces generated by T cells, especially at TCR-antigen bonds. If possible, manipulating these forces could help elucidate the role of mechanical forces in T cell signaling.

## 1.3 Tools to investigate cell mechanical forces

### 1.3.1 Summary of current force measurement tools

To better understand mechanotransduction and elucidate its roles in immune activities, many tools have been developed to visualize and quantify T cell forces. Traction force microcopy (TFM) was the earliest force measurement technique used to quantify cellular forces by monitoring the deformation of the material underneath the cell.[58, 59, 60, 61] Typically, cells are cultured on an elastic substrate, such as polyacrylamide, and fluorescent beads are embedded within the substrate as reference markers. These beads can be tracked in both space and time using optical microscopy to monitor the substrate's deformation resulting from cellular forces (**Figure 1.8 a, b**). However, accurately tracking bead displacement can be a demanding and time-consuming task, sometimes involving cell lysis or detachment from the substrate. Furthermore, the analysis of these bead

displacements and their subsequent conversion into force measurements demands specialized software and techniques, which may not be readily available to standard laboratories. A simpler method for quantifying cell traction force is Atomic Force Microscopy (AFM).[62, 63] In AFM, the cantilever possesses elasticity with a specific spring constant. Once coated with ligands, cells will undergo spreading and tug on the cantilever. The force exerted by the cell during this process can be computed by assessing the deflection of the cantilever (**Figure 1.8c, d**). It's worth noting that, unlike traction force microscopy, the AFM platform employs only a single deformable component, the cantilever, the deformation of which indicates the traction force of the entire cell, unlike TFM measure forces spanning the cell with a micro scale resolution. Later, an adapted form of TFM appeared, replacing the flat elastic substrate with micro-sized polydimethylsiloxane (PDMS) pillar structures.[64] When cells adhere to these miniature pillars, their deformation and deflection can be conveniently monitored over time, allowing for the calculation of the forces exerted by the cells using the spring constant of the polymer structure. Consequently, this method has gained preference and proven to be a superior approach for examining T cell mechanics. For example, with micropillar assay, Kam et al. demonstrated that T cell generates up to 100 pN centripetal force along of the edge of the cell (**Figure 1.8 e, f**).[65] Additionally, they noted that the TCR complex and CD28 perform complementary roles in generating these forces. Furthermore, Huse et al. made additional observations, finding that CTL degranulation events take place in areas where intense force is exerted, suggesting a significant role of mechanical forces in potentiating target killing.[66] Although micropillar arrays offer a convenient and adaptable setup for measuring T cell traction forces, the force information acquired is an average taken from a large number, approximately $10^3$ to $10^5$ receptors, present within micron-scale pillar elements. Mechanosensor model explains TCR

signaling at a molecular level focusing on individual TCR-pMHC bonds. To investigate it, one requires tools that enable the detection of forces acting on single TCR-pMHC bonds.

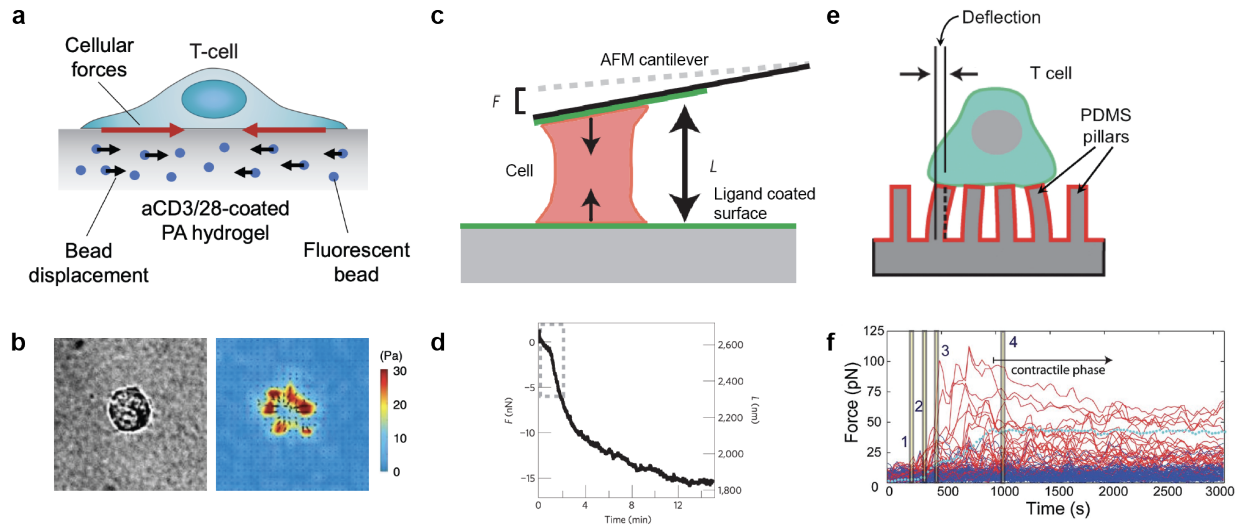


**Figure 1.8. Deformable platforms for studying forces at cellular levels. a** Scheme of traction force microscopy where cell seeds on a PA gel coated with antibodies and embedded with fluorescent beads. Traction forces are quantified by imaging the displacement of beads in the gel. **b** Representative images showing the pressure cell applied to its surface, which was calculated from bead displacement. **c** Schematic showing that AFM measures cell traction force based on the cantilever deflection. **d** Plot illustrating the force experienced by the cantilever versus the length of the cell (platelet). **e** Scheme of micropillar array setup where a T cell is plated onto PMDS micropillar coated with ligands. The force is calculated from the deflection of pillars underneath the cells. **f** Representative plot showing the magnitude of force applied to individual pillars as a function of time. Red traces indicate forces on individual pillars under the cell, whereas the blue traces represent pillars away from the interface. Reprinted from ref. 59, 62 and 65 with permission.

Over the past decade, researchers, including our lab, have made significant strides in bridging this knowledge gap by developing a series of molecular tension sensors. These sensors enable the spatial and temporal mapping of forces experienced by individual receptors. The typical design involves modifying an elastic molecule, such as a polymer, with a fluorophore-quencher FRET pair and presenting a ligand at one end to engage the receptor of interest. Upon binding to tension sensor, forces transmitted to the receptor will extend the elastic molecule and separate the

fluorophore-quencher pair, leading to a massive fluorescence enhancement. In 2011, our lab introduced the first tension sensor utilizing a polyethylene glycol (PEG) polymer backbone to map the forces experienced by the epidermal growth factor receptor (EGFR) (**Figure 1.9a**).[67] Subsequently, this sensor was adapted to measure integrin forces. Later, to expand the capabilities and applications of molecular tension sensing, we and other researchers replaced the PEG "spring" with alternative extendable molecules such as spider silk peptide,[68] and folded proteins[69] (**Figure 1.9b**).

One concern regarding this tension sensor design is that the extension of elastic molecules under force results in a graded "analog" response, which makes it challenging to precisely determine the absolute magnitude of receptor force from an ensemble fluorescence signal containing multiple tension sensors. To address this limitation, several research groups have opted to reduce the sensor surface density to the single-molecule level so that each tension sensor can be analyzed individually. For example, in single molecule experiments of $(GPGGA)_8$ peptide tension sensor (**Figure 1.9c**), Dunn and colleagues demonstrated that integrins transmit ~2-5 pN forces to their ligands.[70] Additionally, using the same design, Schutz et al. reported that TCR transmits a peak force of 5 pN to its ligands anchored on synthetic substrates.[71] However, working with single molecule data involves laborious analysis and comes with a limited signal-to-noise (S/N) ratio. Additionally, single molecule experiments have an extremely low surface density, which may not be representative of the ligand density on the plasma membrane. Moreover, due to the limited dynamic range of peptide entropic springs, which is around ~8 pN, there is a possibility of underestimating forces exceeding this range.

To address these limitations, we and colleagues designed a DNA hairpin-based tension probe where the elastic spring was replaced with a DNA hairpin (**Figure 1.9d)**.[72, 73] Unlike PEG and

peptide repeats, DNA hairpin only unfolds at a specific force threshold and thus reports cellular forces in a "digital" manner. With DNA hairpin probes, one can still use ensemble fluorescence imaging to accurately map and measure receptor forces with a high S/N. Additionally, DNA hairpin tension probe are highly tunable and able to detect force up to 19 pN.

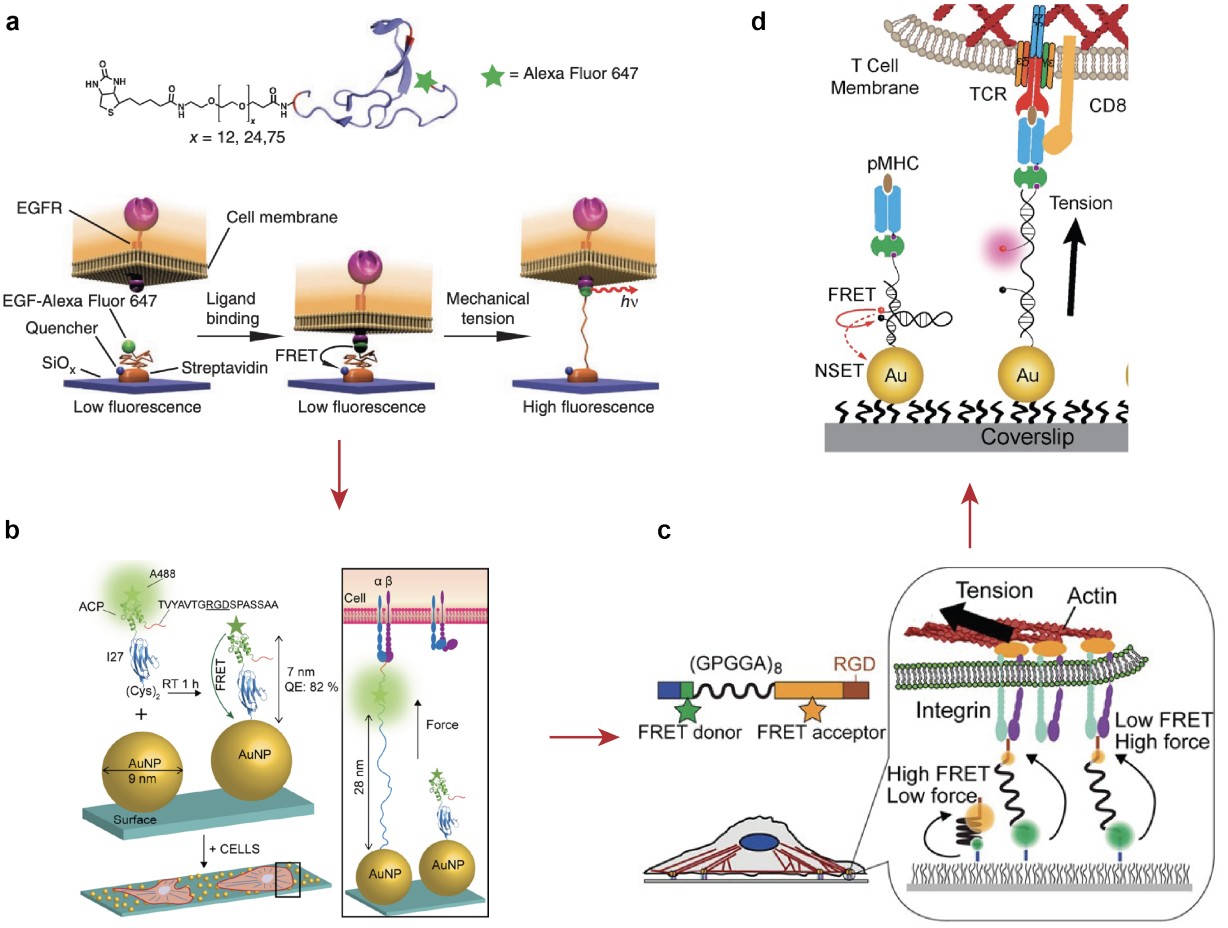


**Figure 1.9. Molecular tension sensors for studying forces at molecular levels.** **a** Scheme of traction force microscopy where cell seeds on a PA gel coated with ligands and embedded with fluorescent beads. Traction forces are quantified by imaging the displacement of beads in the gel. **b** Representative confocal images showing displacement of bead positions before (Cyan) and after (magenta) the application of traction force. **c** Scheme of micropillar array where CTL is plated onto PMDS micropillar coated with ligands. The force applied by force is calculated from the deflection of pillars underneath the cells. **d** Representative images showing deflections of pillars which are indicated by yellow arrows. Green asterisks indicate ''hotspots'' of strong force exertion. Reprinted from ref. 67-70 with permission.

The tension sensors described above operate by detecting tension through the extension of an elastic backbone molecule. This extension separates the FRET pair, resulting in a fluorescence response. It's important to note that this force only extends the molecule without breaking it, making the extension reversible. When the force stimulus is removed, the molecule returns to its original folded state, causing the fluorescence signal to disappear. This property is advantageous because it allows for the temporal and spatial tracking of real time mechanical events.

However, there are limitations to this approach, particularly when dealing with low numbers of mechanically active receptors or very transient force events with a short duration that is challenging to capture with a microscope camera. Fortunately, another DNA based tension sensor, developed by Wang et al. and Ha and coworkers, addresses these issues. They designed "tension gauge tethers (TGTs)" consisting of DNA duplexes with a defined force tolerance.[74] In this method, a DNA duplex irreversibly denatures when subjected to forces exceeding the tension tolerance ($T_{tol}$), which depends on the number of DNA base pairs over which the force is distributed. DNA duplex is modified with FRET pairs at the opposite ends, this denaturation separates the FRET pair and induces a permanent change in the fluorescence signal.[75] With the TGT approach, force can be detected in the range of 10 to 60 pN.

### 1.3.2 DNA hairpin-based tension sensors

#### 1.3.2.1 DNA hairpin mechanics

DNA hairpin is a good candidate for tension sensor because it is responsive to mechanical forces and its mechanical property has been well characterized in prior work.[76] Most of the chemistry community is very familiar with the idea that heating double stranded DNA (dsDNA) will lead to

its denaturation into random coil single strand DNA (ssDNA). **Figure 1.10a** illustrates the reversable unfolding of a hairpin stem-loop secondary structure into ssDNA. This transition can be quantified using a temperature-controlled UV-vis spectrophotometer as the extinction coefficient of ssDNA differs from that of dsDNA, which allows one to easily determine the thermal melting temperature ($T_m$) of a transition (**Figure 1.10a**).[77] The $T_m$ of any given hairpin or duplex is highly dependent on its thermodynamic stability, i.e. the GC content, length, and other solution parameters. Interestingly, one can also melt DNA hairpins mechanically (**Figure 1.10b**) by applying external force in an orientation that pulls apart the folded structure. The probability of mechanical unfolding at any given force is dictated by how the force shifts the free energy diagram of a DNA structure. Because of the well characterized structure of B-form DNA, the melting and hybridization of a hairpin can be approximated using an ideal two-state system separated by an activation barrier (**Figure 1.10c**).[76, 78] At zero force, the folded structure is more thermodynamically stable, but as the external force is increased, the unfolded state becomes more stable. Interestingly, the applied F can shift the equilibrium, and the $F_{1/2}$, akin to the $T_m$, is defined as the force that renders these two states isoenergetic and equally probable. DNA will thus spend half its time in each state. The applied force can also accelerate the rate of unfolding by dampening the barrier to unfolding (**Figure 1.10c** and Equation 1).[79]

$$\boldsymbol{k_{unfold}(F) = k_{unfold}(F = 0)e^{\left(\frac{F\Delta x^{\ddagger}}{k_B T}\right)}} \qquad \text{Equation 1}$$

Importantly, the barrier of DNA unfolding is fairly simple and lacks complex hidden states that are characteristic of protein unfolding transitions. As a result, the time scale for hairpin unfolding transitions is typically at the msec time scale.[80, 81] This is important, as it means that hairpin tension sensors are effectively real time probes that dynamically adopt the equilibrium state in response to external force within short duration that are smaller than the time scales of biological biophysical

events. This is particularly relevant to immune receptors that display ~msec - sec bond lifetimes.[24] Much of our understanding of the biophysical chemistry of mechanical transitions in DNA come from single-molecule force spectroscopy (SMFS) measurements along with theoretical modeling.[76, 82, 83, 84] This vast library of literature provides the metaphorical "shoulder of giants" that has allowed the rational design of DNA hairpin probe as a tool for studying mechanotransduction at molecular scales.

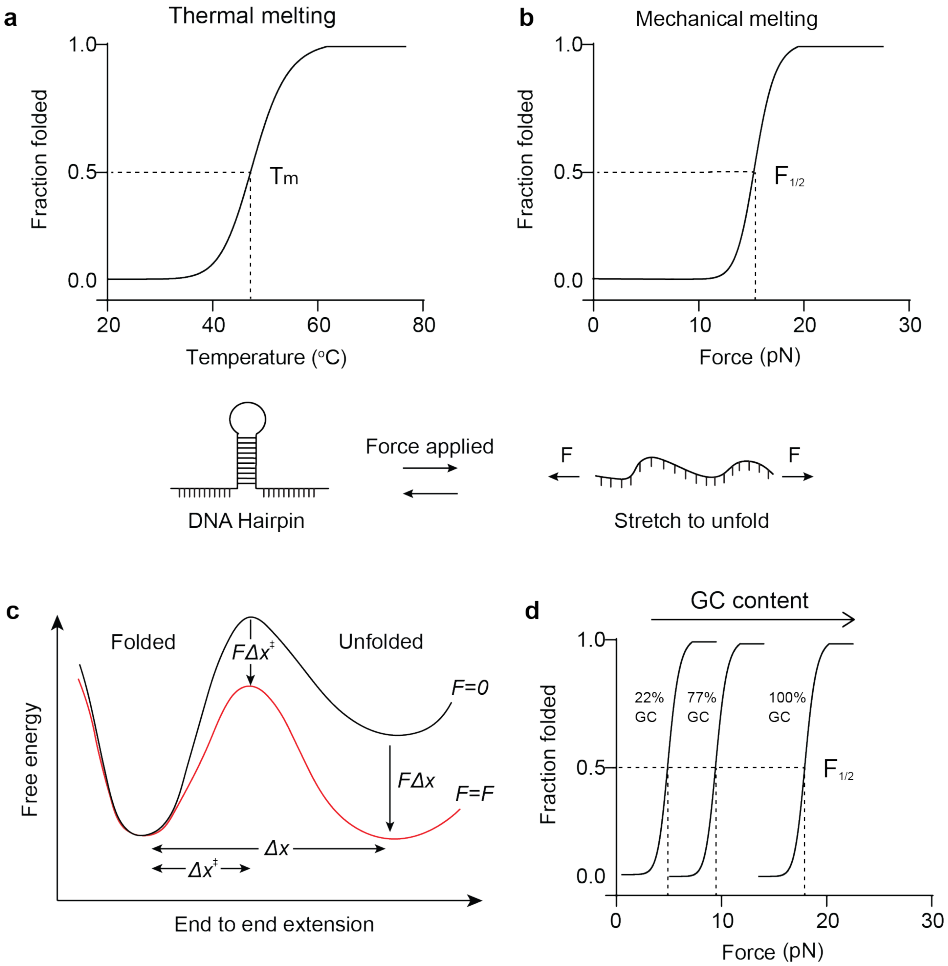


**Figure 1.10. Mechanical melting vs thermal melting of DNA hairpins**. **a-b** DNA melting curves showing that the DNA hairpin unfolds with increased temperature or increased mechanical forces. **c** Energy landscape of DNA mechanical unfolding "reaction". Applied force alters the rate and the equilibrium of the reaction by lowering the transition state energy and unfolded state energy, respectively. **d** Theoretical plot showing F1/2 increases with the GC content of the DNA hairpin stem region.

For DNA hairpin structures, the free energy change during the unfolding process under an applied F can be described as:

$$\boldsymbol{\Delta G = \Delta G_{unfold} + \Delta G_{stretch} - F\Delta x + k_B T ln\left(\frac{[unfolded]}{[folded]}\right)} \qquad \text{Equation 2}$$

When $F = F_{1/2}$, at equilibrium ($\Delta G=0$) the molecule has an equal probability of being in folded and unfolded states such that ([unfolded])/([folded]) = 1. Accordingly, equation 2 can be reorganized as the following:

$$\boldsymbol{F_{1/2} = \frac{(\Delta G_{unfold} + \Delta G_{stretch})}{\Delta x}} \qquad \text{Equation 3}$$

where, $\Delta G_{unfold}$ is the free energy for unfolding the hairpin without force. $\Delta G_{stretch}$ is the free energy for stretching the ssDNA from its folded coordinates, which can be calculated with the worm like chain model below:

$$\boldsymbol{\Delta G_{stretch} = \left(\frac{k_B T}{L_p}\right)\left[\frac{L_o}{4\left(\frac{1-x}{L_0}\right)}\right]\left[3\left(\frac{x}{L_0}\right)^2 - 2\left(\frac{x}{L_0}\right)^3\right]} \qquad \text{Equation 4}$$

where Lp is the persistence length of ssDNA (~1.3 nm), L0 is the contour length of ssDNA and equals (0.63*n) nm, x is the hairpin extension from equilibrium and can be calculated by (0.44*(n-1)) nm, where n is the number of the bases in the stem-loop of the hairpin. Note that to get $\Delta x$ in equation 3, a distance of 2 nm needs to be subtracted from x. 2 nm corresponds to the width of the DNA hairpin stem duplex where the unfolding process starts.

Considering that $\Delta G_{unfold}$ is the free energy of hybridization of the hairpin, it is dependent on the temperature, ion concentration, the GC content and length of the hairpin "stem" region. Meanwhile, these factors also affect $\Delta G_{stretch}$. By varying the hairpin sequence and stem/loop length while keeping constant ion concentration (140 mM $Na^+$, 2 mM $Mg^{2+}$) and temperature, a library of DNA

hairpins can be designed that have $F_{1/2}$ ranging from 2 pN to 19 pN (**Figure 1.9d**).[72] Note that DNA hairpin with a very short stem region have a high probability of nonspecific unfolding. We used at least 7 base pairs stem for the tension sensor design.

#### 1.3.2.2 DNA hairpin tension sensor for studying T cell forces

To map and quantify the force exerted from TCR to its antigen, in 2016 our lab applied DNA hairpin tension sensors to sensitively convert pN TCR forces into fluorescence (**Figure 1.10a**).[85] The sensor was comprised of three DNA strands: an anchor strand labeled with a quencher and a chemical moiety that immobilizes the TP onto the surface, a ligand strand labeled with fluorophore and antigen, and a hairpin with arms that were complementary to these two strands (**Figure 1.10a**). Depending on the needs, our group has employed different surface chemistries to immobilize DNA onto the substrate, including thiol-gold chemosorption (low background signal),[86] copper free click reaction (bioorthogonal),[87] and thiol-maleimide Michael addition (high reaction rate).[88] These chemistries are compatible with biological media, physically stable to withstand mechanical dissociation at the time scales of TCR forces, and afford facile and efficient chemical coupling. Streptavidin-biotin interactions are used to link the immune ligands, such as pMHC and ICAM to the DNA since the ligands can be biotinylated enzymatically with little loss in their avidity. In particular, the biotin-streptavidin interaction is considered the strongest noncovalent bond which is physically robust and can withstand the force exerted by immune receptors. When the TCR engages pMHC ligand and exerts a force greater than half the maximum force, the DNA hairpin tension probes become unfolded. This causes the fluorophore and quencher to separate, leading to the restoration of the fluorescence signal and resulting in a 20-fold increase in fluorescence intensity. In the first proof of concept experiment, our group seeded primary naïve T cells to a substrate coated with DNA hairpin tension probes that present pMHC. Upon the cells adhering to

the substrate, we observed that the DNA hairpin tension probe with a $F_{1/2}$ of 12 pN exhibited a dynamic tension signal, indicating transient TCR forces of up to 12 pN (**Figure 1.11b**). This occurred within seconds of adhesion and binding. The TCR tension signal was rapidly followed by a rise in calcium flux, which is a hallmark of T-cell activation (**Figure 1.11c**), showing the involvement of mechanical force in T-cell activation. It was also found that inhibiting the cytoskeleton activity modulated the tension signal and demonstrating that DNA hairpin unfolding arises from TCR tension, and the cytoskeleton regulates T-cell mechanics (**Figure 1.11d**). Importantly, tension was highly sensitive to co-receptor binding as well as proximal kinase activity – which further underscores that mechanics are highly regulated and related to TCR functional responses.

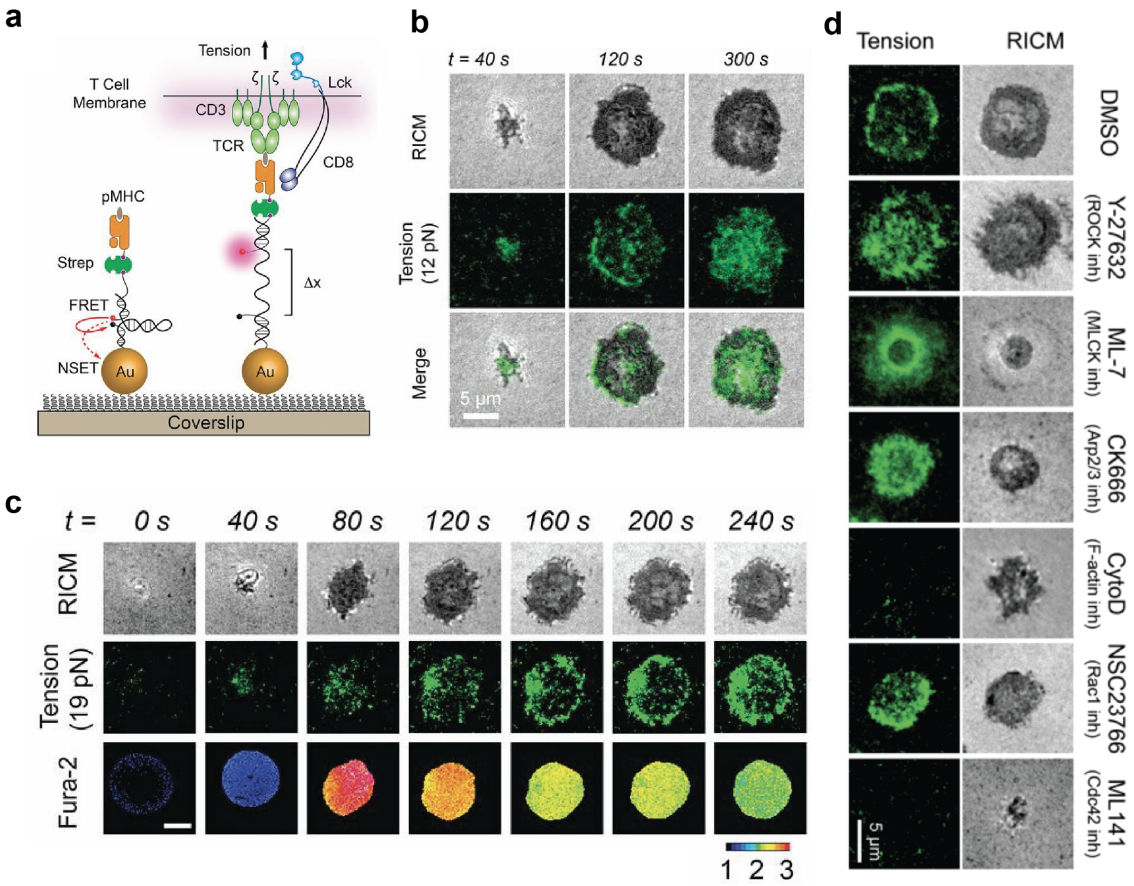

**Figure 1.11. Studying TCR force with DNA hairpin tension sensor. a** Schematic of DNA hairpin tension probes for mapping TCR-mediated tension. **b** Time lapse images showing T-cell spread on DNA hairpin tension probes surface, and 12 pN tension signal was observed underneath the T-cell. **c** TCR tension signal was correlated with calcium flux signal. **d** Representative images showing that cytoskeleton inhibitors abolished TCR tension signal. Reprinted from ref. 85 with permission.

#### 1.3.2.3 Variants of DNA hairpin tension sensors

As this field progressed, our lab and collogues incorporated other elements into probes for better investigation of forces. In most experiments, DNA hairpin sensors were directly anchored on the glass coverslip. However, glass is chemically and physically different from the cell membrane or extracellular matrix where cell adhere and generate forces. Also, sensors immobilized on glass surfaces are not mobile and thus cannot cluster when ligands on the sensors engage receptors. Clustering is an important and indispensable characteristic of receptor signaling.[89, 90, 91] To improve the physiological relevance of tension sensor, our group and others tethered DNA hairpins to a glass supported lipid bilayer (SLB) substrate, which are phospholipid membranes that self-assemble onto a glass slide and retains high lateral fluidity as to cell membrane so that sensors diffuse laterally on the surface and clusters upon engaging receptors (**Figure 1.12a**).[92, 93] With this assay, we revealed that TCR experienced forces during lateral translocation. Tolar et al. utilized a similar design and reported that B-cell receptor (BCR) transmit mechanical force to its antigen.[94, 95] It is important to note that SLBs used in these studies were created on glass substrates which has a mobile feature but the glass support is $10^9$ fold stiffer than the cell. Additionally, it possesses a flat and contiguous geometry for cell to adhere. In contrast, T cell receptor-antigen interactions occur in a physiological T cell-target cell contacts, which are highly dynamic, characterized by sporadic and curved interactions, often involving microvilli or invadosome-like protrusions. To best investigate the role of mechanical forces in T cell signaling, one need to find a way to visualize

force at authentic cell-cell junctions. Ming et al. introduced DNA hairpin tension sensors to the plasma membranes by incorporating cholesterol motifs onto the DNA terminals (**Figure 1.12b**).[96] This modification allows cholesterol to interact with the membrane lipid bilayers, effectively anchoring the DNA onto the plasma membrane. Through this design, they demonstrated the E-cadherin and integrin receptors experienced forces at cell-cell junctions (**Figure 1.12c**). However, to the best of my knowledge, there is no study trying to measure the mechanical forces at immune cell-cell junctions (immune synapse), which is a very important topic to study since more and more work suggests that immune synapse dynamics regulate T cell activation and target cell killing. Understanding the role mechanical forces involved in this process would provide new insights for immunotherapy. Additionally, despite that SLBs and cell membrane offered higher physiological relevance, the clustering of DNA hairpins introduces a challenge in accurately quantifying forces. This is because when DNA hairpins cluster, the FRET pairs located on neighboring DNA hairpins come into close proximity, potentially resulting in intermolecular crosstalk and the suppression of force-induced fluorescence emission. A portion of my thesis research is dedicated to addressing this challenge.

In addition to physiological relevance, another limitation of DNA hairpin tension sensor pertains to low signal to background ratio. As mentioned before, DNA hairpin is an irreversible tension sensor and visualize real-time receptor forces. Sometimes receptors of interest such as TCR are expressed at relatively low levels (e.g.,~$10^5$ TCRs expressed on the surface of T cell) and therefore offer a sparse density of mechanical events to image.[97] In addition, TCR-antigen interactions are highly transient with a subsec lifetimes, which is difficult to capture by CCD cameras.[24] To enhance the tension signal, one could use irreversibly ruptured DNA duplex as a tension sensor. However, DNA duplexes require as a minimum $F > 12$ pN and therefore this threshold is not

suitable for detecting weak mechanical events. To address this need, our lab developed a general strategy for force-induced binding (**Figure 1.12c**).[98] Essentially, the hairpin conceals a binding site for a "lock" oligo, but the binding is kinetically hindered by the hairpin. Only when the $F>F_{1/2}$ and the hairpin unravels is the binding site exposed. The binding prevents hairpin refolding and thus this "locking" strategy allows the DNA hairpin to accumulate force signal. The scheme in **Figure 1.12c** shows a locking DNA strand that selectively hybridizes to mechanically opened hairpin and prevents its refolding. With this strategy, the force signal at TCR-antigen bonds accumulated overtime and was enhanced ~190 fold after 10 min (**Figure 1.12c**). Apart from signal intensity, we explored alternative methods for detecting tension signals. Fluorescence lifetime represents an inherent characteristic of a fluorophore. It is influenced by the FRET effect, but unlike fluorescence intensity, it is not correlated with fluorophore intensity. Our laboratory investigated the tension map of itegrins in podosomes by monitoring the changes in the fluorescence lifetime of fluorophores attached to DNA hairpins (**Figure 1.12d**).[99]

Most force studies focus on the magnitude of forces. However, other aspects of the cell forces such as directions and spatial location also of importance to study. Accumulating evidence suggests TCR is an anisotropic mechanosensor. In optical tweezer experiments, T-cell was activated only when force was applied tangentially relative to the T cell, suggesting TCR is sensitive to shear force.[28] Alternative explanation, however, may exist. For example, tangentially pulling the bead will make the applied force unevenly distributed on TCR-pMHC complexes and concentrate the magnitude of forces at the area where fewer TCRs engage. Nonetheless, it is necessary to develop a tension probe that can sense both the magnitude and direction of molecular TCR forces to complement the TCR mechanosensor model. Our lab coupled fluorescence polarization microscopy with DNA hairpin tension probes to visualize the orientations of platelet integrin

forces (**Figure 1.12e)**.[100] This approach called molecular force microscopy could also be applied to immune cells to map the 3D orientation of TCR forces and help investigate anisotropic TCR mechanosensing. Another factor of force pertains to its spatial distribution. DNA hairpin tension sensor is capable of visualizing real-time tension and provide a tension map of the cell, but the resolution is limited. As more and more of the mysteries of receptor mechanics and its role in cell biology have been solved,[101] recent research has been pushing imaging resolution to the nanometer level for force mapping. Recently our lab and Jungmann et al. combined DNA hairpin tension probes with DNA-PAINT to visualize integrin tension signal at a resolution below 100 nm (**Figure 1.12f**).[102, 103] This technique if applied to immune cells would help resolve the mechanical events at TCR clusters composed of hundreds of TCR-antigen bonds in nm size. Another important factor of receptor forces pertains to its direction.

*For higher physiological relavance*

**a**. Supported lipid bilayer to better mimic plasa membrane

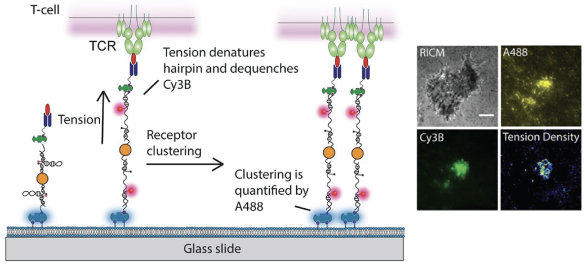


**b**. Visualize mechanical forces at cell-cell junctions

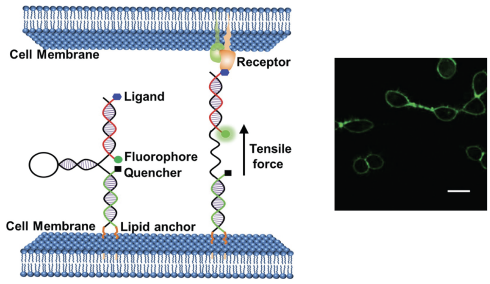


*For better force signal*

**c**. Locking strategy to amplify force signal

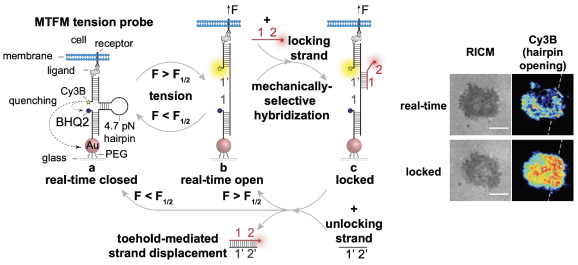


**d**. Fluorescence lifetime readouts for cluster receptor forces

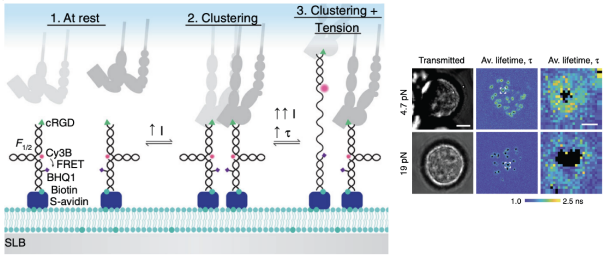


*For more force information*

**e**. Fluorescence polarization microscopy for mapping force direction

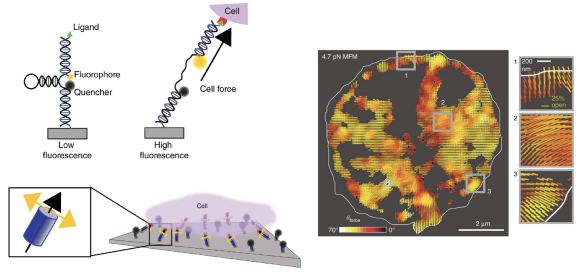


**f**. DNA-PAINT to super-resolve force events

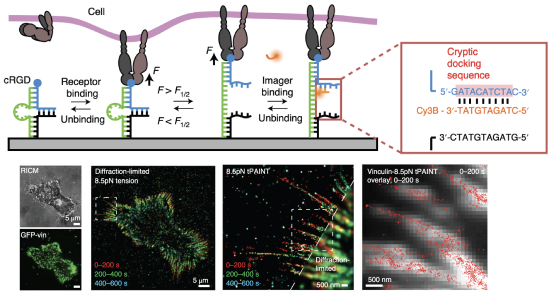


**Figure 1.12. Variants of DNA hairpin tension sensors. a** DNA hairpin tension sensor visualize force at cell-SLB interfaces **b** DNA hairpin tension sensor visualize force at cell-cell junctions. **c** A DNA strand complementary to the stem-loop region of the hairpin is introduced to "lock" mechanically open hairpin to amplify the tension signal. **d** DNA hairpin probe maps receptor forces in clusters with a fluorescence lifetime readout. **e** Combination of DNA hairpin tension sensor and fluorescence polarization microscopy to detect force directions. **f** Combination of DNA-PAINT and DNA hairpin tension sensor to map force in super resolution. Reprinted from ref. 92, 96, 98, 99, 100, 102 with permission.

### 1.3.3 DNA duplex-based tension sensors

#### 1.3.3.1 DNA duplex mechanics

In the previous section, DNA hairpins were discussed which can be reversibly extended by force, another important class of mechanically responsive probes is comprised of DNA duplexes that are irreversibly ruptured by forces in the piconewton scale.[104] The rupture force is highly dependent on the force application geometry and can be divided in to two geometries - unzipping, shearing.[105, 106] As is shown in **Figure 1.13a**, shearing of a duplex requires applying antiparallel forces to either the opposite 3' -3' or 5'-5' ends of the bound duplex while unzipping of a duplex involves applying 5'-3' pulling perpendicularly to the duplex. Because there is no connection between the two strands after separation, DNA duplex rupture under force is irreversible and hence the process is highly dependent on F duration.

For example, one cannot define a $F_{1/2}$ for the mechanical unfolding of DNA duplexes because the process is irreversible. Instead, we use the term $T_{tol}$ which is dependent on F orientation and duration.[74] Unzipping and shearing of identical DNA duplexes will lead to different $T_{tol}$. Previously, SMFS experiments done at room temperature in PBS buffer showed that the force required to open a DNA duplex in the shearing geometry is dependent on the number of base pairs (bp). Shearing $T_{tol}$ reaches a limit of ~60 pN at a length of about ~30 bp because for a long DNA, the force is only distributed onto a finite number of base pairs closed to the DNA terminus instead of all the base pairs in the whole duplex.[107, 108] In contrast, $T_{tol}$ for unzipping geometry is significantly smaller (~12 pN) because the external force is focused onto the terminal base pair, and breaks base-pairs one at a time (**Figure 1.3b**). The rupture force can be estimated using the de Gennes model which describes dsDNA as an elastic ladder held together using hydrogen bonds.[109] The rupture F is described as:

$$F = 2f_c \left[\chi^{-1} \tanh\left(\chi \frac{L}{2}\right) + 1\right]$$

where fc is the rupture force for a single bond (fc = 3.9 pN), L is the number of DNA base pairs between the two anchor points, and X-1 represents the finite length that can be calculated with the spring constant (Q) of stretched DNA backbone and spring constant (R) of the stretched hydrogen bond between base pairs. Note that several refinements to the de Gennes "toy" model have been developed and these updated models more accurately capture the sequence specific response of DNA shearing and unzipping as well as the length and temperature dependence of the force response. I would particularly encourage readers to review the work by Mosayebi et al. as this model offers an optimal match to experimental force spectroscopy results.[110] Also, recently Yan et al. investigated the duration of TGT under force and highlighted the use of TGT as a tension duration sensor to study force dynamics. [111]

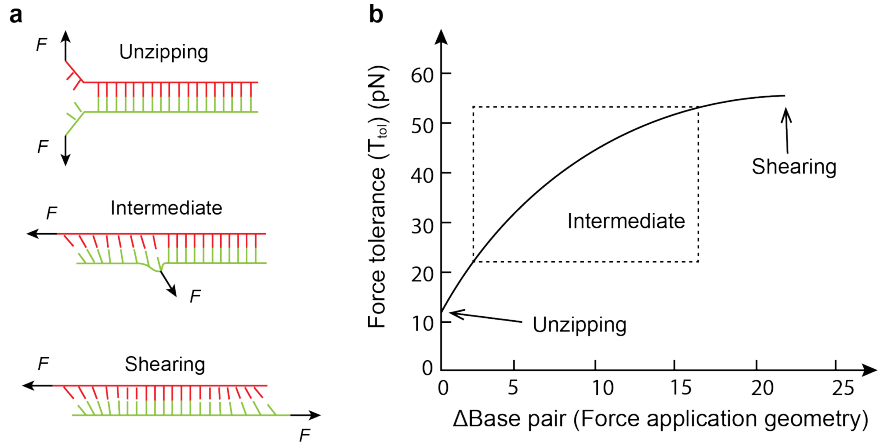


**Figure 1.13. DNA duplexes melting under force.** **a** Schematic showing rupturing a DNA duplex with different force application geometries (unzipping, shearing and intermediate). **b** Δ Base pair determines the force application geometry, and it represents the number of base pairs between force application points. Plot showing the $T_{tol}$ of a 21 mer DNA duplex increases with Δ Base pair.

#### 1.3.2.3 DNA duplex for studying T cell mechanics

In the study of mechanotransduction, it is important not only to quantify the forces acting on receptors but also to establish a correlation between these forces and subsequent signaling events. (calcium, phosphorylation, conformational changes, etc…). However, in biochemistry, a very important tool to determine causal relationships is the ability to introduce mutations at the single protein or single amino-acid level.[112] Thus, it is desirable to develop probes that induce "mechanical mutations" that modulate a force at a single ligand-receptor complex and then determine signaling consequences. To address this need, Ha and coworkers designed "tension gauge tethers (TGTs)" comprised of DNA duplexes with a defined force tolerance ($T_{tol}$) that terminates the mechanotransduction when the force exceeds the $T_{tol}$.[74] With this design, Ha and co-workers controlled the forces experienced by the Notch receptors and found that $F < 12$ pN is able to activate Notch receptors.[113] Later, our group and others applied the TGT concept to manipulate immunoreceptor mechanotransduction and demonstrated that the mechanical force is of great importance to immune responses and its presence amplifies antigen discrimination and receptor signaling.[85, 114] In this experiment, T cells were plated onto surfaces coated with TGT which has a 12 pN $T_{tol}$ and presents antigen at the terminal to engage receptors (**Figure 1. 14a**).[85] We have demonstrated using DNA hairpin tension probe that TCR transmit >12 pN forces to its antigen. With the 12 pN TGT design, the force would rupture the DNA duplex and terminate the mechanotransduction thus dampening TCR signaling. This is in contrast to the 56 pN TGTs, which remains intact under TCR force and maintain force transduction. As expected, T-cell displayed stronger Zap70 phosphorylation level (pYZAP70, marker of early TCR signaling) when spreading on 56 pN TGT antigen surfaces compare to 12 pN TGT, suggesting that the mechanical force enhanced the TCR signaling (**Figure 1.14b**). By contrast, the less potent antigens did not show

different pYZAP70 responses to forces (**Figure 1.14c** and **d**) and there was no significant difference among antigens with 12 pN TGT. This work demonstrated that mechanical forces at the TCR-antigen bonds enhance the TCR signaling and antigen discrimination.

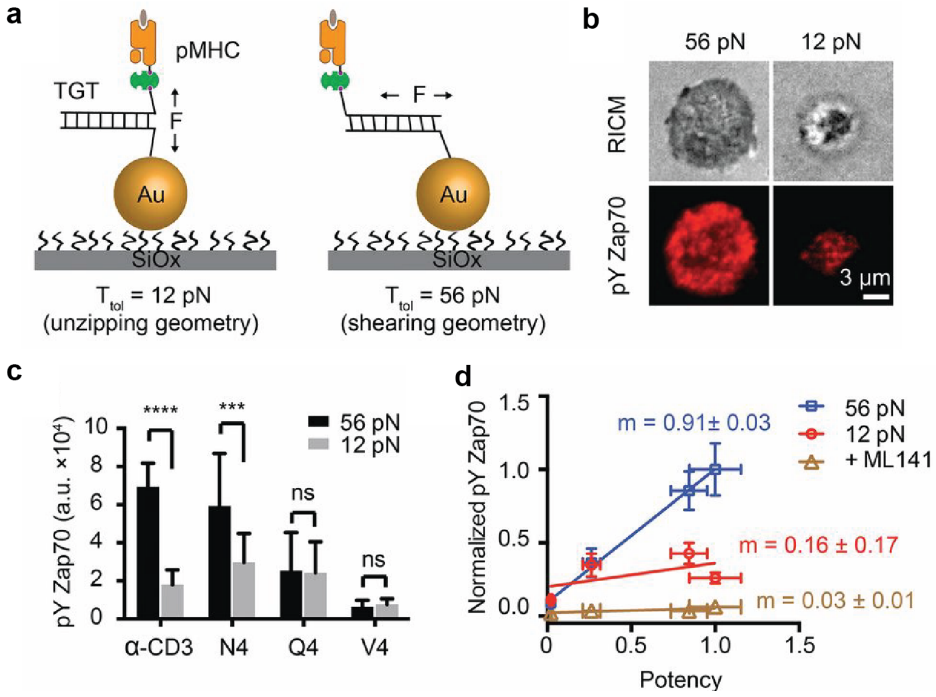


**Figure 1.14. TCR forces amplify the specificity of T-cell recognition.** **a** Schematic showing pMHC tagged TGTs can be utilized to manipulate TCR forces. The threshold of TGT is dependent on the force applying geometry which is tuneable by changing the ligand position. **b** Representative images showing stronger T-cell activation signal on 12 pN TGT surfaces compared with 56 pN TGT surfaces. **c** Bar graphs showing pYZap70 levels of T-cells seeded on surface presenting antigens with different potencies. Antigens were anchored on 12 and 56 pN TGTs. **d** Plot showing pYZAP70 levels of T-cells in response to antigens on 12 and 56 pN TGT surfaces. The slopes (m) of lines indicate the specificities of T-cells to antigens in each condition. Reprinted from ref.85 with permission.

In addition to manipulating force, TGT can be decorated with a FRET pair to detect forces exceeding its $T_{tol}$. In this method, a DNA strand is linked to a ligand and chemically modified with a quencher, while simultaneously, the complementary lower strand is modified with a fluorophore and positioned in close proximity to the quencher. This arrangement leads to the suppression of

fluorophore emission in an inactive state. When a receptor engages the ligand and transmits force, if the force exceeds the $T_{tol}$, the probe ruptures. This rupture causes the separation of the quencher from the fluorophore, triggering a sustained "turn-on" signal (**Figure 1.15a**). In 2017, Wang et al. covalently conjugate an integrin peptide ligand (RGD) to the TGT and anchor TGT to glass surface through streptavidin-biotin interactions. This design, named integrative tension sensor (ITS), was used to measure the forces experienced by integrin receptors on the platelets.[75] Their research revealed that platelets generate forces ranging from 12 to 54 pN during adhesion and exceeding 54 pN during contraction (**Figure 1.15b**). Subsequently, this design was extended to study integrin forces generated by fibroblasts, keratocytes and epithelial cells, and cadiomyocyte.[115, 116, 117, 118] The force signal was observed to be linked to cytoskeletal proteins, including talin, myosin, vinculin, and F-actin, indicating their involvement in the generation and transmission of forces (**Figure 1.15c**). Despite its advantages such as a high signal-to-noise ratio and a broad force detection range, the "turn-on" TGT method has not yet been utilized for the study of T cell forces. It's important to note that, unlike integrin ligands that can be conveniently represented by the RGD peptide motif, ligands for receptors on the T cell membrane feature complex binding sites. These ligands need to be employed in their native and unaltered state to effectively engage with the receptors. These proteins can be expressed in a biotinylated form and attached to TGT using streptavidin interactions. However, an alternative approach must be developed for anchoring TGT onto the substrate and must be designed to be compatible with the specific context of T cell mechanical behavior.

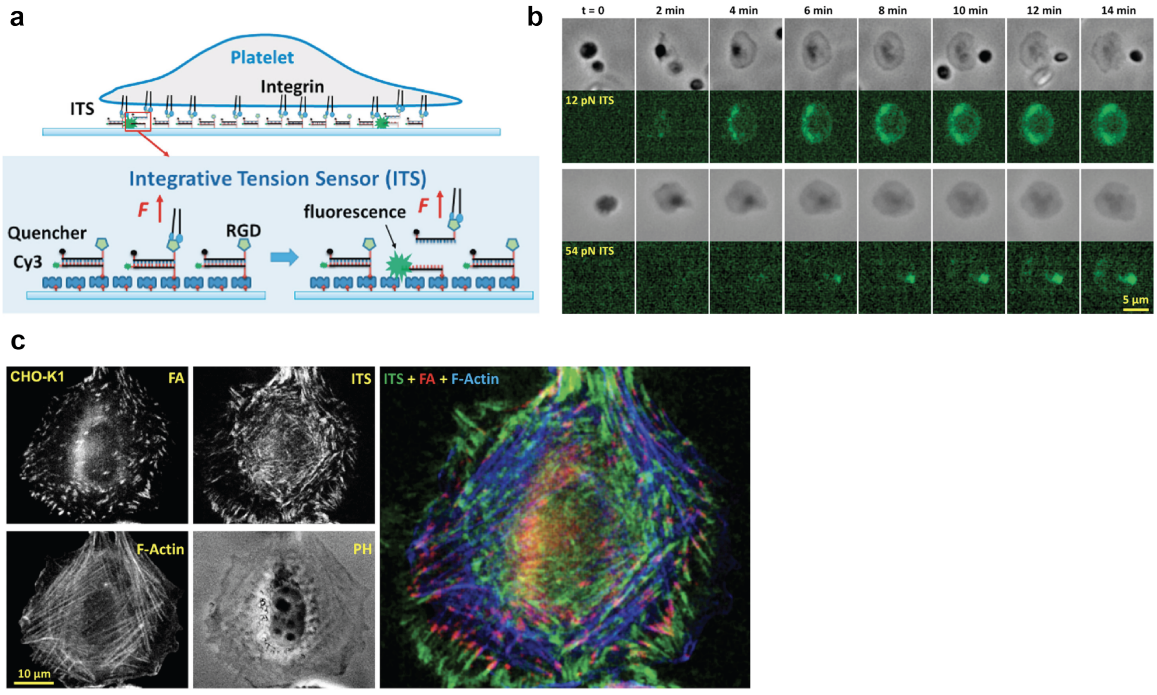


**Figure 1.15. Turn-on TGT tension sensor to detect integrin forces. a** Schematic showing that TGT tension sensor (integrative tension sensor) detect force with a turn-on fluorescence response. **b** Time lapse images showing platelet generate different levels of forces during adhesion and contraction process. **c** Representative images showing the tension signal is associated with the focal adhesion proteins (vinculin) and actin. Reprinted from ref. 115-116 with permission.

### 1.3.2.3 Variants of DNA duplex tension sensors

Similar to DNA hairpin tension sensors, several techniques developed afterwards to enhance the effectiveness of TGT design for investigating cellular forces. These improvements primarily revolved around two aspects: signal resolution and signal intensity. To increase the resolution, Zhao et al. performed multiple cycles of tension imaging, in each cycle to first localize and then photobleach the active fluorophore which was separated from quencher by force. By superposing tens of frames into one, they obtained a force image of platelet integrin force with 50 nm resolution (**Figure 1.16a**).[119] However, it is important to ensure that in each frame, the tension signal spots

are sufficiently dispersed for accurate localization. However, this can pose challenges when there is a high density of receptors or TGT tension sensors on the cell membrane and surface, respectively. Later, our lab applied DNA-PAINT technique to TGT.[102] In this method, cells were permitted to spread continuously on TGT-coated surfaces. Following this, an imager DNA strand, which was partially complementary to the exposed ssDNA regions on TGT, was applied to super resolve force events (**Figure 1.16b**).

Given the established significance of mechanical forces in cell signaling, the mechanical activity of cells can serve as a valuable predictor for various aspects of a patient's health. For instance, research has shown that the measurement of a patient's platelet traction force can forecast the necessity for a blood transfusion.[120] Additionally, mechanically active T cells have demonstrated heightened effectiveness in targeting and killing tumor cells.[121] Leveraging traction force signals could potentially lead to improved therapeutic outcomes in clinical settings. However, force signals are typically weak and require analysis using high-resolution fluorescence microscopes, which are not readily available in many laboratories or hospitals. To make these measurements more accessible, there is a need to amplify the tension signal so that it can be analyzed using more readily available instruments, such as a plate reader. To achieve this goal, our lab took advantage of the exposed ssDNA when TGT is ruptured by force and conducted reaction on it to further generate massive but force specific fluorescence signal. For example, exposed ssDNA can serve as a primer for rolling circle amplification (RCA), which can amplify DNA by generating long-tandem DNA repeats.[122] Fluorescent DNA strands that are complementary to these repeats are then introduced to bind with them, resulting in a strong force-specific fluorescence signal that can be detected using a plate reader (**Figure 1.16c**). Another approach involves using the exposed ssDNA as an initiator to initiate a local DNA hybridization chain reaction, leading to an accumulation of

the fluorescence signal (**Figure 1.16d**).[123] More recently, we also employed the exposed strand as an activator DNA to trigger CRISPR-Cas12a, which cleaves the surrounding DNA strands containing fluorophore-quencher pairs. This cleavage releases the fluorophores, resulting in a robust fluorescence readout for analysis (**Figure 1.16e**).[124]

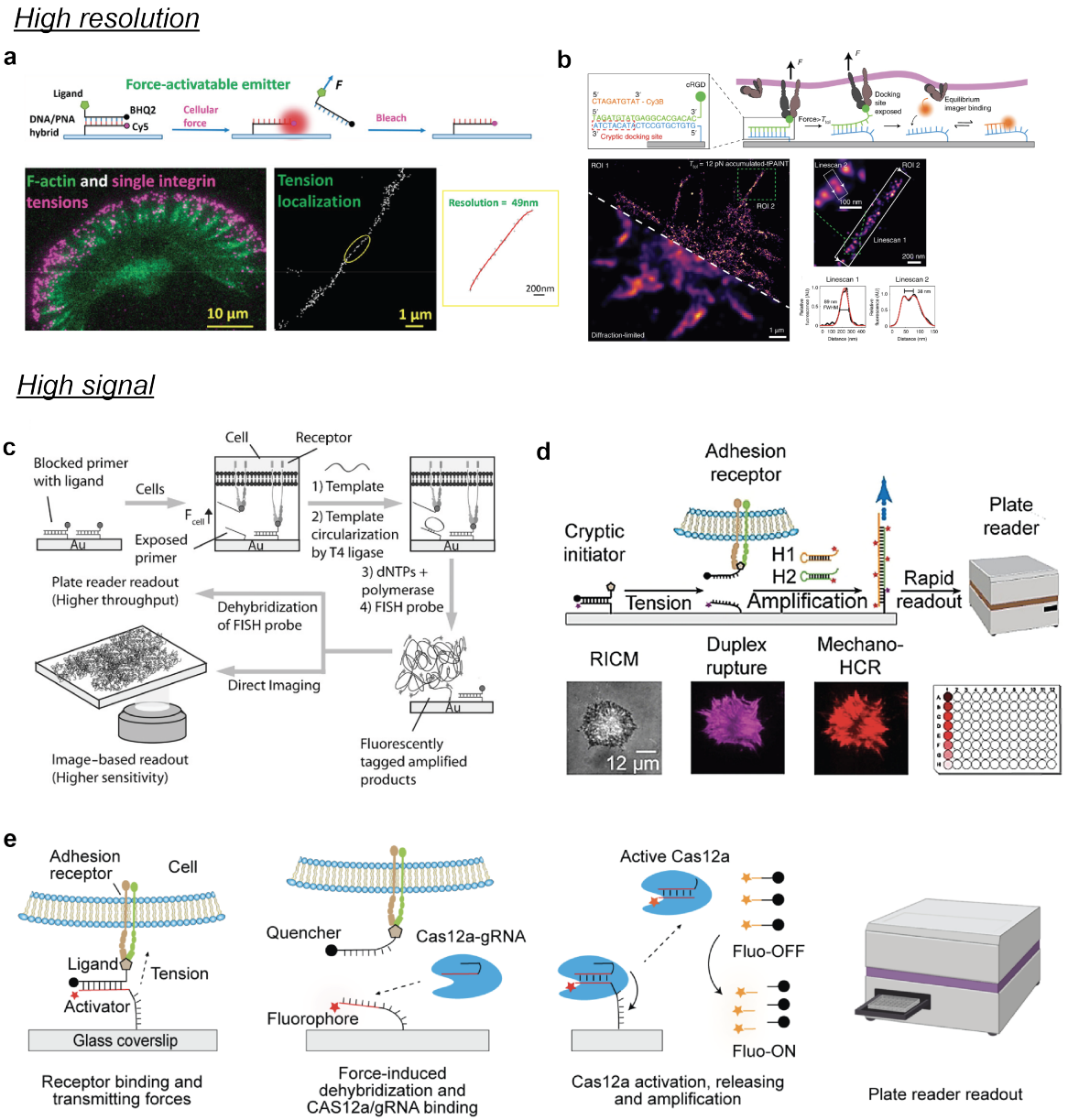


**Figure 1.16. Variants of Turn-on TGT tension sensor.** **a** Multiple imaging-bleaching cycles to reconstruct single intergern force map. **b** DNA-PAINT technique to super-resolve mechanically rupture TGTs. **c** Perform RCA reaction on mechanically exposed ssDNA to amplify force signal.

**d** Perform hybridization chain reaction on mechanically exposed ssDNA to amplify force signal. **e** Mechanically exposed ssDNA serves as a activator to activate Cas12a-gRNA to cleave reporter DNA, releasing fluorophores to amplify force signal. Reprinted from ref. 102, 119, 122-124 with permission.

### 1.4 Aim and Scope of the Dissertation

In the adaptive immune response, killer T cells crawl across cells and tissues scanning the surface of target cells using the TCR to seek specific cancer antigens and help eradicate tumors. Emerging evidence strongly suggests that mechanical forces play a pivotal role in governing T cell recognition and the subsequent immune response. Researchers have started harnessing the mechanical properties of T cells to identify stimulatory TCR/antigen interactions and potent T cells for use in immunotherapy.[125] However, there is still a significant gap in our understanding: the exact magnitude of the mechanical forces that receptors on the T cell membrane experience and how these forces govern T cell signaling remain largely unknown. Addressing these questions is of paramount importance, as it can offer groundbreaking insights into the mechanoregulation of T cell responses and push the boundaries of mechanical immunotherapy.[126] Over the past decade, there have been significant advancements in the development of molecular tension sensors designed to measure and manipulate the forces experienced by receptors. The application of tension sensors within the T cell system has faced certain limitations. Typically, these tension sensors have been anchored on synthetic substrates based on glass, aiming to mimic the extracellular matrix or cell plasma membrane where cells spread and generate force. However, these substrates do not accurately represent the dynamic and non-planar nature of the immunological synapse formed during interactions between T cells and target cells.[127] In reality, the immunological synapse involves various protrusions and is a highly dynamic structure. Secondly, the current methods for characterizing these mechanical forces rely on microscopy,

which is both low-throughput and time-consuming. As a result, these methods are not suitable for clinical applications or large-scale studies. Thirdly, while many investigations have delved into T cell mechanics, they have predominantly focused on the T cell receptor (TCR). Other receptors such as LFA-1 and CD28 have also been identified as crucial players in T cell mechanosensing,[65, 128] but their mechanical properties have not been thoroughly studied.

In my doctoral research, I developed a series of innovative platforms and DNA-based structures designed to address these critical questions. **Chapter 2** introduces a DNA based microparticle tension sensor which allows to measure T cell forces at non-planar geometries as well as enables the high throughput quantification of force with flow cytometry. **Chapter 3** describes a DNA origami nanodevice that improves the accuracy and physiological relevance of force measurement. This nanodevice is inserted onto fluid membranes and immune cell plasma membranes, allowing for the determination of the magnitude of TCR forces and their sources. Furthermore, I demonstrated the potential utility of this design for antigen screening. **Chapter 4** focuses on the investigation of LFA-1 mechanics. This involves the measurement of forces at the LFA-1-ICAM interface and the deciphering of LFA-1's role in processes such as antigen discrimination, TCR signaling, and cytotoxic killing. Finally, **Chapter 5** will summarize my doctoral research and highlight some intriguing questions that remain to be answered and outline several promising directions to push the frontier of immunomechanobiology.

# Chapter 2. DNA-based Microparticle Tension Sensors (μTS) for Measuring Cell Mechanics in Non-planar Geometries and for High-throughput Quantification

Adapted from Hu, Y.; Ma, V.; Ma, R.; Chen, W.; Duan, Y; Glazier, R; Petrich, B; Li, R and Salaita, K. DNA-based Microparticle Tension Sensors (uTS) for Measuring Cell Mechanics in Non-planar Geometries and for High-throughput Quantification. *Angew. Chemie.,* **2021**, 60, 18044-18050 Adapted with permission.

## 2.1 Abstract

Mechanotransduction, the interplay between physical and chemical signaling, plays vital roles in many biological processes ranging from cell differentiation to metastasis. The state-of-the-art techniques to quantify cell forces employ deformable polymer films or molecular probes tethered to glass substrates. These types of flat substrates limit applications in investigating mechanotransduction on non-planar geometries where physiological activities such as phagocytosis and immunological synapse formation mostly occur. A second challenge is the low throughput of microscopy readout which limits the application of current assays in fundamental and clinical research. We address these challenges by developing a DNA-based microparticle tension sensor (μTS), which features a spherical surface and thus allows for investigation of mechanical events at curved interfaces or within groups of cells in suspension. Importantly, the micron-scale of μTS enables flow cytometry readout, which is rapid and high throughput. To demonstrate the scope of μTS, we applied the method to map and measure T-cell receptor (TCR) forces and platelet integrin forces at 12 and 56 pN thresholds. Furthermore, we quantified the inhibition efficiency of two anti-platelet drugs providing a proof-of-concept demonstration of μTS to screen drugs that modulate cellular mechanics.

## 2.2 Introduction

Cells function as force generators and sensors, constantly transmitting molecular forces to their extracellular matrix ligands and adjacent cells. These mechanical forces are generated by actomyosin contractility and actin polymerization and play vital roles in numerous activities throughout the lifetime of a cell including adhesion, migration and differentiation.[129, 130] Mechanotransduction, or the coupling between mechanical forces and biochemical signaling, is mediated at the molecular level through individual receptor-ligand bonds.[131, 132] To date, many

strategies have been developed to measure cell forces. Amongst them, traction force microscopy (TFM) maps force at the single cell and subcellular length scale by tracking deformation of elastic substrates underneath cells.[133, 134, 135] However, the length scale and force range of these methods are limited to μm and nN respectively, thus hindering high resolution imaging and investigation of mechanotransduction at the molecular (pN) level. To measure the receptor forces applied to individual ligands, our lab previously developed molecular tension fluorescence microscopy (MTFM), in which "spring-like" extendable molecules, such as polymers of PEG with defined lengths,[67] proteins,[69] and DNA hairpin,[72] are engineered as fluorescence force sensors and generate turn-on fluorescence signal in response to molecular forces transmitted by cells through their membrane receptors. A complementary method to MTFM that was originally developed to manipulate cell forces, and then later adapted to recording cell force history is the DNA-based tension gauge tether (TGT) which was developed by Ha and colleagues.[74] In this method, a DNA duplex is irreversibly denatured when it experiences forces that exceed the tension tolerance ($T_{tol}$), causing a change in fluorescence signal. Unlike thermal or chemical denaturation, the mechanical energy that leads to DNA denaturation is highly dependent on force orientation. For example, the Ttol value is maximum (~60 pN) when a duplex experiences forces in a shearing geometry, with forces parallel to the long axis of the duplex; in contrast, forces perpendicular to the duplex, in an unzipping geometry, lower the Ttol to ~10 pN. Fluorophore labeled TGTs anchored to a glass coverslip and imaged using high-resolution fluorescence microscopy have been used to study many pathways including integrin,[75] T cell receptor,[85] and Notch receptor signaling.[74]

Molecular methods such as MTFM and TGT, hold great promise for force quantification and elucidation of molecular mechanism in mechanobiology, but they are performed on planar coverslips whereas physiological cell activities such as the immunological synapse (IS) formation

and phagocytosis occur on non-planar geometries and have reported to depend on the curvature of the substrate.[136, 137] According to recent work, this dependency may be attributed to enhanced mechanical activities such as actin polymerization at curved membranes.[138] To fill this gap in knowledge, we are aiming to develop a force sensor that allows one to investigate mechanotransduction on non-planar geometries. A number of groups, including Ning et al.,[139] Ingber et al.,[140] Theriot et al.[141] and Moraes et al.[142] have developed force-deformable microspheres to investigate cellular forces in processes that range from phagocytic engulfment to 3D cell spheroid mechanical homeostasis. However, these particles do not reveal the forces transmitted by individual receptor-ligand complexes, which is required to elucidate the molecular mechanisms of mechanobiology. A general problem that pertains to current molecular probes as well as these dispersible microparticle force sensors is their reliance on microscopy-based characterization, which is limited in throughput and at best, may allow for measuring tens to hundreds of samples per day. Ideally, molecular force measurements need to be increased in throughput to facilitate screening of biological samples and for efficient screening drugs that modulate mechanics.

Herein, to address these challenges, we developed a DNA-based microparticle tension sensor (μTS), where probes are immobilized on cell-sized dispersible particles that enables analysis of cell forces on non-planar interfaces as well as in high throughput by flow cytometry. We created μTSs displaying different ligands to engage cells that generate a fluorescence signal in response to forces transmitted through receptor-ligand bonds at the cell surface, which were then visualized by high resolution microscopy. Complementing force microscopy performed on planar substrates, μTS provides a novel geometric tool to measure cell forces generating on curved geometries, and thus may allow one to investigate mechanotransduction on curved interfaces and help understand

how curvature influences mechanical events. We characterized TCR forces in a hybrid immunological synapse (IS) formed between μTSs and T-cells using confocal microscopy and found that force signals were concentrated in a ring- like pattern and colocalized with the enriched actin filaments. This finding is consistent with the centripetal force observed along the cell edge in micropillar array and the actin enrichment at the periphery of IS formed on support lipid bilayer.[143, 144] In addition to 3D high resolution imaging, the cellular scale of μTS enables flow cytometry-based high throughput characterization. We applied this assay to measure platelet forces, revealing that integrin receptors transduce forces up to 56 pN. Since high throughput analysis is of significant interest for drug screening, we further applied μTS to investigate how drugs modulate cell traction forces. The mean fluorescence intensity of μTS was observed to decrease with increasing drug dose, showing the utility of μTS in screening drug that modulates cell mechanics. μTS measured mechanical inhibition (mechanical $IC_{50}$) for Y-27632 and eptifibatide are 2.1 and 3.2 μM, respectively, for mouse platelets. These mechano-$IC_{50}$ values are consistent with literature values determined using indirect readouts such as secondary messenger signaling and cell aggregation phenotypes.[145, 146]

## 2.3 Result and discussion

### 2.3.1 Design, synthesis and characterization of μTS

μTSs were constructed by immobilizing molecular tension probes on cell-sized silica microparticles. Here, we chose fluorophore-quencher labeled TGTs (**Figure A2.1**) as tension probes because these provide an irreversible signal that accumulates with time, and thus generating greater levels of signal/noise compared to that of real- time MTFM probes. In principle, one can select a wide variety of microparticle materials that can be employed as a scaffold for μTS. The most desirable materials are monodisperse, show low autofluorescence, and afford facile and

efficient chemical coupling to nucleic acids. Based on these criteria we used amine-modified silica beads with a diameter of 5 μm. We covalently linked the DNA probes to the particle using thiol-Michael reaction to immobilize thiolated-TGTs onto maleimide-modified spherical surfaces (**Figure A2.2**).[147] Recent measurements showed that this bond can withstand forces up to 100's of pNs in aqueous environments.[148] By tuning the thiol position on the TGT, and hence controlling the geometry of anchoring (shearing versus unzipping), we tuned the $T_{tol}$ of the 21 base pairs TGT from 12 pN in the unzipping geometry to 56 pN in the shearing geometry. Probe sensitivity was optimized by selecting fluorophore-quencher pairs with the highest quenching efficiency. Cy3B-BHQ2 showed QE of ~95%, and thus generate a ~20-fold enhancement in signal upon mechanical denaturation (**Figure A2.3**). The TGT grafting chemistry was optimized such that the probe density on the spherical surfaces was 3660+/-200 molecules/μm2 (**Figure A2.4**). This probe density is markedly greater than the TCR receptor density on T cells, and is at the same order of magnitude as the density of $a_{II}b_3$ integrin receptors on platelets, and thus guarantees effective ligand presentation and robust interaction between μTS and cells.[30, 149]

### 2.3.2 Visualizing TCR mechanics in hybrid immunological synapse formed with spherical μTS

Tension probes were first validated using lymphocytes cultured on planar surfaces. To study primary CD8+ T cell receptor forces, we employed the peptide major histocompatibility complex (pMHC) antigen that was loaded with the ovalbumin (OVA) derived 8-mer peptide: SIINFEKL (N4 peptide). The C-terminus of the pMHC antigen was modified with a biotin ligase sequence that allowed for conjugation to the TGT with biotin-streptavidin. In these experiments, naïve CD8+ cells were harvested from OVA-specific TCR transgenic mice (OT-1) and were then plated on glass coverslips presenting N4 peptide tagged 12 pN and 56 pN TGT probes. (**Figure A2.5**). Strong

fluorescence (up to 5-fold over background) was exclusively observed underneath the cells engaged with 12 pN TGT surfaces, but not with the 56 pN TGT surfaces, indicating that TCR forces did not exceed 56 pN. Given that the thiol-maleimide anchored TGTs generated robust signal in response to TCR forces on planar surfaces, we next constructed μTS that displayed N4 peptide tagged TGT to investigate mechanical events occurring at the curved cell-μTS junction (**Figure 2.1a**). To facilitate sequential modifications and microscopy imaging, μTSs were immobilized on the glass coverslip through click reaction (**Figure A2.6**). Afterwards, naïve CD8+ T-cells were plated on μTS coated surface and incubated for 30 min to allow cells to form adhesions on μTS. By focusing on the z-position that roughly corresponds to the mid-section of the junction (~2.5 μm above the coverslip), strong turn-on signal (up to 6-fold over background) was observed at the junction between T-cell and 12 pN μTS (3 independent experiments, 20 μTS-cell binding events **Figure 2.1b** and **2.1c**). Note that we did not detect significant tension signal for the 56 pN μTS particles, showing that even in the spherical geometry, TCR-pMHC forces do not achieve peak forces exceeding 56 pN. This experiment serves as an additional control since the thermal melting temperature of the 56 pN μTS is identical to that of the 12 pN μTS probes.

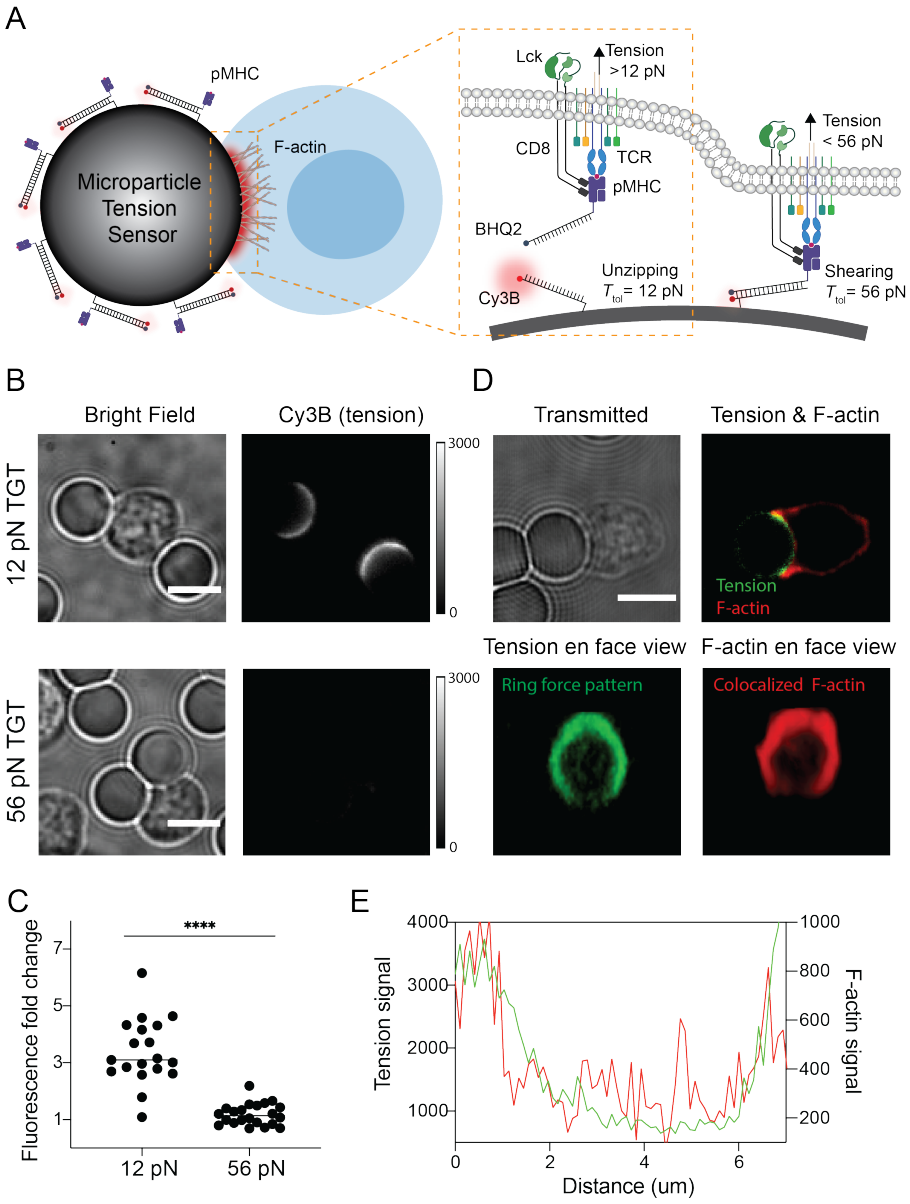


**Figure 2.1. Mechano-imaging of TCR forces on spherical surfaces. a** Schematic of μTS for mapping TCR forces transmitted through TCR-pMHC bonds at cell-μTS junctions. **b** Representative bright field and Cy3B fluorescence images showing adhesion and tension signals localized at junctions between T-cells and 12 pN μTS. **c** Plot showing fluorescence intensity fold change of junctions on μTS compared to background. Each dot represents single junctions from 3 different animals in independent experiments. **** indicates p<0.0001. **d** Representative confocal images showing ring-like tension signal (green) and F-actin signal (red) at T-cell-μTS synapse. (E) Linescans of F-actin signal (red line) and tension signal (green line) at the interface from junction shown in d. Scale bars = 5 μm.

The 12 pN tension distribution across the hybrid immunological synapse was further resolved by z-stack reconstruction of confocal images. As shown in **Figure 2.1d**, cells that encountered the μTS spread and engaged the particle surface that in some cases covered an area that was ~ 1/4 of the entire particle, as determined by the tension signal. Strikingly, the tension signal showed a ring-like spatial pattern that coincided with the cell perimeter, suggesting that TCR-pMHC mechanical events accumulate at the periphery of the T cell-antigen presenting cell junction. A similar geometric pattern was observed on planar surfaces modified with molecular tension sensors presenting pMHC ligands (**Figure A2.3**). This force pattern is consistent with our prior MTFM measurements as well as the centripetal forces observed along the cell edges on micropillar arrays.[85, 92, 144] Since actin polymerization and actomyosin contraction play important roles in force generation,[2, 130] we next investigated the colocalization between actin filament and tension signal. After allowing cells to spread on the spherical and planar surfaces, cells were fixed and stained with the SiR-Actin stain (dye conjugated to F-actin stabilizing macrocycle). As expected, at the same z position, F-actin and tension signal were colocalized and both enriched at the edge of interface (**Figure 2.1d-e** and **Figure A2.7**). 3D view of F-actin obtained by combining z-stack images showed a ring-like pattern similar to the ring-shaped force signal pattern (**Figure 2.1e** and **Movie A2.1**).

### 2.3.3 Mapping platelet adhesion forces by μTS

We next aimed to broaden the scope of the μTS platform by applying it to investigate force transmission through integrin receptors on a mouse platelet model. Platelets are small (1-2 micron) anuclear blood cells that play key roles in hemostasis including coagulation. Each platelet presents tens of thousands of integrin receptors (primarily αIIbβ3) that selectively bind to fibrinogen, the third most abundant protein in the blood plasma, which leads to platelet-to-platelet aggregation

and contraction at the injury sites.[150] Our lab previously employed DNA hairpin-based MTFM and TGT probes to investigate integrin forces applied by human platelets, demonstrating that integrin transmit up to 19.3 pN to its ligand. These forces are important to platelet activation and aggregation.[98] The results from the TGT showed that platelet integrins can apply peak forces that exceed 56 pN. Wang et al. confirmed this conclusion, and by using turn-on TGTs, they showed that integrin receptors in canine platelets can shear and unzip the TGT probe, with greater signal in the unzipping mode.[75] However, these experiments were performed on isolated platelets (non-aggregated) engaged to planar glass surfaces. The collective aggregation of platelets that are bridged by fibrinogen will likely modulate the magnitude of molecular forces applied to ligands on a particle surface. Here we created μTS displaying cyclized RGD, which was conjugated to TGT top strand by Cu(I)-catalyzed azide-alkyne cycloaddition (CuAAC) (**Figure A2.2**). The goal was to investigate aggregated mouse platelet integrin mechanics on a non-planar geometry (**Figure 2.2a**).

In a typical experiment, μTS were incubated with millions of mouse platelets at approximately 1:50 ratio in Tyrode buffer supplemented with 10 μM adenosine diphosphate (ADP), 2 mM MgCl2 and 1 mM CaCl2 for 30 min to allow platelets to adhere and form aggregates on μTS surface (**Figure 2.2b** and **c**). Afterwards, forces transmitted by the platelet integrin receptors to μTS were visualized using epi fluorescence microscopy. As shown in **Figure 2.2b**, up to a 10-fold fluorescence increase was observed with the 12 pN μTS. The tension signal was primarily localized to the particle-platelet junctions. In contrast, when we employed the shearing, 56 pN μTS, there was weak tension signal suggesting that only small subset of receptors transmitted peak forces $F > 56$ pN in these conditions. The brightest particles in the 56 pN case showed a 3-fold intensity increase (**Figure 2.2c**). These results indicate that platelets within aggregate transmit

similar integrin traction forces compared to the levels observed for single platelets engaged to planar glass slides. In addition, this result dispels the prediction that untether beads engaged to aggregates of platelets linked by fibrinogen would experience diminished tension.

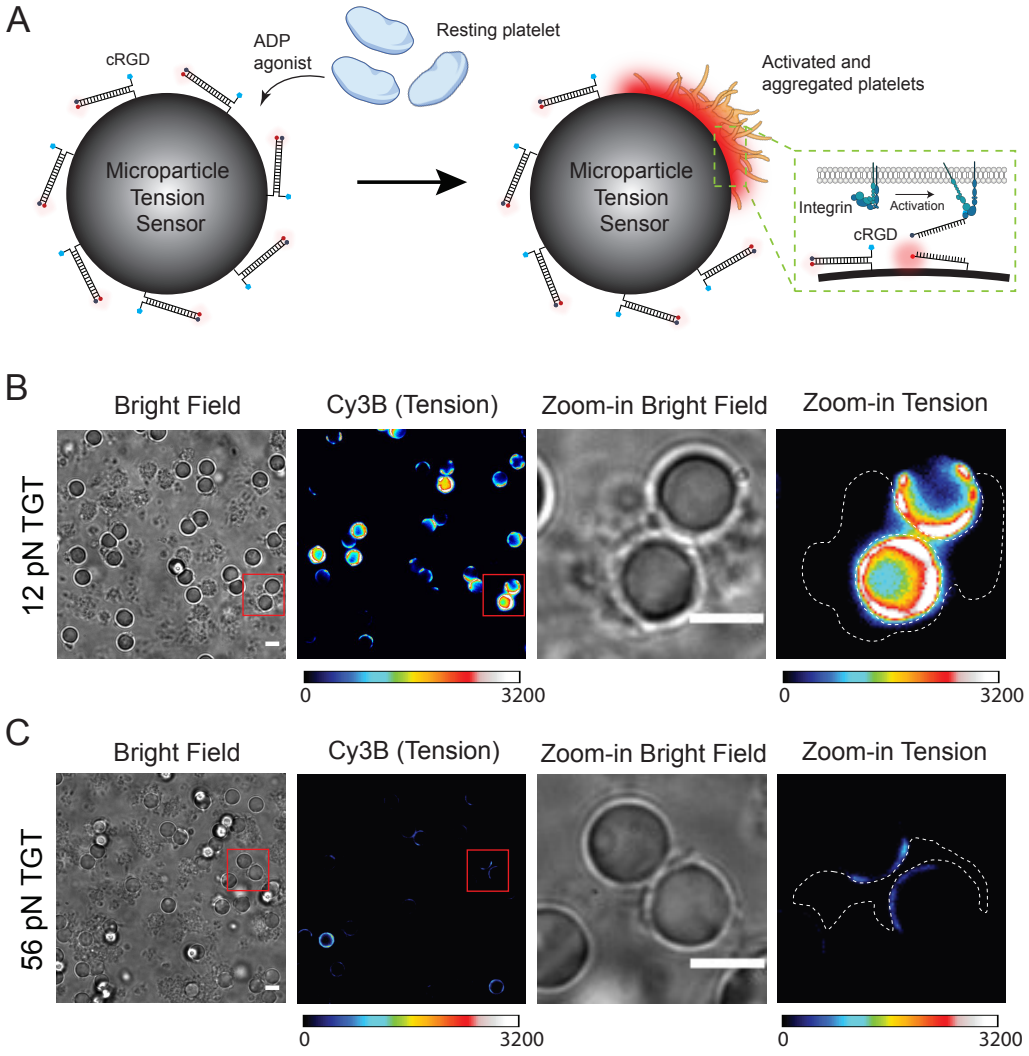


**Figure 2.2. Visualizing integrin forces with µTS. a** Schematic showing how µTS reveals platelet integrin tension through cRGD coated DNA probes on the µTS. **b** Representative bright field and tension images of 12 pN µTS-platelet complexes. The platelets were mixed with µTS for 30 min and then imaged. **c** Representative bright field and tension images of 56 pN µTS-platelet complexes. The images in B and C are displayed at identical contrasts and can be compared directly. Scale bars = 5 µm.

### 2.3.4 Quantifying integrin forces in high throughput by μTS

Since μTSs efficiently interact with platelets and exhibit strong fluorescence signal in response to integrin forces, we next wondered whether the force signal recorded on the surface of individual particles could be quantified in a high throughput fashion using flow cytometry. In principle, the micrometer diameter of the probes strongly suggests that it would be amenable to flow cytometry analysis. Prior work by Tom Soh and colleagues showed that flow cytometry of microparticles can be used for screening libraries of nucleic acids to identify improved aptamers and deoxyribozymes.[151] Moreover, flow-based analysis is widely used in immunology and cell biology to characterize heterogenous cell populations.[152, 153] This precedent provides the rationale and motivation for pursuing flow-based analysis to study molecular mechanobiology. To the best of our knowledge, this approach would represent the first example of using flow cytometry to quantify molecular mechanics of cells in high throughput.

In the suspension, the number of platelets was significantly larger than that of μTS, and the aggregate size was heterogeneous, gating discrete stoichiometries of cell-platelet assemblies was not possible. Therefore, after 30 min incubation at room temperature, we lysed all platelet aggregates and then collected μTS particles for flow cytometry analysis. After adding lysis buffer, all aggregates disappeared rapidly (~min) (**Figure 2.3a** and **Figure A2.8**). μTS fluorescence remained stable in the lysis buffer for at least 15 min, indicating that this buffer did not lead to DNA denaturation (**Figure A2.8**). In light of this, we next acquired 10,000 μTS events through flow cytometry and quantified the force signal by comparing the mean fluorescence intensity (MFI) of these events to that of μTS that were not incubated with platelets but subjected to the lysis buffer protocol (**Figure 2.3b**). We found that the MFI of 12 pN μTS monomers increased 90±7% after binding to platelets while 56 pN μTS monomers only increased 39±9% (3 independent

experiments, **Figure 2.3c**). This result is highly consistent with microscopy readouts (**Figure A2.9**). As a negative control, μTS coated with TGT tension probe presenting cyclized RAD peptide weakly engaged platelets and exhibited negligible fluorescence change (**Figure A2.10**). These results show that platelet integrin receptors apply peak forces in the range of 12 to 56 pN, with a small subset of receptors transmitting forces that exceed 56 pN. To further demonstrate the advantage of μTS flow readout compared to that of microscopy-based methods, we also tested the potential for barcoding and multiplexing multiple levels of force in a single experiment (**Figure A2.11**). Here, we spectrally encoded the 12 pN and 56 pN μTS probes and mixed these with platelets. The barcoded μTS confirmed our single color experiments with 12 pN signal far exceeding that of the 56 pN signal. Past AFM work showed that the contractile forces applied by platelets are proportional to the stiffness of the substrate,[62] and given that molecular probes on the μTS experience similar forces to probes anchored on planar glass slides, this suggests that the platelet integrins are sensing the local mechanical properties of the silica particle and forces are not dampened due to having the particles in suspension.

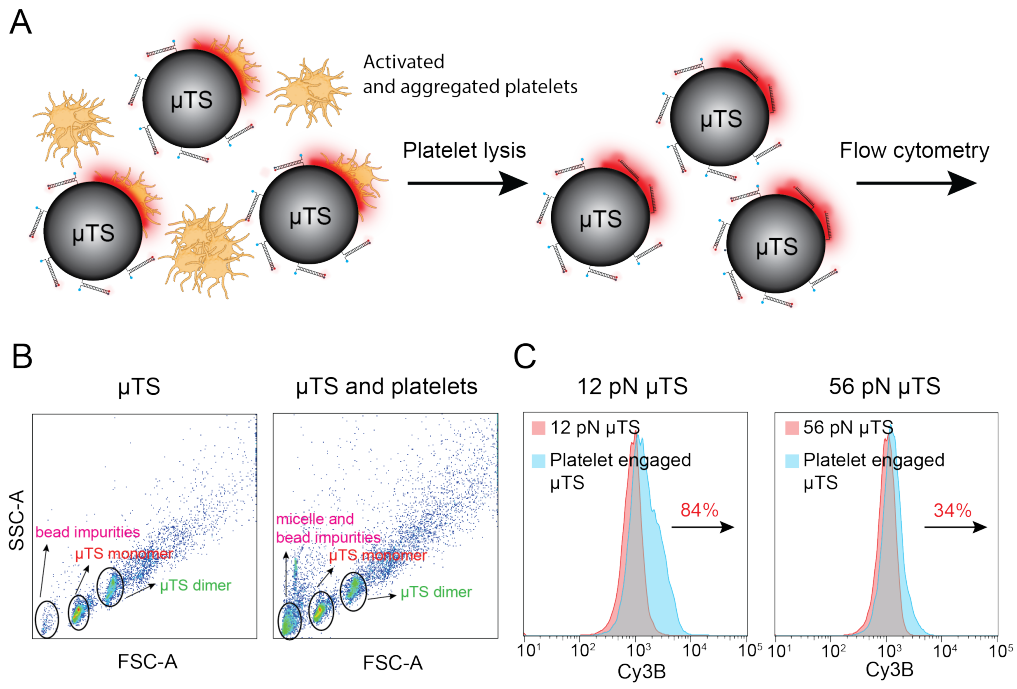


**Figure 2.3. Flow cytometry-based characterization of integrin forces. a** Schematic showing the procedure used for preparing platelet samples for μTS flow cytometry analysis. **b** SSC vs FSC plots of μTS control sample (left) and platelet-engaged μTS (right). Based on a series of controls, events were assigned as μTS monomers (red), μTS dimers (green), and impurities (defective μTS particles or other debris shown in pink). **c** Fluorescence histograms of gated events of μTS monomers for the 12 and 56 pN probes. The red population corresponds to the control μTS not incubated with platelets while the blue indicates μTS that engaged platelets. The percent change indicates the change in the mean fluorescence intensity of μTS. N=10000 events for each group.

### 2.3.5 Mechanopharmacology using the μTS platform: Testing how anti-platelet drugs impact platelet integrin forces.

Since probes amenable to high throughput analysis are of significant interest for their potential application in drug screening, we next aimed to demonstrate the suitability of μTS in measuring how platelet contractile forces can be modulated using drugs. It is notable that platelet traction forces have been shown as a prognostic marker of coagulation both in trauma patients as well as for hereditary mutations in coagulation cascades,[120, 154] and hence μTS readout offers physiological

relevance to clotting. Here we tested two anti-platelet drugs that inhibit platelet mechanics via different mechanisms. Y-27632 inhibits Rho-associated protein kinase (ROCK) and diminishes actomyosin contractility while the second drug eptifibatide is FDA approved to treat acute coronary syndrome, and binds competitively to αIIbβ3 integrin to block the interaction between integrins and adhesive ligands. To investigate the effects of these drugs on tension signals, platelets were pretreated with different concentrations of drugs for 20 min and then cultured with 12 pN μTS for 1 hour, which was followed by microscopy and flow cytometry characterization. After Y27263 drug treatment, fluorescence signals at the μTS-platelet junctions decreased with increasing drug concentration (**Figure 2.4a**). Consistently, flow cytometry data revealed that the MFI of μTS displayed a dose dependent relationship with a relative $IC_{50}$=2.08 μM (**Figure 2.4b**). However, platelet-to-platelet aggregation was not affected by Y27632 (**Figure A2.12**), indicating that ROCK is an important but dispensable factor in platelet aggregation. The aggregation was maintained by the highly concentrated ADP in the suspension, which bound to ADP receptors such as P2Y12 on the platelet membrane to trigger platelet aggregation.[155] Additionally, past work showed that ADP could induce a burst of talin activation to trigger inside-out integrin activation, which leads to platelet activation and aggregation.[156] The tension signal of eptifibatide treated platelets exhibited similar dose-dependent relationship with $IC_{50}$=3.24 μM (**Figure 2.4c**). However, in contrast to Y27632 which can only abolish the tension signal up to 60%, eptifibatide is able to inhibit 80 % of the tension signal, indicating that eptifibatide is a more potent drug compared with Y27632 in modulating applied integrin forces. Note, in addition to force signal changes, aggregation and the adhesion of eptifibatide treated platelets was significantly reduced despite the presence of ADP agonist (**Figure 2.4a** and **Figure A2.10**). This is because the blockade

of integrin directly inhibits the interaction with μTS and surrounding platelets, confirming the necessity of ligand binding in integrin activation and platelet aggregation.

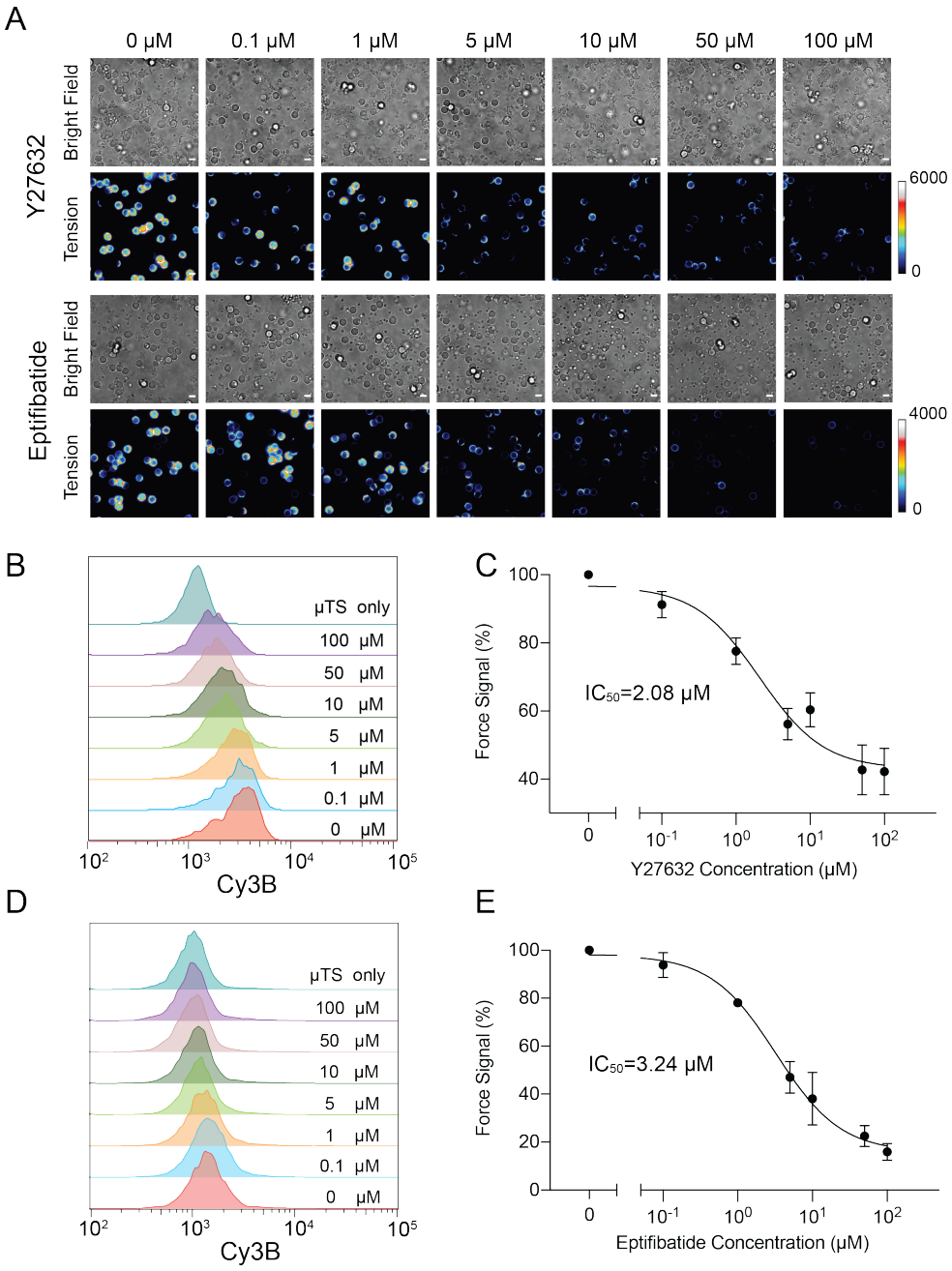


**Figure 2.4. Proof-of-concept demonstration of measuring dose-response curve for drugs that modulate platelet mechanics. a** Representative bright field and fluorescence images showing a mixture of platelets with μTS probes that were allowed to interact for 1 hr and then seeded on a substrate. Platelets were pretreated with a range of concentrations of Y27632 and eptifibatide (0-

100μM) for 20 min. **b** Flow-cytometry based histograms of fluorescence intensity of μTS that engaged platelets treated with different concentrations of Y27632. **c** Dose-response curve plotting the tension signal obtained from flow cytometry plotted against the log concentration of Y27632. **d** Flow-cytometry based histograms of fluorescence intensity of μTS probes that engaged platelets pre-treated with different concentrations of eptifibatide. **e** Dose-response curve plotting the tension signal obtained from flow cytometry against the log concentration of eptifibatide. Each histogram is plotting N = 10000 events. Error bars show the standard error of the mean from three independent measurements from three animals. Scale bars = 5 μm

## 2.4 Conclusion

DNA-based microparticle tension sensors (μTS) show great potential in investigating cell receptor mechanics. In contrast to planar coverslip-based force measurement assays, for T cells, the μTS features a spherical surface that allows the characterization of molecular forces at this curved interface. We applied μTS to investigate T-cell and platelet forces, revealing that TCR and integrin receptors transduce forces ranging from 12 to 56 pN, with a subpopulation of integrin receptors experiencing F>56 pN. Impressively, we observed a highly resolved 3D ring-like force pattern at the hybrid synapse formed between μTS and T-cell, showing that T-cell receptors are mechanically active at the periphery of cells adhered on non-planar surfaces. To the best of our knowledge, no study to date has mapped molecular forces on non-planar geometries. Note that microparticles have been instrumental in investigating actin distribution,[157] receptor-ligand interactions,[158] and traction forces[141] on non-planar geometries, and thus μTS may complement previous methods and allow one to investigate these mechanical events with molecular detail. In principle, the curvature of μTS can be tuned by varying the size of the microparticle template, suggesting that this approach has the potential to facilitate the study of how cell curvature can modulate cell activities. In addition to the non-planar geometry, another advantage of μTS is its micrometer diameter, which enables flow cytometry-based high throughput characterization. Through flow cytometry, hundreds of thousands of force signal-associated events were acquired and analyzed within

minutes, which is in contrast to microscope-based arrays that are orders of magnitude slower in throughput and would take ~ 1 day for analyzing hundreds of events even upon integration of automated robotic imaging. In addition, flow cytometers with up to 14 fluorescence channels would allow for simultaneous and multiplexed force investigation reporting the magnitude of tension transmitted by different receptor-ligand pairs on the cell surface. Complementing this future direction, recently developed imaging flow cytometry instruments generate high resolution images of each particle, thus providing spatial information in a massively high throughput manner in comparison to conventional confocal or TIRF microscopy that are used in high-content screening assays.[159] The potential application of the μTS platform in drug screening was demonstrated by investigating the effect of two anti-platelet drugs. The IC50 values for Y27632 and eptifibatide were 2.08 and 3.24 μM, respectively, which are consistent with literature reported values of ~1 μM for both of these drugs.[145, 160] Note that the literature values were recorded using secondary messenger assays (aggregation, morphology or calcium influx) and thus our molecular probes offer a more precise measure of platelet contractility. The μTS platform still has important limitations. First, the μTS core is comprised of silica which is a hard material compared to that of cells and tissue. Also, the S/N depends on the stoichiometry between cells and beads, as the fraction of the μTS surface that engages cells tunes the strength of the signal. We anticipate that future work using amplification strategies and gel-based particles may address these limitations. In summary, we demonstrated that μTS is an efficient platform for molecular force quantification capable of visualizing molecular force on non-planar geometry in high spatial resolution as well as determining its magnitude in high throughput.

## 2.5 Materials and Methods

### 2.5.1 Materials

#### 2.5.1.1 Reagents

All reagents were purchased from Sigma-Aldrich (St. Louis, MO) unless otherwise specified. Cy3B NHS ester (Cat# PA63101) was purchased from GE Healthcare Life Sciences (Pittsburgh, PA). Azido-PEG4-NHS ester (Cat# AZ103-100) and Alkyne-PEG4-NHS ester (Cat# TA103-100) were purchased from Click Chemistry Tools (Scottsdale, AZ). 6-Azidosulfonylhexyltriethoxysilane (Cat# SIA0780.0) was purchased from Gelest (Morrisville, PA). SMCC (succinimidyl 4-(N-maleimidomethyl)cyclohexane-1-carboxylate) (Cat# 22360), Azide-NHS ester (Cat# 88902) and Bond-Breaker™ TCEP Solution (Cat# 77720) were purchased from Thermo Fisher Scientific (Waltham, MA). No. 2 round glass coverslips (Cat# 48382-085) were purchased from VWR (Radnor, PA). P2 size exclusion gel (Cat#1504118) was purchased from Bio-Rad (Hercules, CA). Silica-NH2 beads (Cat# SA05000) were purchased from Bangs Laboratories, Inc (Fishers, IN). Red blood cell lysis buffer (Cat# 420301) and biotinylated anti-mouse CD3e (Cat# 100243) were purchased from Biolegend (San Diego, CA). Biotinylated pMHC ovalbumin (SIINFEKL) was obtained from the NIH Tetramer Core Facility at Emory University. Midi MACS (LS) startup kit (Cat# 130-042-301) (separator, columns, stand), and mouse CD8+ T cell isolation kit (Cat# 130-104-075) were purchased from Miltenyi Biotec (Bergisch Gladbach, Germany). Cyclo[Arg-Gly-Asp-D-Phe-Lys(PEG-PEG)] (Cat# PCI-3696-PI) and Cyclo(Arg-Ala-Asp-D-Phe-Lys) (Cat# PCI-3883-PI) were obtained from Peptides International. SiR-Actin (cat# CY-SC001) was purchased from Cytoskeleton.

### 2.5.1.2 Oligonucleotides

All oligonucleotides were purchased from Integrated DNA Technologies (Coralville, IA) except for BHQ2 strands, which were custom synthesized by Biosearch Technologies (Novato, CA).

**Table A2.1 List of Oligonucleotides in Chapter 2**

| Name | Sequence (5' to 3') |
|---|---|
| Unmodified top Strand | CAC AGC ACG GAG GCA CGA CAC |
| Alkyne-BHQ2 top strand | /5Hexynyl/ - CAC AGC ACG GAG GCA CGA CAC - /3BHQ2/ |
| Biotin-BHQ2 top Strand | /5Biosg/ - CAC AGC ACG GAG GCA CGA CAC - /3BHQ2/ |
| 12 pN bottom strand | /5UniAmM/ - GTG TCG TGC CTC CGT GCT GTG TTT TT - /3ThioMC3-D/ |
| 56 pN bottom strand | /5ThioMC6-D/ - TTT TT/iUniAmM/ GTG TCG TGC CTC CGT GCT GTG |

### 2.5.1.3 Instruments

Barnstead Nanopure water purifying system (Thermo Fisher), High-performance liquid chromatography (Agilent 1100), Nanodrop 2000 UV-Vis Spectrophotometer (Thermo Scientific), Matrix-assisted laser desorption/ionization time-of-flight mass spectrometer (MALDI-TOF-MS, Voyager STR), Nikon Eclipse Ti microscope equipped with Evolve electron multiplying charge coupled device (Photometrics), an Intensilight epifluorescence source (Nikon), a CFI Apo 100X NA 1.49 objective and TIRF launcher. Nikon confocal microscope with a 60x oil objective and a C2si scanhead. BD LSR II flow cytometer. Beckman coulter CytoFLEX flow cytometer. Amnis ImageStreamX Mk II imaging flow cytometer.

### 2.5.2 Methods

#### 2.5.2.1 OT-1 T-cell harvesting and purification

OT-1 T cell receptor transgenic mice were housed and bred in the Division of Animal Resources Facility at Emory University in accordance with the Institutional Animal Care and Use Committee. OT-1 T cells express the CD8 co-receptor and specifically recognize chicken ovalbumin epitope 257–264 (SIINFEKL) in the context of the MHC allele H-2Kb. Naïve OT-1 T cells were enriched from the spleen using magnetic activated cell sorting according to manufacturer instructions provided with the CD8+ T cell Isolation Kit (Miltenyi Biotec, Germany). Briefly, a single cell suspension of splenocytes was obtained and incubated with biotinylated antibodies specific for unwanted splenic cell populations. These populations were separated from the OT-1 T cells following incubation with anti-biotin magnetic beads and enrichment on a magnetic column. Purified T cells were washed and resuspended in HBSS solution and kept on ice before experiment.

#### 2.5.2.2 Preparation of mouse platelets

Blood from C57Bl/6J mice was collected by cardiac puncture, anticoagulated with acid citrate dextrose, added to equal volumes modified Tyrode's buffer (140mM NaCl, 2.7mM KCl, 0.4mM NaH2PO4, 10mM NaHCO3, 5mM Dextrose, 10mM HEPES) containing 3U apyrase and centrifuged at 200xg for 5min. The platelet fraction was removed and to it added 1U apyrase and 1uM prostaglandin E1. Platelets were centrifuged at 700xg for 5min and resuspended in Walsh buffer (137mM NaCl, 2.7mM KCl, 1mM MgCl2, 3.3mM NaH2PO4, 20mM HEPES, pH 7.4, 0.1% glucose, 0.1% bovine serum albumin) at a concentration of 1x109 platelets/mL.

#### 2.5.2.3 DNA strand modification

Labeling DNA strands with dyes: Aminated bottom strand (either 12 pN or 56 pN) (100 μM) was mixed with excess Cy3B-NHS ester / Atto647-NHS ester (500 μg/mL) and allowed to react in aqueous solution (pH=9) for 3 hours at room temperature. The mixture was then filtered by P2 gel to remove salts and unreacted dyes and purified by HPLC. (solvent A: 0.1 M TEAA, solvent B: 100% MeCN; initial condition was 10% B with a gradient of 1% per min, flow rate: 0.5 mL/min). The product was characterized by MALDI-TOF mass spectrometry.

Labeling DNA strands with RGD/RAD ligand: 100 nmols of Cyclo [Arg-Ala-Asp-D-Phe-Lys(PEG-PEG)] (Cat# PCI-3696-PI) or Cyclo(Arg-Ala-Asp-D-Phe-Lys) peptide was reacted with 150 nmoles of azide-NHS ester in 20 μL DMSO overnight. Afterwards, the azido RGD/RAD product was purified by HPLC. (solvent A 0.1 M TEAA, solvent B: 100% MeCN; initial condition was 10% B with a gradient of 0.5% per min, flow rate: 1 mL/min). Azido cRGD/RAD was then conjugated to alkyne DNA strand via copper catalyzed click reaction. Briefly, a mixture of azido-RGD from last step, Alkyne DNA strand (100 μM), CuSO4 (400 μM), THPTA (2 mM) and sodium ascorbate (10 mM) in 1X PBS solution was allowed to react in room temperature for 2 hours. The mixture was then subjected to P2 gel filtration and purified by HPLC. (solvent A: 0.1 M TEAA, solvent B: 100% MeCN; initial condition was 10% B with a gradient of 1% per min, flow rate: 0.5 mL/min). The product was characterized by MALDI-TOF mass spectrometry following drying.

#### 2.5.2.4 Preparation of μTSs presenting pMHC

First, maleimide particles were synthesized by mixing 3 mg of 5 μm aminated silica beads (Bangs Laboratories) with 1 mg SMCC crosslinker in 1 mL DMSO and reacting on a shaker for 2 hours.

Afterwards, the particles were centrifuged down at 5000 rpm for 5 minutes. The supernatant was discarded, and the particles were resuspended to DMSO. This process was repeated for four times to remove unreacted SMCC. Afterwards, the beads were washed with PBS three times to remove excess DMSO to prepare the beads for the following step of DNA conjugation. During the preparation of maleimide coated particles, the tension probes were assembled in 1M NaCl by mixing the fluorophore labeled 12/56 pN bottom strands (500 nM) and biotin-quencher strand (1 μM) in the ratio of 1:2. The mixture was heat annealed at 95 oC for 5 min and cool down to 25 $^{o}$C for 30 min. 1 μL 5 mM TCEP (100-fold) was added to 100 μL of the assembled probes to activate thiol group on bottom strands. After 15 min, the probe was diluted with 400 μL PBS to 100 nM and added to maleimide coated beads. The reaction was incubated for 1 hour and the resulting DNA conjugated particles were purified by centrifugation. Specifically, the particles were centrifuged in BSA blocked microcentrifuge tubes at 800 rpm for 5 min, after which the supernatant was discarded and the particles were resuspended into 1 mL PBS. This process was repeated four times. The particles were then resuspended into 0.1% BSA and incubated for 30 min to block the particle surface, followed by washing with PBS for three times. The beads were then incubated with 10 μg/mL streptavidin and 10 μg/mL biotinylated OVA-N4 sequentially for 45 min at room temperature with thrice PBS washes in between. Finally, particles were buffer exchanged with HBSS and ready for imaging with T-cells.

#### 2.5.2.5 Preparation of μTSs presenting cyclized RGD

First, maleimide particles were synthesized by mixing 3 mg of 5 μm aminated silica beads (Bangs Laboratories) with 1 mg SMCC crosslinker in 1 mL DMSO and reacting on the shaker for 2 hours. Afterwards, the particles were centrifuged down at 5000 rpm for 5 minutes. The supernatant was discarded, and the particles were resuspended to DMSO. This process was repeated four times to

remove unreacted SMCC. Afterwards, the beads were washed in PBS three times to remove DMSO for the following DNA conjugation. During the preparation of maleimide coated particles, the tension probes were assembled in 1M NaCl by mixing the fluorophore labeled 12/56 pN bottom strands (500 nM), RGD conjugated quencher strand (1µM) in the ratio of 1:2. The mixture was heat annealed at 95 oC for 5 min and then cooled down to 25 ºC for 30 min. 100 µL of the assembled probes were reacted with 100-fold excess TCEP for 15 min to activate thiol groups on the bottom strands. Afterwards, the probe was diluted with 400 µL PBS to 100 nM and added to the above maleimide conjugated bead and incubated for 1 hour at room temperature, followed by 3X PBS washes. Particles were finally buffer exchanged with Tyrode buffer for platelet experiments.

**2.5.2.6 Preparation of TGT probes on planar glass surfaces**

No. 1.5H glass coverslips (Ibidi) were sequentially sonicated in MilliQ water (18.2 MΩ cm-1) and 200 proof ethanol, 10 min each. The glass coverslips were rinsed copiously with MilliQ water and immersed in freshly prepared piranha solution (3:1 sulfuric acid:H2O2) for 30 min to remove organic adsorbates and activate hydroxyl groups on the surface (CAUTION: Piranha is highly reactive and explosive on contact with organics!). The cleaned substrates were rinsed with MilliQ water in a 200 mL beaker at least 6 times and further washed with ethanol thrice. Slides were then transferred to a 200 mL beaker containing 3% APTES in ethanol for 1 h, washed with ethanol thrice and baked in an oven (~110ºC) for 30 min. After cooling, the slides were incubated with 10 mg/mL SMCC for one hour, then washed with ethanol thrice and water one time and finally dried under nitrogen. The slides were then mounted to 6-channel microfluidic cells (Sticky-Slide VI 0.4, ibidi). Subsequently, TGT probes were assembled in 1M NaCl by mixing the fluorophore labeled 12/56 pN bottom strands (100 nM) and quencher strand (200 nM) in a ratio of 1:2. The mixture

was heat annealed at 95 oC for 5 min and then cooled down to 25 oC for 30 min. 500 µL of the assembled probe was reacted with 100-fold TCEP (5µL x 1mM) for 15 min to activate the thiol group and then added to channels and incubated for 1 hour at room temperature, which was then followed by 3X PBS washes. Then 10 µg/mL streptavidin was added to the substrates and incubated for 45 min at room temperature followed by 3X PBS washes. Next, 10 µg/mL biotinylated OVA-N4 was added to the substrates, incubated for 45 min at room temperature and washed thrice with PBS. Surfaces were buffer exchanged with HBSS buffer before imaging.

#### 2.5.2.7 DNA density measurement

Aminated silica beads were incubated with 1 mg/mL SMCC in DMSO for 2 hours to yield maleimide coated bead. Beads were then centrifuged down and washed with DMSO for four times and PBS three times. DNA duplexes were assembled in 1M NaCl by mixing unmodified 12 pN TGT bottom strands and top strand in a ratio of 1:2. The mixture was heat annealed at 95 $^{o}$C for 5 min and then cooled down to 25 oC for 30 min. 100-fold excess TCEP was added to the assembled probes to activate thiol groups on bottom strands. After 15 min, 100 nM DNA was mixed with maleimide coated beads and incubated at room temperature for 1 hour. Afterwards, the particles were washed with PBS 4 times, resuspended into 1 mL 30 mM NaOH to denature the DNA duplexes on the particle surface. After 20 min, particles in the suspension were counted using a hemocytometer and centrifuged down at 15000 rpm for 5 min. The supernatant was then collected for quantitating single strand DNA through Oligreen Kit. The density was calculated given the number of DNA strands, number of particles and particle surface area.

#### 2.5.2.8 Immobilizing µTS onto glass coverslips

<u>Method 1: copper catalyzed alkyne-azide click reaction</u>

Step 1 (glass coverslip modification): No. 2 round glass coverslips (VMR) were sequentially sonicated in MilliQ water (18.2 MΩ cm-1) and 200 proof ethanol, 10 min each. The glass coverslips were rinsed copiously with MilliQ water and immersed in freshly prepared piranha solution (3:1 sulfuric acid:H2O2) for 30 min to remove organic adsorbates and activate hydroxyl groups (CAUTION: Piranha is highly reactive and explosive on contact with organics!). The glass coverslips were then washed six times with water, twice with ethanol and dried under nitrogen. Afterwards, the substrates were incubated with 50 mg/mL 6-Azidosulfonylhexyltriethoxysilane in DMSO for 2 hours, washed with ethanol thrice and baked in oven (~110 ºC) for 30 min.

Step 2 (bead modification and immobilization): 3 mg aminated silica beads were incubated with 2mg/mL Alkyne-PEG4-NHS ester and 2 mg/mL SMCC in DMSO for overnight. On the next day, the beads were then centrifuged down at 15000 rpm for 5 min and washed with DMSO three times and PBS two times. Next, particles were mixed with 55 µL DMSO, 10 µL 2M TEAA, 10 µL 10mM CuTBTA, 15 µL water, 10 µL 18 mg/mL ascorbic acid and then added to azide coated glass coverslips prepared in step 1. Another coverslip was put on top to make a "sandwich" and left overnight. On the next day, unfixed beads were washed away gently in a beaker filled with PBS. Fluorophore labeled 12/56 pN bottom strands and quencher strand were mixed and annealed at a ratio of 1:2 in 1 M NaCl at a 100 nM concentration. The DNA was added to bead coated coverslip and allowed to be immobilized onto bead for 1 hour. After washing away excess DNA with PBS, 10 µg/mL streptavidin was added to the substrates and incubated for 45 min at room temperature followed by 3X PBS washes. Next, 10 µg/mL OVA-N4 was added to the substrates, incubated for 45 at room temperature and washed thrice with PBS. Substrates were buffer exchanged with HBSS before imaging.

<u>Method 2: copper free DBCO-azide click reaction</u>

Step 1 (glass coverslip modification): No. 2 round glass coverslips (VMR) were sequentially sonicated in MilliQ water (18.2 MΩ cm-1) and 200 proof ethanol, 10 min each. The glass coverslips were rinsed copiously with MilliQ water and immersed in freshly prepared piranha solution (3:1 sulfuric acid:H2O2) for 30 min to remove organic adsorbates and activate hydroxyl groups (CAUTION: Piranha is highly reactive and explosive on contact with organics!). The glass coverslips were then washed six times with water, twice with ethanol and dried under nitrogen. Afterwards, the substrates were incubated with 3% APTES in ethanol for 1 h, washed with ethanol thrice and baked in oven (~110$^{o}$C) for 30 min. 50 µL 5 mg/mL NHS-PEG4-DBCO (50% water pH=9, 50% DMSO) was added onto coverslip. Another coverslip was put on top to make a "sandwich" and left for 2 hours.

Step 2 (bead modification and immobilization): 3 mg aminated silica beads were incubated with 2mg/mL Azide-PEG4-NHS ester and 2 mg/mL SMCC in DMSO for overnight. On the next day, the beads were then centrifuged down at 15000 rpm for 5 min, washed with DMSO three times and resuspend into 50 µL DMSO. Bead suspension was then added onto DBCO coated glass in step 1. Another coverslip was put on top to make a "sandwich" and left overnight. On the next day, unfixed beads were washed away gently in a beaker filled with PBS. Fluorophore labeled 12/56 pN bottom strands and quencher strand were mixed and annealed at a ratio of 1:2 in 1 M NaCl at a 100 nM concentration. The DNA was added to bead coated coverslip and allowed to be immobilized onto bead after 1 hour. After washing away excess DNA with PBS, 10 µg/mL streptavidin was added to the substrates and incubated for 45 min at room temperature followed by 3X PBS washes. Next, 10 µg/mL OVA-N4 was added to the substrates, incubated for 45 at room temperature and washed thrice with PBS. Substrates were buffer exchanged with HBSS before imaging.

#### 2.5.2.9 Immunostaining

After tension imaging, the cells on surfaces were fixed using 4% formaldehyde in PBS for 10 min. The surfaces were then gently washed with PBS thrice to prevent cell detachment. Afterwards, cells were permeabilized in 0.1% Triton 100X in PBS for 5 min followed by washing with PBS. The surfaces were then rinsed with 2% BSA and incubated overnight at 4ºC. On the next day, the surfaces were washed with PBS thrice. 1 μM SiR-Actin was added to the surface and incubated for 1 hour at room temperature. Afterwards, the surfaces were washed with PBS thrice and imaged on microscope.

#### 2.5.2.10 MALDI-TOF characterization and sample preparation

MALDI-TOF was performed on a Bruker Daltonics ultraflex II TOF/TOF. Purified oligonucleotides in nanopure water were spotted in a 1:1 (v/v) ratio with saturated matrix solution. To prepare the matrix, 3-hydroxypicolinic acid was added in excess to a solution containing 50% acetonitrile and 0.1% trifluoroacetic acid. Dried samples were measured using the linear negative mode. If samples displayed a low signal-to-noise ratio, multiple spectra were collected using the summation function. Spectra were analyzed in Bruker's Flex Analysis 3.4 software.

#### 2.5.2.11 Fluorescence imaging

2D imaging was conducted with a Nikon Eclipse Ti inverted microscope driven by the NIS Elements software. The microscope features an Evolve electron multiplying charge coupled device (EMCCD, Photometrics), an Intensilight epifluorescence source (Nikon), a CFI Apo 100× NA 1.49 objective (Nikon), a TIRF launcher with three laser lines: 488 nm (50 mW), 561 nm (50 mW), and 640 nm (40mW), and a Nikon Perfect Focus System which allows the capture of multipoint and time-lapse images without loss of focus. All of the experiments were performed using bright

field, reflection interference contrast microscopy (RICM) and the following Chroma filter cubes: TRITC, FITC, Cy5. Imaging was performed on 96 well plates and glass coverslips using Hank's Balanced Salts supplemented with 0.35 g/L NaHCO3 and 10 mM HEPES as cell imaging media for T-cells and Tyrode's buffer (134 mM NaCl, 12 mM NaHCO3, 2.9 mM KCl, 0.34 mM $NaH_2PO_4$, 5 mM HEPES, 5 mM glucose, 2 mM $MgCl_2$, 1 mM $CaCl_2$, 0.1% BSA, pH=7.4) for platelets. All imaging data was acquired at room temperature.

3D imaging was conducted with a Nikon confocal microscope with a 60x oil objective and a C2si scanhead. Experiments were performed using three laser lines (488 nm, 561 nm and 640 nm) and the filters with the following bandpasses: 445/50+60LP, 525/50, and 600/50. Z-stack imaging was performed using the ND Acquisition module in Nikon Elements. For 3D reconstructions, a step size of 150 nm was used. Images were reconstructed in ImageJ.

#### 2.5.2.12 Flow cytometry experiments

Flow experiments were conducted on BD LSR II flow cytometer with five laser lines: 355 nm, 407 nm, 488 nm, 561nm, 633 nm and Beckman coulter CytoFLEX flow cytometer with two laser lines: 488 nm and 638 nm. Cells and μTS were mixed in desired media in 96 well plate for microscope imaging and transferred to 1 mL microcentrifuge tube for flow cytometry characterization. μTS population was gated out in the side scatter vs forward scatter plots. Tension signals were compared according to the mean fluorescence intensity of populations.

## 2.6 Appendix

A

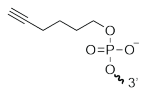

/5Hexynyl/

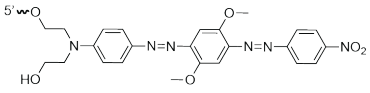

/3BHQ2/

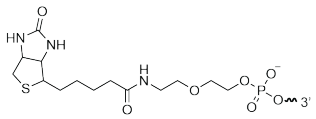

/5Biosg/

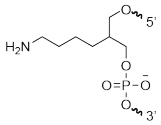

/iUniAmM/

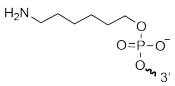

/5UniAmM/

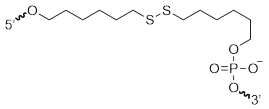

/5ThioMC6-D/

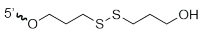

/3ThiolMC3-D/

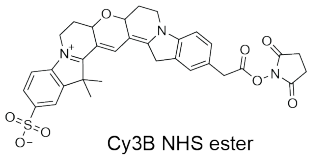

Cy3B NHS ester

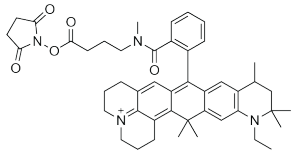

Atto647N NHS ester

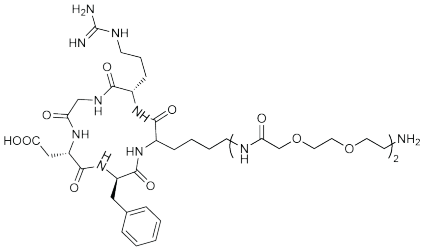

c(RGDfK(PEG-PEG))

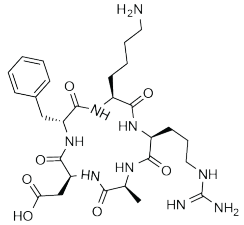

c(RADfK)

B

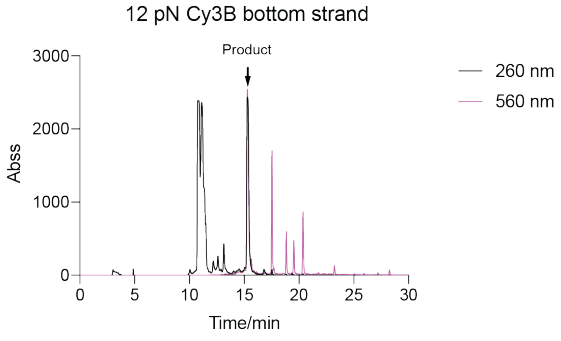


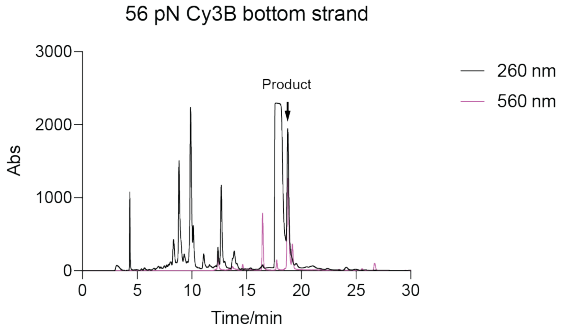

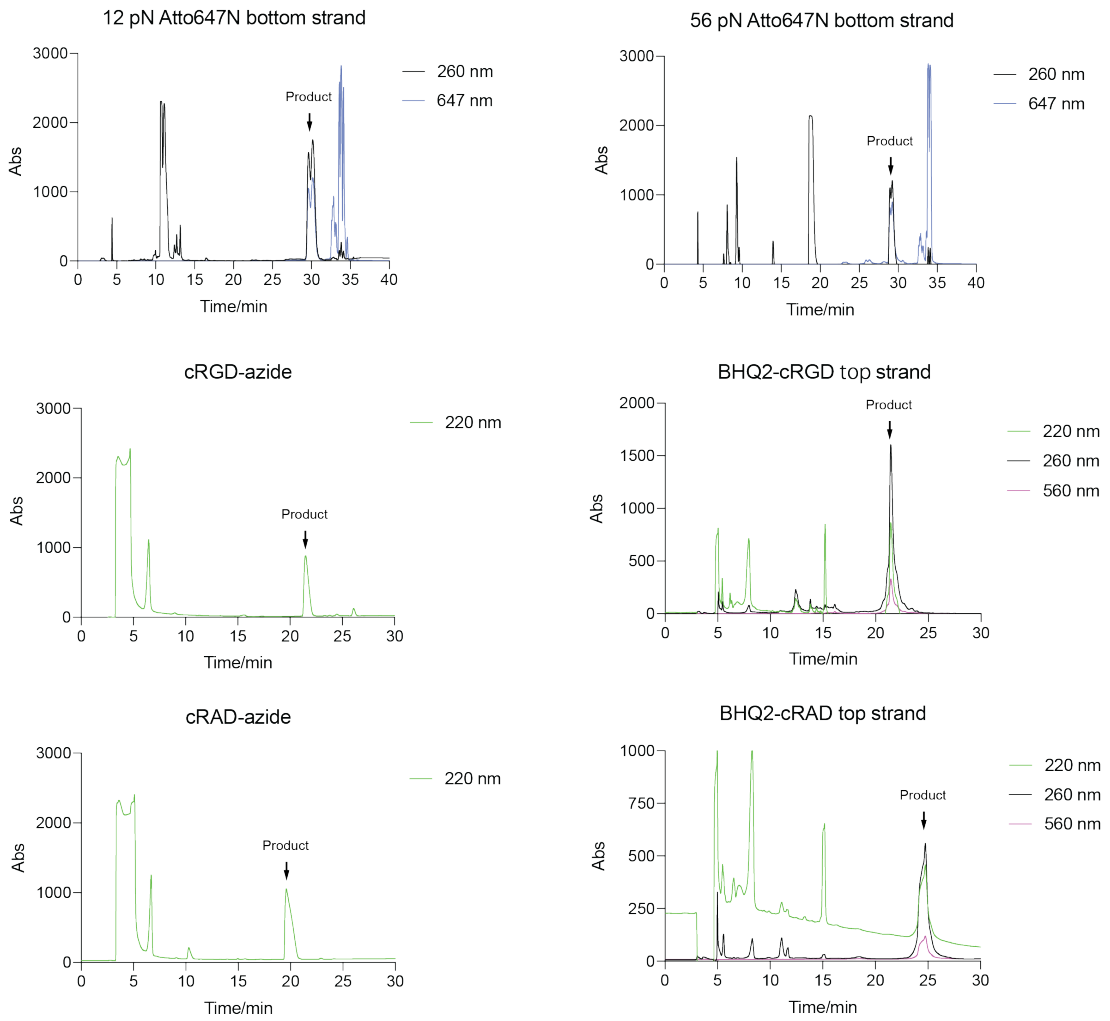


C

| Sample | Calculated mass | m/z found (MALDI-TOF) | Error |
|---|---|---|---|
| 12 pN Cy3B bottom strand | 8953.3 | 8987.507 | 0.4% |
| 56 pN Cy3B bottom strand | 9037.3 | 9072.352 | 0.4% |
| 12 pN Atto647N bottom strand | 9138.5 | 9069.506 | 0.8% |
| 56 pN Atto647N bottom strand | 9223.5 | 9158.754 | 0.7% |
| BHQ2-cRGD top strand | 8112.9 | 8109.8 (ESI-MS) | |
| BHQ2-cRAD top strand | 7836.6 | 7835.8 (ESI-MS) | |

**Figure A2.1. Characterization of modified oligonucleotides.** (A) Chemical structures of oligonucleotides, dye NHS esters and RGD/RAD peptides. (B) HPLC traces of reaction products. Arrows indicate the peaks associated with the products and that were isolated for mass spectrometry analysis. (C) Calculated mass/charge ratio and mass/charge ratio found using MALDI-TOF and ESI-MS.

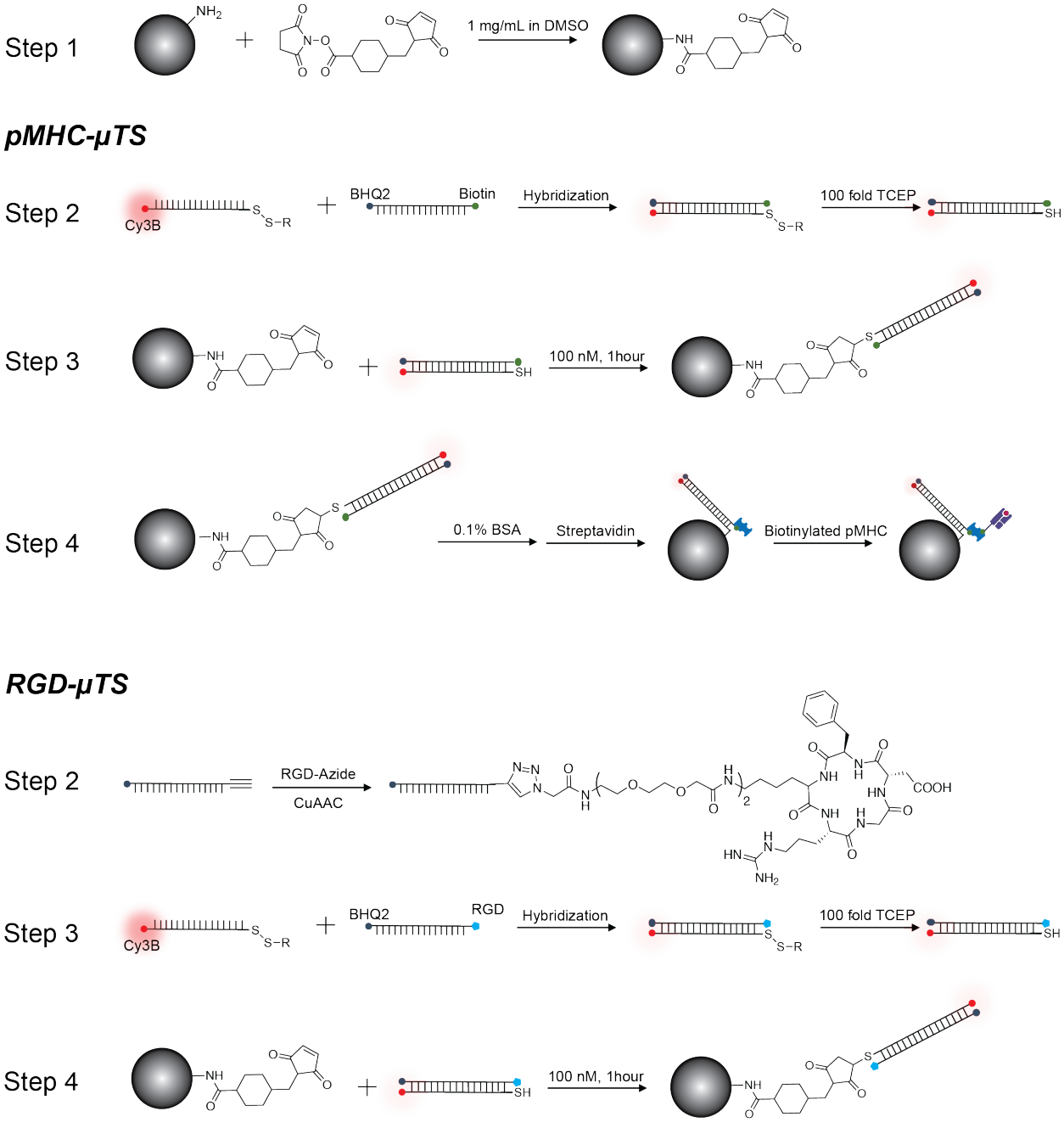


**Figure A2.2. Preparation of Microparticle Tension Sensor (μTS) presenting pMHC and cRGD ligands for detecting TCR and integrin forces, respectively.**

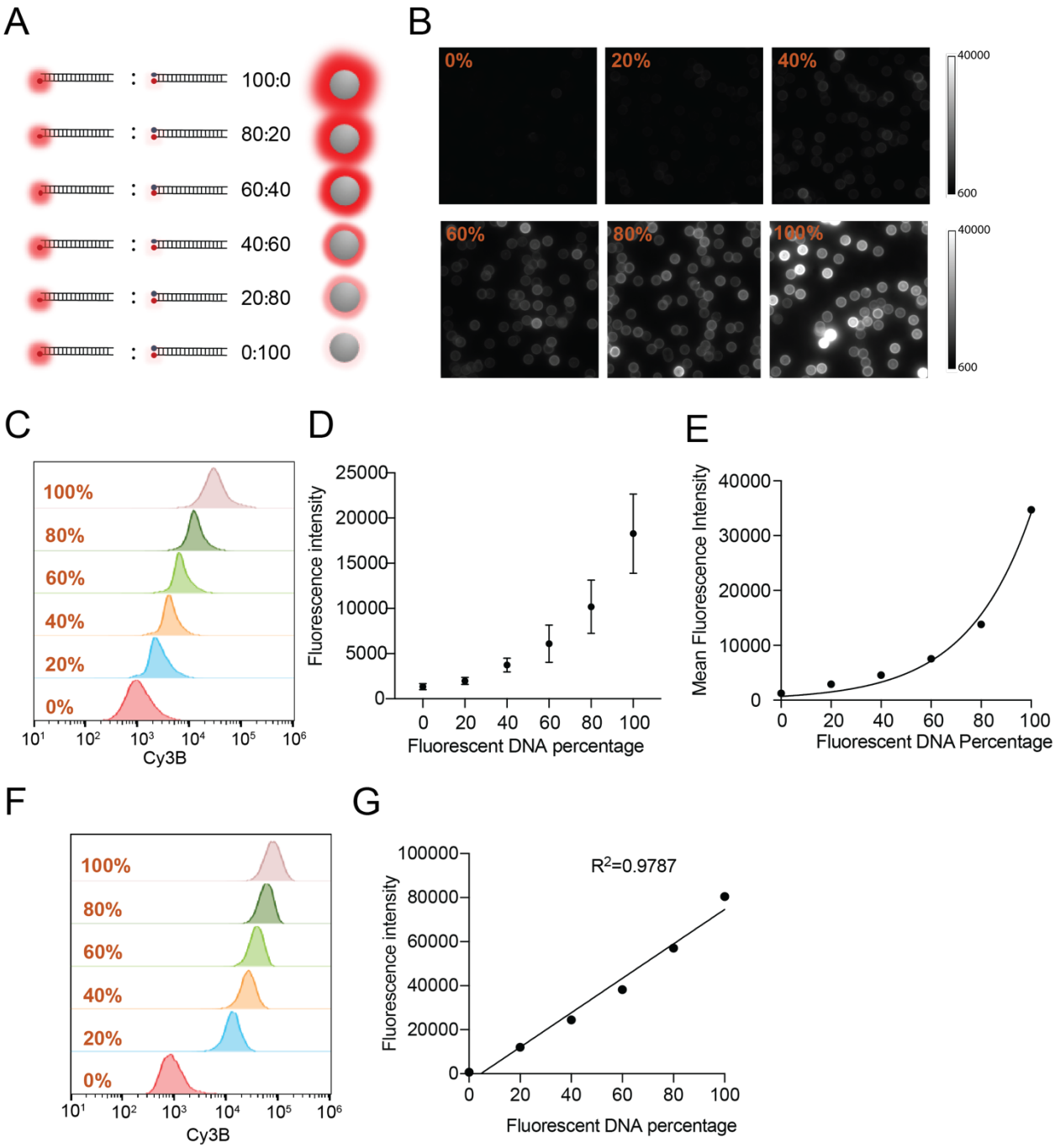


**Figure A2.3. Determination of probe sensitivity and quenching efficiency.** (A) Particles were modified with binary mixtures of quenched and non-quenched TGTs of different ratios while maintaining a total TGT concentration = 100 nM. (B) Representative Cy3-fluorescence channel images of particles prepared with fluorescent TGT concentrations ranging from 0% to 100%. Microscope images were constructed by selecting max intensity from 21 z-stacks using the Z projection plugin in ImageJ. (C) Intensity histograms of particles (from A) analyzed using flow cytometry. (D-E) Plots showing the fluorescence intensity measured using microscopy and flow cytometry as a function of fluorescent TGT ratio. The function appears non-linear likely due to

intermolecular FRET because of the high DNA density on the particle surface. (F) Histograms of particle fluorescence measured using flow cytometry. In this case, the particles were prepared using a low density of DNA. (G) Plots of mean fluorescence intensity of particles obtained from (F) and this shows a linear relation between the fraction of fluorescent DNA and the intensity of a particle. Thus, the plot in (G) supports the premise of intermolecular FRET at high DNA densities.

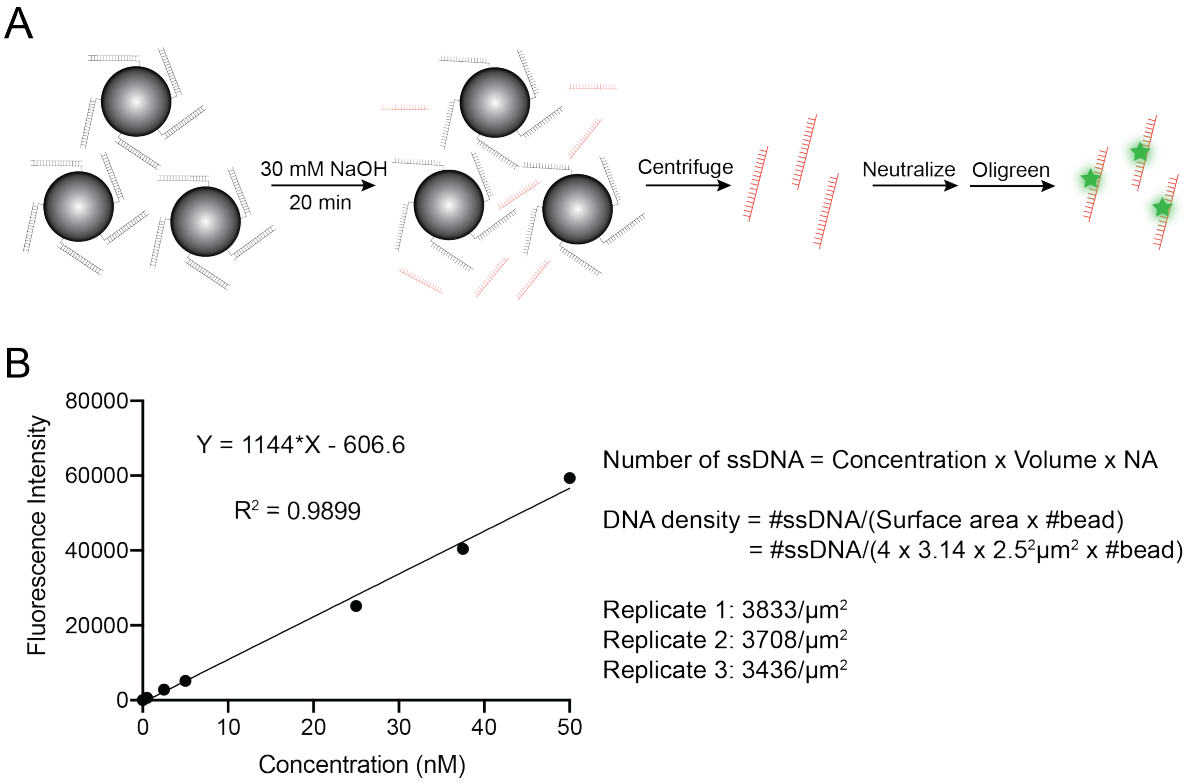


**Figure A2.4. Quantifying DNA probe density on μTS.** (A) Schematic shows denaturation of DNA in high pH and further quantification of DNA strand via the Oligreen kit. (B) Standard curve of DNA top strand and equations showing how to convert concentration of top strand in the supernatant to DNA density on particles (average 3660/μm2).

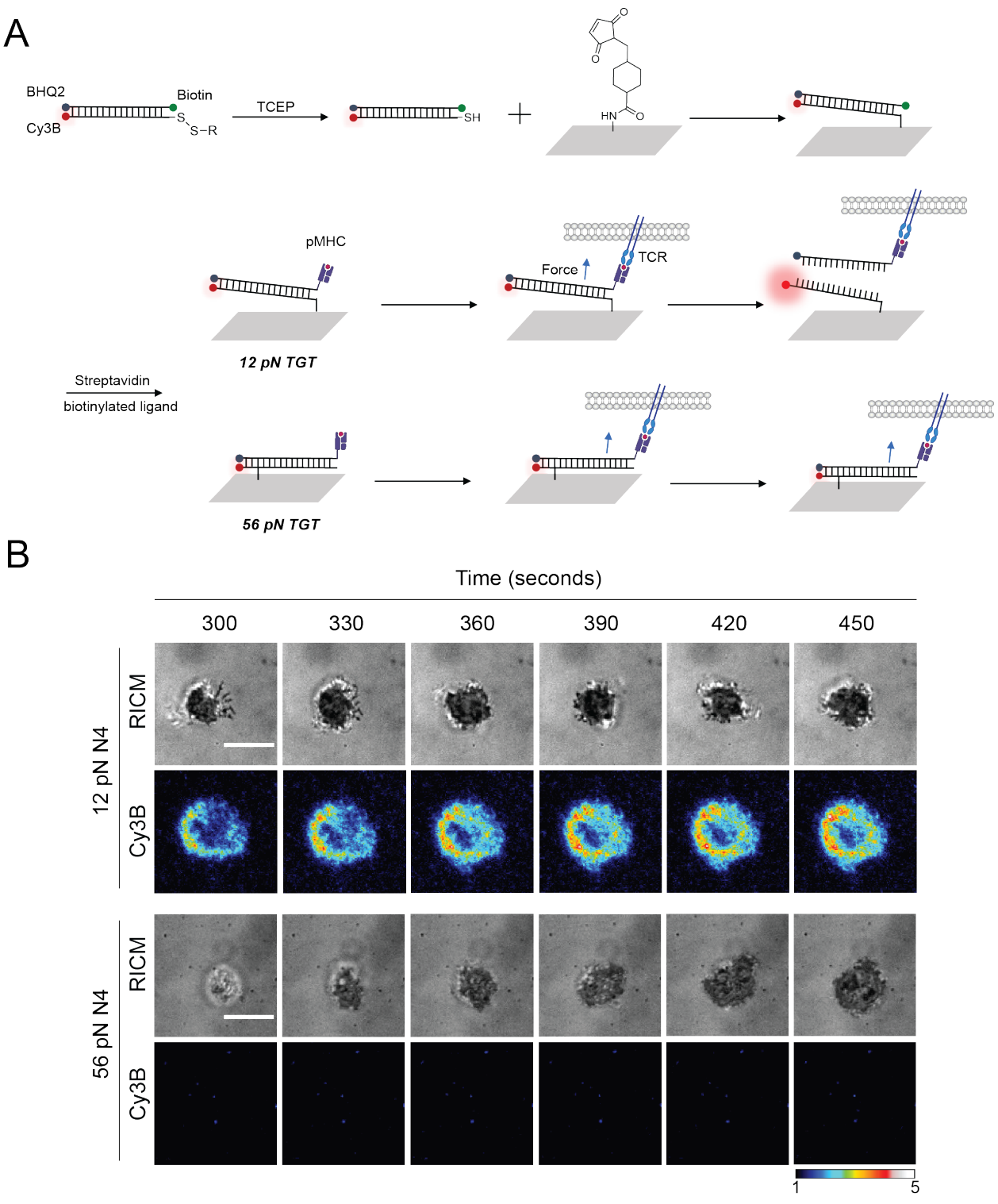


**Figure A2.5. Visualizing TCR forces on planar surfaces.** (A) Schematic showing the preparation and response of TGT tension probes presenting pMHC in the 12 pN and 56 pN geometries. (B) Representative RICM and Cy3B time-lapse images showing T-cell spreading and force generation (fluorescence intensity fold change) on 12 and 56 pN TGT surfaces starting at 5 min after cell plating. Scale bar = 5 μm

**Method 1 Copper catalyzed Alkyne-azide click reaction**

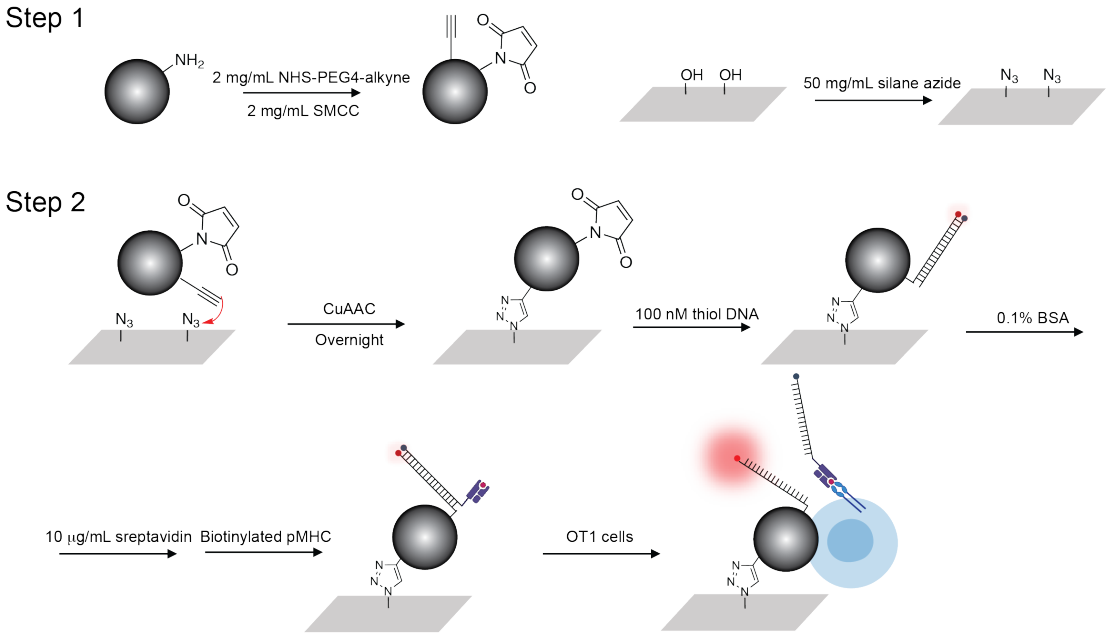


**Method 2 Copper free DBCO-azide click reaction**

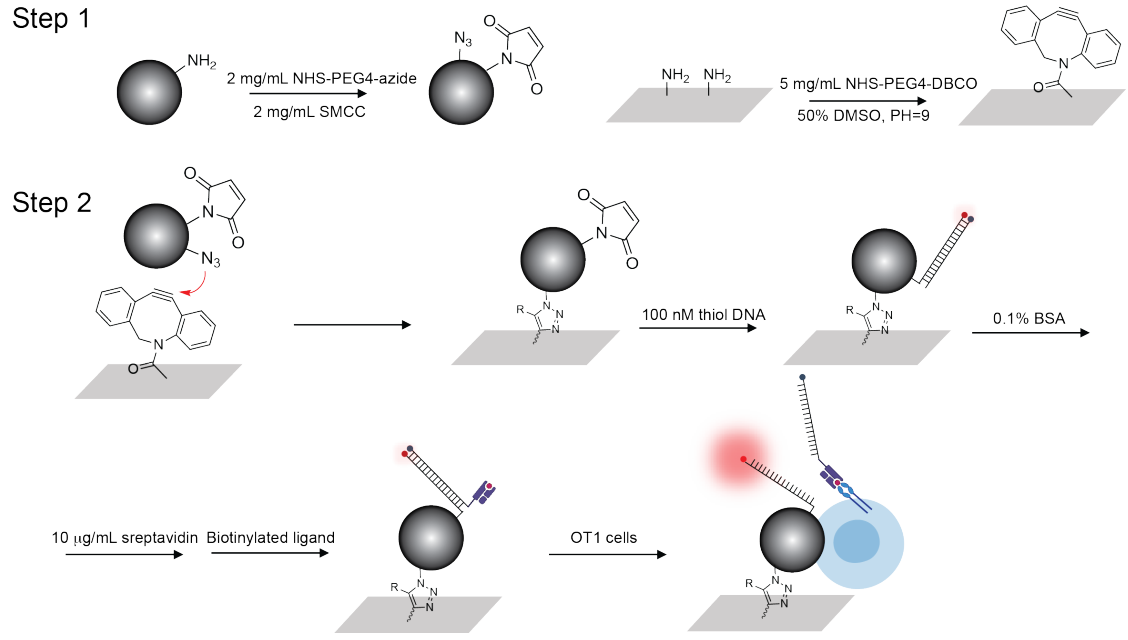


**Figure A2.6. Schematic showing immobilization of μTS onto glass coverslips through click chemistry.**

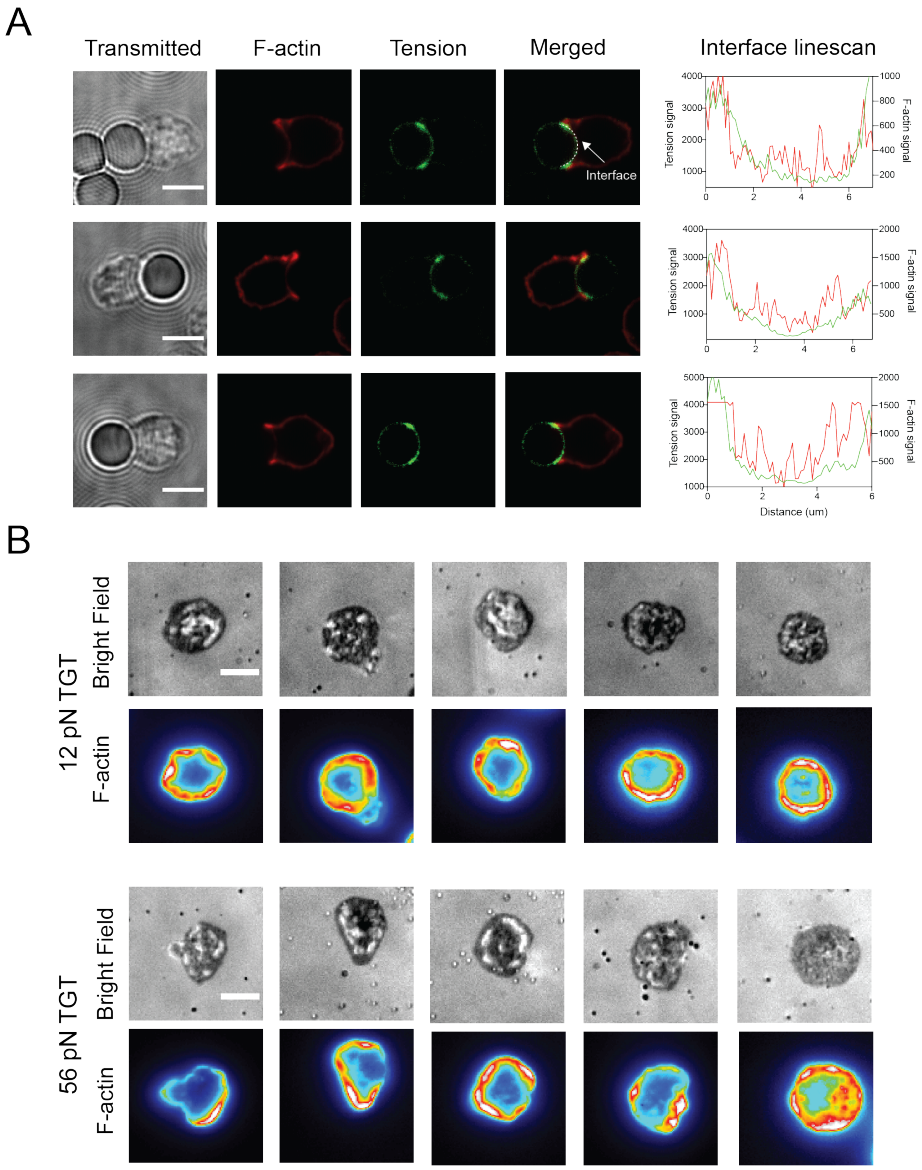


**Figure A2.7. Colocalization between F-actin and tension on non-planar and planar surfaces.** (A) Representative confocal microscope images of T cell-12 pN μTS contacts. Images of transmitted light and fluorescence images of F-actin staining and tension signal show colocalization between F-actin and tension. Plots show intensity profiles of F-actin stain and tension signal along the dotted white line, and confirm the high colocalization between these two signals. (B) Representative TIRF images showing F-actin enrichment of T-cells plated on 12 pN and 56 N4 TGT planar surfaces. Scale bar = 5 μm

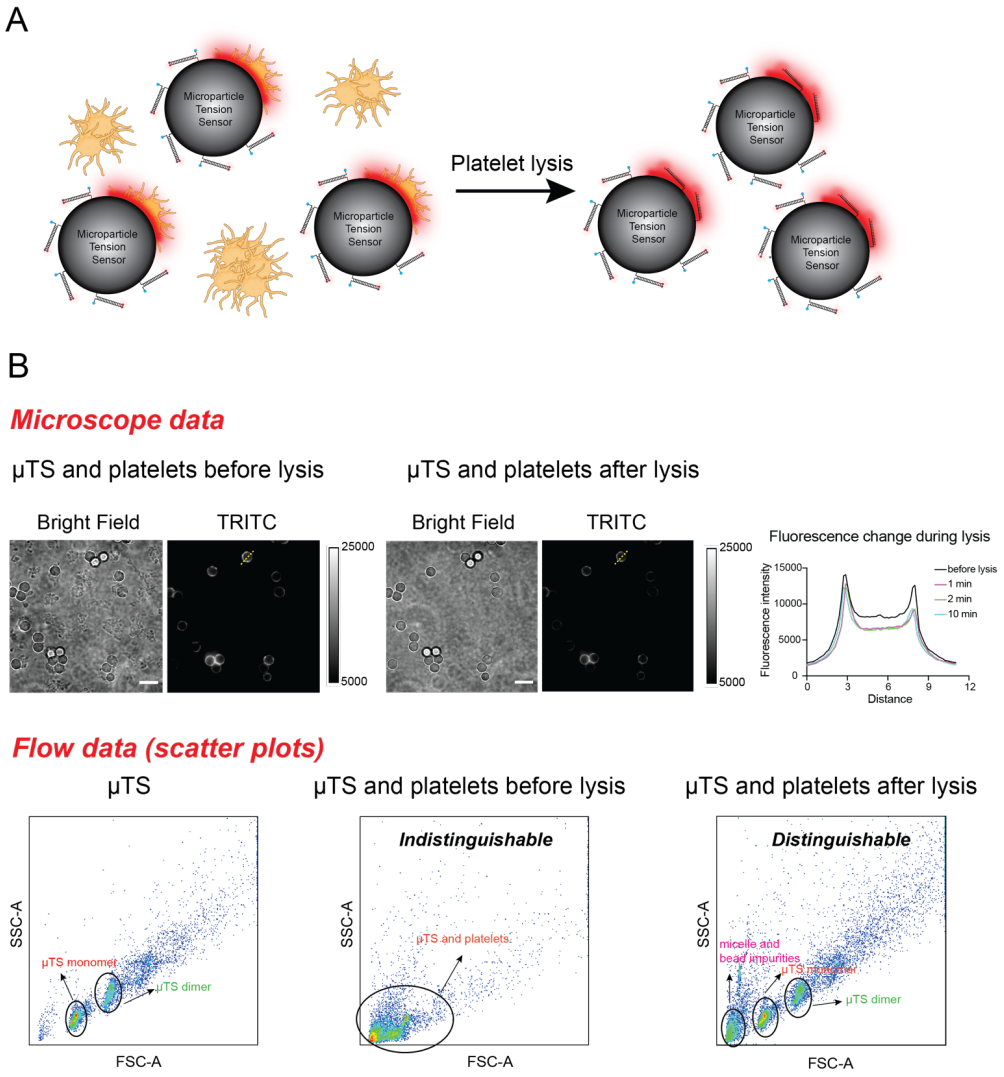


**Figure A2.8. Lysing platelets in μTS-platelets suspension for flow cytometry characterization.** (A) Schematic showing force signal at the junction between μTS and platelets. To lyse the platelets, platelets were incubated with lysis buffer (10 mM Tris HCl, 150 mM NaCl, 0.5 mM EDTA, 0.5% NP 40) for 15 min. (B) (top) Representative bright field and fluorescence images showing changes after adding lysis buffer. Platelets were completely lysed after 1 min. Fluorescence of μTS subtly changed after adding lysis buffer and remained stable, indicating the lysis buffer did not denature DNA. Line scan is shown for the dotted yellow line in the images. (bottom) Flow data: forward and side-scatter plots of μTS and platelet-μTS mixed samples. Platelet population and μTS population are indistinguishable prior to adding lysis buffer. Scale bar = 5 μm.

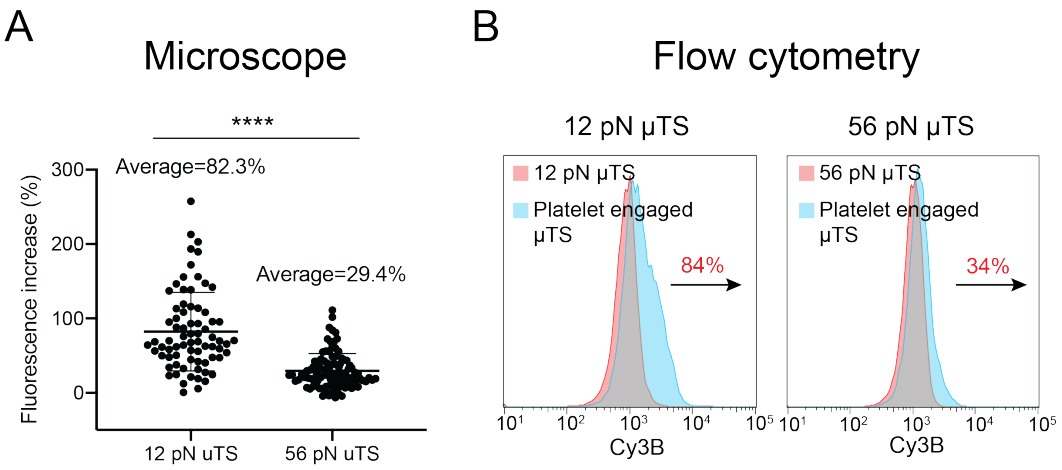


**Figure A2.9. Comparison of force signal for 12 and 56 pN µTS as measured by microscopy and flow cytometry.** (A) Mean fluorescence increase normalized to the background of the µTS. The signal was measured at the mid-plane of the µTS for particles that strongly engaged platelets. 12 pN µTS showed an 82.3% fluorescence increase while 56 pN µTS exhibited a 29.4% increase. Each data point represents a single µTS particle and there were n = 80 particles in each group. The error bar shows the standard deviation. (B) Mean fluorescence intensity (MFI) of 12 pN and 56 pN µTS increased 84% and 34%, respectively after engaging platelets for 1 hr at room temperature.

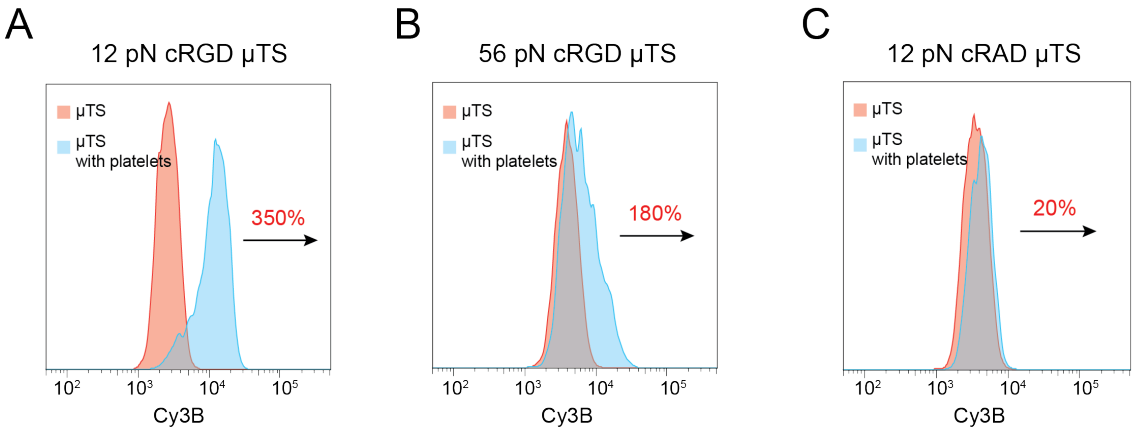


**Figure A2.10. RAD as a negative control to confirm force dependent fluorescence change.** (A) Mean fluorescence intensity (MFI) of 12 pN cRGD µTS increased 3.5-fold after engaging platelets for 1 hr at room temperature. (B) MFI of 56 pN cRGD µTS increased 1.8-fold after engaging platelets for 1 hr. (C) MFI of 12 pN cRAD µTS increased 0.2-fold after engaging platelets. Note: the intensity values shown in these experiments are different from the ones in the main figures because this platelet-µTS samples were allowed to engage for 1 hr, and these experiments were conducted on a different type of flow cytometer (BD LSR II flow cytometer) with different voltage settings. The total number of events analyzed in each experiment was approximately 10,000 events.

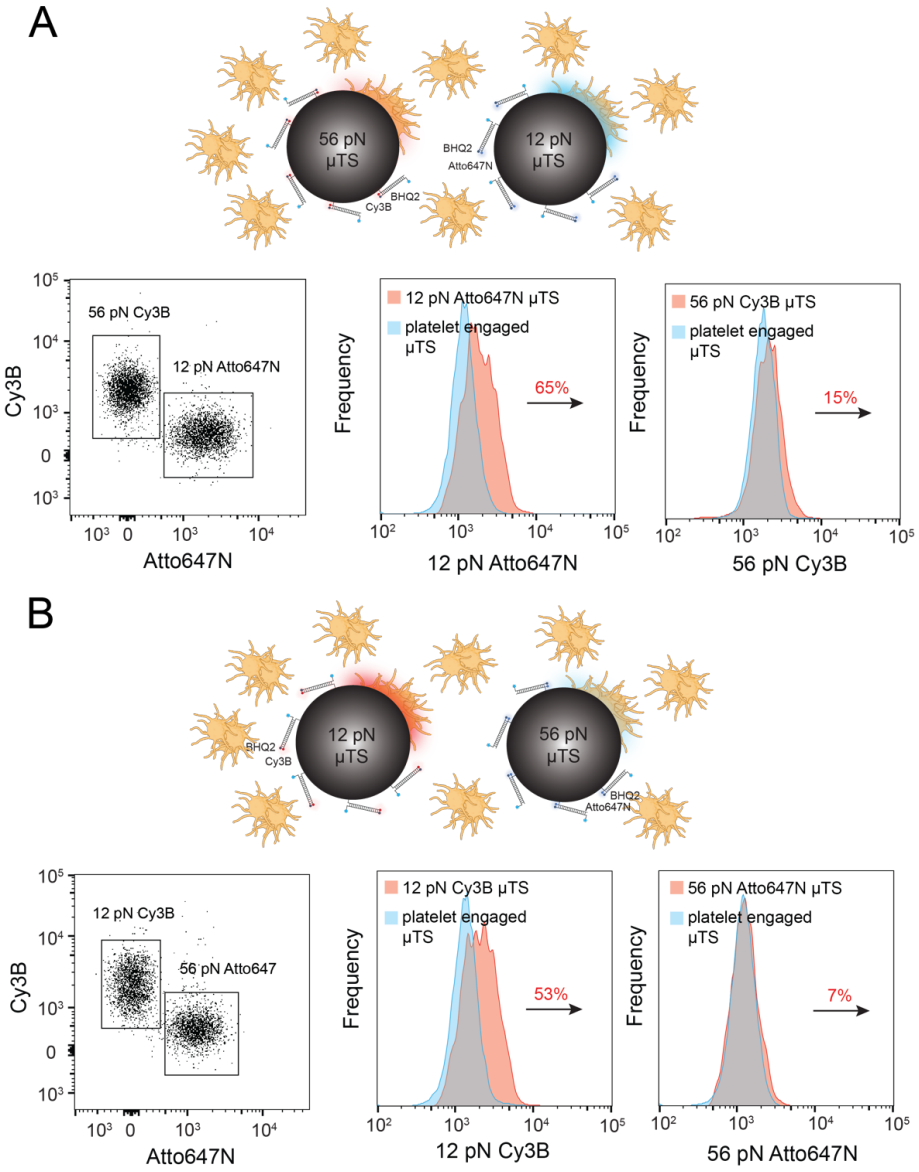


**Figure A2.11. Demonstration of spectrally barcoding µTS tension threshold magnitude.** (A) Multiplexing the 12 pN Atto647N µTS and 56 pN Cy3B µTS probes. (B) Multiplexing the 12 Cy3B µTS and 56 pN Atto647N µTS. In both experiments, the mixture of two µTS beads were simultaneously added to the platelet suspension. After 1 hour of incubation, lysis buffer was added to lyse platelet aggregates to allow for flow analysis. µTSs with different force thresholds were gated out according to Cy3B vs Atto647N scatter plots. MFI of these µTSs were then compared to µTS that were not incubated with platelets.12 pN µTS showed a higher fluorescence change than 56 pN µTS. Similar results was observed after swapping the spectral encoding.

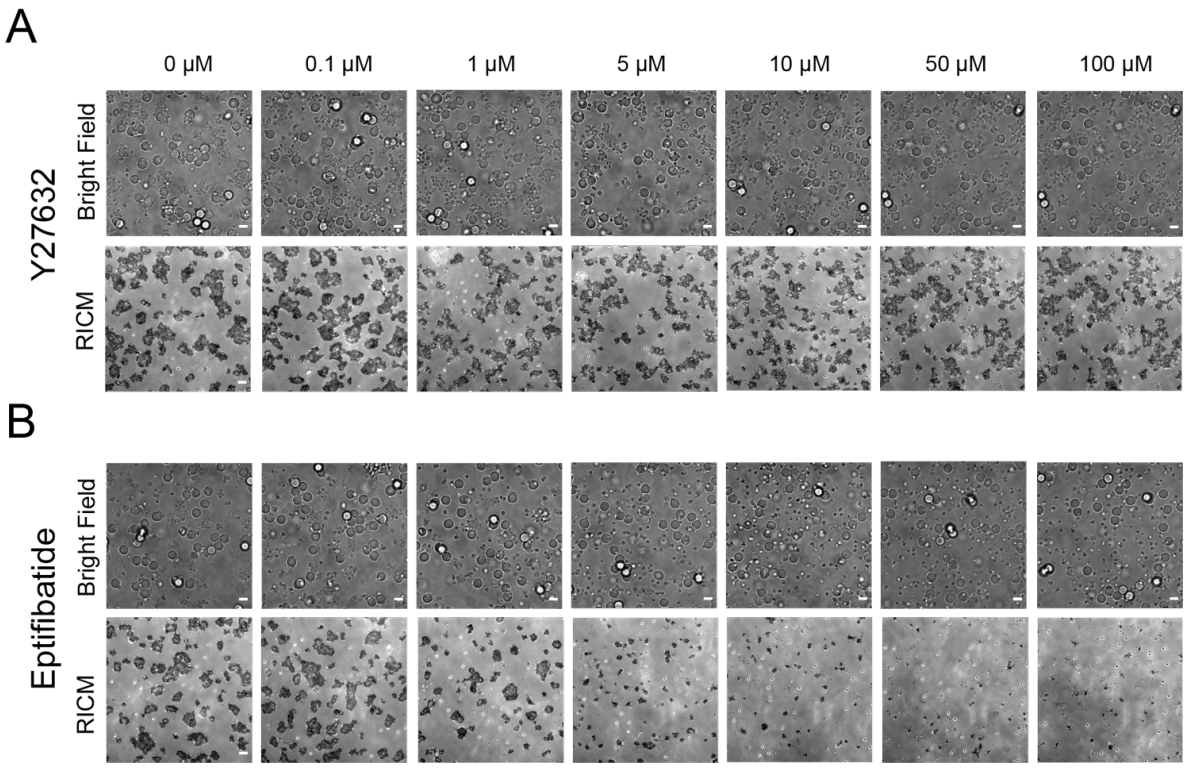


**Figure A2.12. Representative bright field and RICM images showing platelet aggregation and adhesion changes with increasing concentrations of Y27632.** (A) and eptifibatide (B). Mouse platelets were incubated with the drug for 30 min and then add to 96 well plates for 1 hr and then imaged. Scale bar = 5 μm.

**Movie A2.1. Tension and F-actin signal distribution at the interface between T cell and μTS.**

# Chapter 3. DNA Origami Tension Sensors to Study TCR Mechanics at Membrane Junctions

## 3.1 Abstract

The T cell receptor (TCR) is thought to be a mechanosensor, meaning that it transmits mechanical force to its antigen and leverages the force to amplify the specificity and magnitude of TCR signaling. The past decade has witnessed the development of molecular probes which have revealed many aspects of receptor mechanotransduction. However, most force probes are immobilized on hard substrates, thus failing to reveal mechanics in the physiological context of cell membranes. In this report, we developed DNA origami tension sensors (DOTS) which bear force sensors on a DNA origami breadboard and allow mapping of TCR mechanotransduction at dynamic intermembrane junctions. We demonstrate that the mechanical forces at fluid TCR-antigen bonds regulate TCR signaling and are dependent on cell state, antigen mobility, antigen potency, antigen height and F-actin activity. The high programmability of DOTS allows us to tether it onto a microparticle to mechanically screen antigen in high throughput using flow cytometry. Additionally, DOTS were anchored onto live B cell membranes thus producing the first quantification of TCR mechanics at authentic immune cell-cell junctions.

## 3.2 Introduction

To protect against cancer and viral infections, the T cell receptor (TCR) actively scans the surface of target cells seeking to recognize abnormal protein fragments presented by the major histocompatibility complex, pMHC. Remarkably, the TCR exhibits an exceptional level of specificity and sensitivity towards antigens. Even the presence of just one or two abnormal pMHC molecules among approximately 100,000 normal pMHCs on a single cell, is sufficient to trigger T cell activation.[17] The molecular mechanisms responsible for such a robust T cell response are still not fully understood. However, an emerging hypothesis suggests that TCR-pMHC bonds within the dynamic environment of cell-cell junctions experience mechanical forces and these

forces can cause conformation changes in the TCR-pMHC complexes, thereby prolonging the lifetime and exposing kinase docking sites to facilitate the subsequent phosphorylation cascade necessary for TCR signaling.[29, 161, 162] Indeed, studies using single molecule force techniques have demonstrated that ~10 piconewton (pN) forces is capable of triggering calcium flux, hallmark of T-cell activation.[24, 28] However, these forces were externally applied to the pMHC-TCR complexes leaving the question of whether the magnitude and duration of such forces are representative of the native immune junction. This important inquiry highlights a prevailing challenge in the field, namely the need to develop a tool to investigate the TCR mechanotransduction at intermembrane junctions.

In the past decade, our lab and colleagues developed a series of molecular tension sensors (MTS) to detect the forces transmitted to individual receptor-ligand bonds. Briefly, an elastic molecule (DNA hairpin, peptide, or polymer) is modified with a FRET pair and anchored to a surface at one terminus and presenting a ligand to bind a receptor of interest at its other terminus.[67, 70, 72] Cellular forces transmitted to the probe extend it and separate the FRET pair, leading to a fluorescence enhancement. With this sensor, we revealed that TCRs transmit 10-20 pN forces to antigens and these forces contribute to antigen discrimination, TCR proximal signaling, T cell activation, and cytotoxic degranulation.[25, 85, 121] However, in these studies, sensors were immobilized on a hard glass slide, restricting lateral motion, unlike the case in cell membranes. This type of immobilization inhibits TCR clustering and centralization, potentially resulting in an overestimation of the force magnitude. Several studies, including our own, used glass supported lipid bilayers (SLBs) to mimic the plasma membrane and inserted MTS to SLB to measure force at laterally fluid TCR-antigen bonds.[71, 92] However, at TCR clusters, MTS are likely placed within sufficient proximity that causes crosstalk between FRET pairs at adjacent sensors. This would lead

to suppressed fluorescence emission, thereby compromising the reliability of the results. This inconsistency in fluorescence levels may provide an explanation for the discrepancies observed in the magnitudes of TCR forces previously reported by different research groups utilizing MTS-based approaches. Additionally, it is important to note that the SLBs used in these studies were created on planar glass substrates. Planar SLBs lack deformability and exhibit a flattened topology, thus resulting in a flat and contiguous T cell/SLB contact zone. In contrast, physiological T cell-target cell contacts are highly dynamic, characterized by sporadic and curved interactions, often involving microvilli or invadosome-like protrusions.[163, 164] Moreover, glass substrates are chemically and physically different from that of an antigen presenting cell. For example, the stiffness of glass is $10^9$-fold greater than that of the plasma membrane and prior studies have showed that T cell mechanotransduction is influenced by the stiffness of the surrounding matrix.[11, 12]

Herein we developed membrane-tethered DNA Origami Tension Sensors (DOTS) to address these limitations. DNA origami, due to its high programmability and functionality, has emerged as a versatile approach to fabricate nanodevices for spatial patterning, sensing and molecular manipulation and provides a powerful platform for force sensor design.[165, 166, 167] Specifically, we made a rectangular nanosheet origami carrying a DNA hairpin that is responsive to TCR forces. The dimensions of the origami set the minimum distance between adjacent hairpins at 40 nm thus fully suppressing the crosstalk between FRET pairs. With DOTS, we revealed that TCR-antigen bonds experience force exceeding 8 pN at fluid interfaces and these forces was generated by F-actin dependent cytoskeleton contraction and repulsion from large proteins at the immune synapse. This conclusion was validated using both ratiometric fluorescence intensity measurements as well fluorescence lifetime-based imaging. To best mimic the geometry of antigen presenting cells and

reconstitute the three-dimensionality of immune synapse, DOTS were tethered to SLB functionalized microparticles which allowed for measuring TCR force in suspension and in a high-throughput manner using flow cytometry, thus offering a potential tool for mechanically based antigen screening. Finally, we anchored DOTS to live B-cell membranes and thus creating the first molecular device that allows for measuring force transmission at authentic immune cell-cell junctions. Taken together, DOTS represent a powerful tool to study immunoreceptor forces and the technique is expected to promote advances in the emerging field of immunomechanobiology.

## 3.3 Results

### 3.3.1 Design and characterization of DOTS

We designed a single layer DNA origami nanostructure with dimension of 40 x 80 nm, which was folded by hybridizing 84 single stranded DNA oligos (staples) to p7560 phage DNA scaffold (**Figure 3.1a** and **Figure A3.3**). A DNA hairpin sequence was incorporated into one staple and extended out of the origami to detect TCR forces. The integrity and structure of assembled DOTS was confirmed by gel electrophoresis and atomic force microscopy (AFM) (**Figure 3.1b**). No degradation of origami was observed even after 1 hour incubation in cell imaging media at room temperature (RT) (**Figure A3.4**). The origami was anchored to the SLB surface by hybridizing eight single-stranded DNA overhangs located at the bottom of the origami to preinserted complementary cholesterol DNA strands on the SLB surface. Throughout this work, unless otherwise specified, we utilized a concentration of 5 nM origami to prepare the surfaces, resulting in a density of 214±8 molecules/$\mu m^2$ (**Figure A3.5**). Fluorescence Recover After Photobleaching (FRAP) measurements showed that DOTS were laterally mobile on DOPC SLB and exhibited a physiological diffusion coefficient of ~0.04 $\mu m^2/s$. Note the fluidity of DOTS is similar to that of

murine antigens on the plasma membrane. This is in contrast to previously reported fluid MTS which exhibited a supraphysiological fluidity that was 10-20 times higher (**Figure 3.1c**).

### 3.3.2 The dimension of DOTS eliminates intermolecular FRET at high molecular density

We hypothesized that MTS anchored to membranes would exhibit intermolecular FRET at high molecular density, which is observed in TCR clusters (**Figure 3.1d**). To test this concern, we anchored a conventional MTS backbone-DNA hairpin to the DOPC SLB surface. (**Figure 3.1f**). Initially, a fixed quantity of Alexa 488-DNA hairpins was added to the SLB, following by washing away the excess. Subsequently, different concentrations of Cy3B hairpins were added into the SLB to tune the density. In principle, as the density of Cy3B hairpin increases, we anticipate a higher degree of intermolecular FRET, resulting in a reduction in Alexa 488 fluorescence intensity. The density of Cy3B hairpins exhibited an increase with the incubation concentration and saturated around 200 nM (**Figure 3.1h** and **3.1j**). As expected, the fluorescence signal of Alexa 488 showed a decline as the density of Cy3B acceptor hairpins rose, providing confirmation of robust intermolecular FRET. (**Figure 3.1h** and **3.1j**). We hypothesized that our DOTS design would circumvent this problem by physically separating hairpins (**Figure 3.1e**). In the 40 x 80 nm DOTS design, the nearest possible distance between fluorophores on adjacent origamis is 40 nm, which is 6-fold greater than the Forster radius and therefore effectively eliminates the possibility of intermolecular FRET occurring. We tested this claim by adding different concentrations of Cy3B-DOTS to SLBs precoated with Atto488-DOTS (**Figure 3.1g**). As predicted, no fluorescence decrease in the 488 channel was observed even as the Cy3B DOTS density reached saturation at 8 nM concentration (**Figure 3.1i** and **3.1k**).

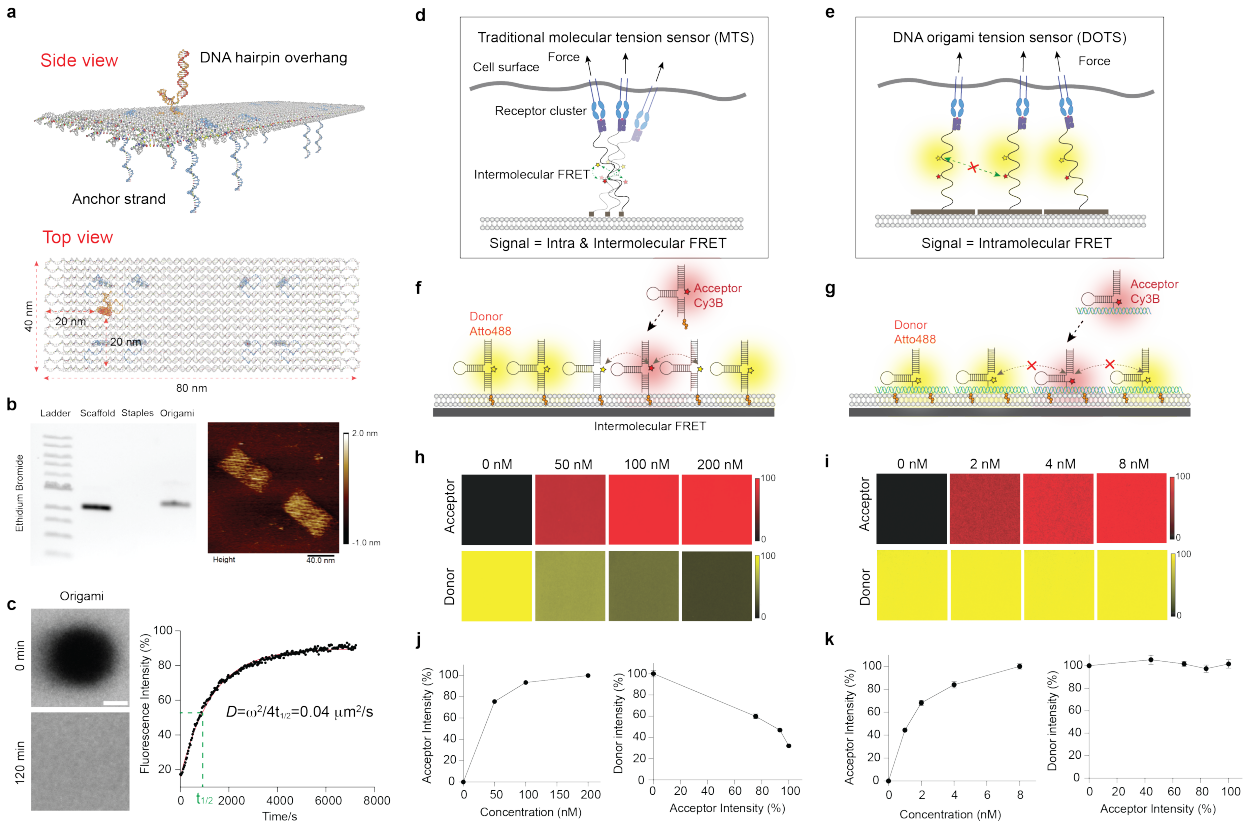


**Figure 3.1. Characterization of DOTS. a** Schematic of DOTS comprised of a rectangular nanosheet that presents a single hairpin on one face and eight anchor strands on the other face for anchoring DOTS to membrane. **b** Left: agarose gel electrophoresis showing the bands of DNA origami scaffold, staples, and annealed DOTS. Right: liquid AFM image of DOTS. **c** FRAP of DOTS on the DOPC SLB surface. Left: fluorescence images showing the fluorescence recovery of the photobleached area after 120 min. Right: FRAP curve with a recovery half time $t_{1/2}$ of 910 seconds. Scale bar=10 μm **d** Schematic showing intermolecular FRET between adjacent MTS at high molecular density. **e** Schematic showing the dimension of DOTS prevents crosstalk between fluorophores, thus eliminating the intermolecular FRET. **f-g** Schematic showing the process of adding of acceptor fluorophore tagged MTS/DOTS to SLBs that were precoated with donor tagged MTS/DOTS. **h** Representative fluorescence images showing MTS acceptor (Cy3B) fluorescence signals on the SLB surface under different incubation concentrations. The MTS donor (Atto488) fluorescence intensity decreased after addition of acceptor MTS. **i** Representative fluorescence images showing DOTS acceptor fluorescence signals on the SLB surface under different incubation concentrations. The donor fluorescence intensity remained constant regardless of the density of the acceptor. **j-k** Plot showing the correlation between the fluorescence intensities of donor and acceptor MTS (j) or DOTS (k) on the SLB surface

### 3.3.3 DOTS detect TCR tension at fluid intermembrane interfaces

To measure TCR forces at fluid junctions, we proceeded by seeding naïve CD8+ T cells, isolated from OT-1 transgenic mice, onto DOPC fluid SLB coated with pMHC-loaded DOTS, in conjunction with intercellular adhesion molecule 1 (ICAM-1) (**Figure 3.2a**). Upon initial contact of the T cell with the SLB, a simultaneous decrease in DOTS fluorescence intensity was observed in the cell spreading area, indicating the exclusion of DOTS from that region. Subsequently, the remaining DOTS, after engaging TCRs, clustered and centralized, ultimately accumulating at the center of the cell/SLB junction within a 10-minute timeframe. Concurrently, ICAM-1 tagged with GFP engaged LFA-1 and concentrated at the periphery (**Figure 3.2b** and **Movie A3.1**). This phenomenon can be attributed, in part, to the reorganization of receptor-ligand interactions at T cell intermembrane junctions in a manner that is dependent on the height, aiming to minimize energy. However, the exclusion of origami was not solely due to axial crowding. This is supported by the observation that replacing the origami-tethered antigen with one tethered using a single DNA hairpin resulted in a significant decrease in the exclusion level, from 60% to 17%, despite the DNA hairpin being capable of extending to a greater axial height (**Figure 3.2c** and **3.2d**). We thus hypothesized the DOTS exclusion was induced by lateral crowding and was independent of protein-protein interactions. DNA origami are bulky DNA structures spanning 40 x 80 nm in the lateral dimension. The T cell expresses glycocalyx and large proteins such as CD45 phosphatase which could impose a physical constraint that sterically excludes DOTS. To confirm this, we primed T cells with anti-CD3 and then plated these cells onto blank DOTS surface lacking pMHC. Blank DOTS did not centralize due to lack of TCR engagement (**Figure 3.2d**, **Figure A3.6**). However, they were still excluded, and the exclusion level was comparable to that of pMHC loaded DOTS. To validate the mechanism of DOTS translocation, both inward flow and outward

exclusion, we performed single molecule imaging of DOTS. Here, we reduced the density of DOTS by incubating the SLB with a 1000-fold dilution of DOTS and performed timelapse fluorescence imaging during the initial stages of T cell spreading. As shown in **movie A3.2**, free DOTS rapidly moved out of the cell adhesion zone, a small subset of DOTS (~1-10) remained confined to the cell junction. TCRs at the leading edge engaged DOTS and centralized to form what is typically described as the central supramolecular activation complex (cSMAC).

After successfully establishing the ability of DOTS to interact with the TCR and lead to the formation of immune synapse, our subsequent objective was to further demonstrate DOTS's ability to eliminate intermolecular FRET in the case of physiological TCR clusters. We seeded T cells onto SLBs coated with a mixture of Cy3B-DOTS and Atto647-DOTS and acquired the lifetime map of Cy3B fluorophore through fluorescence lifetime imaging microscopy (FLIM) (**Figure A3.7a**). FLIM measures the fluorophore excited state lifetime ($\tau$), which is highly sensitive to FRET efficiency and is independent of probe density. In principle, if intermolecular FRET exists in TCR clusters, Atto647N DOTS would quench surrounding Cy3B DOTS and decrease the fluorescence lifetime of Cy3B. As anticipated, we did not observe any significant change in Cy3B fluorescence lifetime within TCR clusters compared to the background or TCR clusters formed on surfaces with Cy3B-DOTS alone, suggesting the absence of intermolecular FRET. (**Figure 3.2e** and **Figure A3.7d-e**). In contrast, MTS exhibited strong intermolecular FRET as indicated by a strong Cy3B lifetime shift at TCR clusters (**Figure 3.2f** and **Figure A3.7d**).

Next, we utilized DOTS to detect TCR forces by monitoring the mechanical unfolding of the DNA hairpin on the origami. The unfolding force of DNA hairpins depends on the GC content and stem-loop structure of the hairpin. We initially designed a DNA hairpin with 22% GC content and nine nucleotide (nt) stem. The unfolding force ($F_{1/2}$, the equilibrium force leading to 50% probability

of unfolding of hairpin) of this hairpin is calculated as 8 pN using the equations described in Chapter 1.3.2 (**Supplementary note 3**). DNA hairpin unfolding leads to dequenching of the dye (Cy3B-BHQ2) and results in a 3.3-fold fluorescence enhancement (**Figure A3.8** and **Figure A3.9a**). DOTS incorporated with this hairpin can thus reveal > 8 pN TCR forces with a fluorescence readout. Note that DOTS clustering with TCRs also leads to a fluorescence increase. To deconvolve tension and cluster-induced fluorescence increases, a Atto647N fluorophore was incorporated onto the origami structure 40 nm away from the DNA hairpin to function as a density reporter as it was insensitive to force (**Figure A3.9a** and **Figure A3.3**). Tension information was obtained by quantifying the ratio between Cy3B (tension + density) and Atto647N (density). Values > 1 indicate mechanical unfolding of the hairpin and are referred to as tension signal (See **Figure A3.10** for analysis details). TCR-pMHC interactions are highly transient with a subsecond bond lifetimes, which is difficult to capture by real time imaging (**Figure A3.9b**). In order to enhance the tension signal, we added a 15 nt ssDNA "locking strand" at a concentration of 200 nM into the cell imaging media to hybridize mechanically unfolded hairpins and lock it in the opened state (**Figure 3.2g**). This locking strategy gradually accumulated unfolded (dequenched) DOTS at the junction and make force signals exceeding $F_{1/2}$, if any, became visible. Of note, locking strand did not cause nonspecific hairpin opening and hybridization to DNA hairpins was mechanically selective (**Figure A3.9c-e**). Within 10 min of cell-surface contact, TCR-antigen tension gradually accumulated from puncta into cSMAC (**Figure 3.2h**).

We also applied FLIM to further confirm the mechanical unfolding of the DNA hairpins. Because the Cy3B/BHQ2 pair is subject to static quenching, we replaced Cy3B with Atto488 given its excellent imaging properties and larger $\tau$ shift after being quenched by BHQ2. We captured FLIM images of cells on the SLB before and after adding locking strand and generated a phasor plot for

the FLIM datasets (**Figure 2i**). From the phasor plot, we identified pixels containing fluorescence lifetimes of $\tau$ = 2 ns and 4 ns corresponding to folded ($\tau_{closed}$) and unfolded ($\tau_{open}$) hairpin Atto488 lifetimes (conformations), respectively,[99] and obtained photon count maps for these two lifetimes. We then examined the change of these two populations before and after adding locking strand. As shown in **Figure 3.2i**, after adding locking strand, the $\tau_{closed}$ population decreased at the T cell-SLB junction (indicated by yellow dash lines) whereas the $\tau_{open}$ population significantly increased in count. This result confirmed the accumulation of mechanically opened hairpins at the immune synapse and successfully mapped TCR-antigen mechanical events with a fluorescence lifetime readout.

Next, we adjusted the GC content of the hairpin stem to 77% to obtain a higher $F_{1/2}$ of 11.7 pN to detect TCR forces with a higher magnitude (**Supplementary note 3**). TCR forces still opened 11.7 pN DOTS and generated strong tension signal, indicating that the TCR transmits F> 11.7 pN on laterally fluid antigen (**Figure 3.2j**). To further validate these findings, we substituted the DNA hairpin on the origami structure with another force-sensitive DNA element known as the tension gauge tether (TGT), which is a DNA duplex that ruptures at a specific force threshold: 12 pN in an unzipping geometry and 56 pN in a shearing geometry (**Figure A3.11a**).[74] We observed that the cSMAC volume of T cells seeded on 12 pN TGT was smaller than that on 56 pN TGT (**Figure A3.11b**). This suggests that a subset of TCRs generated 12 pN forces, leading to the dissociation of TCR from 12 pN DOTS and subsequent translocation to the center to form the cSMAC.

To study how the fluidity of antigen influences force transmission, we replaced DOPC with DPPC lipid to create a non-fluid SLB. In this case, no clustering or exclusion of DOTS was observed as indicated by the Atto647 channel (**Figure 3.2k**). Notably, the tension signal on gel-phase SLBs was greater than that observed on fluid SLBs (**Figure A3.9d** and **3.2k**). This is because fluid SLBs

offer little resistance to pulling in the lateral direction and confirms that TCRs experience pulling force in both shear and normal vectors when the antigen is immobilized.

We also compared the tension signal generated by naïve and effector T cells which present the same TCR but are reported to exhibit different response to antigen.[168] Interestingly, we found the effector T cells also opened DOTS but the signal intensity was much lower than that of naïve T cell (**Figure 3.2l**). The differential tension signal was likely due to the difference in cytoskeletal dynamics and coupling to TCRs.[169] We found F-actin was less dense and more heterogeneously distributed in effector T cells (**Figure A3.12**). Additionally, effector T cells exhibit a faster rate of immune synapse formation. After engaging antigen surface, TCRs on effector T cells rapidly centralized to form cSMAC within 2-3 minutes with a significant F-actin clearance (**Movie A3.3**). In contrast, naïve T cells took 10 min to mature the immune synapse, and F-actin clearance was less pronounced (**Figure A3.12**). The differential dynamics may also account for the discrepancy in DOTS tension signal, which reports the history of TCR mechanical events.

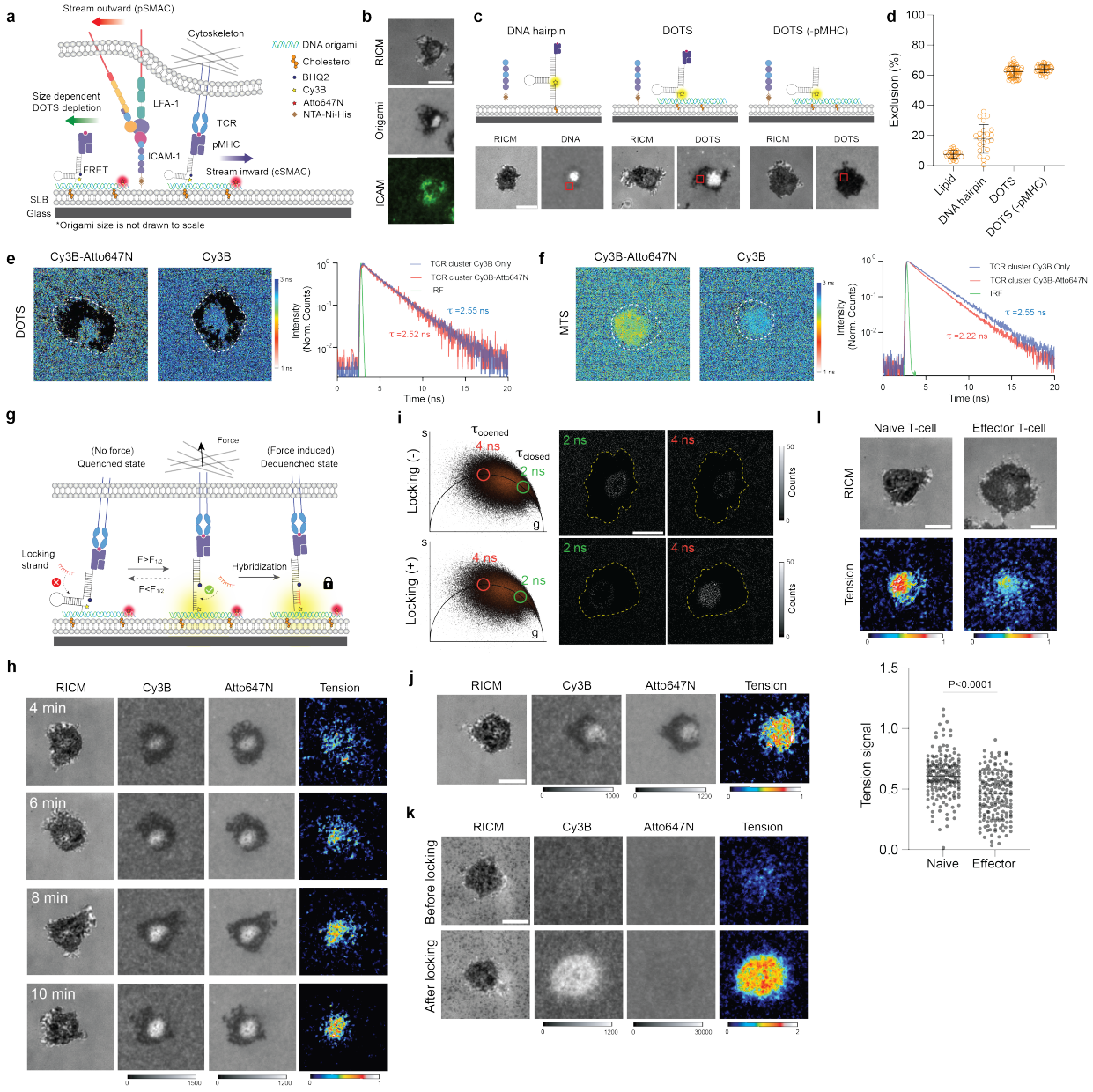


**Figure 3.2. TCRs transmit mechanical force to laterally fluid antigen**. **a** Schematic of functionalized SLB. Upon T cell spreading, free DOTS, TCR engaged DOTS and LFA-1-ICAM underwent reorganization at the T cell-SLB junction. **b** Representative microscope images showing the signal of T cell, DOTS and ICAM-1-GFP on the DOPC SLB surface. **c** Schematic and representative images showing different exclusions of DNA structures (hairpin, DOTS, DOTS lacking pMHC antigen) from the T cell spreading area **d** Plot comparing the exclusion levels of different DNA structures. The level of exclusion was quantified by measuring the decrease in DNA fluorescence intensity within the cell spreading area (ROIs indicated by red squares in panel (c)). n>23 cells for each condition. **e** Representative FLIM images of Cy3B fluorophore on the SLB surface functionalized with Atto647-DOTS and Cy3B-DOTS or Cy3B-DOTS alone. White dash

lines indicate the T cell spreading areas. Black pixels in the lifetime image indicate pixels with <25 photons or lifetime > 3.2 ns (Supplementary note 1). FLIM decay curves of pixels at TCR clusters formed on Atto647/Cy3B-DOTS SLB or Cy3B-DOTS only SLB. Averaged lifetimes of pixels were noted next to the curves. **f** Representative FLIM images of Cy3B fluorophore on the SLB surface functionalized with Atto647-MTS and Cy3B-MTS or Cy3B-MTS alone. Black pixels in the lifetime image indicate pixels with <25 photons or lifetime > 3.1 ns. FLIM decay curves of pixels at TCR clusters with averaged lifetime noted. **g** Schematic showing that locking strand hybridizes to mechanically opened DNA hairpin to capture transient TCR force events. **h** Time lapse images showing the dynamics of 8 pN TCR tension signal in the immune synapse. **i** Comparison of $\tau_{closed}$ and $\tau_{open}$ population before and after adding locking strand. The pixel images of specific lifetime were obtained by back-projection of the points within the green circles ($\tau_{closed}$ population) and red circles ($\tau_{closed}$ population) in the phasor plots. **j** Representative RICM and tension images (11.7 pN) of T cell cultured on fluid DOPC SLB. **k** Representative images of 8 pN TCR tension on non-fluid DPPC SLB. **l** Representative images showing TCR tension signal of naïve and effector T cell after 20 min spreading on DOPC fluid SLB. Dot plot comparing the tension signals of naïve T cells and effector T cells. n>170 cells from 3 independent experiments. Scale bars = 5 μm

### 3.3.4 Actin polymerization and membrane bending contribute to TCR forces

After establishing the presence of TCR forces at intermembrane junctions, we next employed DOTS to identify the sources of TCR forces. Prior work suggested that cytoskeleton dynamics are crucial to mechanotransduction.[129] We treated T cells with cytoskeletal drugs to identify which component of the cytoskeleton dominates TCR force transmission at fluid interfaces. In these experiments, T cells were allowed to spread on fluid SLB surface and subjected to drug treatment for 5 min, followed by the introduction of DNA locking strand to record TCR force (**Figure 3.3a**). Blebbistatin (50 μM), which inhibits myosin II ATPase, did not cause a notable change in force signal compared to the vehicle control (**Figure 3.3a** and **3.3b**). In contrast, the actin targeting drugs, CK666 (50 μM) and Lat-B (5 μM) dramatically decreased the force signal to 60%, and 20%, respectively (**Figure 3.3b**). CK666 targets the Arp2/3 complex, thus dampening actin nucleation and branching, while latrunculin-B directly binds to actin monomers and prevents polymerization. These results suggest that myosin is less involved in TCR mechanotransduction and the

cytoskeleton transmits forces to TCRs mainly through F-actin. TCRs are coupled to F-actin branches with the aid of adaptor proteins (WASP, Nck) and actin nucleating regulators (Arp 2/3) (**Figure 3.3c**). We inhibited the recruitment of Nck to the TCR complex using AX-024, a small molecule that binds to the SH3 domain pocket on Nck and disturbs the interaction between Nck and CD3 subunits. When treated with AX-024 (500 nM), T cells exerted less tension, further confirming the role of F-actin in transmitting tension to TCR-pMHC bonds (**Figure 3.3d** and **3.3e**).

TCR mechanosensor model postulates that mechanical forces contribute to antigen discrimination and TCR signaling. If this is true, TCR-antigen bond should experience forces during the initial interaction but before T cell activation. Paradoxically, there is minimal TCR-actin coupling prior to TCR activation. Other work also suggests that actin polymerization is not a cause but a consequence of TCR signaling.[52, 170] Therefore, there must be another source of mechanical energy that is transmitted to the TCR-antigen complex to trigger initial signaling. The process of TCR-pMHC complex formation involves bringing the intermembrane space to a distance of ~15 nm. This bond formation can induce membrane bending and generate tensile force, primarily due to the presence of large proteins at the junction. One such example is the LFA-1-ICAM-1 complex, which spans ~36-45 nm and causes repulsion at the sites of initial TCR-pMHC engagement. Furthermore, bulky proteins like the phosphatase CD45, which extends up to 40 nm in the extracellular region, may also play a role. To validate this hypothesis, we adjusted the height of the antigen by elongating the DNA hairpin on DOTS and then recorded TCR-pMHC tension change (**Figure 3.3f** and **Supplementary note 2**). All surfaces presented identical antigen and origami densities. The force threshold of the DNA hairpin was not changed by the elongated DNA tether (**Figure A3.13**). T cells spread similarly across the three TCR-antigen dimensions, but the tension signal intensity significantly decreased with increasing antigen extension (**Figure 3.3g** and

**3.3h**). These differences in TCR-antigen mechanics were also associated with difference in signaling levels, as phosphorylated ZAP70 levels after 10 min of cell seeding were significantly decreased for the elongated antigen (**Figure 3.3i**). Taken together, this data supports a mechanosensor model where initial forces are mediated by the size mismatch of proteins and the bending modulus of the plasma membrane at the cell-cell junction.

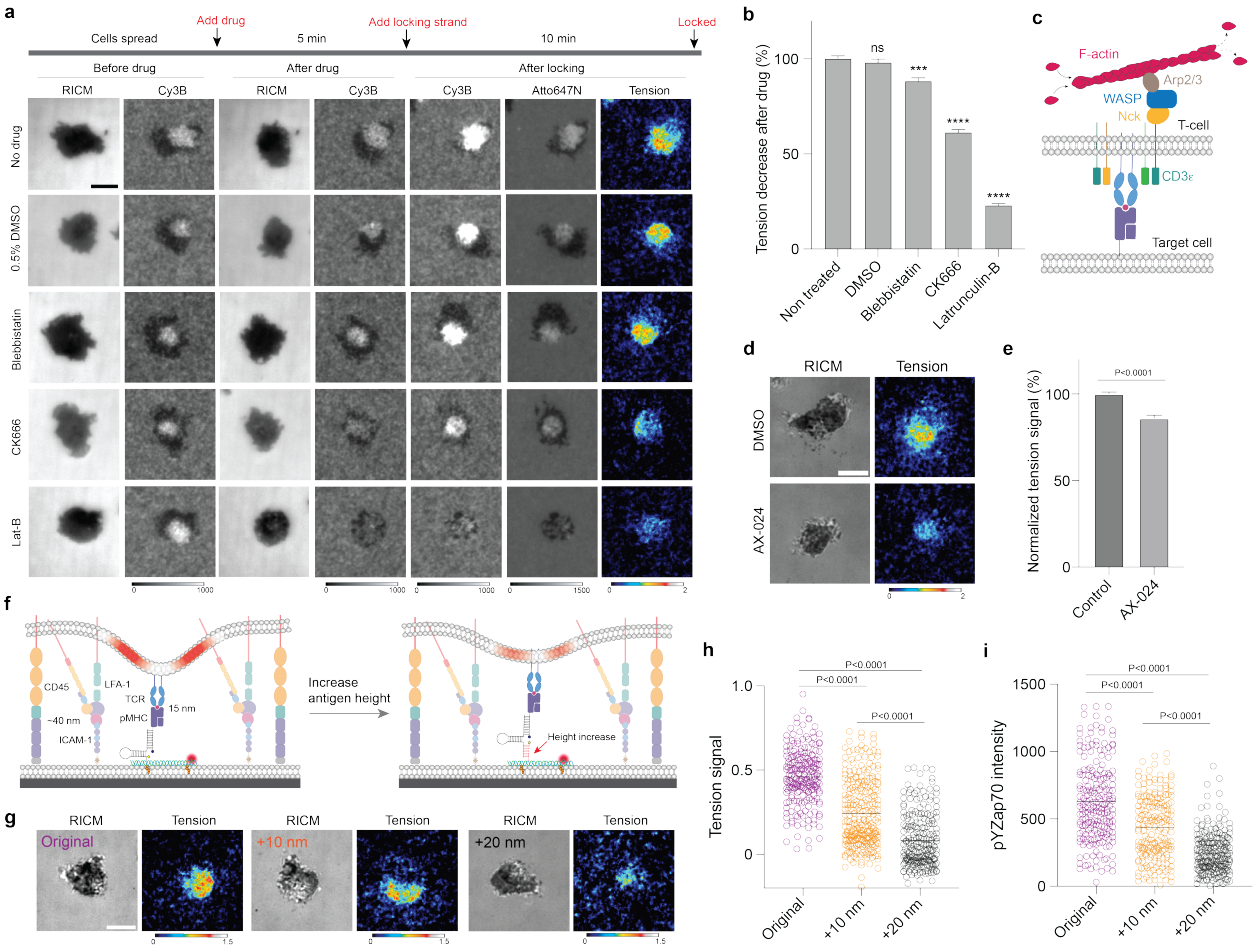


**Figure 3.3. F-actin and membrane bending contribute to TCR force generation. a** Representative microscope images showing the spreading and tension signals of T cells treated with cytoskeleton inhibitors. **b** Bar graph quantifying the tension decreases when T cell were treated with cytoskeleton drugs. n>120 cells for each group from three independent experiments. Error bar indicates SEM. ns, not significant P=0.4188, ***P = 0.0001, ****P < 0.0001 **c** Schematic showing the recruitment of F-actin to TCR engagement sites with the aid of adaptor proteins. **d** Representative images showing the tension signal of T cells with and without AX-024 treatment. **e** Bar graph quantifying the tension signal decrease when the T cells were treated with AX-024. **f**

Schematic showing that elongating DNA hairpin increases the maximum antigen height, which decreases the membrane bending and the strain transmitted to TCR-pMHC bonds. **g** Representative images showing TCR tension signals under different antigen heights. **h-i** Dot plot quantifying intensities of TCR tension (**h**) and pYZap70 (**i**) of T cells engaging antigens with different heights. At least 200 cells from three independent experiments were analyzed. Lines indicate the mean. Scale bars = 5 μm.

### 3.3.4 Spherical SLB for investigating TCR mechanics in suspension

Although planar SLBs mimic the biochemical and biophysical properties of the plasma membrane, the surface displays a flattened topology and lacks the 3D free standing properties of target cells. In contrast, microparticles better mimic target cells and have been used as artificial antigen presenting cells to stimulate T cells and capture signaling molecules released into the immune synapse.[171, 172] Accordingly, we created a spherical SLB (SSLB) platform by coating a 5 μm particle with SLB and then tethered DOTS onto it to measure TCR forces at T cell/SSLB junctions (**Figure 3.4a**). In a typical experiment, DOTS-SSLBs and T cells were mixed at 1:1 ratio in suspension in the presence locking strand and imaged on a confocal microscope after 30 min incubation. TCR engaged DOTS and translocated to the center to form cSMAC (**Figure 3.4b**). Similar to the approach used with planar SLB DOTS, we extracted tension information by analyzing the Cy3B/Atto647N ratios (**Figure A3.14**). At the T cell-SLB junctions, the average Cy3B/Atto647N ratio was found to be 2.2-fold higher and returned to background levels when the locking strand was absent. This indicated the presence of 8 pN forces that caused the opening of hairpins at the junction (**Figure 3.4c**). We next conducted z-scanning across the junction and performed image arithmetic on successive focal planes to construct the 3D view of tension signal. As shown in **Figure 3.4d** and **movie A3.4**, the tension signal covered the whole synapse and overlapped with the DOTS central clusters. Taken together, T cells generated and transmitted F >8

pN to TCR-pMHC complexes, even if the pMHC was laterally fluid and tethered to a microparticle in suspension.

One advantage of the DOTS-SSLB platform is that each particle is at the cellular scale and thus amenable to flow cytometry analysis and enables high throughput quantification of TCR forces. In suspension, three distinct populations were present- single T cells, single SSLBs, as well as conjugates of the two entities with various stoichiometries. The SSLBs were identified with the DOTS fluorescence signal (Atto647N). Note that here we used the Atto647N/BHQ2 instead of Cy3B/BHQ2 dye pair to decorate hairpin because Atto647N is better suited for flow analysis and displays minimal spectral overlap with CFSE dye used to label the T cells (**Figure 3.4e**). Events that showed dual positive signals (Atto647N+CFSE) were identified as SSLB-T cell conjugates (purple box in **Figure 3.4e**), from which 1:1 stoichiometry conjugates were selected using the forward scattering profiles for comparison with single SSLBs. In principle, TCR forces would light up the DOTS on the SSLB surface, making conjugate events exhibit a stronger Atto647N signal than individual SSLB events. Of note, unlike microscopy, flow cytometry measures the integrated fluorescence intensity of particles, thereby obviating the need for ratiometric analysis. We analyzed 200,000 events and observed a 40% mean fluorescence intensity (MFI) difference between these two populations (**Figure 3.4f**). This MFI change was due to tension as control experiments without locking strand did not show notable difference (**Figure 3.4g**).

The high throughput readout of SSLB signal enables the use of this platform as a potential tool for rapid antigen screening. In contrast to affinity-based antigen screening, the identification of potent antigens based on their biophysical parameters has proven to be more accurate and has gained increasing prominence.[31, 125] To demonstrate this concept, we mutated the fourth amino acid of the cognate OVA derived peptide SIINFEKL (N4) to obtain SIIQFEKL (Q4), SIITFEKL (T4),

SIIVFEKL (V4) altered peptide ligands (APLs). DOTS were modified with APLs and tethered to SSLBs to engage T cells. Compared to cognate N4 antigen, APLs SSLB displayed a lower conjugation efficiency to T cells (**Figure A3.15**) and did not show any fluorescence change after engaging T cells (**Figure 3.4h-i**). This shows that the TCR-antigen tension signal at the intermembrane junction is highly specific to the agonist antigen and confirms the potential of flow analysis of DOTS to be used as a tool for antigen screening.

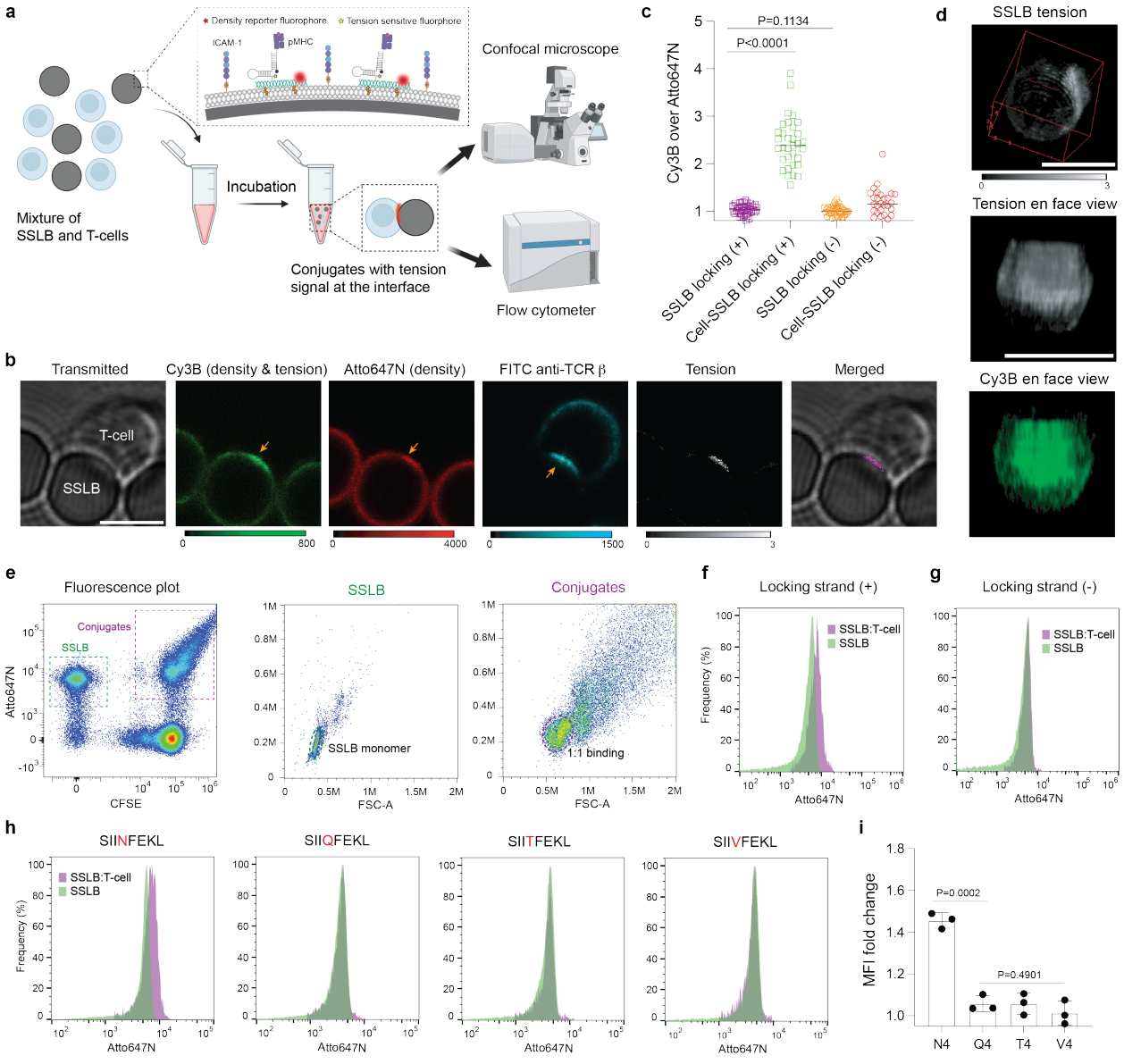

**Figure 3.4. SSLB as a platform to study 3D TCR tension. a** Schematic showing the workflow of using SSLBs to study TCR mechanics through high resolution confocal microscopy and high throughput flow cytometry. **b** Representative images showing the spatial distribution of DOTS, TCR, and tension signal at the middle layer of the T cell-SSLB junction. **c** Plot comparing the Cy3B/Atto647N ratios on SSLB surfaces and SSLB-T cell junctions with and without locking strand. Data from each group was acquired from >25 cells. All data points were normalized to the mean value of Cy3B/Atto647N ratios in SSLB locking (-) condition for standardized comparison. **d** 3D reconstructed image showing the 3D distribution of DOTS and tension signals at the junction. **e** Flow cytometry fluorescence dot plot (Atto647 vs CFSE) showing T cells, SSLBs (green dash line), and conjugates events (purple dash line). Forward vs side scatter plot was used to gate out SSLB monomers (green dash line) and T cell-SSLB conjugates at 1:1 binding stoichiometry (purple dash line). **f** Atto647N fluorescence histograms of SSLBs (green) and 1:1 T cell/SSLB conjugate (purple) events. **g** Atto647N fluorescence histograms of SSLBs and 1:1 T cell-SSLB conjugates when locking strand was absent. **h** Atto647N fluorescence histogram of SSLBs and 1:1 T cell/SSLB conjugates where SSLBs were modified DOTS presenting antigens with different potencies. **i** Plot quantifying the Atto647N mean fluorescence intensity (MFI) difference between 1:1 T cell/SSLB conjugates and SSLBs. Scale bars = 5 μm.

### 3.3.5 DOTS revealed TCR tension at the physiological T cell-B cell junctions

There is always the question of whether the native TCR-pMHC complex experiences the same magnitude of pN forces as those recorded on synthetic surfaces. Membrane protrusions, contractility of target cells, and proteins on the target cell membrane could alter the forces experienced by the TCR-pMHC complex. Thus, we next aimed to anchor DOTS onto target cell membranes to study forces at authentic cell-cell junctions. We screened different conjugation chemistries including maleimide-thiol, streptavidin-biotin, and cholesterol-lipid to anchor DOTS to cell membranes (**Figure A3.16 a-c**).[96, 173, 174] Origami labeling efficiency was dependent on the number and locations of the binding sites.[175] Overhangs near the edge of the origami sheet offered more robust tethering compared to overhangs in the middle. Therefore, we introduced 12 additional anchor strands at the edges of DOTS (**Figure A3.1**). In addition, because glycocalyx hindered origami access to the membrane, [176] we used a long "bridge strand" to link the cholesterol strand and anchor strand on the DOTS to help minimize steric crowding at the plasma membrane

(Figure 5a). We labeled three target cell lines (EL-4, B16-F10 and B cells) and ended up selecting resting murine B cells for the following studies because they have a comparable size to T cells, exhibit high binding efficiency and simple binding stoichiometry with T cells (**Figure A3.16d-f**). With all these efforts, DOTS anchored to B cell membrane homogenously distributed across the surface and maintained its integrity for hours at RT (**Figure A3.17**).

To measure TCR forces, we loaded anti-CD3ε onto 8 pN DOTS before anchoring to the B-cell membrane. DOTS modified B cells were mixed with T cells and allowed to engage for 30 min before imaging and analysis. We found that B cells strongly interacted with T cells and accumulated DOTS at the interface (**Figure 3.5b**). TCR forces separated Atto647N from the quencher, leading to a fluorescence increase over the force insensitive label of Cy3B. We analyzed 25 T-B conjugates and obtained an average of 5 ± 3% (Mean difference ± SEM) Atto647/Cy3B ratio increase at the T-B cell junctions compared to that on B-cell surfaces (**Figure 3.5d**). Note that this change corresponded to real-time TCR forces as no locking strand was added to lock the mechanically unfolded hairpin. After introduction of locking strand (200 nM), the ratio further increased at the T-B cell junctions by 36 ± 4 % (**Figure 3.5c** and **5d**). These results demonstrate that the TCR transmits >8 pN forces to its antiCD3ε ligands at cell-cell junctions. We next labeled B-cells with DOTS presenting pMHC antigen to visualize the force at TCR-pMHC bonds. In contrast to anti-CD3e, in the absence of locking strand, we did not observe a statistically significant Atto647N/Cy3B ratio change at the T-B cell junction. However, Atto647/Cy3B ratio increased by 84 ± 5% when the locking strand was added (**Figure 3.5c** and **3.5e**) and even surpassed that of the antiCD3ε DOTS signal. In retrospect, this finding is consistent with the known short lifetime but high frequency sampling and scanning that is inherent to TCR-pMHC interactions which leads to greater accumulated signal at the T-B cell interface (**Figure 3.5f**).

We next used flow cytometry to analyze the tension signal in high throughput following the methods described under the SSLB-T cell measurements in **Figure 3.4**. 1:1 T-B conjugate and B-cell monomer populations were gated out from the fluorescence and forward scatter plots, and their Atto647N intensities were compared. In the absence of locking strand, we observed a 20 ± 5% MFI change in anti-CD3e DOTS coated B-cells after its binding to T cells (**Figure 3.5h**). Consistent with the microscopy data, a smaller change of 9 ± 3% was observed for pMHC-DOTS coated B-cells (**Figure 3.5i**). However, in the presence of locking strand, the MFI change significantly increased from 9% ± 3% to 21 ± 2% for pMHC-DOTS modified B-cell (**Figure 3.5i**). An increase was also observed in antiCD3e but was less pronounced than that of pMHC-DOTS (**Figure 3.5h**). Collectively, the findings from both microscopy and flow cytometry analyses demonstrated the presence of >8 pN mechanical events at immune cell-cell junctions, with their characteristics modulated by the affinity of TCR ligands.

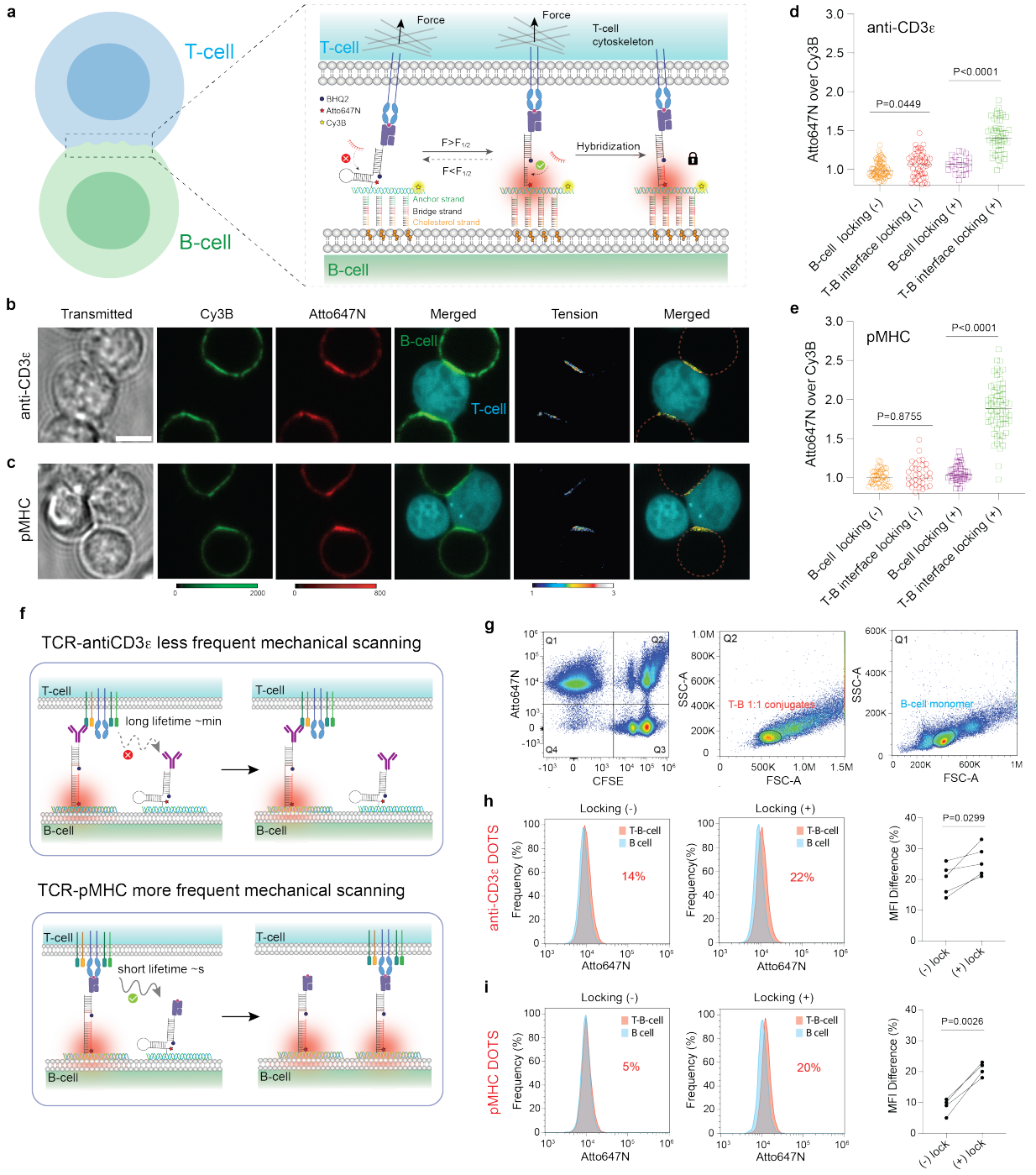


**Figure 3.5. TCR tension at T-B cell interfaces. a** Schematic showing the functionalization of B-cell membrane with DOTS. Locking strand was used to capture the tension signal at the T-B cell interface. **b-c** Representative images showing the DOTS and tension signals at the T-B cell interfaces. DOTS were modified with anti-CD3ε (b) or pMHC (c). **d-e** Plot comparing the Atto647N/Cy3B ratios on the B-cell surface and T-B interfaces with and without locking strand

after 30 min incubation. B-cells are modified with anti-CD3ε DOTS (d) or pMHC DOTS (e). Data from each group was acquired from >25 T-B cells. All data points were normalized to the mean value of Atto647N/Cy3B ratios in B cell locking (-) condition for standardized comparison. **f** Schematic showing that TCR-anti-CD3ε has a higher bond lifetime than TCR-pMHC and thus scans and lights up fewer DOTS within a specific period (30min). **g** Flow cytometry fluorescence plots and forward scatter plots were used to gate out the B-cell monomer and T-B 1:1 binding population. **h-i** Atto647N fluorescence histograms of B-cells (blue) and T-B 1:1 conjugates (red) with and without locking strand. Plot quantifying Atto647N MFI difference between B-cells and T-B cell 1:1 conjugates with and without locking strand present in the media. Data were acquired from 4 independent experiments and 4 independent mice. B-cells are modified with anti-CD3ε DOTS (h) or pMHC DOTS (i). Scale bars = 5 μm.

### 3.4 Conclusions

In this work, we developed DOTS by combining the idea of molecular tension sensors and DNA origami nanodevices and established its performance in investigating TCR mechanotransduction at intermembrane junctions. This contrasts with previously reported tension sensor designs which suffered from intermolecular FRET and displayed many supraphysiological characteristics regarding stiffness and either ultrahigh or limited lateral diffusion. With DOTS, we demonstrated that TCRs transmit >11.7 pN forces to its antigen at SLB-cell junction, and >8 pN forces at cell-bead and cell-cell junctions. Forces were not only characterized by widely used widefield microscope, but further validated using fluorescence lifetime-based imaging as well as flow cytometry with a high throughput readout.

It has been long assumed that the endogenous force transmitted to receptor-ligand bonds are generated by the cell cytoskeleton. In this report, we identified another source of force caused by the protein size mismatch at the immune synapse. TCR-pMHC complexes, displaying a shorter size compared to CD45 and LFA-1-ICAM-1, must “pinch” the intermembrane junction bringing it closer in order to interact, which causes strain in the interaction to trigger TCR signaling. The well-documented cell cytoskeleton does contribute to TCR forces but only after initial triggering

and proximal kinase activation. Moreover, cytoskeletal force generation and transmission to the TCR is mediated by F-actin dynamics and is less reliant on myosin activity. This finding mirrors the published work that F-actin maintains synapse persistence whereas myosin is dispensable in synapse formation.[143, 177]

It is worth noting that DOTS are highly programmable. For example, DOTS were tethered to microparticles creating a spherical tension sensor platform that demonstrated a correlation between force intensity and antigen potency and provided a new approach for antigen screening. Additionally, we successfully functionalized target cell membrane with a homogenous DOTS layer which allowed us to investigate the TCR tension at T cell-target cell junctions. Previously, DNA hairpin structures were inserted onto epithelial cells to study E-cadherin mediated tensile force. However, along with intermolecular FRET issue, this design is susceptible to endocytosis as DNA hairpins are only composed of three short DNA strands. In contrast, DOTS preserved their structural integrity for hours and no internalization was observed. Moreover, ideally one can functionalize the DNA origami with different ligands through straightforward DNA hybridization to investigate the mechanical communication between receptors. Prior work reported that CD28 engagement increases traction forces associated with CD3.[65] To explain this finding at the molecular level and validate the programmability of DOTS in force sensing, we labeled anti-CD28 with DNA and incorporated it to the DOTS platform to investigate how CD28 engagement tunes the forces experienced by individual TCR-antigen bonds. Consistently, we observed a stronger TCR tension signal when CD28 was ligated (**Figure A3.18**). One limitation of DOTS pertains to its low signal to background ratio in detecting real-time TCR tension, but this limitation will likely be resolved by introducing additional FRET pairs onto the DOTS so that TCR tension would lead to separation of multiple FRET pairs with a stronger fluorescence response.

## 3.5 Materials and Methods

### 3.5.1 Materials

DOPC (Cat# 850375C-200mg), Ni-NTA-DGS (Cat # 790404C-5 mg), DPPC (Cat# 850355C-25mg), 18:1 Biotinyl Cap PE (Cat# 870273C-25mg), were purchased from Avanti Polar Lipids Inc. (Alabaster, AL). Heat-inactivated fetal bovine serum (FBS) (Cat# 35-015-CV), penicillin-streptomycin solution (Cat# 30-234-CI), and gentamicin sulfate solution (Cat# 30-005-CR) were purchased from Corning Mediatech (Corning, NY). 1M Tris (Cat#: AM9856), 0.5 M EDTA (Ca#: AM9260G), 1M $MgCl_2$ (Cat# AM9530G), RPMI (Cat#11835030), Texas Red™ DHPE (Cat# T1395MP), human IL-2 (Cat# PHC0026) and CellTrace™ CFSE (Cat# C34570) were purchased from ThermoFisher (Waltham, MA). Bovine serum albumin (BSA) (Cat# 10735078001), Latrunculin B (Cat# L5288, >80%), Atto647N NHS ester (Cat# 18373-1MG-F), Atto488 NHS ester (Cat# 41698-1MG-F), 100 kDa Amicon ultra-0.5 centrifugal filter (Cat# UFC510096) and Hank's balanced salt solution (H8264-6X500ML) were purchased from Sigma Aldrich (St. Louis, MO). Cy3B NHS ester (Cat# PA63101) was purchased from GE Healthcare (Pittsburgh, PA). CK666 (Cat# ab141231) was purchased from Abcam (Cambridge, United Kingdom). Blebbistatin (Cat# 72402) was purchased from STEMCELL (Vancouver, Canada). Streptavidin (Cat# S000-01) was purchased from Rockland Immunochemicals Inc. (Rockland, NY). Biotinylated pMHC ovalbumin (SIINFEKL) was obtained from the NIH Tetramer Core Facility at Emory University. P2 size exclusion gel (Cat#1504118) was purchased from Bio-Rad (Hercules, CA). 3 mL syringes were purchased from BD bioscience (San Jose, CA). Cell strainers (Cat# 15-1100) were bought from Biologix (Shandong, China). Midi MACS (LS) startup kit (Cat# 130-042-301) (separator, columns, stand), mouse CD8+ T cell isolation kit (Cat# 130-104-075), and resting mouse B-cell isolation kit (Cat# 130-090-862) were purchased from Miltenyi Biotec (Bergisch Gladbach,

Germany). Oligonucleotides were obtained from Integrative DNA Technologies (Coralville, IA) and Biosearch Technologies (Hoddesdon, United Kingdom). His-ICAM-1 (Cat# 50440-M03H) was purchased from Sino Biological (Beijing, China). Anti-mouse CD28 (Cat# 102102), biotinylated anti-mouse CD3e (Cat# 100304) and FITC anti-mouse TCRb antibody (Cat# 109206) were purchased from BioLegend (San Diego, CA). Azide-PEG4-NHS ester (Cat# AZ103-100) and Sulfo-DBCO NHS ester (Cat# A124-10) were purchased from Click Chemistry Tools (Scottsdale, AZ). Alexa 488 Mouse Anti-ZAP70 (pY319)/Syk (Y352) (Cat# 557818) was purchased from BD Biosciences (Franklin Lakes, NJ). Single-stranded scaffold DNA, type p7560 was purchased from tilibit nanosystems (Munich, Germany).

### 3.5.2 Methods

#### 3.5.2.1 Harvest and purification of primary naïve OT1 T cell

OT-1 T cell receptor transgenic mice were bred and housed at Emory University's Division of Animal Resources Facility, following the guidelines of the Institutional Animal Care and Use Committee. The OT-1 T cells express the CD8 co-receptor and have a specific recognition for the chicken ovalbumin epitope 257–264 (SIINFEKL) in the context of the MHC allele H-2K. Naïve OT-1 T cells were isolated from the spleen using magnetic activated cell sorting, as instructed by the manufacturer's CD8+ T cell Isolation Kit (Miltenyi Biotec, Germany). In brief, a single cell suspension of splenocytes was obtained and incubated with biotinylated antibodies targeting unwanted splenic cell populations. These populations were separated from the OT-1 T cells using anti-biotin magnetic beads and enrichment on a magnetic column. The purified T cells were then washed, suspended in HBSS solution, and kept on ice until the experiment.

#### 3.5.2.2 Preparation of effector OT1 T cells

Splenocytes from OT-1 transgenic mice were pulsed with 100 nM OVA peptide in RPMI media containing 10% FBS for 2 days. Afterwards, activated lymphoblasts were purified by density gradient centrifugation and adjusted to a concentration of 1 million cells/mL in RPMI media containing 10% and 30 IU/mL IL-2. Cells were then maintained and split as needed in RPMI media containing 10% FBS and 30 IU/mL IL-2 until imaging on day 7.

#### 3.5.2.3 Retroviral transduction

To generate retrovirus, Phoenix E cells were transfected with expression vectors (Lifeact-GFP) and packaging plasmids (kindly provided by Morgan Huse lab at Sloan Kettering Institute) using the calcium phosphate method. After 48 hours at 37°C, viral supernatants were collected and added to OT1 blasts two days following peptide stimulation. The mixtures were centrifuged at 1400 × g in the presence of polybrene (4 μg/ml) for 2 hours at 35°C. T cells were then split at a 1:3 ratio in medium containing IL-2 and cultured at 37°C. After overnight culture, selection was conducted to removed untransduced T cells. The remaining T cells were further cultured for additional two days before use.

#### 3.5.2.4 Synthesis of dye-labeled DNA strands

Oligonucleotide-dye conjugates were prepared by coupling the amine on the DNA strand with activated NHS-ester of the organic dye. Briefly, aminated DNA strands (100 μM) was mixed with excess Cy3B-NHS ester, Atto647-NHS ester or Atto488-NHS ester (500 μg/mL) and allowed to react in aqueous solution (pH=9) for 3 hours at room temperature. The mixture was then filtered by P2 gel to remove salts and unreacted dyes and then purified by HPLC with an Agilent AdvanceBio Oligonucleotide C18 column (4.6 x 150 mm, 2.7 μm). The mobile phase A: 0.1 M

TEAA and B: ACN were used for a linear gradient elution of 10-100% B over 50 min at a flow rate of 0.5 mL/min. The desired products were characterized by ESI mass spectrometry (**Figure A3.1 and A3.2**).

### 3.5.2.5 Preparation of DOTS

DOTS was assembled by mixing p7560 DNA scaffold strand (30 nM), eight anchor strands (300 nM), dye modified DNA hairpin strand (600 nM), dye modified density reporter strand (600 nM), ligand strand (1500 nM) and other 82 staple strands (300 nM) in the folding buffer (5 mM Tris, 1 mM EDTA, 8 mM $MgCl_2$). Anchor strands were elongated at its 5' end with 32 bases complementary to the DNA scaffold. DNA hairpin strands were elongated at its 3' end with 32 bases complementary to the DNA scaffold. Note that DOTS for cell-cell experiments had additional 12 anchor strands. Sequences of these strands were shown in **Table A3.2-3.4**. The locations of these strands on the origami platform were shown in **Figure A3.3**. DNA origami were annealed by heating at 90 °C for 15 min and cooling down to 4 °C at a rate of 1 °C/min. Afterwards, excess oligonucleotides were removed via ultrafiltration (100 kDa 0.5 mL Amicon Ultrafilters). Purified origami structures were stored at -30 °C in PBS supplemented with 8 mM MgCl2 and used within one week. Successful assembly of DNA origami was confirmed through agarose gel electrophoresis (0.75 % agarose gel, 0.5 X TBE buffer, 8 mM $MgCl_2$). Agarose gel was run on ice for 2 hours at 70V and stained with ethidium bromide.

### 3.5.2.6 Preparation of small unilamellar vesicles (SUVs)

Lipids with desired composition were mixed in a round-bottom flask. The lipid mixture was dried using a rotary evaporator to remove the chloroform. The lipids were further dried under a steam of compressed N2 and then hydrated with PBS to a concentration of 2 mg/mL. Three cycles of

freeze-thaw were performed to disrupt large, multilamellar vesicle suspensions. The resulting lipids were then repeatedly extruded through an 80-nm polycarbonate membrane filter at least 10 times and stored at 4°C before use.

**3.5.2.7 Preparation of functionalized planar SLB**

The wells in optically transparent 96-well plates (ThermoFisher) were washed with 5 mL ethanol and water and etched with 6.5 M NaOH for 1 hour at room temperature. The etched wells were washed with 10 mL water and treated with 100 μL 0.5 mg/mL SUVs for 5 min. SUVs containing 98% DOPC and 2% DGS-NTA (Ni) lipids were used for making fluid phase SLB, and SUVs containing 98% DPPC and 2% DGS-NTA (Ni) lipids were used for non-fluid phase SLB. After treatment, unbounded vesicles were removed by washing with 5 mL PBS. SLBs were subsequently blocked with bovine serum albumin (BSA, 0.05%) in PBS for 30 min and washed with 5 mL PBS. Then, cholesterol DNA strands (250 nM) was added to SLB, incubated for 1 hour and rinsed with PBS. Subsequently, DOTS (5 nM) was added for 1 hour to bind to cholesterol strands on the SLB. The wells were then washed with PBS supplemented with 8 mM $MgCl_2$ to remove excess DOTS. Streptavidin (5 μg/mL) was added to the SLB, incubated for 45 min and then washed with PBS supplemented with 8 mM $MgCl_2$. Subsequently, pMHC ligand (5 μg/mL) was added to the SLB, incubated for 45 minutes, and washed using PBS supplemented with 8 mM $MgCl_2$. Finally, His-tagged ICAM-1 (1 μg/mL) was added for 1 hour (resulting in a molecular density of ~60 molecules/$\mu m^2$). Wells were then washed with PBS supplemented with 8 mM $MgCl_2$ and buffer-exchanged with Hank's balanced salt solution (HBSS) before adding cells.

### 3.5.2.8 Preparation of DOTS functionalized spherical SLB

Transfer 10 μL non-functionalized silica beads (5.00 μm diameter, 10% w/v) into a 1.5 mL microcentrifuge tube and wash with PBS twice with bench centrifuge. SSLBs were formed by incubating beads with 500 uL 0.5 mg/mL SUVs (2% DOGS-NTA and 98% DOPC) on the rocker for 30 min at room temperature. The resultant SSLB were washed three times with PBS by centrifuging at 300g for 3 min and then blocked with 0.05% BSA for 30 min. After three PBS washes, the SSLB were resuspended into 250 nM cholesterol strand, incubated for 1 hour on the rocker at room temperature and washed with PBS. Meanwhile, to DOTS solution, 20-fold streptavidin was added for 40 min to functionalize DOTS with streptavidin. Streptavidin modified DOTS was purified via ultrafiltration (100 kDa 0.5 mL Amicon Ultrafilters) and incubated with 20-fold biotinylated pMHC for 40 min. Without further purification, pMHC functionalized DOTS were added to above cholesterol strand coated SSLBs at a concentration of 5 nM and incubated for 1 hour at room temperature. The DOTS coated SSLBs were then washed with PBS supplemented with 8 mM $MgCl_2$ to remove excessive DOTS. Finally, DOTS-SSLB were incubated with His-tagged ICAM-1 (1 μg/mL) for 1 hour, washed with PBS supplemented with 8 mM $MgCl_2$ and rinsed with HBSS before being mixed with T cells. A total of 300,000 DOTS-SSLB particles were combined with 300,000 T cells in a 300 μL HBSS, with the mixing taking place either in a 96-well plate for confocal microscopy characterization or in an Eppendorf microcentrifuge tube for flow cytometry characterization. To capture the tension signal, the locking strand with a concentration of 200 nM was introduced into the medium. The mixture was incubated at RT for 30 minutes before proceeding with imaging and flow analysis.

### 3.5.2.9 Quantitative fluorescence microscopy

Surface density of DOTS and ICAM-1 was measured using a quantitative fluorescence microscopy technique developed by Groves and others.[178] Briefly, SUVs containing 0.1 mole percent (mol %) Texas Red-DHPE (TR-DHPE) and 99.9 mol % DOPC were mixed to generate vesicle mixtures with TR-DHPE ranged from 0 to 0.1 mol %. These solutions were diluted to 0.5 mg/ml and added to a cleaned 96-well plate to establish a lipid calibration curve. The lipid head has an area of ~0.72 $nm^2$, allowing for ~$2.78 \times 10^6$ lipid molecules to be packed in 1 μm2 surface. Given the ratio of the TR-DHPE in the lipid vesicle, the TR-DHPE density could be calculated. We measured the fluorescence intensities of the SLB with different ratios of TR-DHPE and generated a calibration curve based on this (**Figure A3.5a**). To determine the density of samples (e.g. DOTS or ICAM-1 ligand), a scaling factor (F factor) was introduced to account for the difference in brightness between the sample fluorophores and TR-DHPE. We prepared varying concentrations of TR-DHPE liposome and samples and plotted the fluorescent intensity against concentration (**Figure A3.5 b-e**). The slope of sample was directly compared to the TR-DHPE to yield a F factor. The F factor was subsequently used to infer the molecular density of the sample from the SLB calibration curve.

### 3.5.2.10 Harvest and purification of primary naïve OT1 T cell

Resting B-cells were enriched from the spleen using the B-cell Isolation Kit (Miltenyi Biotec, Germany, Cat# 130-090-862). 1 mL 8 million/mL B-cells in HBSS buffer were sequentially incubated with 1 μM cholesterol strand (30 min, room temperature), 1 μM bridge strand (30 min, 4 °C), 1 μM fortifier strand (30 min, 4 °C) and washed with PBS after each incubation. In a separate tube, DOTS were functionalized with streptavidin and biotinylated ligand (anti-CD3ε or pMHC)

sequentially at a 20-molar excess for 45 min at room temperature. DOTS were purified after each functionalization via ultrafiltration (100 kDa 0.5 mL Amicon Ultrafilters). Finally, ligand functionalized DOTS were added to DNA strand modified B-cells at a concentration of 35 nM in PBS (supplemented with 0.5 % BSA and 8 mM $MgCl_2$) and incubated for 1 hour at 4 °C followed by two washes with HBSS to get DOTS modified B cells. In an Eppendorf microcentrifuge tube, 300,000 DOTS-B cells were combined with 300,000 CFSE-stained T cells in 300 μL HBSS. The mixture was gently centrifuged at 94 rcf for 5 minutes and incubated for 10 minutes at RT, allowing the T cells and B cells to come into contact and form conjugates. Afterwards, the mixture was gently pipetted to disrupt any nonspecific conjugates. Subsequently, the locking strand with a concentration of 200 nM was introduced into the medium. The mixture was incubated at RT for 30 minutes before proceeding with imaging and flow analysis.

**3.5.2.11 Immunostaining**

A total of ~$1 \times 10^5$ T cells cultured on 96 well plate surfaces were fixed by 4% formaldehyde in PBS for 10 min. The surfaces were gently washed with PBS to remove the formaldehye. Cells were then permeabilized in 0.1% Triton X-100 for 5 min and washed with PBS. Subsequently, 2% BSA was added to the surfaces and incubated overnight at 4°C. On the next day, the surfaces were washed with PBS. 20 uL Alexa 488 Mouse Anti-ZAP70 (PY319)/Syk (PY352) (Cat# 557818 from BD Biosciences) was mix with 80 uL staining buffer (0.5% BSA in PBS) and added to the surface for 1 hour at room temperature. Surfaces were then washed with PBS before imaging on total internal reflection fluorescence (TIRF) microscope. For actin staining, after fixation and permeabilization, the cells were incubated with 1X phalloidin-ifluor488 (Cat# ab176753 from Abcam) in 1% BSA for 1 hour at room temperature and washed with PBS before imaging on TIRF.

#### 3.5.2.12 DNA-anti-CD28 conjugation via click chemistry

300 uL 0.5 mg/mL anti-mouse CD28 was loaded into Amicon ultrafilters (0.5 mL, 100 KDa) and spun at 14, 000 g for 5 min at 4 °C. The volume was adjusted to 100 µL with PBS, resulting in an approximate concentration of 1.5 mg/mL. Next, Sulfo-DBCO-NHS reagent was resuspended into DMF at a concentration of 30 mM. The reagent was then added to the antibody solution at a molar ratio of 10:1 and incubated on ice for 2 h. Excessive Sulfo-DBCO-NHS was then removed using 7K MWCO Zeba Spin Desalting columns (ThermoFisher). Azide modified DNA strands was added to DBCO modified anti-CD28 at a molar ratio of 12:1. The reaction was incubated overnight at 4 °C. On the following day, the DNA-anti-CD28 mixes were added to Amicon ultrafilters (0.5 mL, 30 KDa) and washed 8 times to remove unreacted azide DNA strands. Conjugation was confirmed using SDS-PAGE gel (**Figure A3.18**). The concentration of DNA-antiCD28 was determined using Micro BCA protein Assay kit (ThermoFisher).

#### 3.5.2.13 Atomic force microscopy imaging

After purification, DNA origami structure was confirmed through AFM imaging. Imaging was conducted on Bruker MultiMode NanoScope V AFM using tapping mode in liquid with a Bruker ScanAsyst-Fluid+ cantilever. For sample preparation, DNA origami was first diluted to 1 nM in TE-Mg buffer (5 mM Tris,1mM EDTA,10 mM $MgCl_2$) and then 20 uL of diluted origami was added onto freshly cleaved mica precoated with 0.1 ug/ml poly-L-ornithine.

#### 3.5.2.14 Fluorescence Microscopy imaging

Epi fluorescence microscopy and TIRF microscopy experiments were performed on a Nikon Eclipse Ti inverted microscope driven by the NIS Elements software. The microscope features an Evolve electron-multiplying charge-coupled device (Photometrics), an Intensilight

epifluorescence source (Nikon), a CFI Apo 100 X (numerical aperture 1.49) objective (Nikon) and a total internal reflection fluorescence launcher with three laser lines: 488 (10 mW), 561 (50 mW), and 638 nm (20 mW). This microscope also includes the Nikon Perfect Focus System, an interferometry-based focus lock which allows the capture of multi-point and time-lapse images without loss of focus. Cell-SSLB and cell-cell experiments were imaged on a Nikon confocal microscope. This microscope is equipped with a 60 X oil objective and a C2si scan head. Experiments were performed using three laser lines (488 nm, 561 nm and 640 nm) and the filters with the following bandpasses: 445/50+60LP, 525/50, and 600/50 nm. Z-stack imaging was performed using the ND Acquisition module in Nikon Elements.

#### 3.5.2.15 Fluorescence lifetime imaging microscopy (FLIM)

FLIM imaging for intermolecular FRET experiments (**Figure 3.2e-f**) was performed on a Nikon Ti Eclipse Inverted confocal microscope with a Plan Apo Lambda 60✕/1.40 Oil objective. The confocal microscope is equipped with a Picoquant Laser Scanning microscope TCSPC Upgrade with SymPhoTime 64. Samples were excited with a 40 MHz pulsed 485 ± 10 nm laser. The laser light was reflected using a 560 nm dichroic filter and the detector collected emitted photons that passed a 582/75 nm bandpass filter. Tension FLIM (**Figure 3.2l**) was performed on Timebow imaging on Abberior STED microscope equipped with 60✕/1.40 Oil objective, two pulsed STED lasers (595 and 775 nm), four excitation lasers (405, 485, 561, 640 nm) and a MATRIX array detector.

#### 3.5.2.16 Flow cytometry analysis

Flow cytometry experiments were conducted on CytoFlex flow cytometer (Beckman coulter) which features 488 nm and 638nm laser lines and bandpass filters (450/45, 585/42, 660/10 nm).

#### 3.5.2.17 Statistical analysis

All experiments were conducted as at least three technical and biological replicates. Statistical significance was determined on GraphPad Prism using either one-way analysis of variance or two-tailed student's t tests. Data were presented as bars with mean±SEM or scatter plots showing all data points with lines representing mean.

## 3.6 Appendix

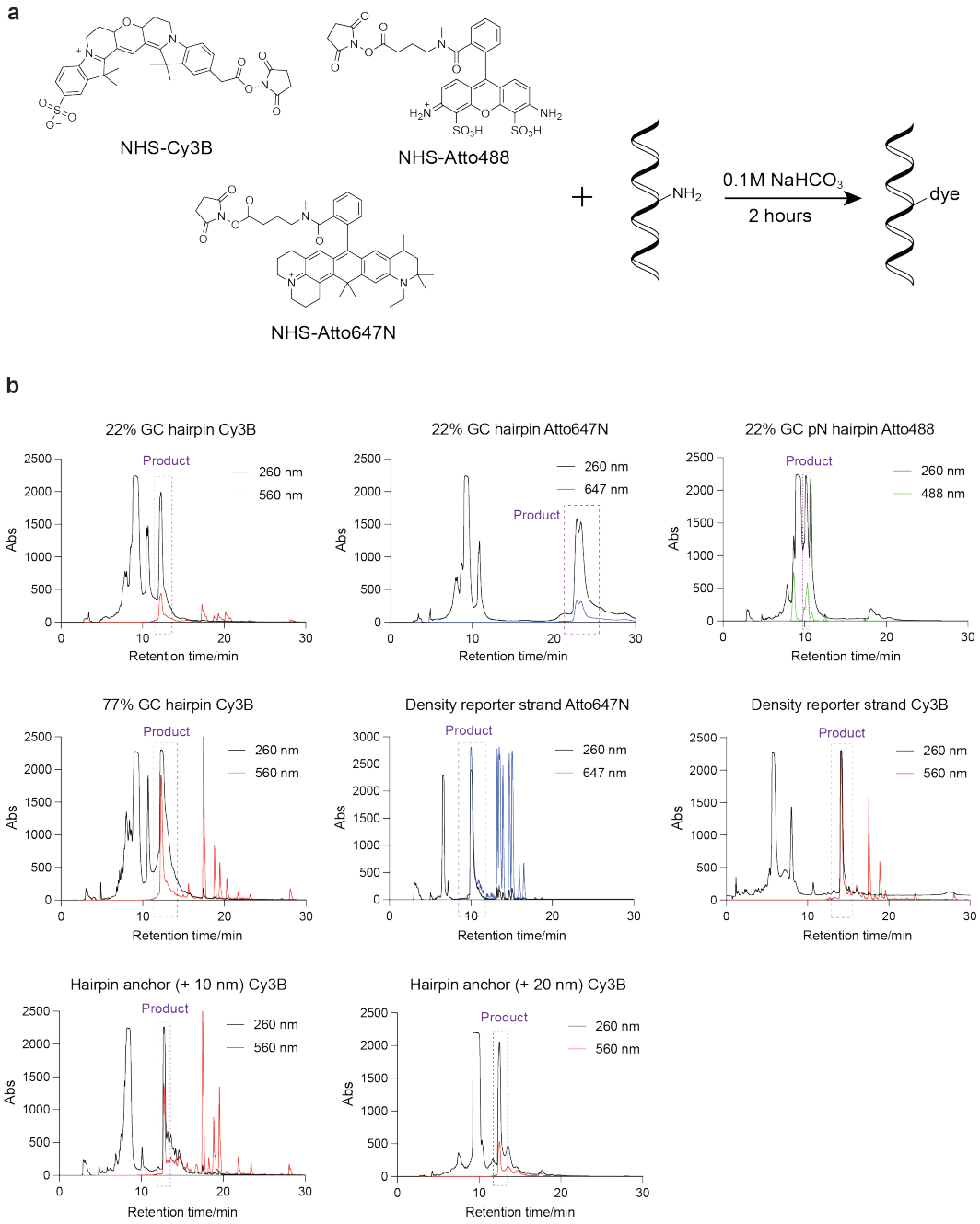


**Figure A3.1. Synthesis and purification of dye labeled oligonucleotides.** **a**. Reaction scheme for conjugation of amine-modified oligonucleotides with NHS-dyes **b.** HPLC traces of the dye-labeled targets. The dashed box represents the collected products which were validated by MS.

## 22% GC hairpin Cy3B

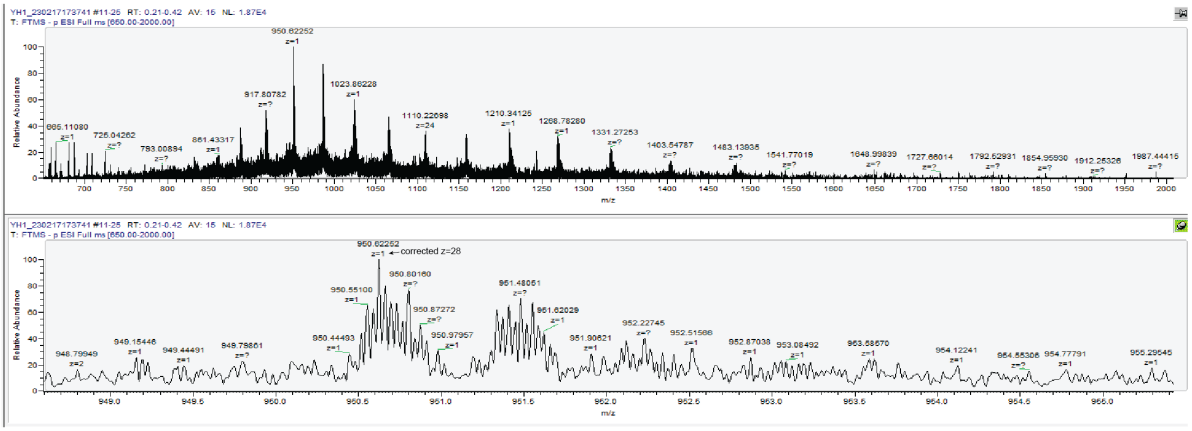

## 22% GC hairpin Atto647N

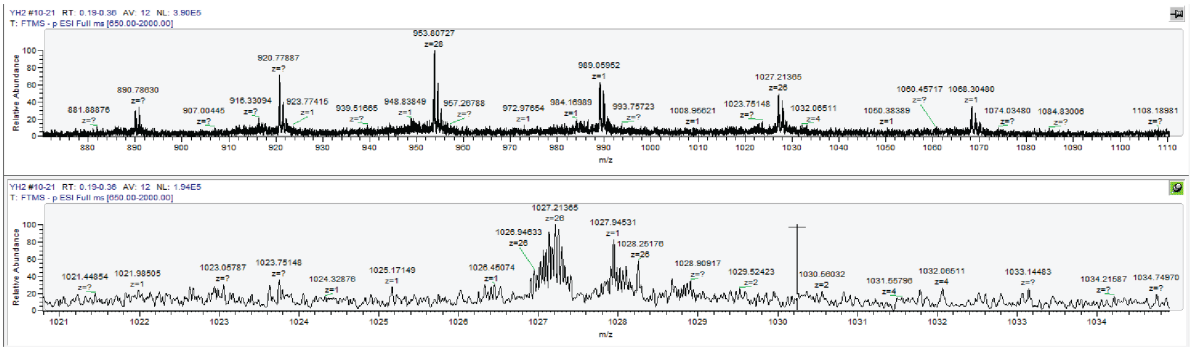

## 22% GC hairpin Atto488

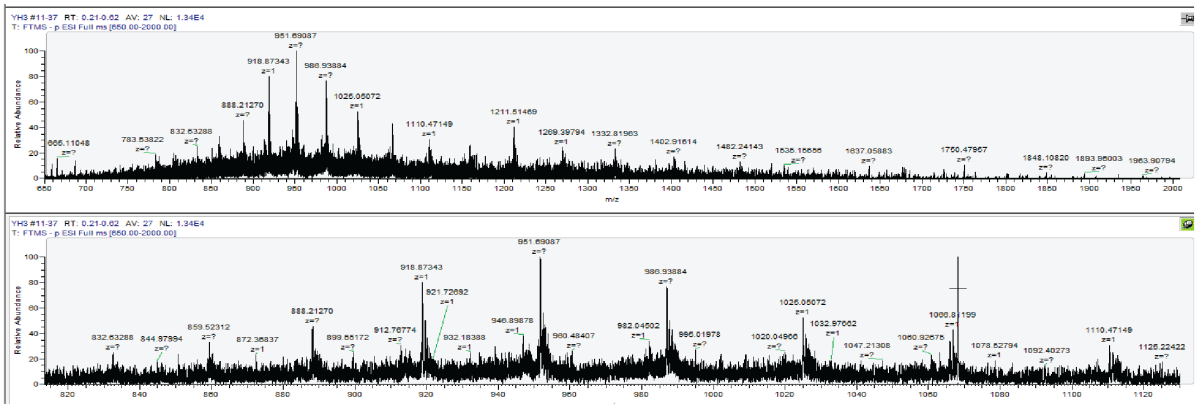

## 77% GC hairpin hairpin Cy3B

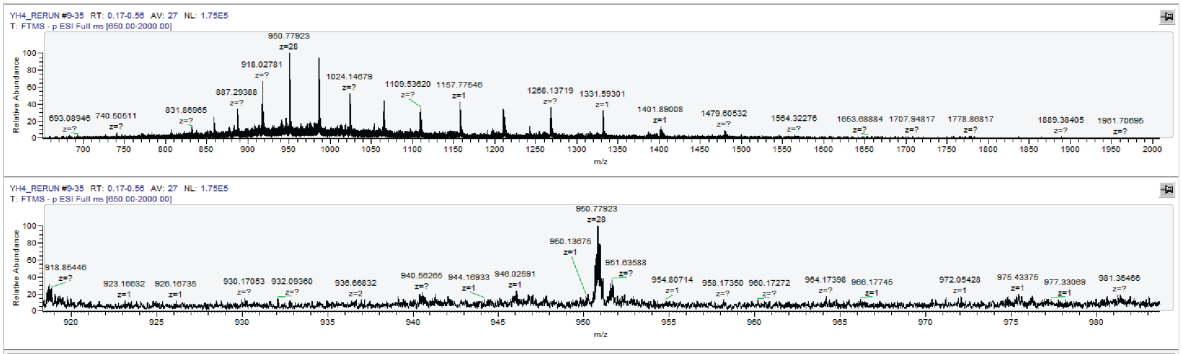

## Density reporter Atto647N

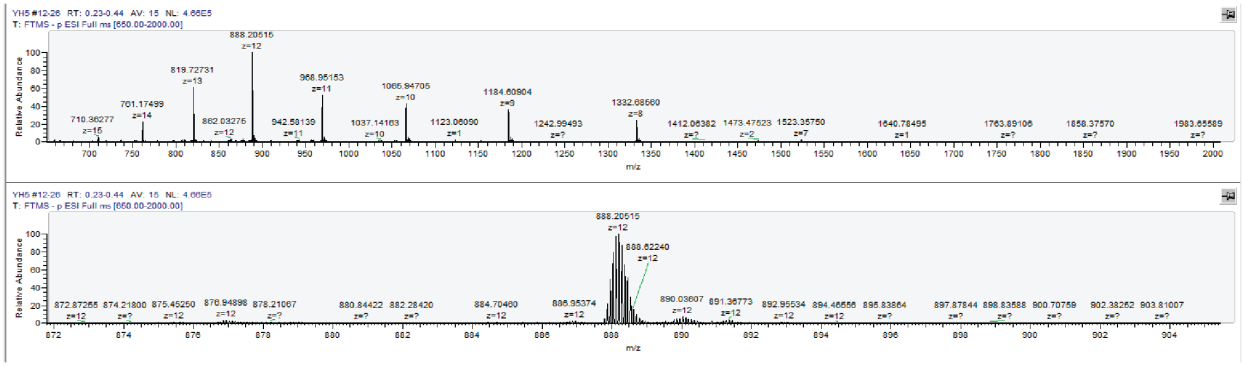

## Density reporter Cy3B

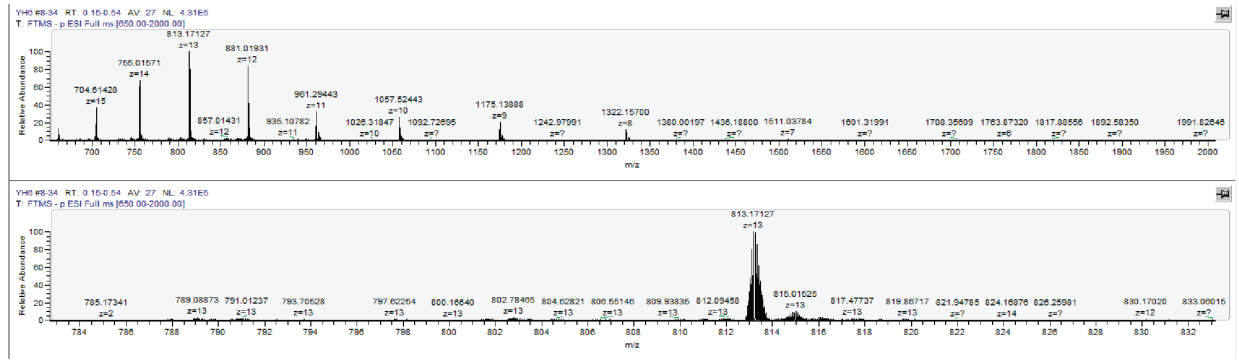

## Hairpin anchor (+ 10 nm) Cy3B

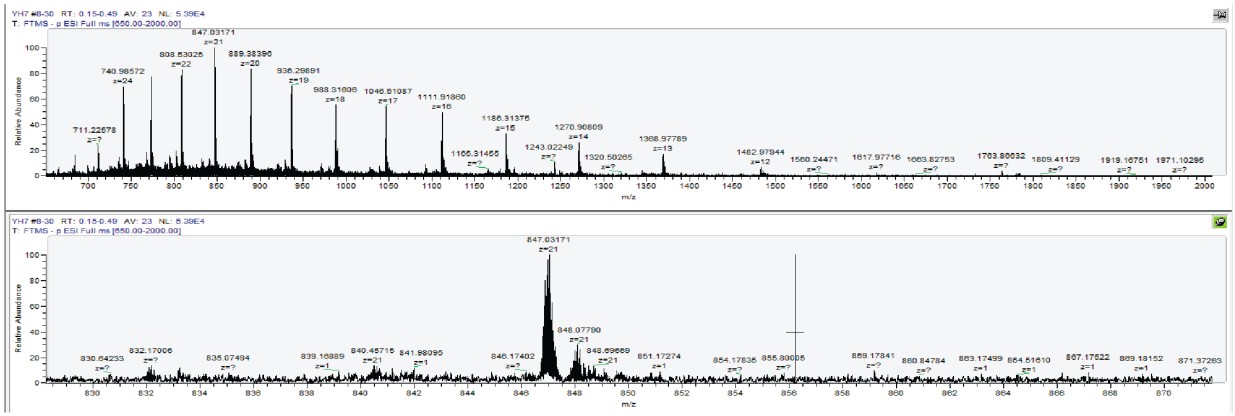

## Hairpin anchor (+ 20 nm) Cy3B

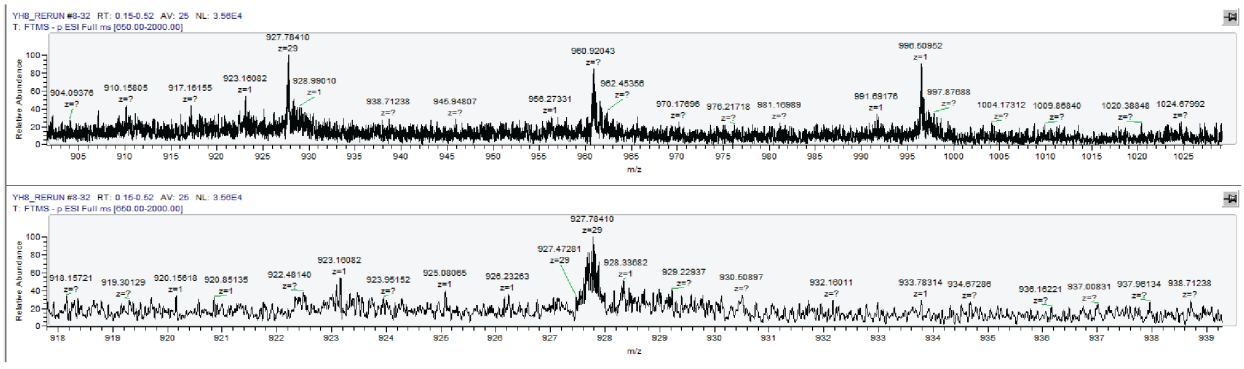

| Sample | Calculated mass | m/z found | Difference |
|---|---|---|---|
| 22% GC hairpin Cy3B | 26646.85 | 26646.43 | 0.42 |
| 22% GC hairpin Atto647N | 26733.08 | 26734.55 | 1.47. |
| 22% GC hairpin Atto488 | 26676.78 | 26676.34 | 0.44 |
| 77% GC hairpin Cy3B | 26651.65 | 26650.82 | 0.83 |
| Density reporter Atto647N | 10671.48 | 10671.46 | 0.02 |
| Density reporter Cy3B | 10585.25 | 10585.22 | 0.03 |
| Hairpin anchor (+ 10 nm) Cy3B | 17807.85 | 17809.67 | 1.82 |
| Hairpin anchor (+ 20 nm) Cy3B | 26933.75 | 26935.74 | 1.99 |

**Figure A3.2. Mass spectrometry characterization of dye labeled DNA oligos.** High resolution mass spectra of dye labeled oligos. Table shows calculated masses and measured masses.

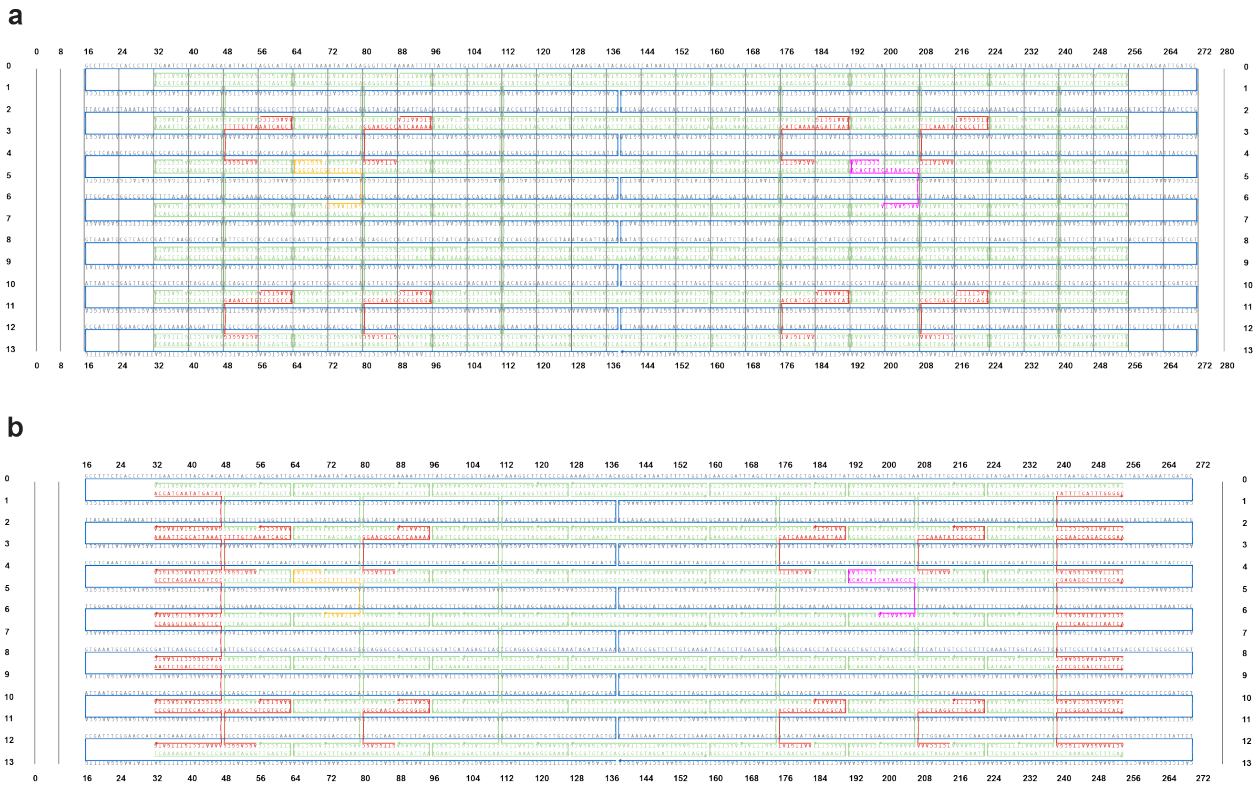


**Figure A3.3. Schematics of DNA origami structures used in this work. a** DNA origami was designed using CaDNAno based on the p7560 scaffold (blue). One staple strand (pink) was elongated at the 5' end with the DNA hairpin sequence for visualizing TCR forces. One staple (orange) was labeled with Atto647N at the 3' end to serve as a density reporter. Eight staple strands (red) were elongated at the 3' end with 21 base pairs that are complementary to DNA strand preinserted into SLBs to anchor DOTS to the SLB. **b** DNA origami design for cell-cell force experiment. 20 staple strands (red) were elongated at the 3' end with 21 base pairs that are complementary to DNA strand on the cell membrane to attach DOTS to cell membrane.

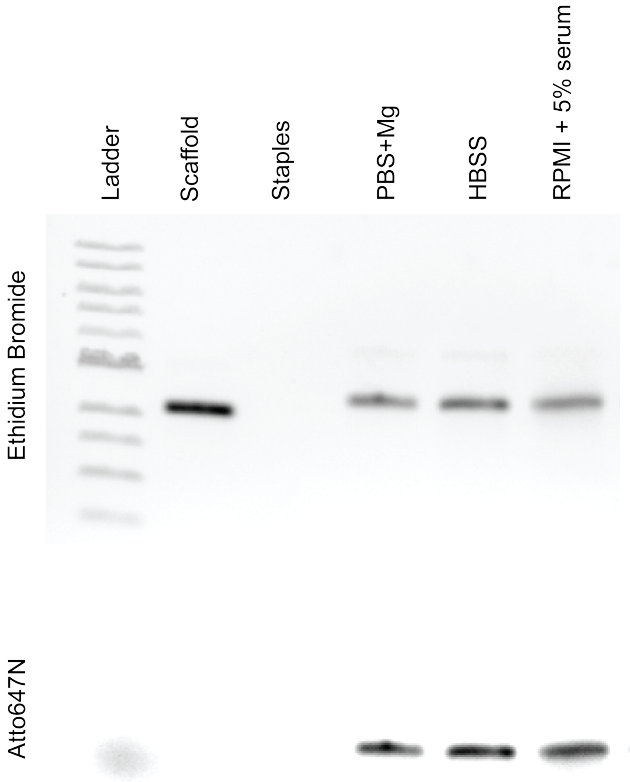


**Figure A3.4. Stability analysis of DNA origami under different cell imaging conditions.** DNA origamis were incubated in different imaging buffers/media for 1 hour at room temperature and subjected to gel electrophoresis. Overall structure stability and overhang stability were confirmed via Ethidium Bromide and Atto647N signal, respectively. No degradation was observed under all the imaging conditions.

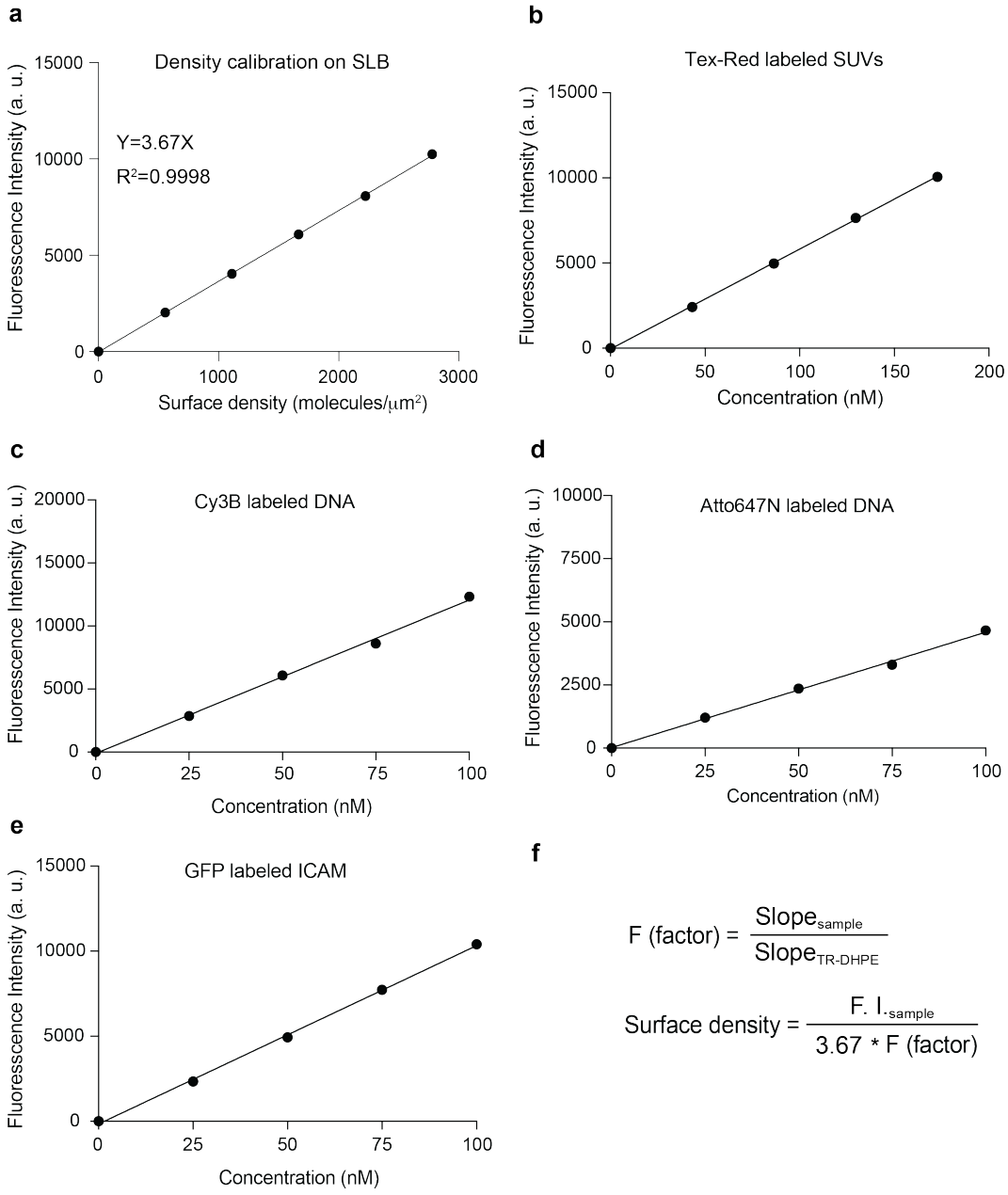


**Figure A3.5 Quantitative fluorescence microscopy to determine surface density. a** TR-DHPE bilayer fluorescence calibration curve with known molecular densities. The intensity was obtained by averaging at least 6 images from each surface. Error bars indicate the SD which was smaller than the size of data symbol. **b-e** Plot showing the fluorescence intensities across various concentrations of fluorophores. Since sample fluorophore and Texas Red fluorophore on the lipid have different absorption and emission characteristics, the fluorescence intensity of the sample fluorophore needs to be calibrated to bilayer standard fluorophore. To obtain the F Factor, sample fluorescence and TR-DHPE lipid fluorescence at different concentrations were measured on a microscope. The F Factor was generated by dividing the slope of sample to that of TR-DHPE. **f** Equations used to calculate F factor and surface molecule densities.

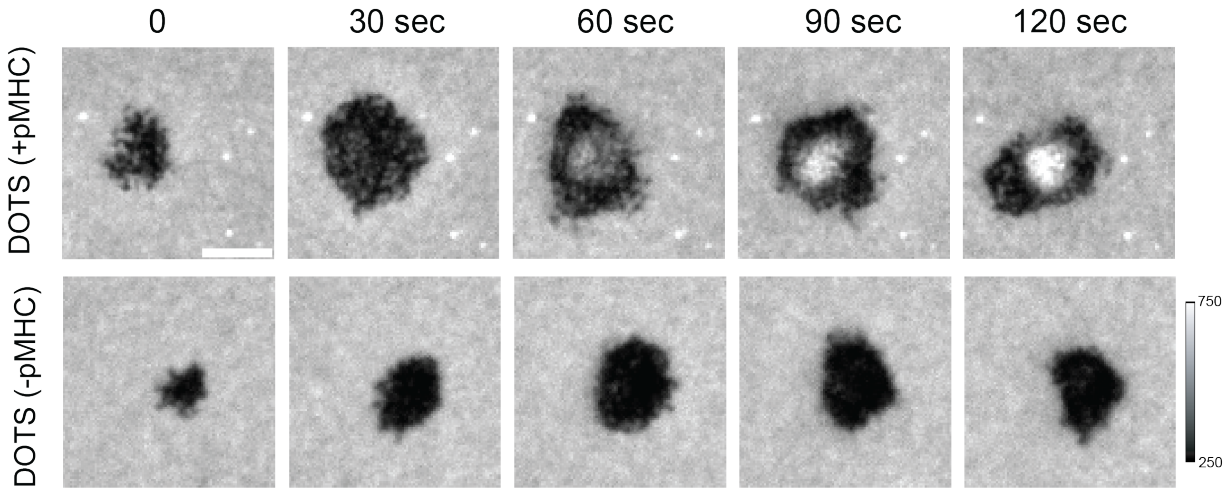


**Figure A3.6. Exclusion of DOTS from the cell spreading area.** Representative time lapse images showing the exclusion and clustering of DOTS in the T cell/SLB junctions. DOTS lacking antigen showed comparable levels of exclusion but did not exhibit any accumulation and clustering under T cells.

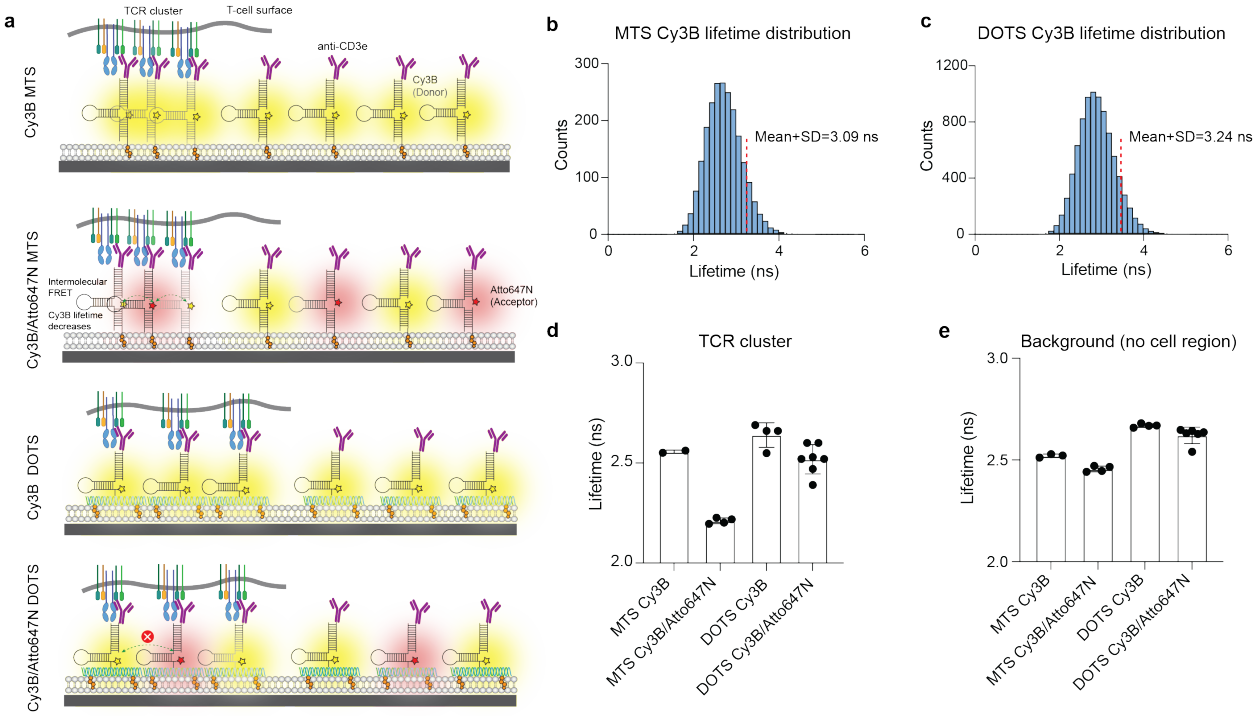


**Figure A3.7. FLIM data showed that DOTS eliminated intermolecular FRET between tension sensors at TCR clusters. a** Schematics showing SLBs coated with DOTS or MTS. **b** Fluorescence lifetime histogram of pixels on SLB surfaces containing only Cy3B MTS. **c** Fluorescence lifetime of pixels on SLB surfaces containing only Cy3B DOTS. Red dash lines indicate average lifetime + 1SD. **d** Bar graphs quantifying the average lifetimes of pixels in TCR clusters formed on Cy3B only MTS, Cy3B&Atto647N MTS, Cy3B only DOTS and Cy3B&Atto647N DOTS surfaces. **e** Bar graphs quantifying the average lifetimes of pixels at no cell region on Cy3B only MTS, Cy3B&Atto647N MTS, Cy3B only DOTS and Cy3B&Atto647N DOTS surfaces.

**Supplementary note 1**: FLIM fitting and thresholding. Fluorescence lifetime imaging microscopy (FLIM) requires data fitting to exponential decay curves, typically with a reconvolution decay model involving the instrument response function (IRF). A benefit of FLIM is that both spatial and temporal information are recorded; however, this creates a challenge as data is recorded separately within pixels rather than as an aggregate. From prior experience and reports from our lab,1 we observe that pixels containing low photon counts (<25 photon/px) are noisy and can contain unreasonable lifetime values, both high and low. This can be avoided with spatial pixel binning or by thresholding pixels during analysis. To maintain spatial resolution and address this challenge through thresholding, we measured the lifetime values from surfaces containing only donor fluorescence (Cy3B) without cells. This is assumed to be the maximum theoretical lifetime. Data was fitted to a histogram and the average maximum lifetime + 1 SD was recorded (Figure S7b and Figure S7c). Note that SD refers to histogram width. This determined the lifetime cut-off as values above the lifetime max + 1SD are assumed to be noise (3.09 ns and 3.24 ns for hairpin and DOTS surfaces respectively). We then measured the mean photon count of pixels with

lifetimes above the lifetime cut-off and determined that pixels under 25 photons should be excluded from analysis (SNR <5). FLIM fitting was conducted using both lifetime thresholding (<3.09 ns or 3.24 ns) and photon count thresholding (SNR > 5).

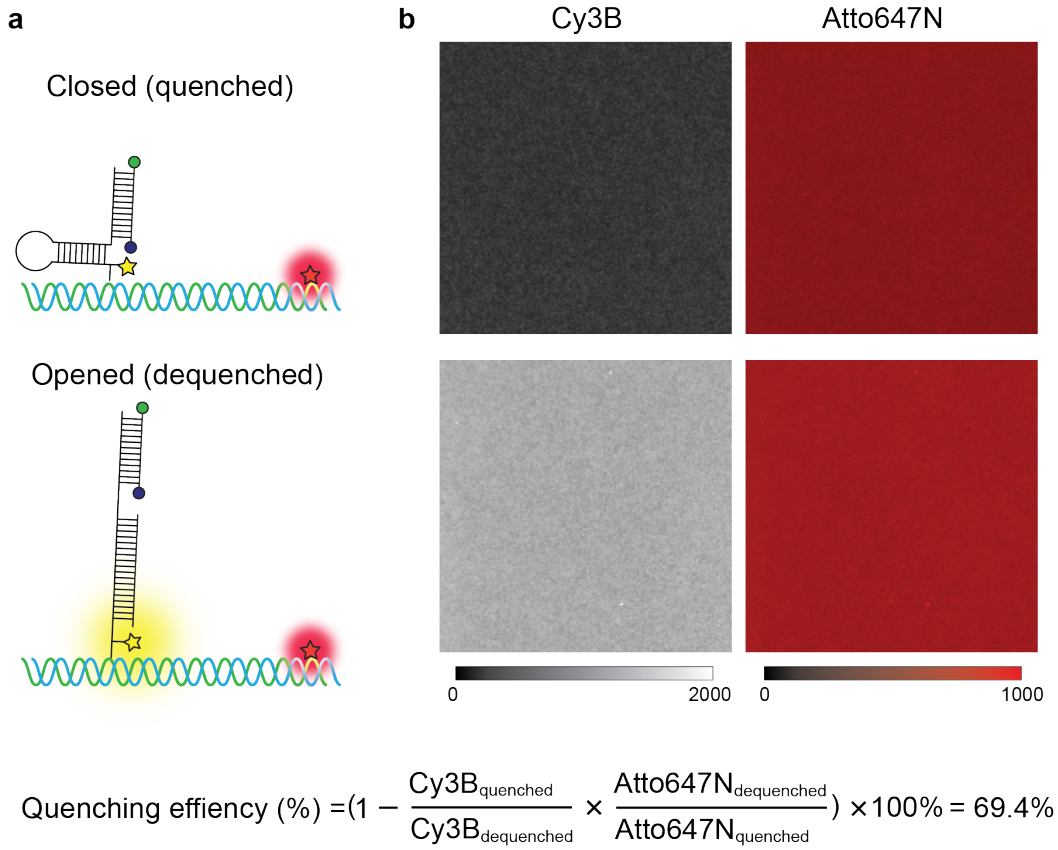


**Figure A3.8. Quenching efficiency of DOTS. a** Schematic showing "closed" and "opened" hairpin probes on SLB surface. **b** Representative images showing the fluorescence of Cy3B and Atto647N of opened and closed DOTS. Quenching efficiency was calculated by dividing quenched Cy3B and dequenched Cy3B intensities normalized to Att647N intensities.

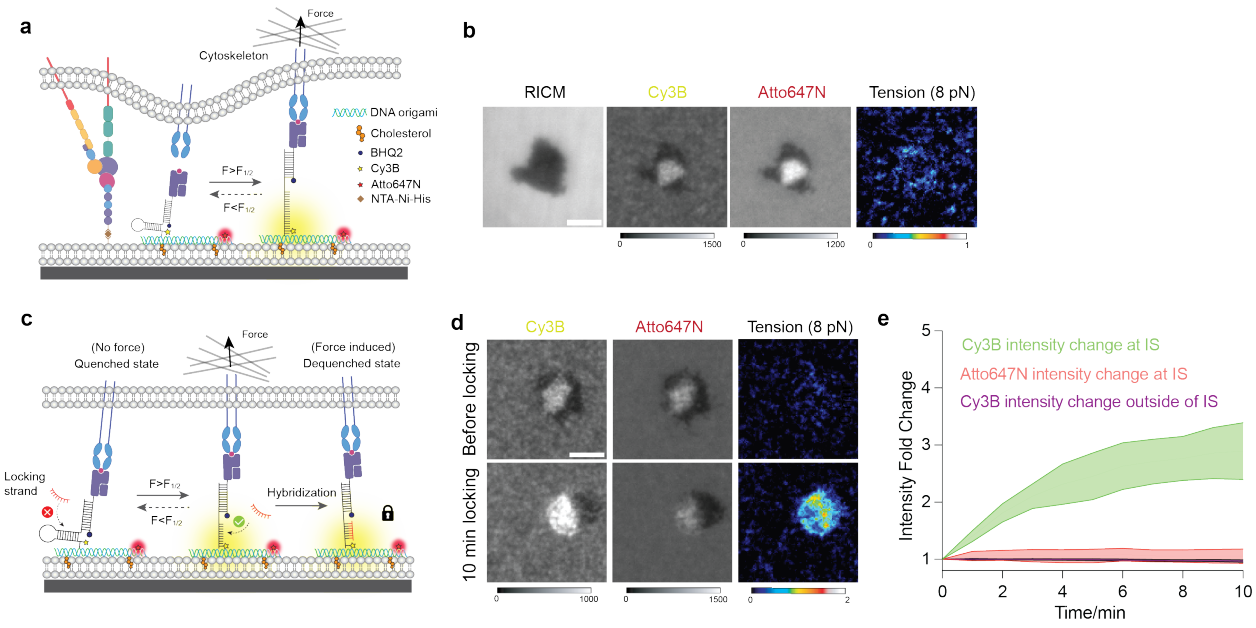


**Figure A3.9. Locking strategy specifically amplified tension signal at the immune synapse. a** Schematic showing that DOTS engages TCR and reports TCR force with a fluorescence increase in the Cy3B channel. **b** Representative microscope images showing T-cell spread on DOTS-SLB surface, but tension signal was not detectable. **c** Schematic showing that locking strand binds to mechanically unfolded hairpin and locks the hairpin in unfolded state to capture transient TCR force signal. **d** Representative images showing the addition of locking strand increased Cy3B fluorescence at the immune synapse, but Atto647N remained unchanged. **e** Plot showing the fluorescence increase after adding locking strand. At the immune synapse, Cy3B fluorescence increased up to 3-fold but Atto647N stayed constant. Cy3B fluorescence of ROI lacking cells did not change after addition of locking strand, confirming locking strand did not nonspecifically open hairpin. Data were obtained from >30 cells.

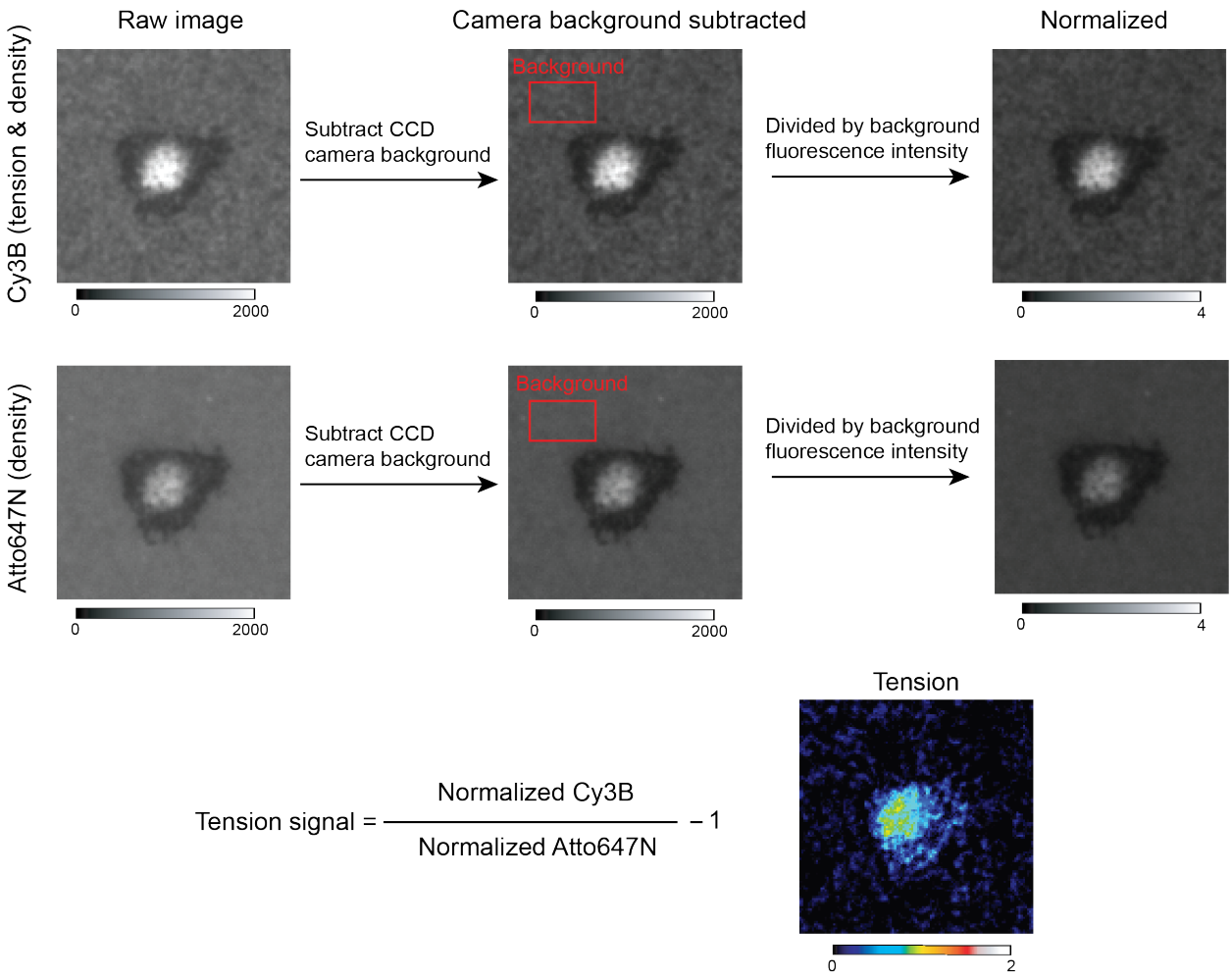


**Figure A3.10. Ratiometric analysis of TCR force signal.** To obtain tension signal, a series of image analysis was performed to extract tension signal from raw fluorescence images. First, raw Cy3B (signal includes both tension and density) and Atto647N (signal only includes density) fluorescence images were subtracted from EMCCD background of 200 a.u.. Afterwards, the images were normalized to background which was calculated by averaging ROIs lacking cells. Then the normalized Cy3B and Atto647N images were converted to tension signal by dividing Cy3B image by Atto647N image and subtracting the resulting image by 1.

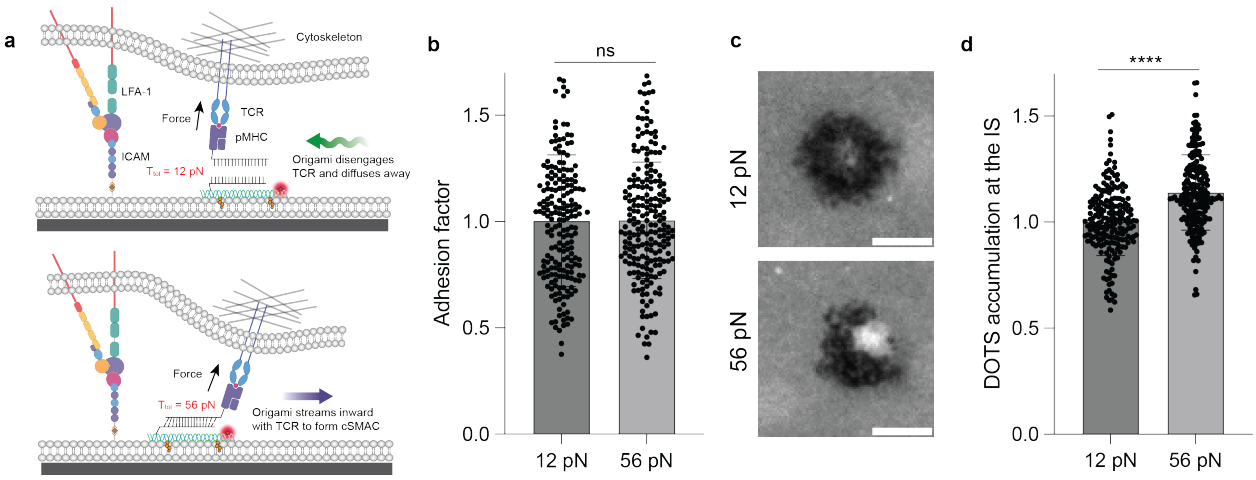


**Figure A3.11. TGT demonstrated that a subset of TCRs experience force > 12 pN. a** Schematic showing that TCR force ruptures TGT with a low force threshold (12 pN), and ruptured origami diffuses out of the immune synapse. By contrast, TGT with a high threshold (56 pN) is not ruptured by TCR force while translocating to the center of immune synapse. **b** Plot quantifying the area of immune synapse/adhesion zone formed on 12 and 56 pN TGT-DOTS surfaces. No statistical significance was observed. n>200 cells from three independent experiments and three independent mice. **c** Representative images showing the accumulation of DOTS signal at cSMAC on 12 and 56 pN TGT. **d** Plot quantifying the accumulation level of DNA origami at the immune synapse formed on 12 and 56 pN surfaces. In each replicate, data points were normalized to the mean of 12 pN condition for comparison. Error bars represent SD. **** $p<0.0001$

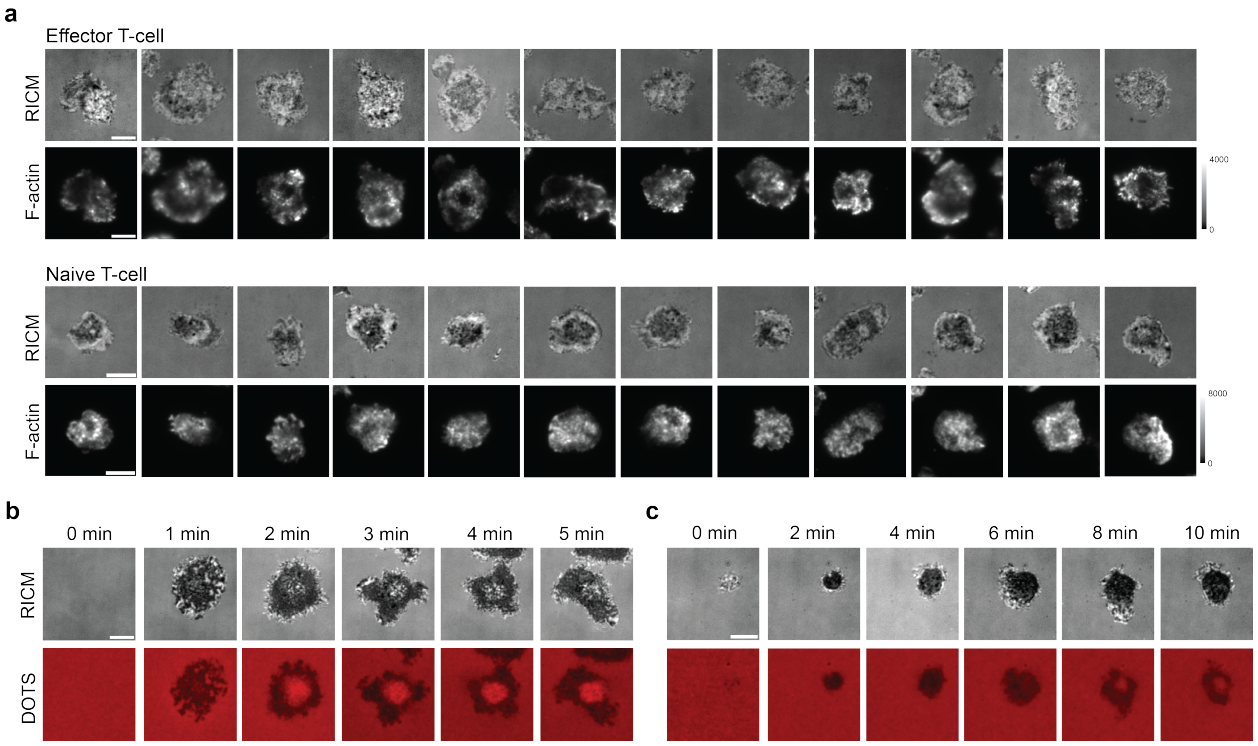


**Figure A3.12. F-actin dynamics of naïve and effector T-cell at the T-cell-SLB junctions. a** Representative F-actin staining images showing the actin distribution of naïve T-cell and effector T-cell after 30 min spreading on SLB surfaces. Effector T-cell F-actin distribution was more heterogenous with a pronounced clearance at the cSMAC region. In contrast, naïve T-cell F-actin was more evenly and tightly distributed in the spreading area. **b-c** Representative time lapse images showing the formation of immune synapse of effector T-cell (b) and naïve T-cells (c) on SLB. Effector T-cell displayed a faster rate of immune synapse formation than that of naïve T-cell. Scale bars = 5 μm

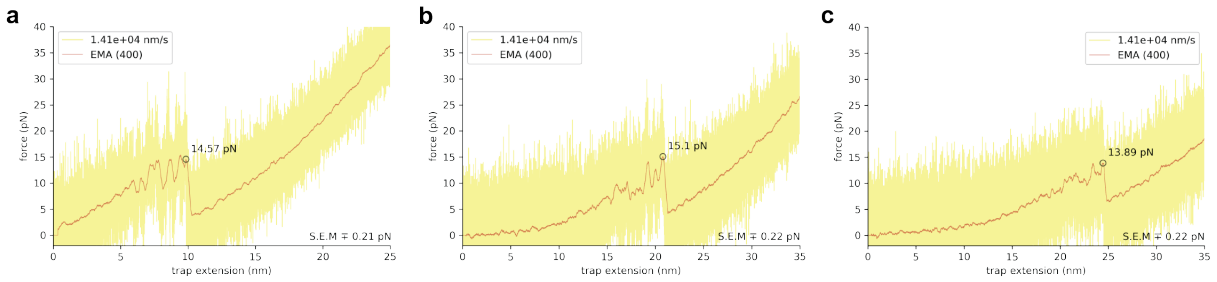


| DNA hairpin length | Original length | + 10 nm | + 20 nm |
|---|---|---|---|
| Replicate 1 (pN) | 14.57 | 10.35 | 13.89 |
| Replicate 2 (pN) | 12.52 | 15.1 | 14.82 |
| Replicate 3 (pN) | 12.27 | 12.06 | 13.69 |
| Average (pN) | 13.12 | 12.50 | 14.13 |

**Figure A3.13. Force threshold and height of DOTS are not correlated.**
Force-extension curves of hairpin tension sensors on DOTS (a original length, b + 10 nm, c +20 nm) pulling at the rate of $1.4x10^4$ nm/s in oxDNA simulations. The red curves indicate the smoothened data (400-point exponential moving average). The estimated force is marked at its peak in the graph along with its standard error of mean at the bottom right.

**Supplementary note 2:**
DOTS height estimation: The trajectories (oxDNA simulation timelapse) of the hairpin probes were imported into the oxView webserver. The transition point at which the structures start to unfold was noted and an earlier snapshot without the loss of any base pairing was used to measure heights. Since snapshots of the structure are printed in the simulation every millionth step ($10^6$), each frame in the simulation has a time interval of 10^6 ×0.005 × 3.03 × 10^(-12) s=15.15 ns. Hence, the height measurement was done ~15 ns before the start of hairpin rupture in the oxDNA simulation.

oxDNA simulation parameters and conditions: To validate that increasing linker length did not increase the force required to unfold DNA hairpin, we used oxDNA2 (version 2.4 published in June 2019) to simulate unfolding hairpins with different linker lengths (10.1063/1.4921957). We ran MD simulations on oxDNA on CPU to predict the rupture force of hairpins under force along the z-axis. The following parameters were used in the simulations:

backend = CPU
sim_type = MD
T = 37C
steps = 5e9
time_scale = linear
interaction_type = DNA2
use_average_seq = 1
verlet_skin = 0.05
salt_concentration = 0.156
thermostat = john
newtonian_steps = 103
diff_coeff = 2.5
dt = 0.005
print_conf_interval = 1e6

For all the simulations, harmonic traps of stiffness of 11.40 pN/nm were placed at the nucleotides of interest (i.e. the pMHC linked nucleotide and the nucleotide anchored to the origami). The effective trap stiffness can be calculated using the following equation: 1/k_eff = 1/k_1 + 1/k_2 The ligand nucleotide traps were moved at a rate of 5 x $10^{-8}$ (length per unit of time in oxDNA units) along the z-direction and when converted into SI units it yields a loading rate = (5 × 10^(-8)× 0.8518 nm)/(3.03 × 10^(-12) s)= 1.4×10^4 nm/s. To obtain the force-extension curves, we extracted the extensions of individual harmonic traps from the corresponding attached nucleotides and then projected it along the z-axis. The force is calculated by multiplying the total projected trap extension with k_eff. Combined trap extensions were used along with k_eff to average random thermal fluctuations as previously done in literature (10.1021/acsnano.8b01844). The graph with 1.9×105 data points is then smoothed with a 400-point exponential moving average (EMA) of the data points using python (10.1038/s41586-020-2649-2). The peak rupture force was then estimated using SciPy find peaks module on the smoothened graph (10.1038/s41592-019-0686-2).

From the simulations, the rupture of hairpins remained relatively within the range of 10-14 pN and did not correlate with linker length. It must also be noted oxDNA runs have an inherent level of stochasticity (as seen in the replicates) that results in small variations in force estimation. Note that in oxDNA simulations we measure peak force as the maximum force before the hairpin unfolding transition, therefore this can lead to higher estimation of forces compared to calculated $F_{1/2}$. In a typical “force ramp” setup, the rupture force is highly dependent on the loading rate (i.e. the greater the loading rate the greater the rupture force).

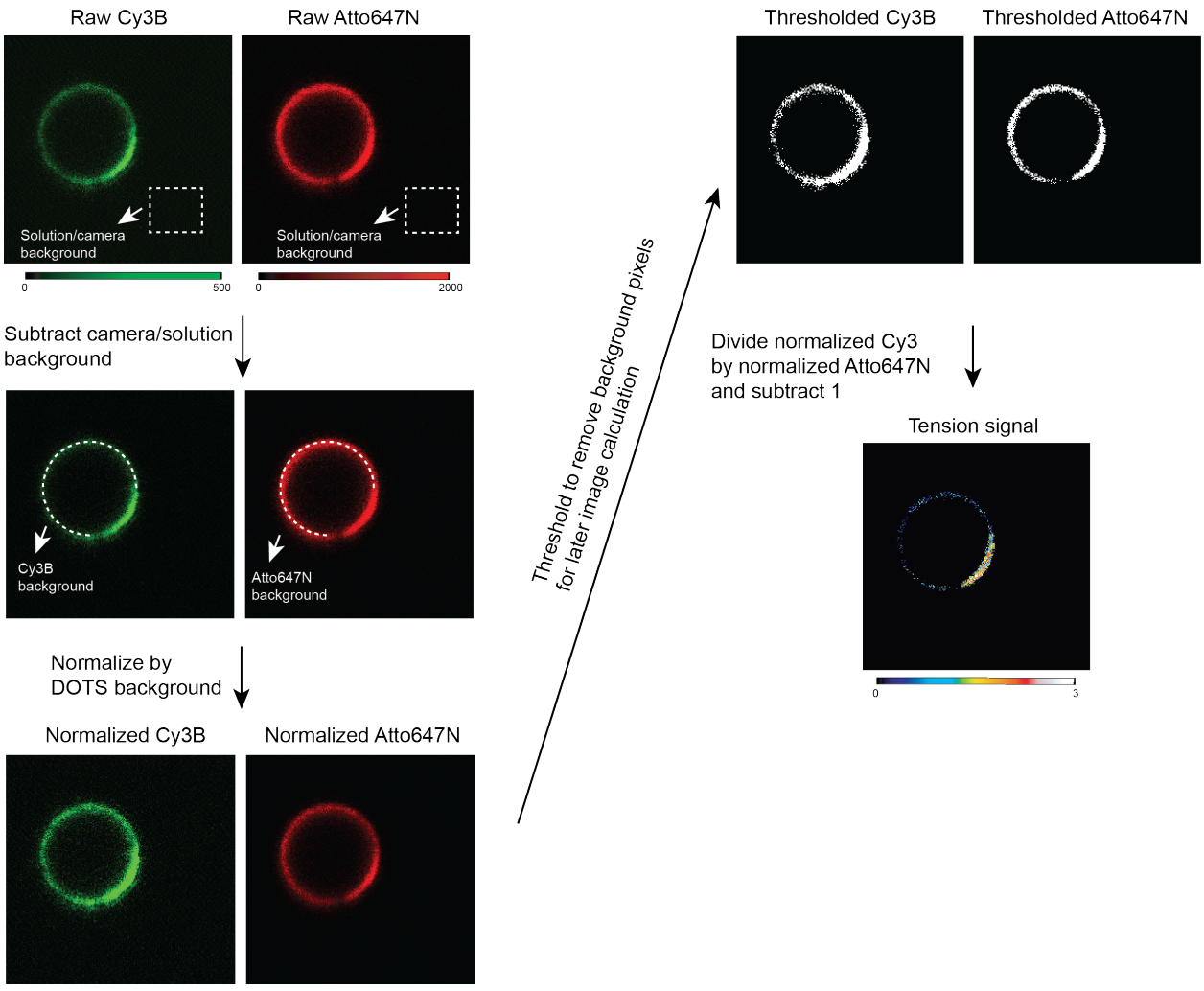


**Figure A3.14. TCR force analysis protocol for cell-SSLB experiment.** First, raw Cy3B (signal includes both tension and density) and Atto647N (signal only includes density) fluorescence images were subtracted from camera and solution background (intensity of regions lacking SSLB). Second, Cy3B and Atto647N images were normalized by a defined region not engaging cells. Third, because background subtracted images have zero values which would introduce infinite values/errors in following image calculations, a threshold mask was applied to exclusively select the pixels associated with the SSLB. Fourth, tension signal was obtained by dividing normalized Cy3B image (signal includes both tension and density) by Atto647N image (signal only includes density) and subtracting 1.

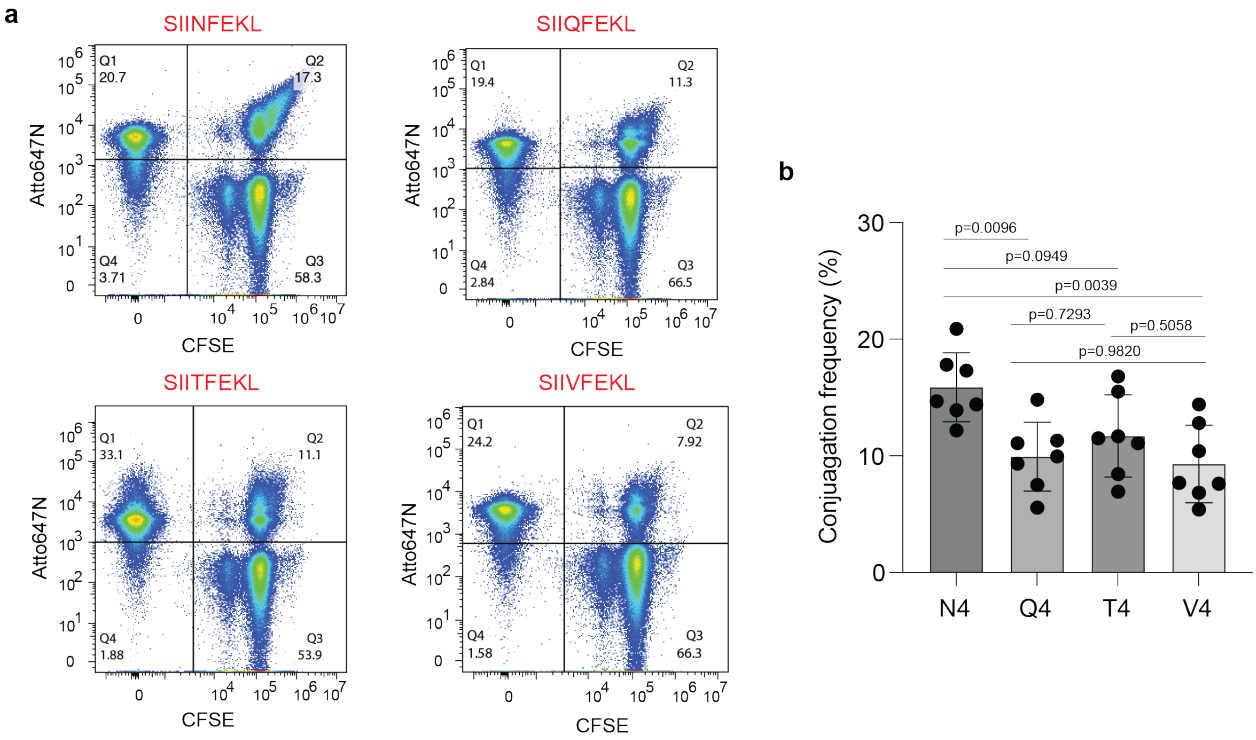


**Figure A3.15. Flow analysis of T-cell-SSLB conjugates under different antigen conditions. a** Flow fluorescence quadrant plots showing the T-cell (CFSE positive), SSLB (Atto647N positive) and T-cell-SSLB conjugate (Dual positive) populations. SSLB were coated with DOTS modified with different antigens. **b** Plot quantifying the frequency of conjugates. Conjugates formed more efficiently under agonist (N4) condition compared to antagonists. n= 6 replicates from 6 independent experiments.

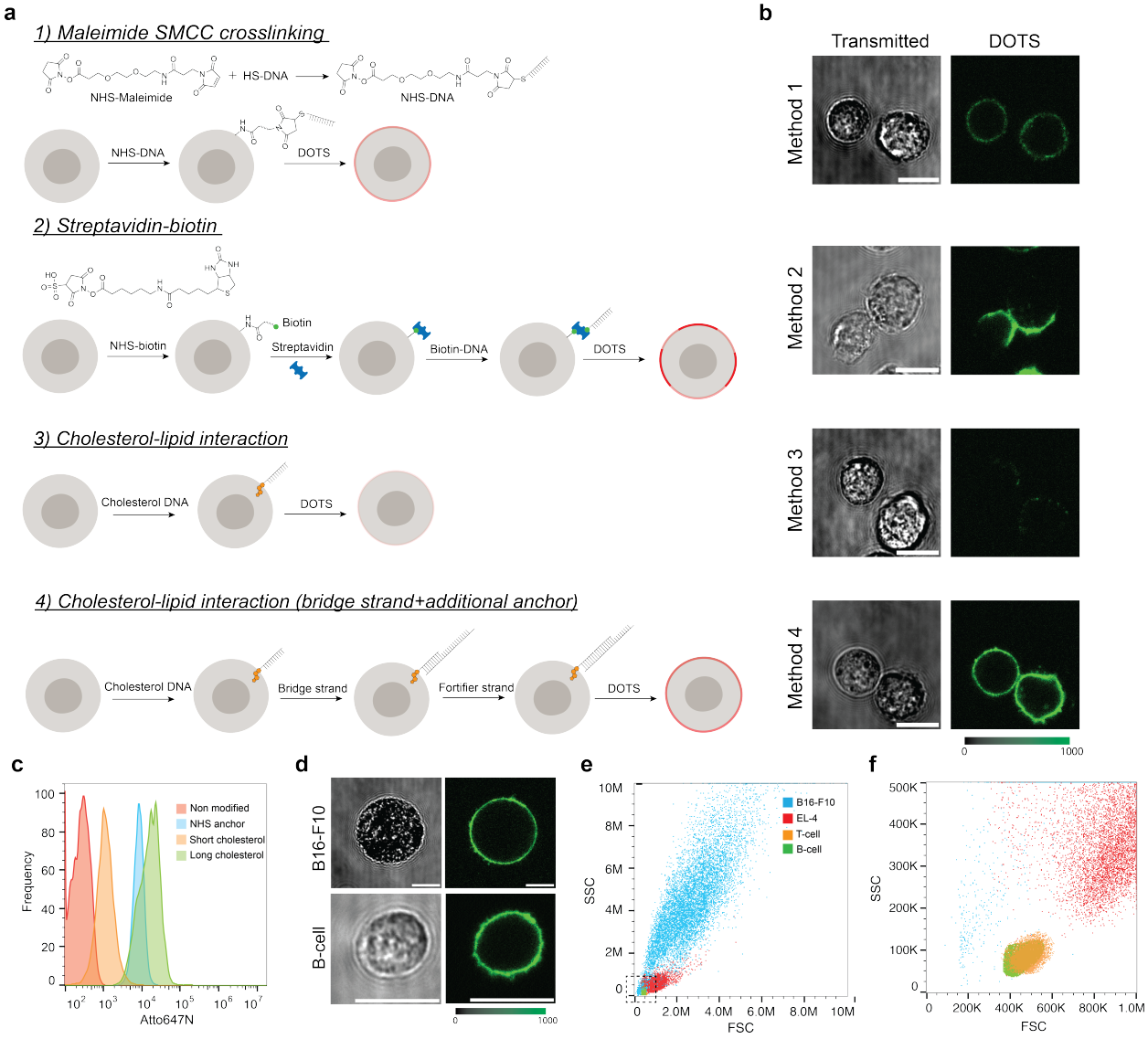


**Figure A3.16. Different strategies to functionalize cell membrane with DOTS. a** Schematics showing different chemistries used to modify cell membrane with DOTS. DNA strands complementary to the elongations on the DOTS were anchored onto cell membrane through thiol-maleimide reaction, streptavidin-biotin interaction or cholesterol lipid interaction. **b** Representative images showing the DOTS labeling intensities on EL-4 membrane with different functionalizing strategies. **c** Flow cytometry fluorescence histogram quantifying the labeling intensities under different functionalizing strategies. **d** Representative images showing DOTS signal on B16-F10 and resting B-cell membranes. DOTS were anchored through strategy 4 in panel a **e** Flow cytometer scatter plot showing the size distribution of different cell lines f Zoom-in scatter plot of selected ROI in e showing the resting T-cell and B-cell have comparable size. Scale bars = 10 μm

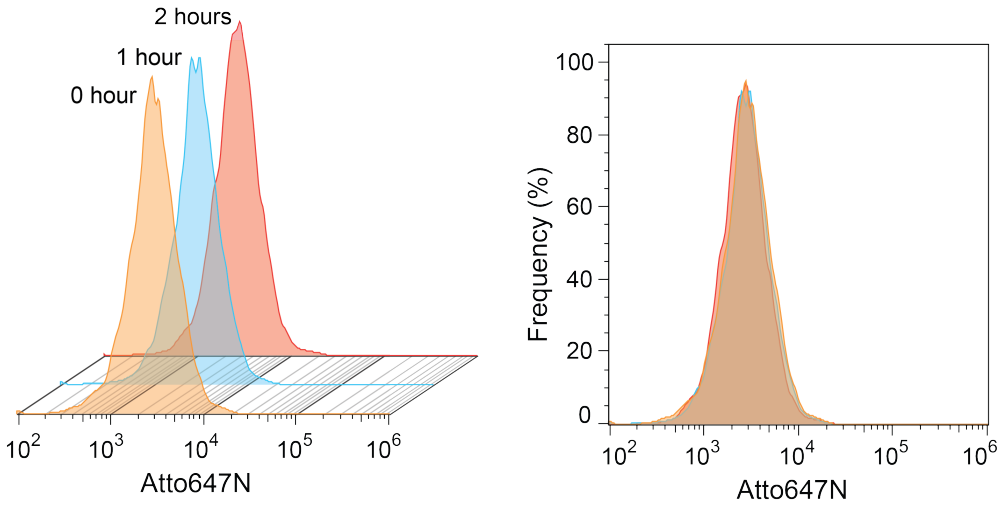


**Figure A3.17. Stability of DOTS on the B-cell membrane.** Flow fluorescence histograms of DOTS modified B-cells. No fluorescence change was observed within two hours at room temperature, indicating a strong stability of DOTS on B-cell membrane and low dissociation rate.

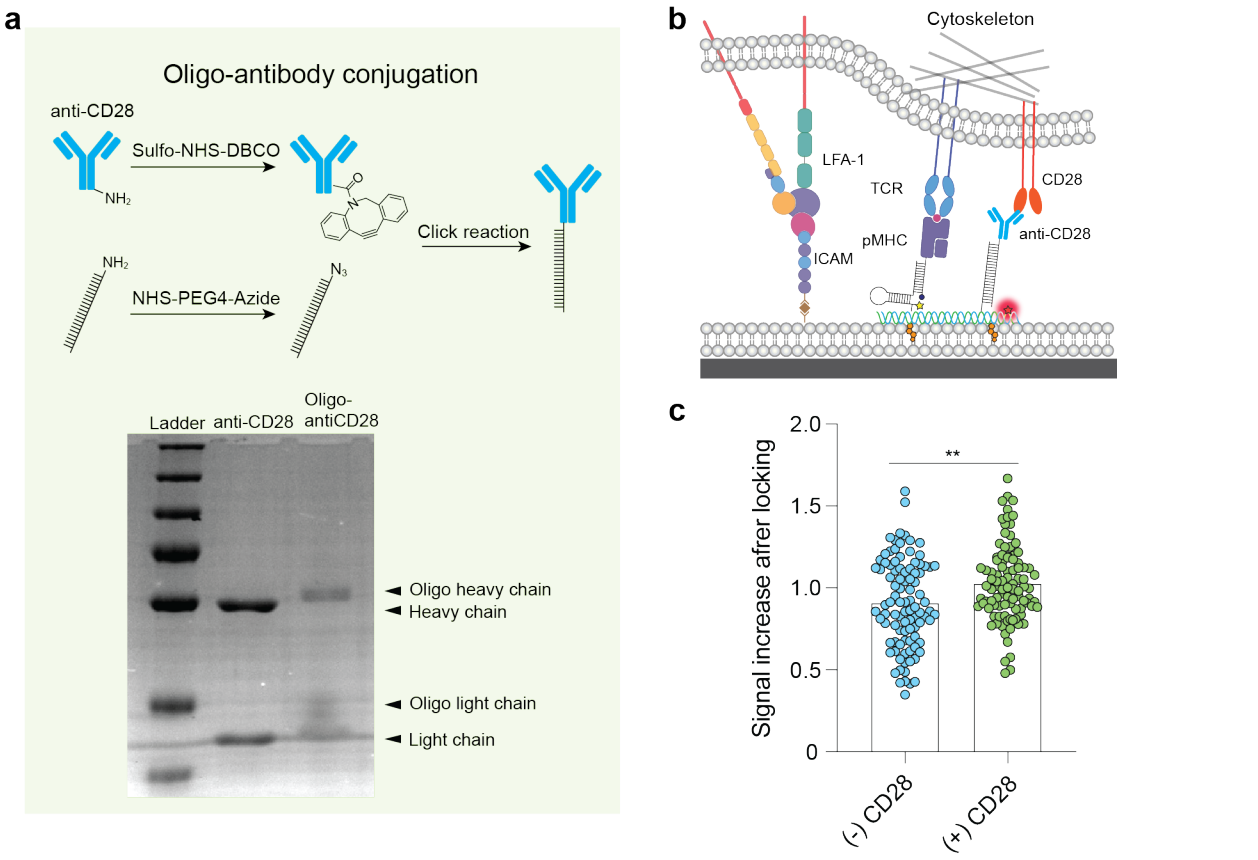


**Figure A3.18. CD28 engagement enhances TCR force signal. a** Schematic showing the workflow of conjugating anti-CD28 to DNA through copper free click reaction. Amine-DNA and Anti-CD28 was labeled using Azide-NHS and DBCO-NHS, respectively. Successful conjugation was confirmed using reducing SDS-PAGE. Arrows indicate anti-CD28 and DNA-anti-CD28 fragments. **b** Schematic showing the anti-CD28 was introduced to DNA origami platform through DNA hybridization. pMHC and anti-CD28 were on the same DOTS surrounded by ICAM-1 ligands. **c** Dot plot comparing the TCR force signals in the presence and absence of anti-CD28 on the DOTS. At least 95 cells from two independent mice were analyzed. ** p=0.0013

**Supplementary note 3: Design of DNA hairpin tension sensors**

The unfolding force of DNA harpins, $F_{1/2}$ (defined as the force at which the hairpin has a 50% probability of being unfolded) was determined primarily based on the assumptions and measurements used by Woodside et al. For DNA hairpin structures, the free energy change during transition from the folded state to the unfolded state under an applied F can be described as:

$$\Delta G = \Delta G_{\text{unfold}} + \Delta G_{\text{stretch}} - F\Delta x + k_B T ln\left(\frac{[unfolded]}{[folded]}\right)$$

When $F = F_{1/2}$, at equilibrium ($\Delta G=0$), the DNA hairpin molecule has an equal probability of being in folded and unfolded states such that ([unfolded])/([folded]) = 1. Accordingly, above equation can be reorganized as the following:

$$F_{1/2} = \frac{(\Delta G_{\text{unfold}} + \Delta G_{\text{stretch}})}{\Delta x}$$

where, $\Delta G_{unfold}$ is the free energy for unfolding the hairpin without force and opposite to $\Delta G_{fold}$. $\Delta G_{fold}$ was acquired from IDT oligoanalyzer 3.1, which uses the UNAfold software package to calculate $\Delta G_{fold}$ under T-cell imaging condition (25 $^{o}$C, 149.7 mM monovalent salt and 2 mM divalent salt). $\Delta G_{stretch}$ is the free energy for stretching the ssDNA from its folded coordinates, which can be calculated with the worm like chain model below:

$$\Delta G_{\text{stretch}} = \left(\frac{k_{\text{B}}T}{L_{\text{p}}}\right)\left[\frac{L_{\text{o}}}{4\left(\frac{1-x}{L_0}\right)}\right]\left[3\left(\frac{x}{L_0}\right)^2 - 2\left(\frac{x}{L_0}\right)^3\right]$$

where Lp is the persistence length of ssDNA (~1.3 nm), L0 is the contour length of ssDNA (0.63 nm per nucleotide), x is the hairpin extension from equilibrium and can be calculated by using (0.44*(n-1)) nm, where n represents the number of the bases comprising the stem-loop of hairpin. Note we subtract a distance of 2 nm from x to get Δx in equation 2 because initial separation between the stem termini is set by the diameter of the hairpin stem duplex (effective helix width = 2 nm).

**Table A3.1 The parameters and $F_{1/2}$ of DNA hairpins.**

| Name | 22% GC hairpin | 77% GC hairpin |
|---|---|---|
| Stem loop sequence | GTA TAA ATG TTT TTT TCA TTT ATA C | GGG GAG GAG TTT TTT TCT CCT CCC C |
| Nucleotide number | 25 | 25 |
| GC content | 22% | 77% |
| Δx (nm) | 8.56 | 8.56 |
| $\Delta G_{unfold}$ (kJ/mole) | 24.23 | 43.60 |
| $\Delta G_{stretch}$ (kJ/mole) | 16.99 | 16.99 |
| Calculated $F_{1/2}$ (pN) | 7.99 | 11.7 |

**Table A3.2 List of DNA strands**

All oligonucleotides were custom synthesized by Integrated DNA Technologies (Coralville, IA), except for the BHQ1 strand, which was synthesized by Biosearch Technologies (Novato, CA). Table includes the names and sequences for all oligonucleotides used in this work except for DNA origami staples. The colors of the highlighted sequences match the colors in Figure S3. Structures of the modifications are shown in Figure S1.

| Name | Description | Sequence (5' to 3') |
|---|---|---|
| 22% GC hairpin | DNA origami staple with 22% GC stem-loop hairpin and overhang complementary to ligand strand | CCC TCA AAC ACT ATC ATA ACC CTA ACG AAC TA/iAmMC6T/ TTT GTA TAA ATG TTT TTT TCA TTT ATA CTT TGT GTC GTG CCT CCG TGC TGT G |
| Ligand strand | Strand carrying antigen and quencher | /5_Biotin/ CAC AGC ACG GAG GCA CGA CAC /3_BHQ2/ |
| 22% GC locking strand | Strand that is partially complementary to 22% GC hairpin | AAA AAA CAT TTA TAC |
| Fully complementary strand | Strand that is fully complementary to 22% GC hairpin | GTA TAA ATG AAA AAA ACA TTT ATA C |
| Density reporter strand | DNA origami staple labeled with fluorophore as a density reporter | AGG TCA CCG GCA CCG CTT CTG GTG ATT AAG TT/3AmMO/ |
| 77% GC hairpin | DNA origami staple with 77% GC stem-loop hairpin and overhang complementary to ligand strand | CCC TCA AAC ACT ATC ATA ACC CTA ACG AAC TA/iAmMC6T/ TTT GGG GAG GAG TTT TTT TCT CCT CCC CTT TGT GTC GTG CCT CCG TGC TGT G |
| 77% GC locking strand | Strand is partially complementary to 77% GC pN hairpin | AAA AAA CTC CTC CCC |
| TGT bottom strand | DNA origami staple with strand complementary to TGT top ligand strand | CCC TCA AAC ACT ATC ATA ACC CTA ACG AAC TA TT T GTG AAA TAC CGC ACA GAT GCG |
| 12 pN TGT top strand | 12 pN TGT top strand carrying antigen next to DNA origami anchor site (unzipping geometry) | CGC ATC TGT GCG GTA TTT CAC /Biotin/ |

| | | |
|---|---|---|
| 56 pN TGT top strand | TGT top strand carrying antigen at opposite terminal to DNA origami anchor site (shearing geometry) | CGC ATC TGT GCG GTA TTT CAC /Biotin/ |
| Hairpin anchor strand (+ 10 nm) | DNA origami staple with elongation complementary to the conventional hairpin strand | CCC TCA AAC ACT ATC ATA ACC CTA ACG AAC TA T TTG CTG GGC TAC GTG GCG CTC TT /3AmMO/ |
| Hairpin anchor strand (+ 20 nm) | DNA origami staple with elongation complementary to the conventional hairpin strand | CCC TCA AAC ACT ATC ATA ACC CTA ACG AAC TAT TTT TTT TTT TTT TTT TTT TTT TTT TTT TTT TTG CTG GGC TAC GTG GCG CTC TT/3AmMO/ |
| MTS hairpin strand | Hairpin strand with 22% GC stem-loop region and two arms that binds to the hairpin anchor strand and ligand strand for higher antigen | GTG AAA TAC CGC ACA GAT GCG TTT GTA TAA ATG TTT TTT TCA TTT ATA CTT TAA GAG CGC CAC GTA GCC CAG C |
| Ligand strand for higher antigen | Strand carrying antigen and quencher | /5_BHQ1/ CGC ATC TGT GCG GTA TTT CAC /3_Biotin/ |
| Cholesterol SLB strand | Cholesterol SLB strand tha is complementary to elongations on the origami for anchoring origami onto SLB | GTT CGT CCG CTC GCC TGC TTG /3CholTEG/ |
| Second ligand anchor strand | DNA origami staple with elongation complementary to second ligand strand | AGG TCA CCG GCA CCG CTT CTG GTG ATT AAG TT TTT CAC TCC CGT CCA CAT TGC TAC TAC TAT CAT |
| Second ligand strand | DNA strand used to label anti-CD28 | /5AmMC6/ ATG ATA GTA GTA GCA ATG TGG ACG GGA GTG |
| Cholesterol cell membrane strand | Strand used to tag cell membrane with DNA and complementary to part of the bridge strand | GAT GAA TGG TGG GTG AGA GGC /CholTEG/ |
| Bridge strand | Strand that connects cholesterol cell membrane strand and elongations on the DOTS to anchor DOTS onto cell membrane | GCC TCT CAC CCA CCA TTC ATC TTT TTT TTT TTT TTT TTT GTT CGT CCG CTC GCC TGC TTG |

| | | |
|---|---|---|
| Fortifier strand | Strand binds to the remaining portion of bridge strand to rigidify the bridge strand | AAA AAA AAA AAA AAA AAA |
| MTS ligand strand | Strand that is used to present ligand and complementary to the MTS hairpin strand | /5_bitoin/TT TGC TGG GCT ACG TGG CGC TCT T/3AmMO/ |
| MTS anchor strand | Strand that is complementary to the MTS hairpin strand and has a cholesterol group for SLB anchoring | CGC ATC TGT GCG GTA TTT CAC /3_CholTEG/ |

**Table A3.3. List of staple strands for DOTS in SLB experiments**

| Start 5' | End 3' | Note | Sequence |
|---|---|---|---|
| 6[198] | 8[199] | Staple | ACGGAACTGACGAGAAAC ACCAGCGGTGTACA |
| 4[38] | 6[39] | Staple | CCGTGCAGCCTCAGGAAG ATCGCTCACGACGT |
| 8[215] | 6[216] | Staple | CAGATGAAAACGAGTAGT AAATTGAAATCTAC |
| 10[166] | 12[167] | Staple | GGCACCAGCCGACAATGA CAACACGGTTTATC |
| 7[128] | 7[159] | Staple | AATAACCCCGCCATTACCC AAATCAACGTAAC |
| 0[247] | 2[231] | Staple | GCATTAACATCCAATAAAT CATACATAACCTGTTTAGC TATGATAAGAG |
| 12[198] | 12[216] | Staple | CCAAAAGTTGTCGTCTTTC CAGACGTTAGTAAATGAAT TGTTGAAAA |
| 1[128] | 1[159] | Staple | TGAGAGTCTGGAGTTTCAT TCCATATAACAGT |
| 12[230] | 12[248] | Staple | TTTTCACTTCTGTATGGGA TTTTGCTAAACAACTTTCA AACTAAAGG |
| 2[38] | 4[39] | Staple | ATAAGCAAAAATTCGCATT AAATGCATCGTAA |
| 10[70] | 12[71] | Staple | GAAGCATGCTGCATTAATG AATCAAGCGGTCC |
| 10[215] | 8[216] | Staple | CATGAGGAATTTGTATCAT CGCCTAAAGAGGA |
| 4[119] | 2[120] | Staple | CCCGTCGGTTCCTGTAGCC AGCTTGAATCGAT |

| | | | |
|---|---|---|---|
| 0[215] | 2[199] | Staple | CAAAGAATTAGCAAAATT AAGCAATTTGACCATTAGA TACGCTTAATTG |
| 10[87] | 8[88] | Staple | ACACAACAGTGGTGCTTGT TACCTGACAGTGC |
| 13[128] | 13[159] | Staple | ACCGTCTATCACGCCTGTA GCATTCCACAGAC |
| 6[230] | 8[231] | Staple | GGAAGAAGGCTTGAGATG GTTTAGAACTGACC |
| 4[166] | 6[167] | Staple | GAATGACGCCAAAAGGAA TTACGGAAAGATTC |
| 2[119] | 0[120] | Staple | GAACGGTACTATCAGGTCA TTGCCGCGGGAGA |
| 8[55] | 6[56] | Staple | GCACGAATTCTAAGTGGTT GTGAAGCCAGGGT |
| 2[230] | 4[231] | Staple | GTCATTTTAATTCGAGCTT CAAACGTCCAATA |
| 8[198] | 10[199] | Staple | GACCAGGACAAAGTACAA CGGAGAGTTTCCAT |
| 10[38] | 12[39] | Staple | TGAGTGACCCGCTTTCCAG TCGGAAAATCCTG |
| 12[119] | 10[120] | Staple | CTGATTGCTGGGCGCCAGG GTGGTAGCTGTTT |
| 0[87] | 2[71] | Staple | TAGAACCCTCATATATTTT AAATGATAAATTAATGCCG GACCGGTTGAT |
| 6[166] | 8[167] | Staple | ATCAGTTAAAGCTGCTCAT TCAGCCTTCATCA |
| 6[119] | 4[120] | Staple | CTATTACGCAGGCTGCGCA ACTGTAGTAACAA |
| 2[198] | 4[199] | Staple | CTGAATAAGGAAGCCCGA AAGACATTGAATCC |
| 6[247] | 4[248] | Staple | TACCAGTCCGAGAGGCTTT TGCAATGTTTAGA |
| 6[159] | 6[128] | Staple | GAGATTTAGGAATACCAC ATTATCGGTGCGGG |
| 2[166] | 4[167] | Staple | AATATGCGAAGCAAAGCG GATTGAGAAAACGA |
| 8[87] | 6[88] | Staple | GGCCCTGCAAGTGTCCTTA GTGCTGGATGTGC |
| 6[183] | 4[184] | Staple | TACAGGTAAGGCATAGTA AGAGCAATGCTTTA |
| 6[55] | 4[56] | Staple | TTTCCCAGACTCCAGCCAG CTTTCGTTGGTGT |
| 2[87] | 0[88] | Staple | TATGTACCGAGGGTAGCTA TTTTTAAAATTTT |

| | | | |
|---|---|---|---|
| 9[128] | 9[159] | Staple | TCGAATTCGTAAGAATACA CTAAAACACTCAT |
| 0[183] | 2[167] | Staple | CAGAGCATAAAGCTAAAT CGGTTGTGATTCCCAATTC TGCCATGTTTTA |
| 6[70] | 8[71] | Staple | GGGTAACTTCATGCGCACG ACTTCATCTGTAA |
| 8[166] | 10[167] | Staple | AGAGTAACTTTGACCCCCA GCGACACTACGAA |
| 8[38] | 10[39] | Staple | TTGAATCAACTCTGACCTC CTGGGGTGCCTAA |
| 10[198] | 12[199] | Staple | TAAACGGAACCGATATATT CGGTAAAAAGGCT |
| 10[247] | 8[248] | Staple | GCTACAGAATCCGCGACCT GCTCCCAATCATA |
| 4[102] | 6[103] | Staple | GGGAACAAGCGCCATTCG CCATTCCAGCTGGC |
| 12[70] | 12[88] | Staple | ACGCTGGTGTTCCAGTTTG GAACAAGAGTCCACTATTA ACTGAGAGA |
| 6[215] | 4[216] | Staple | GTTAATAACGTTTACCAGA CGACGATCGTCAT |
| 10[119] | 8[120] | Staple | CCTGTGTGTCCCCGGGTAC CGAGCTTACGCTC |
| 10[230] | 12[231] | Staple | GACTAAAGAGTTAAAGGC CGCTTATAATAATT |
| 3[128] | 3[159] | Staple | TCATCAACATTTTACCCTG ACTATTATAGTCA |
| 0[55] | 2[39] | Staple | GAGTAATGTGTAGGTAAA GATTCAACCATCAATATGA TATGAAGATTGT |
| 10[159] | 10[128] | Staple | ACCTAAAACGAAAGAGGC AAAATCATGGTCAT |
| 5[128] | 5[159] | Staple | TGGGAAGGGCGCAACTAA TGCAGATACATAAC |
| 4[159] | 4[128] | Staple | CATAAATCAAAAATCAGG TCTAAATGTGAGCG |
| 8[102] | 10[103] | Staple | TGATACCCGATAAAGACG GAGGAAAATTGTTA |
| 10[183] | 8[184] | Staple | CGTAATGCTTATACCAAGC GCGAACGCATAGG |
| 0[119] | 2[103] | Staple | AGCCTTTATTTCAACGCAA GGATAGAGAGATCTACAA AGGATCGTAAAA |

| | | | |
|---|---|---|---|
| 12[102] | 12[120] | Staple | CCTGGCCAGAACGTGGACT CCAACGTCAAAGGGCGAA AAGGCAACAG |
| 4[230] | 6[231] | Staple | CTGCGGAATAAAAACCAA AATAGAGGACGTTG |
| 2[247] | 0[248] | Staple | GCTCCTTTTATTTTCATTTG GGGCTAGTAGTA |
| 4[247] | 2[248] | Staple | CTGGATAGGCGAACCAGA CCGGAACTTTAATT |
| 8[70] | 10[71] | Staple | GCAACTCACAGGGCTTAA GCTACTACGAGCCG |
| 8[247] | 6[248] | Staple | AGGGAACCATTTCAACTTT AATCAGCTCATTA |
| 10[102] | 12[103] | Staple | TCCGCTCGAGGCGGTTTGC GTATCCTTCACCG |
| 6[87] | 4[88] | Staple | TGCAAGGCGCCGGAAACC AGGCAAAACGGCGG |
| 8[119] | 6[120] | Staple | GCCCTGGAGACAATGTCCC GCCAACCTCTTCG |
| 11[128] | 11[159] | Staple | TTTTCTTTTCACAGCTTGAT ACCGATAGTTGC |
| 8[159] | 8[128] | Staple | TCTTGACAAGAACCGGATA TTTTCTAATCTAT |
| 6[102] | 8[103] | Staple | GAAAGGGGAATTGTCAAC CTTATGTGACTCTA |
| 12[38] | 12[56] | Staple | TTTGATGTCAAAAGAATAG CCCGAGATAGGGTTGAGT GTTTTGCCCC |
| 2[215] | 0[216] | Staple | GGCTTAGAATTTCGCAAAT GGTCAAGGCAAGG |
| 12[166] | 12[184] | Staple | AGCTTGCAGCCCTCATAGT TAGCGTAACGATCTAAAGT TGAGCCTTT |
| 6[38] | 8[39] | Staple | TGTAAAACCAGGGTGGAT GTTCTATAGGGGCC |
| 8[183] | 6[184] | Staple | CTGGCTGATGAATAAGGCT TGCCCAACATTAT |
| 2[159] | 2[128] | Staple | AACTAAAGTACGGTGTCTG GAAGCAAACAAGA |
| 12[247] | 10[248] | Staple | AATTGCGATTGCGGGATCG TCACCTAGCAACG |
| 2[183] | 0[184] | Staple | TAGCTCAAGAACGAGTAG ATTTAGTAAAGCCT |
| 8[230] | 10[231] | Staple | AACTTTGGATAAATTGTGT CGAAGGCTTTGAG |

| | | | |
|---|---|---|---|
| 12[159] | 12[128] | Staple | TTTCGAGGTGAATTTCTTA AACCAGTGAGACG |
| 2[55] | 0[56] | Staple | AAAAACAGTCAACCGTTCT AGCTGCAATGCCT |
| 0[159] | 0[128] | Staple | TACCAAAAACATTATGACC CTGTAATACTTTT |
| 2[102] | 4[103] | Staple | CTAGCATTAATTCGCGTCT GGCCATTCTCCGT |
| 10[55] | 8[56] | Staple | AAGCCTGGTTGGTGTAATG AGTAAGTCGGTGG |
| 2[70] | 4[71] | Staple | AATCAGACATTTTTTAACC AATATAATGGGAT |
| 12[215] | 10[216] | Staple with elongation for SLB anchoring | CAA GCA GGC GAG CGG ACG AAC TTT TCTCCAAACGCTGAGGCTT GCAGGGACTTTTT |
| 12[55] | 10[56] | Staple with elongation for SLB anchoring | CAA GCA GGC GAG CGG ACG AAC TTT AGCAGGCGGAAACCTGTC GTGCCAAAAGTGTA |
| 4[183] | 2[184] | Staple with elongation for SLB anchoring | CAA GCA GGC GAG CGG ACG AAC TTT AACAGTTCCATCAAAAAG ATTAAGTAATGCTG |
| 4[55] | 2[56] | Staple with elongation for SLB anchoring | CAA GCA GGC GAG CGG ACG AAC TTT AGATGGGCTTTTGTTAAAT CAGCTAAAGCCCC |
| 12[87] | 10[88] | Staple with elongation for SLB anchoring | CAA GCA GGC GAG CGG ACG AACTTT GTTGCAGCGGCCAACGCG CGGGGAACAATTCC |
| 12[183] | 10[184] | Staple with elongation for SLB anchoring | CAA GCA GGC GAG CGG ACG AAC TTT AATTGTATACCATCGCCCA CGCATGTAAAATA |
| 4[215] | 2[216] | Staple with elongation for SLB anchoring | CAA GCA GGC GAG CGG ACG AAC TTT AAATATTCTTCAAATATCG CGTTTTTGCGGAT |
| 4[87] | 2[88] | Staple with elongation for SLB anchoring | CAA GCA GGC GAG CGG ACG AAC TTT ATTGACCGGGAACGCCATC AAAAAGTCAATCA |

**Table A3.4 List of staple strands for DOTS in cell-cell experiments**

| Start 5' | End 3' | Note | Sequence |
|---|---|---|---|
| 6[198] | 8[199] | Staple | ACGGAACTGACGAGAAAC ACCAGCGGTGTACA |
| 8[215] | 6[216] | Staple | CAGATGAAAACGAGTAGT AAATTGAAATCTAC |
| 10[166] | 12[167] | Staple | GGCACCAGCCGACAATGA CAACACGGTTTATC |
| 7[128] | 7[159] | Staple | AATAACCCCGCCATTACCC AAATCAACGTAAC |
| 0[247] | 2[231] | Staple | GCATTAACATCCAATAAAT CATACATAACCTGTTTAGC TATGATAAGAG |
| 12[198] | 12[216] | Staple | CCAAAAGTTGTCGTCTTTC CAGACGTTAGTAAATGAAT TGTTGAAAA |
| 1[128] | 1[159] | Staple | TGAGAGTCTGGAGTTTCAT TCCATATAACAGT |
| 10[70] | 12[71] | Staple | GAAGCATGCTGCATTAATG AATCAAGCGGTCC |
| 10[215] | 8[216] | Staple | CATGAGGAATTTGTATCAT CGCCTAAAGAGGA |
| 4[119] | 2[120] | Staple | CCCGTCGGTTCCTGTAGCC AGCTTGAATCGAT |
| 0[215] | 2[199] | Staple | CAAAGAATTAGCAAAATT AAGCAATTTGACCATTAGA TACGCTTAATTG |
| 10[87] | 8[88] | Staple | ACACAACAGTGGTGCTTGT TACCTGACAGTGC |
| 13[128] | 13[159] | Staple | ACCGTCTATCACGCCTGTA GCATTCCACAGAC |
| 6[230] | 8[231] | Staple | GGAAGAAGGCTTGAGATG GTTTAGAACTGACC |
| 4[166] | 6[167] | Staple | GAATGACGCCAAAAGGAA TTACGGAAAGATTC |
| 2[119] | 0[120] | Staple | GAACGGTACTATCAGGTCA TTGCCGCGGGAGA |
| 8[55] | 6[56] | Staple | GCACGAATTCTAAGTGGTT GTGAAGCCAGGGT |
| 2[230] | 4[231] | Staple | GTCATTTTAATTCGAGCTT CAAACGTCCAATA |
| 8[198] | 10[199] | Staple | GACCAGGACAAAGTACAA CGGAGAGTTTCCAT |
| 12[119] | 10[120] | Staple | CTGATTGCTGGGCGCCAGG GTGGTAGCTGTTT |

| | | | |
|---|---|---|---|
| 0[87] | 2[71] | Staple | TAGAACCCTCATATATTTT AAATGATAAATTAATGCCG GACCGGTTGAT |
| 6[166] | 8[167] | Staple | ATCAGTTAAAGCTGCTCAT TCAGCCTTCATCA |
| 6[119] | 4[120] | Staple | CTATTACGCAGGCTGCGCA ACTGTAGTAACAA |
| 2[198] | 4[199] | Staple | CTGAATAAGGAAGCCCGA AAGACATTGAATCC |
| 6[159] | 6[128] | Staple | GAGATTTAGGAATACCAC ATTATCGGTGCGGG |
| 2[166] | 4[167] | Staple | AATATGCGAAGCAAAGCG GATTGAGAAAACGA |
| 8[87] | 6[88] | Staple | GGCCCTGCAAGTGTCCTTA GTGCTGGATGTGC |
| 6[183] | 4[184] | Staple | TACAGGTAAGGCATAGTA AGAGCAATGCTTTA |
| 6[55] | 4[56] | Staple | TTTCCCAGACTCCAGCCAG CTTTCGTTGGTGT |
| 2[87] | 0[88] | Staple | TATGTACCGAGGGTAGCTA TTTTTAAAATTTT |
| 9[128] | 9[159] | Staple | TCGAATTCGTAAGAATACA CTAAAACACTCAT |
| 0[183] | 2[167] | Staple | CAGAGCATAAAGCTAAAT CGGTTGTGATTCCCAATTC TGCCATGTTTTA |
| 6[70] | 8[71] | Staple | GGGTAACTTCATGCGCACG ACTTCATCTGTAA |
| 8[166] | 10[167] | Staple | AGAGTAACTTTGACCCCCA GCGACACTACGAA |
| 10[198] | 12[199] | Staple | TAAACGGAACCGATATATT CGGTAAAAAGGCT |
| 4[102] | 6[103] | Staple | GGGAACAAGCGCCATTCG CCATTCCAGCTGGC |
| 12[70] | 12[88] | Staple | ACGCTGGTGTTCCAGTTTG GAACAAGAGTCCACTATTA ACTGAGAGA |
| 6[215] | 4[216] | Staple | GTTAATAACGTTTACCAGA CGACGATCGTCAT |
| 10[119] | 8[120] | Staple | CCTGTGTGTCCCCGGGTAC CGAGCTTACGCTC |
| 10[230] | 12[231] | Staple | GACTAAAGAGTTAAAGGC CGCTTATAATAATT |
| 3[128] | 3[159] | Staple | TCATCAACATTTTACCCTG ACTATTATAGTCA |

| | | | |
|---|---|---|---|
| 10[159] | 10[128] | Staple | ACCTAAAACGAAAGAGGC AAAATCATGGTCAT |
| 5[128] | 5[159] | Staple | TGGGAAGGGCGCAACTAA TGCAGATACATAAC |
| 4[159] | 4[128] | Staple | CATAAATCAAAAATCAGG TCTAAATGTGAGCG |
| 8[102] | 10[103] | Staple | TGATACCCGATAAAGACG GAGGAAAATTGTTA |
| 10[183] | 8[184] | Staple | CGTAATGCTTATACCAAGC GCGAACGCATAGG |
| 0[119] | 2[103] | Staple | AGCCTTTATTTCAACGCAA GGATAGAGAGATCTACAA AGGATCGTAAAA |
| 12[102] | 12[120] | Staple | CCTGGCCAGAACGTGGACT CCAACGTCAAAGGGCGAA AAGGCAACAG |
| 4[230] | 6[231] | Staple | CTGCGGAATAAAAACCAA AATAGAGGACGTTG |
| 8[70] | 10[71] | Staple | GCAACTCACAGGGCTTAA GCTACTACGAGCCG |
| 6[87] | 4[88] | Staple | TGCAAGGCGCCGGAAACC AGGCAAAACGGCGG |
| 8[119] | 6[120] | Staple | GCCCTGGAGACAATGTCCC GCCAACCTCTTCG |
| 11[128] | 11[159] | Staple | TTTTCTTTTCACAGCTTGAT ACCGATAGTTGC |
| 8[159] | 8[128] | Staple | TCTTGACAAGAACCGGATA TTTTCTAATCTAT |
| 6[102] | 8[103] | Staple | GAAAGGGGAATTGTCAAC CTTATGTGACTCTA |
| 2[215] | 0[216] | Staple | GGCTTAGAATTTCGCAAAT GGTCAAGGCAAGG |
| 12[166] | 12[184] | Staple | AGCTTGCAGCCCTCATAGT TAGCGTAACGATCTAAAGT TGAGCCTTT |
| 8[183] | 6[184] | Staple | CTGGCTGATGAATAAGGCT TGCCCAACATTAT |
| 2[159] | 2[128] | Staple | AACTAAAGTACGGTGTCTG GAAGCAAACAAGA |
| 2[183] | 0[184] | Staple | TAGCTCAAGAACGAGTAG ATTTAGTAAAGCCT |
| 8[230] | 10[231] | Staple | AACTTTGGATAAATTGTGT CGAAGGCTTTGAG |
| 12[159] | 12[128] | Staple | TTTCGAGGTGAATTTCTTA AACCAGTGAGACG |

| | | | |
|---|---|---|---|
| 2[55] | 0[56] | Staple | AAAAACAGTCAACCGTTCT AGCTGCAATGCCT |
| 0[159] | 0[128] | Staple | TACCAAAAACATTATGACC CTGTAATACTTTT |
| 2[102] | 4[103] | Staple | CTAGCATTAATTCGCGTCT GGCCATTCTCCGT |
| 10[55] | 8[56] | Staple | AAGCCTGGTTGGTGTAATG AGTAAGTCGGTGG |
| 2[70] | 4[71] | Staple | AATCAGACATTTTTTAACC AATATAATGGGAT |
| 12[215] | 10[216] | Staple with elongation for cell membrane anchoring | CAA GCA GGC GAG CGG ACG AAC TTT TCTCCAAACGCTGAGGCTT GCAGGGACTTTTT |
| 12[55] | 10[56] | Staple with elongation for cell membrane anchoring | CAA GCA GGC GAG CGG ACG AAC TTT AGCAGGCGGAAACCTGTC GTGCCAAAAGTGTA |
| 4[183] | 2[184] | Staple with elongation for cell membrane anchoring | CAA GCA GGC GAG CGG ACG AAC TTT AACAGTTCCATCAAAAAG ATTAAGTAATGCTG |
| 4[55] | 2[56] | Staple with elongation for cell membrane anchoring | CAA GCA GGC GAG CGG ACG AAC TTT AGATGGGCTTTTGTTAAAT CAGCTAAAGCCCC |
| 12[87] | 10[88] | Staple with elongation for cell membrane anchoring | CAA GCA GGC GAG CGG ACG AACTTT GTTGCAGCGGCCAACGCG CGGGGAACAATTCC |
| 12[183] | 10[184] | Staple with elongation for cell membrane anchoring | CAA GCA GGC GAG CGG ACG AAC TTT AATTGTATACCATCGCCCA CGCATGTAAAATA |
| 4[215] | 2[216] | Staple with elongation for cell membrane anchoring | CAA GCA GGC GAG CGG ACG AAC TTT AAATATTCTTCAAATATCG CGTTTTTGCGGAT |
| 4[87] | 2[88] | Staple with elongation for cell membrane anchoring | CAA GCA GGC GAG CGG ACG AAC TTT ATTGACCGGGAACGCCATC AAAAAGTCAATCA |

| | | | |
|---|---|---|---|
| 4[255] | 3[255] | Staple with elongation for cell membrane anchoring | CAA GCA GGC GAG CGG ACG AAC TTT TGTTTAGACTGGATAGGCG AACCAGACCGGAA |
| 1[32] | 2[32] | Staple with elongation for cell membrane anchoring | CAA GCA GGC GAG CGG ACG AAC TTT ACCATCAATATGATATGAA GATTGTATAAGCA |
| 3[32] | 4[32] | Staple with elongation for cell membrane anchoring | CAA GCA GGC GAG CGG ACG AAC TTT AAAATTCGCATTAAATGCA TCGTAACCGTGCA |
| 9[32] | 10[32] | Staple with elongation for cell membrane anchoring | CAA GCA GGC GAG CGG ACG AAC TTT AACTCTGACCTCCTGGGGT GCCTAATGAGTGA |
| 10[255] | 9[255] | Staple with elongation for cell membrane anchoring | CAA GCA GGC GAG CGG ACG AAC TTT TAGCAACGGCTACAGAAT CCGCGACCTGCTCC |
| 2[255] | 1[255] | Staple with elongation for cell membrane anchoring | CAA GCA GGC GAG CGG ACG AAC TTT CTTTAATTGCTCCTTTTATT TTCATTTGGGGC |
| 12[255] | 11[255] | Staple with elongation for cell membrane anchoring | CAA GCA GGC GAG CGG ACG AAC TTT ACTAAAGGAATTGCGATTG CGGGATCGTCACC |
| 7[32] | 8[32] | Staple with elongation for cell membrane anchoring | CAA GCA GGC GAG CGG ACG AAC TTT CCAGGGTGGATGTTCTATA GGGGCCTTGAATC |
| 5[32] | 6[32] | Staple with elongation for cell membrane anchoring | CAA GCA GGC GAG CGG ACG AAC TTT GCCTCAGGAAGATCGCTCA CGACGTTGTAAAA |
| 6[255] | 5[255] | Staple with elongation for cell membrane anchoring | CAA GCA GGC GAG CGG ACG AAC TTT GCTCATTATACCAGTCCGA GAGGCTTTTGCAA |
| 11[32] | 12[32] | Staple with elongation for cell membrane anchoring | CAA GCA GGC GAG CGG ACG AAC TTT CCCGCTTTCCAGTCGGAAA ATCCTGTTTGATG |

| | | | |
|---|---|---|---|
| 8[255] | 7[255] | Staple with elongation for cell membrane anchoring | CAA GCA GGC GAG CGG ACG AAC TTT CAATCATAAGGGAACCATT TCAACTTTAATCA |

**Movie A3.1. Time lapse video showing origami exclusion from the cell spreading area.** A raw 6-min time lapse showing DOTS fluorescence signal change underneath the spreading OT-1 T-cells. In the video, three T-cells landed on the DOTS SLB surface and excluded DOTS from the spreading area resulting in a dark signal. The remaining DOTS clustered and centralized to form cSMAC. Scale bar = 5 μm

**Movie A3.2. Single molecule experiments showing the spatiotemporal dynamics of DOTS in the immune synapse.** A raw 5-min time lapse of OT-1 T-cells seeded on low density DOTS SLB surface. Left shows the single molecule DOTS signal and right is the RICM channel showing the T-cell spreading. Scale bar = 5 μm

**Movie A3.3. The distribution of F-actin and DOTS at the effector T-cell immune synapse.** Cell spreading (RICM channel), DOTS (red channel), LifeAct-GFP (green channel) were imaged, after 2 min of spreading, for a duration of 20 min. Scale bar = 5 μm

**Movie A3.4. 3D view of DOTS and tension patterns at the SSLB-T-cell interface.** The video represents a 360-degree rotation of the SSLB engaging an OT-1 naïve T-cell. Tension signal (gray channel) and DOTS Cy3B signal (green channel) of the SSLB were imaged after 30 min incubation with T-cell. Scale bar = 1 μm

# Chapter 4. LFA-1-ICAM mechanical force regulates T cell recognition and cytotoxic degranulation

Adapted from Ma, V.; Hu, Y.; Kellner, A.; Brockman, J.; Velusamy, A; Blanchard, A; Evavold, B; Alon, R and Salaita, K. The magnitude of LFA-1/ICAM-1 forces fine-tune TCR-triggered T cell activation. *Science Advances,* **2022**, 8, abg4485

Wang, M.; Hu, Y.; Sanchez, E.; Xie, X.; Roy, N.; Jesus, M.; Winer, B.; Zale, E.; Jin, W.; Sachar, C.; Lee, J.; Hong, Y.; Kim, M.; Kam, L.; Salaita, K. and Huse, M. *Nature Communications*, **2022**, 13, 3222

## 4.1 Abstract

The TCR mechanosensor model has been gaining prominence but it is important to emphasize that the intensity of T cell activation, function and developmental fate, are tuned by additional signaling of other immunoreceptors. T cell integrin-LFA-1 plays a critical role in physically stabilizing the interaction between T cells and APCs by binding to ICAM-1 ligands presented on the APC membrane. It has long been suspected that this receptor transmits and experiences forces as a part of normal T cell function. In this work, with DNA based tension sensors, we demonstrated that the LFA-1 transmit >12 pN forces to ICAM-1. The force potentiates TCR signaling and enhances the antigen discriminatory power of naïve T cells. Additionally, we found that LFA-1 forces are associated with cytotoxic degranulation. Disruption of these forces via depletion of the adaptor molecule talin abrogates cytotoxicity.

## 4.2 Introduction

The specific recognition of the pMHC by the TCR triggers initial T cell activation, yet the intensity of activation, and subsequent T cell function and developmental fate, is fine-tuned by additional ligations of multiple receptors, such as LFA-1, and CD28.[180, 181, 182] LFA-1 ($\alpha_L\beta_2$) plays a critical role in physically stabilizing the junction between T cells and their target antigen-presenting cells (APCs). In response to antigen stimulation of the TCR, the LFA-1 heterodimer adopts a high-affinity state that recognizes the broadly expressed ICAM-1 on target cell membrane to form the LFA-1/ICAM-1 complex at the cell-cell junction.[54, 183] This complex stabilizes transient T cell–APC interactions and hence sustains T cell activation. Given the role of LFA-1/ICAM-1 in mediating T cell adhesion, it has long been suspected that this ligand-receptor complex transmits and experiences forces as a part of normal T cell function. Most recently, Springer and others created a genetically encoded tension sensor and showed that the intracellular LFA-1 β2 subunit

experiences ~2 pN of force at the leading edge of migrating Jurkat lymphoblast.[184] However, the specific magnitude, timing, and location of LFA-1/ICAM-1 forces and the functional roles of these forces in tuning T cell activation and function remain unknown. Are the ~2-pN forces at the β2 intracellular domain transmitted across the plasma membrane and delivered to ICAM-1? More broadly, given that the TCR and LFA-1 receptors differentially engage cytoskeletal elements in the same cell, how are TCR and LFA-1 forces coordinated, and do these forces cooperate to mediate T cell activation and function?

In this chapter we used molecular probes to control and measure LFA-1 forces and reveal that the precise piconewton magnitude of tension fine-tunes TCR signaling and T cell function. Using DNA-based hairpin tension probes, we show that the LFA-1/ICAM-1 complex experiences force equal to or greater than 5 pN, with a small subset of LFA-1 transmitting forces that exceed 19 pN at the periphery of actively spreading T cells. We found that LFA-1 force signal is colocalized with the degranulation signal, suggesting that LFA-1 force regulates the cytotoxic degranulation for target cell killing. To study the role of LFA-1 force in T cell function, we used DNA tension gauge tethers (TGTs) to manipulate LFA-1 forces and demonstrated that LFA-1 forces potentiate TCR activation and enhance the sensitivity of the T cell response to antigen. Additionally, we knocked out adaptor protein talin, which links LFA-1 to the cytoskeleton, using CRISPR/Cas9 and observed a significant reduction of LFA-1 force signal. The abrogation of LFA-1 forces impeded T cell activation and cytotoxic killing. All together suggests LFA-1 is a mechanosensor and plays an important role in TCR signaling and subsequent cytotoxic degranulation.

## 4.3 Results and Discussion

### 4.3.1 Measuring LFA-1 force with DNA based tension sensors

We stimulated naïve OT-1 cells with soluble anti-CD3ε to activate LFA-1 and then immediately plated cells onto glass coverslips presenting dimeric ICAM-1 DNA hairpin tension sensors with a measured $F_{1/2}$ of 4.7 pN (note 4.7 pN is the measured $F_{1/2}$, and measurement was performed using the biomembrane force probe) .[72] Cell spreading and LFA-1 tension were quantified using RICM and epifluorescence microscopy, respectively. After ~3 to 4 min of seeding, OT-1 cells engaged and spread on the tension probe substrate and generated force signals underneath the cell contact area. Control ICAM-1 DNA duplexes lacking the stem loop did not generate fluorescence signal (**Figure 4.1a** and **4.1b**). Also, nonstimulated cells failed to spread, thus confirming that spreading is mediated by primed LFA-1 and the tension signal is driven by mechanical unfolding of the stem loop. To better define the magnitude of LFA-1 forces, we allowed OT-1 cells to adhere onto hairpin probes with a $F_{1/2}$ = 19 pN. Unexpectedly, although the cell adhesion footprint was similar to that of cells plated on $F_{1/2}$ = 4.7 pN probes, here, cells generated tension exclusively at the periphery (**Figure 4.1b**). Thus, the highest-magnitude LFA-1 forces are localized to the cell periphery, and this pattern is likely due to the inability of cells to transport the LFA-1/ICAM-1 because the probe was affixed onto the glass coverslip.

In addition to DNA hairpin tension sensors, we also used TGT tension sensor described above to further validate the conclusion. αCD3ε-primed cells were seeded on turn-on ICAM-1 TGT substrates. Fluorescence imaging confirmed that stimulated cells transmit sufficient forces through LFA-1 to rupture the 12-pN ICAM-1 TGTs (**Figure 4.1c** and **4.1d**). The probe rupture pattern was generally disorganized as the turn-on TGT reported an accumulated history of mechanical events and the cells were highly migratory. In contrast, we did not observe any turn-on TGT signal on the

56-pN probe surfaces (**Figure 4.1d**). Cells on this surface were also highly migratory and showed strong cell-substrate interaction as indicated by the spreading area. These results indicate that LFA-1 transmits forces >12 pN but <56 pN to ICAM-1 ligand.

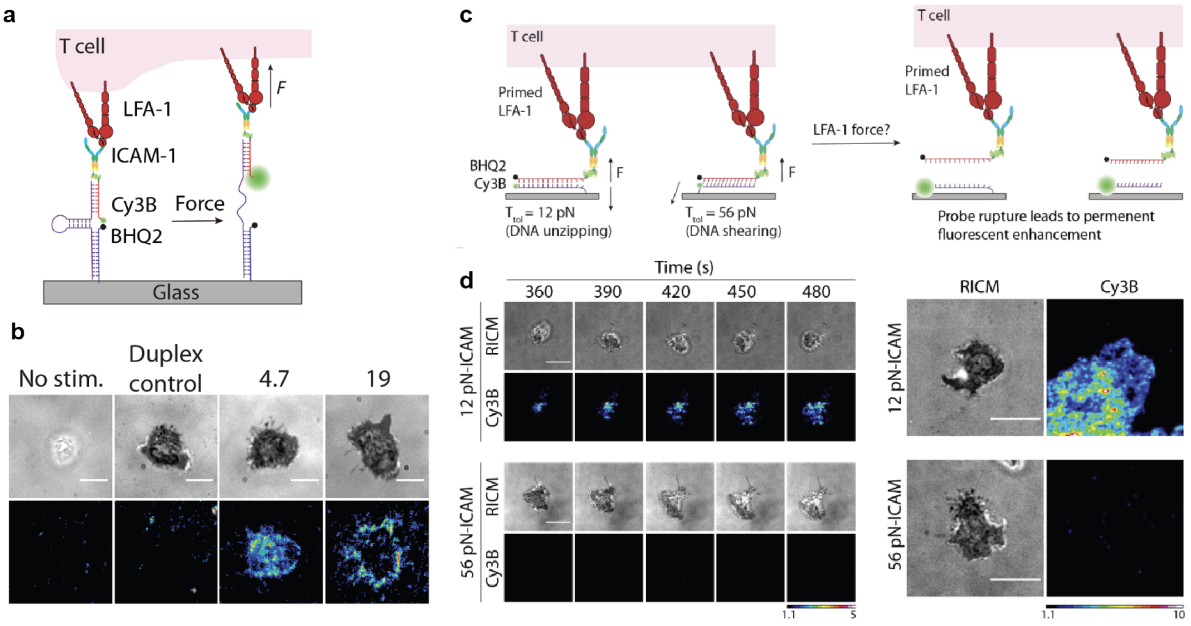


**Figure 4.1. Measuring LFA-1 force using DNA based tension sensors. a** Schematic showing DNA hairpin tension sensors presenting ICAM-1 on the top engage LFA-1 and detect forces at LFA-1-ICAM-1 bond with a fluorescence readout. **b** Representative microscope images showing the spreading and fluorescence signal of T cells plated on surfaces coated with different DNA probes. **c** Schematic showing the design of TGT tension sensors to measure LFA-1 forces with a fluorescence readout. **d** Time lapse images Representative RICM time-lapse images and the corresponding turn-on TGT signal of αCD3 primed OT-1 cells. These cells were seeded on 12 pN ICAM-1-TGT or 56 pN ICAM-1 TGT substrates, and we started recording the time-lapse movies at ~5 min. Scale bar = 5 μm.

### 4.3.2 Mechanical force through the LFA-1/ICAM-1 bond potentiate TCR signaling

We next examined how the magnitude of LFA-1 tension modulates T cell activation. Some literature suggests that LFA-1 is a co-receptor that augments T cell activation,[183, 185] while others indicate that LFA-1 primarily acts as an adhesion molecule.[186] We hoped to resolve this question and further elucidate the role of mechanics in the context of LFA-1 activation. To this end, we

manipulated the mechanical forces at LFA-1-ICAM bonds and tracked the change in early T cell activation markers (phosphorylated Zap70). We reused the TGT design above, not for detection purposes, but to control the force because the DNA duplex–anchored ligand can be mechanically ruptures at a threshold of tension, thus capping the force at LFA-ICAM bonds at the force tolerance of TGT (**Figure 4.2a**). We plated αCD3ε-primed OT-1 cells on dimeric ICAM-1 TGT surfaces. We observed that 56-pN ICAM-1 TGTs triggered more efficient T cell spreading compared to the 12-pN TGTs, indicating TGT ruptures and loss of LFA-1 engagement on 12 pN TGT surfaces (**Figure 4.2b** and **4.2c**). This is consistent with the DNA hairpin and TGT tension sensor results which showed LFA-1 force is above 12 pN. Interestingly, T cells seeded on 56-pN ICAM-1 TGTs displayed increased pY-ZAP70 staining across the entire membrane surface, while T cells on 12 pN TGTs showed minimal pY-ZAP70 activity (**Figure 4.2b** and **4.2d**). As ZAP70 phosphorylation is correlated to TCR signaling, this finding suggests that LFA-1 promotes T cell activation force by tuning TCR signaling.

Note T cells in these experiments were stimulated by anti-CD3. To validate this conclusion in the physiological context, we replaced anti-CD3 and instead immobilized pMHC antigen onto the glass surface while keeping ICAM-1 anchored on the TGT. The antigen density was tuned from ~0.1 to 100 molecules/$\mu m^2$ (**Figure 4.2e**). As expected, cells seeded on antigen surfaces lacking ICAM-1 showed minimal spreading and total pY-ZAP70 levels at all the tested antigen densities. ICAM-1 tethered through 56-pN TGT showed markedly increased cell spreading and enhanced total pY-ZAP70 levels compared to the 12 pN TGT surfaces (**Figure 4.2f-h**). Collectively, these data indicate that mechanically robust LFA-1/ICAM-1 bonds (i.e., ICAM-1 tethered to 56-pN TGT) act as amplifiers to strengthen early T cell signaling by enhancing and stabilizing cell spreading at the cell-substrate interface.

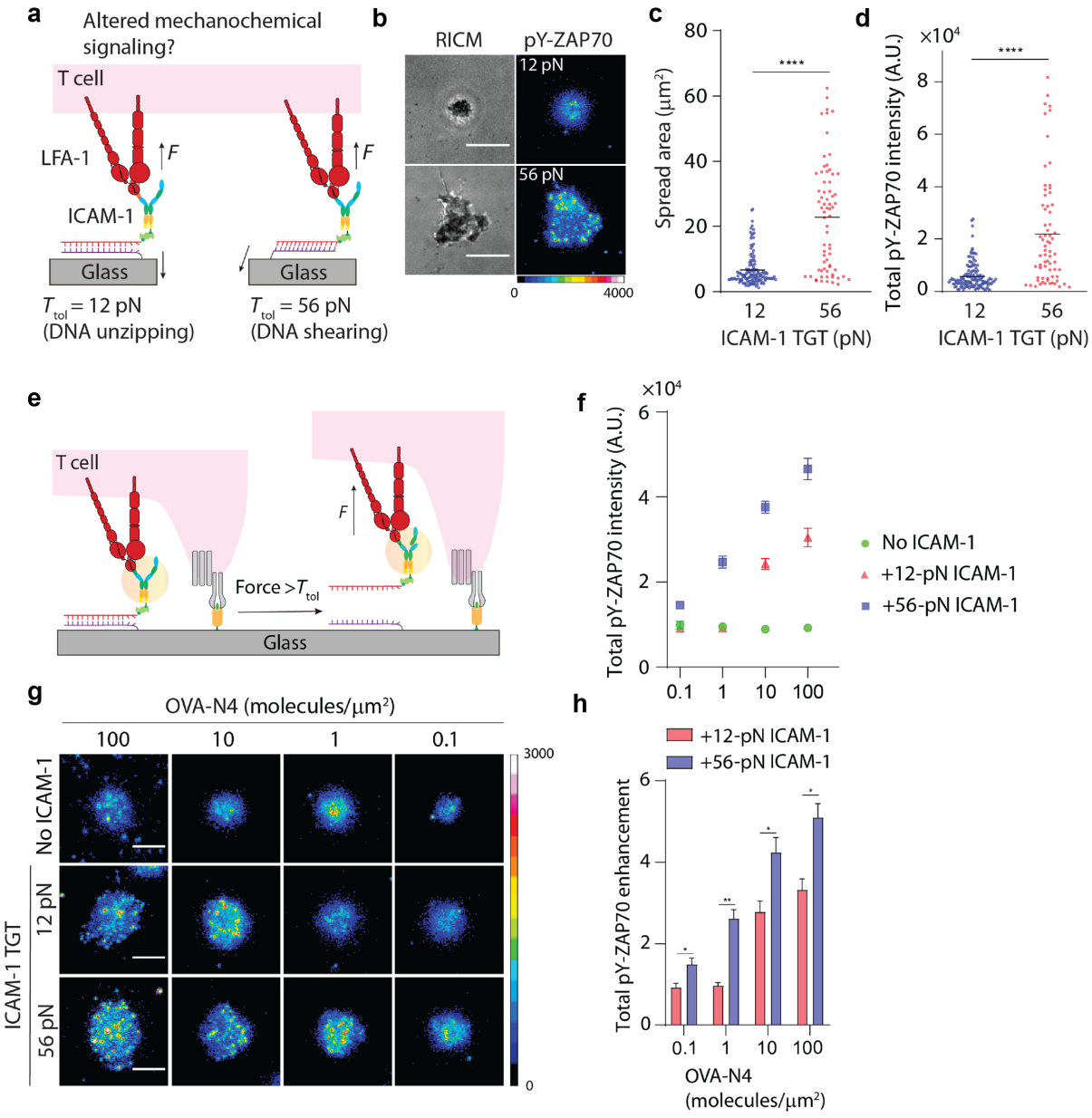


**Figure 4.2. Mechanochemical stabilization of LFA-1/ICAM-1 bonds potentiates TCR signaling. a** Schematic showing the design of TGT assays to cap maximal forces that can be transmitted to LFA-1/ICAM-1 bonds. **b** RICM and immunofluorescence images showing anti-CD3-primed naïve OT-1 cells spread on ICAM-1 TGT substrates after 1 hour of incubation. Cells were stained with Alexa Fluor 647–pY-ZAP70 antibody. **c** and **d** Quantification of spread area and pY-ZAP70 intensity of cells seeded on 12- or 56-pN ICAM-1 TGT substrates. n> 50 cells from three independent experiments. **e** Schematic showing the design of stimulatory surfaces presenting both ICAM-1 ligands (through the TGT) and immobilized agonist pMHC. **f** Quantification of pY-ZAP70 intensity of cells seeded on OVA-N4 only, OVA-N4 and 12-pN ICAM-1 TGT, or OVA-N4 and 56-pN ICAM-1 TGT substrates. **g** Immunostaining for pY-ZAP70 of cells seeded on

surfaces coated with immobilized OVA-N4, immobilized OVA-N4 and 12-pN ICAM1-TGT, or immobilized OVA-N4 and 56-pN ICAM-1 TGT. Antigen densities were varied from ~0.1 to ~100 molecules/$\mu m^2$. **h** Plot showing enhancement of pY-ZAP70 intensity of cells seeded on OVA-N4 and 12-pN ICAM-1 TGT or OVA-N4 and 56-pN ICAM-1 TGT substrates compared to those on antigen-only surfaces.

### 4.3.3 LFA-1 force potentiates antigen discrimination

Because LFA-1 mechanical force amplifies early T cell signaling by enhancing T cell sensitivity to its cognate antigen, we hypothesized that this force may also boost the discriminative power (i.e., selectivity) of the TCR. Here, we used a panel of altered peptide ligands (APLs) of the parental SIINFEKL pMHC (N4), and we tested whether the high-tension LFA-1/ICAM-1 bond augmented antigen discrimination. We choose three APLs that differ in single–amino acid substitution at the fourth position: Q4 (SIIQFEKL), T4 (SIITFEKL), and V4 (SIIVFEKL). These APLs represent a ~24-fold range of two-dimensional (2D) binding affinity and a ~680-fold range in functional avidity in the order of N4 > Q4 > T4 > V4.[187]

We prepared stimulatory surfaces as shown in **Figure 4.2e** and held the density of N4 or APLs at ~1 molecule/μm2. We found that the presence of LFA-1/ICAM-1 and the mechanical strength of this bond were critical in boosting early T cell activation (pY-ZAP70) for the cognate antigen as well as the APLs tested (**Figure 4.3a** and **Figure 4.3b**). To quantify the specificity of the T cell response to the APLs, we generated a plot where the reported functional avidity (median effective concentration of interferon-γ response) of each antigen[188] was plotted on the x axis and the pY-ZAP70 response measured here was plotted on the y axis (**Figure 4.3c)**. The slope of the 56-pN group was greater than that of the 12 pN and the no ICAM substrates. Given that the slope is an indicator of the specificity of the response, this experiment shows that the mechanical strength of the LFA-1/ICAM-1 further enhances the discriminatory power of TCR toward antigens with

different binding affinities. This conclusion is consistent with prior reports that showed TCR-pMHC forces in the 10- to 20-pN range boost the specificity of the TCR in distinguishing between APLs.[24, 85, 189]

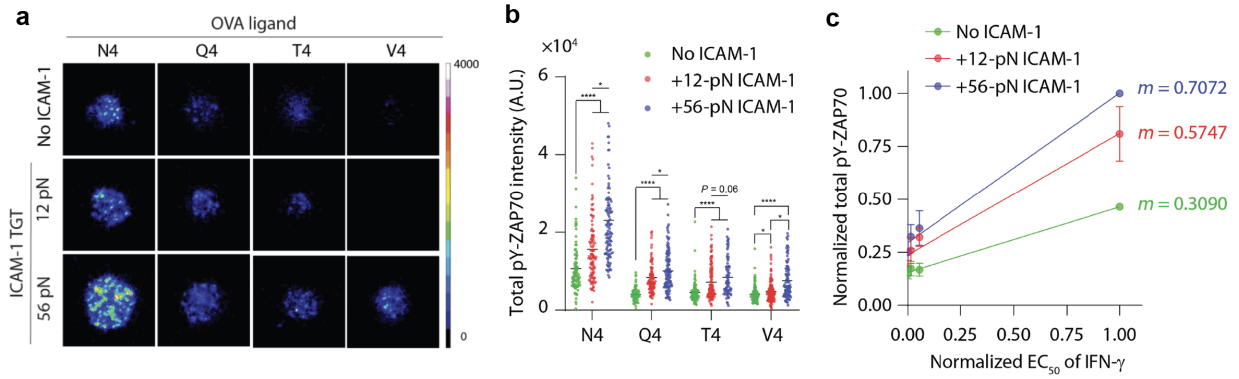


**Figure 4.3. LFA-1 force enhances antigen discrimination. a** Immunostained pY-ZAP70 images of OT-1 cells seeded on surfaces coated with immobilized antigen, immobilized antigen and 12 pN ICAM1-TGT, or immobilized antigen and 56 pN ICAM-1-TGT. Antigen densities was fixed at ~1 molecule/μm2. **b** Plot quantifying the total pY-ZAP70 intensity of cells seeded on surface coated with altered OVA-N4 or altered peptides, OVA-N4 or altered peptides plus 12-pN ICAM-1 TGT, and OVA-N4 or altered peptides plus 56-pN TGT. Antigen density was kept at ~1 molecule/μm2. **c** Plot of relative functional avidity of N4 or APLs against relative total pY-ZAP70–level cells engaging N4 or APLs in the presence (or not) with ICAM-1 TGTs. The slope (m) indicates the T cell sensitivity. *P < 0.05, **P < 0.01, ****P < 0.0001. n > 50 cells from three independent experiments. Error bar represents means ± SEM. Scale bars, 5 μm. Probe density = 400 to 500 molecules/$\mu m^2$.

### 4.3.4 Degranulation occurs in regions of LFA-1-dependent force exertion

Within the immunological synapse, both the TCR and LFA-1 are subjected to F-actin-dependent pulling forces, which are thought to drive the formation of catch bonds between each receptor and its respective ligand, promote conformational changes, and induce signal transduction.[162, 190, 191] Given the importance of these forces for the function of each receptor, we reasoned that they might also play a role in guiding cytotoxic secretion. To investigate this hypothesis, we employed multiplexed DNA hairpin based molecular tension probes (referred to as MTP in this section)

presenting ligand specific for the TCR and LFA-1. Each tension sensor comprised a stimulatory ligand (pMHC or ICAM-1) attached to a DNA hairpin containing a fluorophore at one end (Atto647N or Cy3B, respectively) and a quencher (BHQ-2) at the other (**Figure 4.4a**). Applied forces capable of unwinding the hairpin pull the quencher and fluorophore apart, dramatically increasing fluorescence. Consistent with prior reports,[85] surfaces coated with pMHC-MTPs and ICAM-1-MTPs induced IS formation by OT-1 CTLs and the exertion of dynamic forces through both LFA-1 and the TCR (**Figure 4.4b**), which we visualized by time-lapse imaging. To measure the association between degranulation and receptor-specific forces, we used CTLs expressing pHluorin-Lamp1 to record cytotoxic degranulation event (**Figure 4.4c**). The mean MTP fluorescence in the immediate vicinity of each event (2-μm box) was then compared with the mean fluorescence of the entire IS. This approach revealed a marked enrichment of ICAM-1-MTP signal in the degranulation zone (**Figure 4.4d**), indicative of a spatial correlation between cytotoxic secretion and force exertion through LFA-1. pMHC-MTP pulling was not associated with degranulation in this way (**Figure 4.4d**), arguing against a role for the TCR as a critical force-bearing receptor in this context. To further characterize the pattern of LFA-1 mechanics, we examined ICAM-1-MTP fluorescence along linescans bisecting the degranulation peak. Mean LFA-1 forces reached a local maximum in the 1 μm diameter region surrounding each event (**Figure 4.4e**), consistent with the idea that mechanically active LFA-1 defines permissive zones for cytotoxic secretion. A degranulation zone of this size would accommodate the approach of a typical lytic granule (0.5–1 μm in diameter).

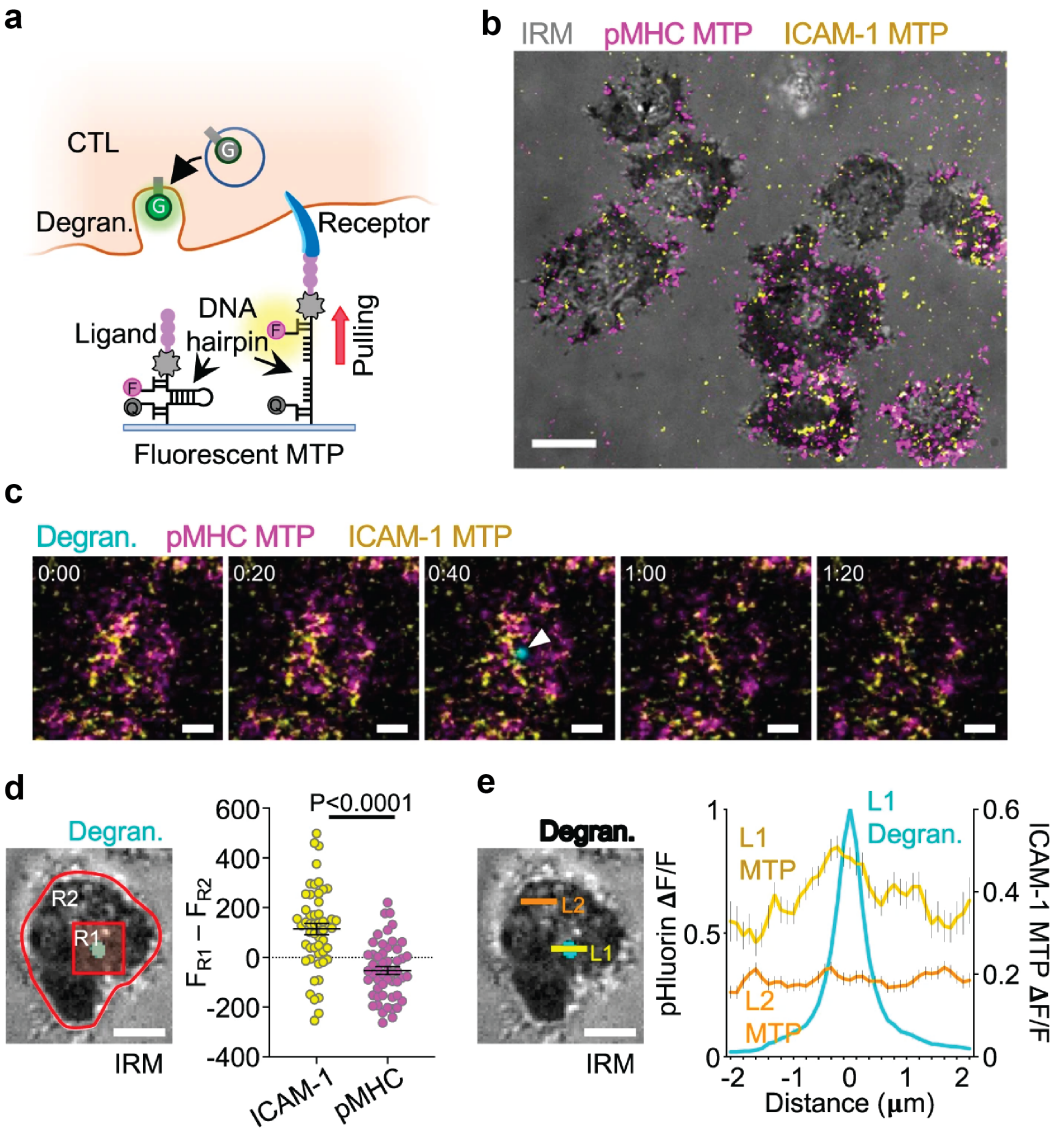


**Figure 4.4. LFA-1 pulling forces define degranulation domains. a** Measuring correlations between degranulation (Degran.) and receptor-specific pulling forces with MTPs. F fluorophore, Q quencher, G pHluorin. (b–e) OT-1 CTLs expressing pHluorin-Lamp1 were imaged by TIRF microscopy on glass surfaces coated with pMHC (H-2Kb-OVA) and ICAM-1 MTPs. **b** Representative image of pMHC-MTP and ICAM-1-MTP signals, overlaid onto the corresponding IRM image. Scale bar = 5 μm. **c** Time-lapse montage showing a representative degranulation event (indicated by a white arrowhead) together with pMHC-MTP and ICAM-1-MTP signals. Time in M:SS is shown at the top left corner of each image. Scale bars = 2 μm. **d** Left, image of a representative degranulation event, overlaid onto the corresponding IRM image. Regions defining the degranulation subdomain (R1) and the entire IS (R2) are indicated. Scale bar = 2 μm. Right, differences in mean fluorescence intensity between R1 and R2 at the moment of degranulation are shown for the indicated MTPs. N = 52 for each sample. Error bars signify SEM. P value calculated

by unpaired, two-tailed Student's t test. **e** Left, the image of a representative degranulation event, overlaid onto the corresponding IRM image. Linescans sampling the degranulating (L1) and inactive (L2) domains are indicated. Scale bar = 2 μm. Right, normalized ICAM-1-MTP fluorescence along L1 and L2 at the moment of degranulation (see "Methods"). The pHluorin-Lamp1 (Degran.) signal along L1 is shown for reference. Error bars signify SEM. N = 122 cells, pooled from two independent experiments. All other data are representative of at least two independent experiments.

### 4.3.4 LFA-1 force defines cytotoxic degranulation

Integrins are coupled to the cytoskeleton via talin, a mechanosensitive scaffolding protein that binds both the β-subunit tail and F-actin (**Figure 4.5a**).[192] To evaluate the importance of the integrin–cytoskeletal linkage for synaptic force exertion, we used CRISPR/Cas9 to deplete talin from OT-1 CTLs and then compared the physical output of these cells to that of controls expressing a nontargeting guide RNA. Although talin-deficient CTLs expressed normal levels of cell-surface LFA-1, their capacity to exert pulling forces against ICAM-1 MTPs was dramatically reduced (**Figure 4.5b** and **4.5c**). By contrast, pMHC-MTP pulling forces were unchanged (**Figure 4.5b** and **4.5c**), indicating that the mechanical contribution of talin is restricted to LFA-1 in this system. In cocultures with OVA-loaded RMA-s cells, CTLs lacking talin exhibited sharply reduced degranulation and target cell lysis (Figure **4.5d** and **4.5e**), implying a central role for integrin adhesions in both processes. These loss-of-function phenotypes were not rescued by PMA/Iono, indicating that they were not caused by impaired T-cell activation. It had only modest effects on CD69 responses (Figure **4.5f**). Talin depletion also suppressed CTL-target cell conjugate formation (Figure **4.5g**).

Talin not only couples integrins to the cytoskeleton (outside-in signaling) but also induces integrin extension into an intermediate affinity state (inside-out signaling).[156, 193] To demonstrate the role of talin-dependent force in cytotoxic degranulation, an experimental strategy was required that

could separate the cytoskeletal coupling function of talin from its capacity to drive integrin extension. Prior studies had demonstrated that the N-terminal head domain of talin mediates integrin binding and integrin activation, while the C-terminal rod domain associates with F-actin.[192] Accordingly, we retrovirally transduced CTLs lacking endogenous talin with a construct encoding the talin head, generating cells that effectively lacked only the talin rod (Figure **4.5h**). Introduction of talin head to talin-deficent CTLs restored their impaired adhesion to and migration on top of ICAM-1-coated surfaces, indicative of rescued integrin binding (inside-out signaling). The same strategy, however, completely failed to restore the mechanical activity of talin-deficient CTLs (Figure **4.5i** and **4.5j**), confirming the importance of talin-F-actin interactions for force exertion through integrins. CTLs lacking just the talin rod domain (talin CRISPR plus talin head) exhibited degranulation and conjugate defects that were indistinguishable from those of CTLs lacking the entire protein (Figure **4.5k** and **4.5l**). Taken together, these results indicate that outside-in mechanotransduction from LFA-1 to the cortical F-actin cytoskeleton is critical for IS mechanics and, cytotoxicity.

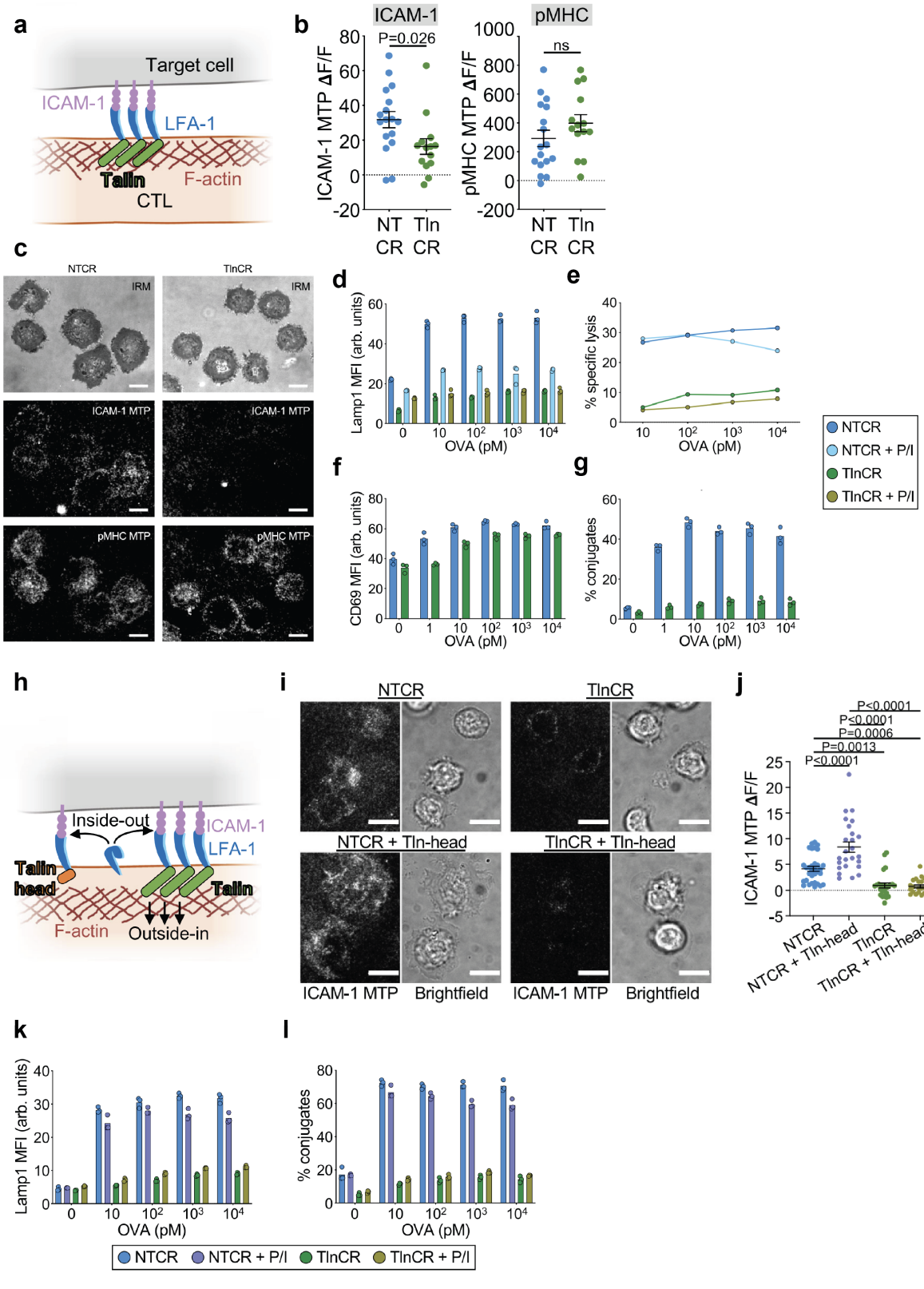
a
Target cell
ICAM-1
LFA-1
Talin
F-actin
CTL
b
ICAM-1
P=0.026
ICAM-1 MTP ΔF/F
NT CR
Tln CR
pMHC
ns
pMHC MTP ΔF/F
c
NTCR
TlnCR
IRM
ICAM-1 MTP
pMHC MTP
d
Lamp1 MFI (arb. units)
OVA (pM)
e
% specific lysis
NTCR
NTCR + P/I
TlnCR
TlnCR + P/I
f
CD69 MFI (arb. units)
g
% conjugates
h
Inside-out
ICAM-1
LFA-1
Talin head
Talin
F-actin
Outside-in
i
NTCR
TlnCR
NTCR + Tln-head
TlnCR + Tln-head
ICAM-1 MTP
Brightfield
j
P<0.0001
P<0.0001
P=0.0006
P=0.0013
P<0.0001
ICAM-1 MTP ΔF/F
NTCR
NTCR + Tln-head
TlnCR
TlnCR + Tln-head
k
Lamp1 MFI (arb. units)
OVA (pM)
l
% conjugates
NTCR
NTCR + P/I
TlnCR
TlnCR + P/I

**Figure 4.5. Talin dependent LFA-1 forces is required for CTL degranulation and cytotoxicity.** **a** Talin couples ligand-bound integrins to the F-actin cytoskeleton. b, c OT-1 Cas9 CTLs expressing talin gRNA (TlnCR) or control nontargeting gRNA (NTCR) were imaged on surfaces bearing the indicated stimulatory MTPs. **b** Representative images showing ligand-specific pulling in synapses. Scale bars = 5 μm **c** ICAM-1-MTP (left) and pMHC (H-2Kb-OVA)-MTP (right) signals, assessed 30 min after the addition of CTLs to the MTP surface. N ≥ 14 cells for each sample. **d–g** OVA-loaded RMA-s target cells were mixed with OT-1 Cas9 CTLs expressing talin gRNA (TlnCR) or control nontargeting gRNA (NTCR). PMA/Iono (P/I) was applied to some samples in order to drive TCR-independent CTL activation. **d** Lamp1 exposure (degranulation), measured 90 min after CTL-target cell mixing (N = 4 replicate experiments). **e** Target cell killing, measured 4 h after CTL-target cell mixing (N = 2 replicate experiments). **f** CD69 expression, measured 90 min after CTL-target cell mixing (N = 2 replicate experiments). **g** Conjugate formation, measured 90 min after CTL-target cell mixing (N = 2 replicate experiments). **h** The talin-head induces inside-out integrin activation without coupling integrins to the cytoskeleton (outside-in) **i** Representative brightfield and ICAM-1 MTP images. Scale bars = 10 μm. **j** Quantification of ICAM-1 MTP pulling forces, assessed 30 min after the addition of CTLs to the MTP surface. N ≥ 24 cells for each sample, representative of two independent experiments (k, l) OVA-loaded RMA-s target cells were mixed with OT-1 Cas9 CTLs expressing the indicated gRNAs ± Tln-head. **k** Lamp1 exposure (degranulation), measured 90 min after CTL-target cell mixing (N = 2 replicate experiments). **l** Conjugate formation measured 90 min after CTL-target cell mixing (N = 2 replicate experiments).

## 4.4 Conclusion

In this chapter, we demonstrated that LFA-1 is a mechanosensor, which experienced forces during T cell migration and regulate cell activities through mechanotransduction. Through DNA based tension sensors, we validated that LFA-1 transmits forces to the ICAM-1 with magnitudes that generally exceed 4.7 pN, and a subset of receptors, possibly high-affinity LFA-1/ICAM-1 bonds, is able to generate forces >19 pN. It's important to highlight that our force measurements align with the results obtained from biomembrane force probe experiments, which have shown that the LFA-1/ICAM-1 bond exhibits catch bond behavior around 10 pN.[190] By manipulating the force at LFA-1-ICAM bonds through DNA molecules, we found that the LFA-1 force is crucial to T cell spreading and ZAP70 phosphorylation, hallmark of TCR signaling. Mechanically stabilized LFA-1/ICAM-1 bonds (F > 12 pN) allow T cells to spread and signal more effectively at the cell-

substrate interface. Weak peptide ligands do not mechanically benefit from the TCR/LFA-1 crosstalk because these APLs fail to form sustained mechanical bonds with TCR when compared to the cognate antigen. Under this condition, LFA-1/ICAM-1 forces augmented antigen discrimination.

Apart from examining TCR signaling, we are also exploring the impact of LFA-1 force during the later stages of the T cell immune response, specifically focusing on cytotoxic degranulation. Within synaptic secretory zones, the integrin-mediated mechanical coupling between the CTL and target cell would enable the CTL to “feel” the presence of the target by pushing or pulling against it. Selective degranulation at sites of synaptic force exertion would thereby ensure that perforin and granzyme are released only in areas of close CTL-target cell apposition, minimizing risk to innocent bystander cells. We tracked the tension signal and degranulation events through DNA hairpin tension sensor and pH sensitive GFP, respectively, and found that degranulation spots are associated with LFA-1 mechanical events whereas TCR force is less involved. By knocking out talin from the CTL, we abrogated the force transduction from cytoskeleton to LFA-1 receptors and observed a reduction in degranulation and cytotoxic killing efficacy. Collectively, in this chapter, we measured LFA-1 forces and demonstrated their crucial role in T cell recognition and cytotoxic killing.

## 4.5 Materials and Methods

### 4.5.1 Chemicals and oligonucleotides

Reagents, unless otherwise specified, were purchased from Sigma-Aldrich (St. Louis, MO) and used as received. All solvents were of analytical grade and purified as needed. No. 1.5H coverslips (#10812) and sticky-Slide VI 0.4 (#80608) were purchased from ibidi (Fitchburg, WI). Cy3B–N-hydroxysuccinimide (NHS) ester (#PA63101) was purchased from GE Healthcare Life Sciences (Pittsburgh, PA). Azide-PEG4-NHS ester (#AZ-103) was obtained from Click Chemistry Tools (Scottsdale, AZ). RPMI 1640 and Dulbecco's modified Eagle's medium (DMEM) (#10-103-CV), heat-inactivated fetal bovine serum (FBS) (#35-015-CV), penicillin-streptomycin solution (#30-234-CI), and gentamicin sulfate solution (#30-005-CR) were purchased from Corning Mediatech (Corning, NY). Oligonucleotides (table S3) were obtained from Integrative DNA Technologies (Coralville, IA) and were purified either by reverse-phase high-performance liquid chromatography (HPLC) or standard desalting. Transfection grade linear polyethylenimine (#23966-1) was purchased from Polysciences Inc. (Warrington, PA). All buffer solutions were made with Milli-Q water (18.2 megohms cm−1) and passed through a 0.2-μm filtration system. Purified anti-mouse CD3ε (clone 145-2C11, #100302) was purchased from BioLegend (San Diego, CA). Alexa Fluor 647 Mouse Anti-ZAP70 (PY319)/Syk (PY352) (#557817) was obtained from BD Biosciences. H-2Kb monomer with the agonist OVA peptide SIINFEKL (OVA-N4) was obtained from the National Institutes of Health (NIH) Tetramer Core Facility (Emory University, Atlanta, GA, USA). The OVA-N4 peptide was synthesized on a Prelude peptide synthesizer (Gyro Protein Technologies) using fluorenylmethyloxycarbonyl chemistry and resuspended in Milli-Q water to 3 mM and sterile-filtered through a 0.22-mm syringe filter.

### 4.5.2 Methods

#### 4.5.2.1 Synthesis of dye-labeled DNA strand

The strand is prepared following a reported protocol. Briefly, a mixture of A21B (10 nmol) and excess Cy3B-NHS ester or Atto647N-NHS ester (50 μg) in 0.1 M sodium bicarbonate solution was allowed to react at RT overnight. The mixture was then subjected to P2 gel filtration to remove salts, organic solvent, and unreacted reactants and was further purified by reverse phase HPLC (solvent A: 0.1 M Triethylamine acetate, solvent B: acetonitrile; initial condition was 10% B with a gradient of 1%/min, flow rate: 1 ml/min). The product was characterized by MALDI-TOF mass spectrometry.

**Table A4.1: List of oligonucleotides used in this chapter**

| Name | Sequence (5' to 3') |
|---|---|
| A21B | /5AmMC6/ - CGC ATC TGT GCG GTA TTT CAC TTT - /3Bio/ |
| Quencher | /5DBCON/ - TTT GCT GGG CTA CGT GGC GCT CTT - /3BHQ_2/ |
| 4.7 pN hairpin strand | GTG AAA TAC CGC ACA GAT GCG TTT GTA TAA ATG TTT TTT TCA<br>TTT ATA CTT TAA GAG CGC CAC GTA GCC CAG C |
| 19 pN hairpin strand | GTG AAA TAC CGC ACA GAT GCG TTT CGC CGC GGG CCG GCG<br>CGC GGT TTT CCG CGC GCC GGC CCG CGG CGT TTA AGA GCG CCA<br>CGT AGC CCA GC |
| 4.7 pN loop complement | GTA TAA ATG AAA AAA ACA TTT ATA C |
| DBCO bottom strand (TGT) | /5DBCON/GT GTC GTG CCT CCG TGC TGT G |
| 12 pN top strand (TGT) | CAC AGC ACG GAG GCA CGA CAC /3Bio/ |
| 56 pN top strand (TGT) | /5Biosg/CA CAG CAC GGA GGC ACG ACA C |
| Biotin-BHQ2 (Top strand, turn-on TGT) | /5Biosg/ - CAC AGC ACG GAG GCA CGA CAC - /3BHQ2/ |

| | |
|---|---|
| 12 pN (Bottom strand, turn-on TGT) | /5UniAmM/ - GTG TCG TGC CTC CGT GCT GTG TTT TT - /3ThioMC3-D/ |
| 56 pN (Bottom strand, turn-on TGT) | /5ThioMC6-D/ - TTT TT/iUniAmM/ GTG TCG TGC CTC CGT GCT GTG |

#### 4.5.2.2 Harvest and purification of OT-1 cells

OT-1 TCR transgenic mice were housed and bred in the Division of Animal Resources Facility at Emory University in accordance with the Institutional Animal Care and Use Committee. OT-1 T cells express the CD8 co-receptor and specifically recognize chicken OVA epitope 257-264 (SIINFEKL) in the context of the MHC allele H-2Kb. For most experiments, naïve CD8+ T cells were enriched from the spleen of heterozygous OT-1 mice [except cells used in Figure 5 (H and I) that were obtained from homozygous OT-1 animals] using magnetic-activated cell sorting according to the manufacturer's instructions provided with the CD8a+ T cell Isolation Kit (Miltenyi Biotec, Germany). Briefly, a single-cell suspension of splenocytes was obtained and incubated with biotinylated antibodies specific for unwanted splenic cell populations. These populations were separated from the OT-1 T cells following incubation with antibiotin magnetic beads and enrichment on a magnetic column. Purified T cells were washed and resuspended in Hanks' balanced salt solution (HBSS) and kept on ice before experiment.

#### 4.5.2.3 Preparation of DNA hairpin-based molecular tension probes (MTP) on glass surfaces

No. 1.5H glass coverslips (ibidi) were sequentially sonicated in Milli-Q water (18.2 megohms cm−1) and 200 proof ethanol, 10 min each. The glass slides were rinsed copiously with Milli-Q

water and immersed in freshly prepared piranha solution (3:1 sulfuric acid:H2O2) for 30 min (CAUTION: Piranha is highly reactive and explosive on contact with organics!). The cleaned substrates were then rinsed with Milli-Q water in a 200-ml beaker at least six times and further washed with ethanol thrice. Slides were then transferred to a 200-ml beaker containing 3% 3-aminopropyltriethoxysilane (APTES) in ethanol for 1 hour, washed with ethanol thrice, and dried with N2. The slides were then mounted onto a six-channel microfluidic cells (Sticky-Slide VI 0.4, ibidi). To each channel, ~50 μl of NHS-PEG4-azide (10 mg/ml) (Click Chemistry Tools) in 0.1 M NaHCO3 (pH 9) was added and incubated for 1 hour. The channels were washed with 1 ml of Milli-Q water thrice, and then the remaining water in the channels was removed by pipetting. The surfaces were further blocked with 0.1% BSA in 1× PBS for 30 min and washed thrice with 1× PBS, and ~50 μl of solution was kept inside the channel to prevent drying. Subsequently, the hairpin tension probes were assembled in 1 M NaCl by mixing the Cy3B-labeled A21B strand (220 nM), quencher strand (220 nM), and hairpin strand (200 nM) in the ratio of 1.1:1.1:1. The mixture was heat-annealed at 95°C for 5 min and cooled down to 25°C over a 30-min time window. The assembled probe (~50 μl) was added to the channels (total volume = ~100 μl) and incubated overnight at RT. This strategy allows for covalent immobilization of the tension probes on azide-modified substrates via strain-promoted cycloaddition reaction. On the next day, the unbound DNA probes were removed with 3× PBS washes. Then, streptavidin (10 μg/ml) was added to the channels and incubated for 45 min at RT. The surfaces were cleaned with 3× PBS washes. Next, ICAM-1 ligand (5 μg/ml) was added to the surfaces, incubated for 45 min at RT, and washed thrice with 1× PBS. Surfaces were buffer-exchanged with HBSS before imaging.

Multiplex tension probes were prepared by a sequential click reaction. First, ~100 nM Atto647N tension probes were incubated with the BSA-blocked azide surface (prepared following the

abovementioned protocol) overnight at RT. On the next day, the unbound probes were washed three times with 1× PBS. Then, streptavidin (10 μg/ml) was added to the channels, incubated for 45 min at RT, and washed with 3× PBS. Subsequently, N4 (5 μg/ml) was incubated with the tension probes for 45 min at RT and washed with 3× PBS. After this wash, the volume of channels was kept at ~50 μl to prevent drying, and preannealed Cy3B tension probes were added to the channel and incubated overnight at RT. On the next day, the surfaces were washed with 3× PBS. The channels were washed with 3× PBS. Then, streptavidin (10 μg/ml) was added to the channels and incubated for 45 min at RT. The surfaces were cleaned with 1× PBS washes. Next, ICAM-1 ligand (5 μg/ml) was added to the surfaces, incubated for 45 min at RT, and washed thrice with 1× PBS. Surfaces were buffer-exchanged with HBSS before imaging.

#### 4.5.2.4 Preparation of conventional TGT substrates

Similar to the tension probe substrate preparation, the TGT probes were assembled in 1 M NaCl by mixing the top strand (biotin-labeled strand, 200 nM) and bottom strand (dibenzocyclooctyne (DBCO)-labeled strand, 200 nM) in a 1:1 ratio. The mixture was heat-annealed at 95°C for 5 min and then cooled to 25°C over a 30-min duration. The assembled TGT (~50 μl) was added to the channels and incubated overnight at RT. Biotinylated ICAM-1 or biotinylated OVA-N4 (5 μg/ml) was anchored on the TGT surfaces in the same way as mentioned in the previous section.

#### 4.5.2.5 Preparation of substrates copresenting ICAM-1 TGT and surface-immobilized antigen

No. 1.5H glass coverslips (ibidi) were sequentially sonicated in Milli-Q water (18.2 megohms cm−1) and 200 proof ethanol, 10 min each. The glasses were rinsed copiously with Milli-Q water and immersed in freshly prepared piranha solution (3:1 sulfuric acid:H2O2) for 30 min to remove

organic residues from and activate hydroxyl groups on glasses (CAUTION: Piranha is highly reactive and explosive on contact with organics!). The cleaned substrates were rinsed with Milli-Q water in a 200-ml beaker at least six times and further washed with ethanol thrice. Slides were then transferred to a 200-ml beaker containing 3% APTES in ethanol for 1 hour, washed with ethanol thrice, and thermally cured in an oven (~110°C) for 15 min. The slides were then mounted to six-channel microfluidic cells (Sticky-Slide VI 0.4, ibidi). To each channel, a solution of ~50 μl of NHS-PEG4-azide (10 mg/ml) and varying amount (0.001 to 1 mg/ml) of NHS-PEG4-biotin (ratio of azide:biotin = 10:1 to 10,000:1) in 0.1 M NaHCO3 (pH 9) was added and incubated for 1 hour.

The channels were washed with 1 ml of Milli-Q water thrice, and the remaining water in the channels was removed by pipetting. The surfaces were further blocked with 0.1% BSA in 1× PBS for 30 min and washed thrice with 1× PBS, and ~50 μl of solution was kept inside the channel to prevent drying. Subsequently, streptavidin (10 μg/ml) was added to the channels and incubated for 45 min at RT. The surfaces were cleaned with 3× PBS washes. Next, OVA-N4 ligand (5 μg/ml) or OVA-APL (e.g., Q4, T4, or V4) was added to the surfaces, incubated for 45 min at RT, and washed thrice with 1× PBS. Preassembled 100 nM TGT probe (12 or 56 pN) was then added to the channels and incubated overnight at RT. On the next day, unbound TGT probe was washed away with 3× PBS. Then, streptavidin (10 μg/ml) was added to the channels and incubated for 45 min at RT. The surfaces were cleaned with 3× PBS washes. Next, ICAM-1 (5 μg/ml) was added to the surfaces, incubated for 45 min at RT, and washed thrice with 1× PBS. Surfaces were buffer-exchanged with HBSS before imaging.

#### 4.5.2.6 Preparation of turn-on TGT substrates

The turn-on TGT substrates were prepared using identical protocol listed in the "Preparation of DNA hairpin-based molecular tension probes on glass surfaces" section until the APTES functionalization step. After functionalization of APTES, the slides were incubated with sulfosuccinimidyl 4-(N-maleimidomethyl)cyclohexane-1-carboxylate (sulfo-SMCC, 10 mg/mL) for 1 hour, washed with ethanol thrice, and dried under nitrogen. The slides were then mounted to six-channel microfluidic cells (Sticky-Slide VI 0.4, ibidi). Subsequently, the turn-on TGT probes were assembled in 1 M NaCl by mixing the fluorophore-labeled 12- or 56-pN bottom strands (100 nM) and the quencher strand (200 nM). The mixture was heat-annealed at 95°C for 5 min and cooled down to 25°C for 30 min. One hundred microliters of the assembled probe was reacted with 10 μM Tris(2-carboxyethyl)phosphine (1 μl, stock concentration = 1 mM) for 10 min to activate the thiol group. The annealed, thiol-activated duplexes were then added to channels, incubated for 1 hour at RT, and washed thrice with 1× PBS. Then, streptavidin (10 μg/ml) was added to the substrates and incubated for 45 min at RT and washed thrice with 1× PBS. Next, biotinylated OVA-N4/ICAM-1 (5 μg/ml) was added to the substrates, incubated for 45 min at RT, and washed thrice with 1× PBS. Surfaces were buffer-exchanged with HBSS before imaging.

#### 4.5.2.7 Retroviral transduction

Phoenix E cells were transfected with expression vectors and packaging plasmids using the calcium phosphate method. Ecotropic viral supernatants were collected after 48 h at 37 °C and added to $1.5 \times 10^6$ OT-1 blasts 24 h after primary peptide stimulation. Mixtures were centrifuged at 1400 × g in the presence of polybrene (4 μg/mL) at 35 °C, after which the cells were split 1:3 in RPMI medium containing 10% (vol/vol) FCS and 30 IU/mL IL-2 and allowed to grow for an additional 4–6 days.

#### 4.5.2.8 Immunofluorescence staining

A total of ~1 × 105 cells cultured on surfaces were fixed by 4% formaldehyde in 1× PBS for 10 min. The surfaces were gently washed thrice with 1× PBS to prevent cell detachment. Cells were then permeabilized in 0.1% Triton X-100 for 5 min and washed thrice with 1× PBS. Subsequently, 50 µl of 2% BSA was added to the surfaces and incubated overnight at 4°C (with a total volume of 100 µl inside the channel). On the next day, the surfaces were washed thrice with 1× PBS and ~50 µl of solution was kept inside the channel. Twenty microliters of the Alexa Fluor 647 Mouse Anti-ZAP70 (PY319)/Syk (PY352) was added to each channel and incubated for 1 hour at RT. Surfaces were then washed thrice with 1× PBS and buffer-exchanged with 1× HBSS before imaging.

#### 4.5.2.9 Image analysis

Fluorescence images were processed using the Fiji ImageJ software. Fluorescence background was subtracted. Cell spreading was measured by the total contact area of cell reflected by RICM. Fluorescence signal (e.g., tension probe signal or immunostained pY-ZAP70) was measured at the cell-substrate interface either by measuring the mean intensity (for tension probe data) or integrated intensity (for immunostaining data). Brightness and contrast of microscopy images were adjusted for presentation. In force/degranulation experiments, LFA-1 force were analyzed by comparing the mean fluorescence intensity of each MTP within the 2 × 2 µm box centered on a pHluorin-Lamp1 signal of interest with the mean fluorescence intensity of the MTP within the entire IS, defined by threshold masking of IRM images (Figure 5d). Linescan analysis of ICAM-1-MTP fluorescence at degranulation sites (Figure 5e) was performed by generating a series of 2-µm linescans bisecting degranulation events of interest. The linescan intensities were aligned around the degranulation, averaged over each pixel, and normalized per linescan. An analogous

set of control linescans, collected from parts of the IS lacking degranulation events, were processed in parallel using the same scripts.

#### 4.5.2.10 Statistics

All experiments were conducted as at least three technical and biological replicates. All tests were performed in Prism 7 (GraphPad Software), and data were presented as means ± SEM or scatter plots showing all data points with line representing mean. Unless otherwise stated, groups were compared using Student's t test.

# Chapter 5. Summary and Perspective

## 5.1 Summary

This dissertation started with a discussion of mechanosensor model for explaining the ultrasensitivity and specificity of TCR signaling. The model posits that the force acting on receptor-ligand bonds extends the bond lifetime of stimulatory TCR-pMHC bonds. Prolonged lifetime facilitates a cascade of phosphorylation signaling pathways, ending up activating T cells. Subsequently, I introduced a range of tools developed for measuring the mechanical forces exerted by T cells. These tools include TFM and PDMS pillar assays, which enable the measurement of cell traction forces at the cellular level. Additionally, molecular tension sensors based on polymers, peptides, and DNA have been discussed, as they offer the capability to measure forces at individual receptor-ligand bonds. Among them, DNA-based tension sensors have gained prominence in this regard due to their exceptional performance attributes, including well-characterized mechanical properties, ease of modification, and high programmability. I summarized the advances of DNA based tension sensors in detecting, resolving and quantifying cell mechanical forces. Despite its popularity, application of DNA for mapping forces in T cell system is still limited because of many supraphysiological features of the setup including substrate stiffness, geometry, and fluidity. The focus of my thesis is to develop next generation DNA tension sensors for better quantification of T cell force and also engineer DNA as a tool to manipulate receptor forces to understand their role in T cell immune responses.

To measure TCR forces, DNA tension sensors are typically labeled with antigens and immobilized on a planar synthetic substrate, often a glass coverslip, to simulate the APC/target cell membrane. However, cells do not adopt a planar shape; instead, they can form curved junctions with T cells. Given this consideration, the primary objective of the first project described in **Chapter 2** of the dissertation was to replace the flat coverslip substrate with a microparticle-based platform named

μTS. This change aimed to better mimic the characteristics of target cells and investigate potential differences in cell mechanics in response to alterations in curvature. In this chapter, I demonstrated that TCRs transmit forces within a range of 12 to 56 pN to antigens. Notably, TCRs at the periphery of the spreading area exhibited greater mechanical activity, exerting higher forces compared to TCRs located in the center. These force signals were found to be colocalized with F-actin, suggesting a mechanism for force generation that depends on F-actin. Additionally, μTS was utilized to measure the forces experienced by integrin receptors on mouse platelets, revealing that integrins are capable of transmitting forces exceeding 56 pN. Due to the small size of μTS and its ability to interact with platelets in suspension, tension signals carried by μTS could be analyzed using flow cytometry, offering a rapid and high-throughput readout that proves beneficial for anti-platelet drug screening purposes. Unfortunately, this high-throughput quantification approach did not prove effective for measuring TCR forces because, in T cell experiments, μTS was not in suspension but instead anchored to a coverslip to facilitate DNA and ligand modifications. Additionally, though this design makes the force measurement more physiologically relevant by providing a curved geometry, there are still some problems such as surface fluidity and stiffness awaiting to be solved.

Moving forward, **chapter 3** advances the quest for more physiological force measurements by introducing DNA origami tension sensors (DOTS), which are anchored onto fluid membranes allowing to investigate the TCR mechanics at dynamic intermembrane junctions.. In comparison to traditional molecular tension sensors, DOTS possess dimensions that impose a minimum separation of over 40 nm between FRET pairs. This effectively eliminates potential crosstalk between adjacent tension sensors within the TCR cluster, thereby enhancing the accuracy of force measurements. With this platform, I demonstrated that TCRs experience forces exceeding 8 pN at

fluid junctions. The magnitude of these forces is influenced by antigen fluidity and the cell state. Furthermore, my findings indicated that these forces are primarily driven by actin protrusions and are less dependent on myosin contraction. Additionally, I observed that a size mismatch between proteins at the immune synapse places strain on TCR-pMHC bonds, which also contributing to force generation. Minimizing the mismatch by increasing the height of the pMHC reduced the force at TCR-pMHC bonds and hindered subsequent TCR signaling. To address the challenge of achieving high-throughput quantification of TCR forces, which was not feasible with the μTS design, I created a spherical supported lipid bilayer (SLB) platform coated with DOTS. This platform allowed for the investigation of TCR mechanics in suspension and demonstrated significant potential for high-throughput quantification of TCR forces, particularly in the context of antigen screening. Lastly, moving away from synthetic substrates, DOTS were anchored directly onto authentic cell membranes. This approach revealed that TCRs transmit forces of approximately 8 pN to antigens at the physiological immune synapse. This discovery provides strong support for the mechanosensor model, reinforcing the notion that TCRs are indeed mechanosensors capable of exerting mechanical forces to facilitate T cell signaling.

TCR forces play a crucial role in regulating TCR signaling, ultimately enhancing the specificity of T cell immune responses. Recent research has suggested that other receptors on the T cell membrane are also sensitive to mechanical forces and work in tandem with the TCR to modulate TCR activities. To test whether these receptors also transmit forces to their ligands and leverage the forces to regulate T cell immune response, in **chapter 4** I used DNA tension sensors to investigate the mechanics of LFA-1-ICAM bonds. It was found that T cell generate and transmit up to 19 pN forces to LFA-1-ICAM ligands. The magnitude of the force fine tunes TCR signaling and help TCR discriminate antigens. Furthermore, LFA-1 forces are associated with degranulation

events. Abrogation of LFA-1 force by knocking talin reduced the degranulation and the cytotoxic killing efficiency.

Taken together, this dissertation aimed to validate the emerging mechanosensor model which postulates that mechanical force plays a crucial role in regulating the specificity and sensitivity of T cell immune response. Leveraging the capabilities of DNA nanotechnology, I successfully quantified the mechanical forces experienced by key immunoreceptors, including TCR and LFA-1. The results align with the catch-bond model and underscore the significant role of force in regulating T cell immune responses. The findings presented in this dissertation hold the potential to drive advancements in the burgeoning field of mechanobiology and offer valuable insights into the development of mechanically based immunotherapies to enhance the efficacy.

## 5.2 Future outlook

### 5.2.1 How target cell tunes mechanotransduction at the immune synapse

I have established that the generation of force at TCR-antigen bonds in the immune synapse is influenced by two key factors: actin protrusion and the physical repulsion of proteins at the IS. These two factors are centered on the T cell itself. Research has shown that the mechanical properties of the substrate on which T cells spread can also modulate T cell mechanics and subsequently impact their functionality.[144, 194, 195] This discovery has been harnessed in the field of immunotherapy to enhance T cell immune responses and generate functionally distinct T cell populations by exposing T cell to substrates with different stiffness, aiming to improve therapeutic outcomes.[196] Recently, Lei et al. utilized TFM to demonstrate that T cells exert higher traction forces when adhering to stiffer gel substrates. Furthermore, when interacting with softer B16 cells, T cells exhibited reduced levels of phosphorylation of proline-rich tyrosine kinase 2 (Pyk2), a focal adhesion kinase that has been positively correlated with cellular forces.[59] However, the exact

mechanism how the target cell stiffness influences the strength of TCR-antigen forces remains unclear. Considering that DOTS demonstrates robust performance in visualizing molecular cell forces at the T cell-target cell junctions, it presents a valuable approach for unraveling the relationship between target cell stiffness and TCR mechanics. This, in turn, offers valuable insights for the field of mechanical immunoengineering.

### 5.2.2 How ligand spacing influences mechanotransduction

Previous research has indicated that T cell activation is impacted by ligand density and spacing, yet the underlying mechanisms remain unclear.[197, 198, 199] One hypothesis is that the spacing of ligand affects the rearrangement of the cytoskeleton, potentially modulating force transduction, which, as per my findings, can influence signaling. Investigating alterations in mechanical forces under various ligand spacing conditions is of particular interest. DNA origami, known for its programmability, has been employed to pattern ligands for the study of immune cell signaling. In pursuit of this goal, we can employ the DOTS design to regulate the spacing between ligands while concurrently examining the behavior of the cytoskeleton and alterations in mechanical forces.

### 5.2.3 Signal amplification

Although DNA based tension sensors exhibit high quenching efficiency, given the low expression level of immunoreceptor on the T cell membrane and the short lifetime of force events, the signal to background ratio of the tension sensors is low. Moreover, their use is limited and requires specialized microscopy equipment for characterization. To promote the exploration of immune mechanobiology and facilitate its adoption by clinical laboratories lacking access to high-resolution microscopes, it becomes crucial to create sensitive assays that generate a strong signal, one that can be easily measured using simple instruments like a microplate reader. In our laboratory, we harnessed the DNA hybridization chain reaction and Cas12a system to amplify the force signal

detected by DNA force probes.[123, 124] These techniques also have the potential to enhance the detection of immunoreceptor forces in immune cells.

### 5.2.4 Leveraging mechanical force for drug delivery and cell therapy

DNA molecules are not only used as a force sensor but also an efficient drug delivery platform. Interestingly, the binding affinity between encapsulated drug and DNA is highly sensitive to external force. Stejskalova et al. have demonstrated that pN scale forces can regulate the binding affinity between the growth factor and its corresponding DNA aptamer by ten to twelve orders of magnitude.[200] Lei et al. recently showed that T-cell force can unzip DNA TGT on the silica beads and release drug preloaded in the mesopores.[201] These findings suggest that cellular forces at immune synapse between T-cell and target cell can be harnessed to unwind force responsive DNA nanostructures encapsulating adjuvant/anticancer drugs and control drug release in a mechanically selective manner to enhance therapeutic outcomes in immunotherapy.

## 5.3 Closing Remarks

As an emerging field, immune-mechanobiology has garnered significant attention. T cells have been shown to be highly sensitive to mechanical cues, for example, exhibiting different behaviors on substrates of varying stiffness. Researchers have utilized these findings to stimulate T cells or modulate their functions in an effort to enhance the efficacy of adoptive immunotherapy. Nevertheless, there exists a significant gap in our understanding of the exact mechanisms through which mechanical forces impact various T cell functions, including antigen recognition, cytokine secretion, degranulation, and proliferation. This knowledge gap poses a substantial obstacle to the development of mechanical approaches for modulating T cell functions. The mechanosensor model, which proposes that mechanical forces can alter the conformation of the TCR-antigen complex and thereby enhance TCR signaling by prolonging its lifetime, has been suggested.

However, there has been a lack of direct evidence supporting the notion that mechanical force exists at the TCR-antigen bonds. Additionally, questions remain regarding the magnitude of such forces and whether they are sufficiently robust to induce these conformational changes to enhance TCR-pMHC binding.

Over the past few decades, the development of molecular tension sensors has provided a means to measure the forces at receptor-ligand bonds. Among these sensors, DNA-based tension sensors are highly programmable and can be easily integrated with existing DNA technologies. This not only allows for the measurement of forces experienced by TCR but also enables the detection and manipulation of these forces at the molecular level. This innovative approach holds great promise for elucidating the role of mechanical force in T cell activation. Such research has the potential to significantly advance the field of immune-mechanobiology and provide essential insights and guidelines for the emerging field of mechanically assisted immunotherapy.

## 6. Bibliography


1. Belardi, B. *et al*. Cell-cell interfaces as specialized compartments directing cell function. *Nat Rev Mol Cell Biol* **21**, 750-764 (2020).
2. Huse, M. Mechanical forces in the immune system. *Nat Rev Immunol* **17**, 679-690 (2017).
3. Dustin, M.L. The immunological synapse. *Cancer Immunol Res* **2**, 1023-1033 (2014).
4. Huppa, J.B. *et al.* T-cell-antigen recognition and the immunological synapse. *Nat Rev Immunol* **3**, 973-983 (2003).
5. Irvine, D.J. *et al.* Direct observation of ligand recognition by T-cells. *Nature* **419**, 845-849 (2002).
6. Siller-Farfan, J.A. *et al.* Molecular mechanisms of T cell sensitivity to antigen. *Immunol Rev* **285**, 194-205 (2018).
7. Vining, K.H. *et al.* Mechanical forces direct stem cell behaviour in development and regeneration. *Nat Rev Mol Cell Biol* **18**, 728-742 (2017).
8. Hoffman, B.D. *et al.* Dynamic molecular processes mediate cellular mechanotransduction. *Nature* **475**, 316-323 (2011).
9. Chen, W. *et al.* Mechanical regulation of T-cell functions. *Immunol Rev* **256**, 160-176 (2013).
10. Rossy, J. *et al.* Role of Mechanotransduction and Tension in T Cell Function. *Front Immunol* **9**, 2638 (2018).
11. Wahl, A. *et al.* Biphasic mechanosensitivity of T cell receptor-mediated spreading of lymphocytes. *Proc Natl Acad Sci U S A* **116**, 5908-5913 (2019).
12. Saitakis, M. *et al.* Different TCR-induced T lymphocyte responses are potentiated by stiffness with variable sensitivity. *Elife* **6** (2017).
13. Gaud, G. *et al.*Regulatory mechanisms in T cell receptor signalling. *Nat Rev Immunol* **18**, 485-497 (2018).
14. Stinchcombe, J.C. *et al.* Secretory mechanisms in cell-mediated cytotoxicity. *Annu Rev Cell Dev Biol* **23**, 495-517 (2007).
15. Sanchez, E.E. *et al.* Apoptotic contraction drives target cell release by cytotoxic T cells. *Nat Immunol* **24**, 1434-1442 (2023).
16. Feng, Y. *et al.* alphabeta T Cell Receptor Mechanosensing Forces out Serial Engagement. *Trends Immunol* **39**, 596-609 (2018).
17. Huang, J. *et al.* A single peptide-major histocompatibility complex ligand triggers digital cytokine secretion in CD4(+) T cells. *Immunity* **39**, 846-857 (2013).
18. Lyons, D.S. *et al.* A TCR Binds to Antagonist Ligands with Lower Affinities and Faster Dissociation Rates Than to Agonists. *Immunity* **5**, 53-61 (1996).

19. Mckeithan, T.W. Kinetic proofreading in T cell receptor signal transduction. *Proc Natl Acad Sci U S A* **92**, 5042-5046 (1995).

20. Lo, W.L. *et al.* Adapting T Cell Receptor Ligand Discrimination Capability via LAT. *Front Immunol* **12**, 673196 (2021).

21. Chakraborty, A.K. *et al.*Insights into the initiation of TCR signaling. *Nat Immunol* **15**, 798-807 (2014).

22. Mustelin, T. *et al.* Protein tyrosine phosphatases and the immune response. *Nat Rev Immunol* **5**, 43-57 (2005).

23. Kalergis, A.M. *et al.* Efficient T cell activation requires an optimal dwell-time of interaction between TCR and the pMHC complex *Nat Immunol* **2**, 229-234 (2001).

24. Liu, B. *et al.* Accumulation of dynamic catch bonds between TCR and agonist peptide-MHC triggers T cell signaling. *Cell* **157**, 357-368 (2014).

25. Zhu, C. *et al.* Mechanosensing through immunoreceptors. *Nat Immunol* **20**, 1269-1278 (2019).

26. Choi, H.K. *et al.* Catch bond models may explain how force amplifies TCR signaling and antigen discrimination. *Nat Commun* **14**, 2616 (2023).

27. Das, D.K. *et al.* Force-dependent transition in the T-cell receptor beta-subunit allosterically regulates peptide discrimination and pMHC bond lifetime. *Proc Natl Acad Sci U S A* **112**, 1517-1522 (2015).

28. Feng, Y. *et al.* Mechanosensing drives acuity of alphabeta T-cell recognition. *Proc Natl Acad Sci U S A* **114**, E8204-E8213 (2017).

29. Kim, S.T. *et al.* The alphabeta T cell receptor is an anisotropic mechanosensor. *J Biol Chem* **284**, 31028-31037 (2009).

30. Huang, J. *et al.* The kinetics of two-dimensional TCR and pMHC interactions determine T-cell responsiveness. *Nature* **464**, 932-936 (2010).

31. Zhao, X. *et al.* Tuning T cell receptor sensitivity through catch bond engineering. *Science* **376**, eabl5282 (2022).

32. Yin, Y. *et al.* Structural basis for self-recognition by autoimmune T-cell receptors. *Immunol Rev* **250**, 32-48 (2012).

33. Korem Kohanim, Y. *et al.* Endocrine Autoimmune Disease as a Fragility of Immune Surveillance against Hypersecreting Mutants. *Immunity* **52**, 872-884 e875 (2020).

34. Sun, Z.J. *et al.* Mechanisms Contributing to T Cell Receptor Signaling and Assembly Revealed by the Solution Structure of an Ectodomain Fragment of the CD3ey Heterodimer. *Cell* **105**, 913-923 (2001).

35. Kjer-Nielsen, L. *et al.* Crystal structure of the human T cell receptor CD3 epsilon gamma heterodimer complexed to the therapeutic mAb OKT3. *Proc Natl Acad Sci U S A* **101**, 7675-7680 (2004).

36. Yin, Y. *et al.* Crystal structure of a complete ternary complex of T-cell receptor, peptide-MHC, and CD4. *Proc Natl Acad Sci U S A* **109**, 5405-5410 (2012).

37. Dong *et al.* Structural basis of assembly of the human T cell receptor-CD3 complex. *Nature* **573**, 546-552 (2019).

38. Susac, L. *et al.* Structure of a fully assembled tumor-specific T cell receptor ligated by pMHC. *Cell* **185**, 3201-3213 e3219 (2022).

39. Notti, R.Q. *et al.* The resting state of the human T-cell receptor. *bioRxiv* (2023).

40. Klieger, Y. *et al.* Unique zeta-chain motifs mediate a direct TCR-actin linkage critical for immunological synapse formation and T-cell activation. *Eur J Immunol* **44**, 58-68 (2014).

41. Wu, P. *et al.* Mechano-regulation of Peptide-MHC Class I Conformations Determines TCR Antigen Recognition. *Mol Cell* **73**, 1015-1027 e1017 (2019).

42. Brazin, K.N. *et al.* The T Cell Antigen Receptor alpha Transmembrane Domain Coordinates Triggering through Regulation of Bilayer Immersion and CD3 Subunit Associations. *Immunity* **49**, 829-841 e826 (2018).

43. Chen, Y. *et al.*Receptor-mediated cell mechanosensing. *Mol Biol Cell* **28**, 3134-3155 (2017).

44. Clarke, D.N. *et al.* Actin-based force generation and cell adhesion in tissue morphogenesis. *Curr Biol* **31**, R667-R680 (2021).

45. Pollard, T.D. *et al.* Cellular Motility Driven by Assembly and Disassembly of Actin Filaments. *Cell* **112**, 453-465 (2003).

46. Koestler, S.A. *et al.* Differentially oriented populations of actin filaments generated in lamellipodia collaborate in pushing and pausing at the cell front. *Nat Cell Biol* **10**, 306-313 (2008).

47. Mehidi, A. *et al.* Forces generated by lamellipodial actin filament elongation regulate the WAVE complex during cell migration. *Nat Cell Biol* **23**, 1148-1162 (2021).

48. Footer, M.J. *et al.* Direct measurement of force generation by actin filament polymerization using an optical trap. *Proc Natl Acad Sci U S A* **104**, 2181-2186 (2007).

49. Kovar, D.R. *et al.* Insertional assembly of actin filament barbed ends in association with formins produces piconewton forces. *Proc Natl Acad Sci U S A* **101**, 14725-14730 (2004).

50. Finer, J.T. *et al.*Single myosin molecule mechanics: piconewton forces and nanometre steps *Nature* **368**, 113-119 (1994).

51. Molloy, J.E. *et al.* Movement and force produced by a single myosin head. *Nature* **378**, 209-212 (1995).

52. Barda-Saad, M. *et al.* Dynamic molecular interactions linking the T cell antigen receptor to the actin cytoskeleton. *Nat Immunol* **6**, 80-89 (2005).

53. Ngoenkam, J. *et al.*Selected signalling proteins recruited to the T-cell receptor-CD3 complex. *Immunology* **153**, 42-50 (2018).

54. Walling, B.L. *et al.* LFA-1 in T Cell Migration and Differentiation. *Front Immunol* **9**, 952 (2018).

55. Al-Aghbar, M.A. *et al.*The interplay between membrane topology and mechanical forces in regulating T cell receptor activity. *Commun Biol* **5**, 40 (2022).

56. James, J.R. *et al.* Biophysical mechanism of T-cell receptor triggering in a reconstituted system. *Nature* **487**, 64-69 (2012).

57. Pettmann, J. *et al.* Mechanical forces impair antigen discrimination by reducing differences in T-cell receptor/peptide-MHC off-rates. *EMBO J* **42**, e111841 (2023).

58. Colin-York, H. *et al.* Cytoskeletal Control of Antigen-Dependent T Cell Activation. *Cell Rep* **26**, 3369-3379 e3365 (2019).

59. Lei, K. *et al.* Cancer-cell stiffening via cholesterol depletion enhances adoptive T-cell immunotherapy. *Nat Biomed Eng* **5**, 1411-1425 (2021).

60. Colin-York, H. *et al.* The future of traction force microscopy. *Current Opinion in Biomedical Engineering* **5**, 1-5 (2018).

61. Kumari, A. *et al.*Traction Force Microscopy to Study B Lymphocyte Activation. *J Vis Exp* (2020).

62. Lam, W.A. *et al.* Mechanics and contraction dynamics of single platelets and implications for clot stiffening. *Nat Mater* **10**, 61-66 (2011).

63. Hu, K.H. *et al.* T cell activation requires force generation. *J Cell Biol* **213**, 535-542 (2016).

64. Schoen, I. *et al.*Probing cellular traction forces by micropillar arrays: contribution of substrate warping to pillar deflection. *Nano Lett* **10**, 1823-1830 (2010).

65. Bashour, K.T. *et al.* CD28 and CD3 have complementary roles in T-cell traction forces. *Proc Natl Acad Sci U S A* **111**, 2241-2246 (2014).

66. Basu, R. *et al.* Cytotoxic T Cells Use Mechanical Force to Potentiate Target Cell Killing. *Cell* **165**, 100-110 (2016).

67. Stabley, D.R. *et al.* Visualizing mechanical tension across membrane receptors with a fluorescent sensor. *Nat Methods* **9**, 64-67 (2011).

68. Morimatsu, M. *et al.* Molecular tension sensors report forces generated by single integrin molecules in living cells. *Nano Lett* **13**, 3985-3989 (2013).

69. Galior, K. *et al.* Titin-Based Nanoparticle Tension Sensors Map High-Magnitude Integrin Forces within Focal Adhesions. *Nano Lett* **16**, 341-348 (2016).

70. Chang, A.C. *et al.* Single Molecule Force Measurements in Living Cells Reveal a Minimally Tensioned Integrin State. *ACS Nano* **10**, 10745-10752 (2016).

71. Gohring, J. *et al.* Temporal analysis of T-cell receptor-imposed forces via quantitative single molecule FRET measurements. *Nat Commun* **12**, 2502 (2021).

72. Zhang, Y. *et al.* DNA-based digital tension probes reveal integrin forces during early cell adhesion. *Nat Commun* **5**, 5167 (2014).

73. Blakely, B.L. *et al.* A DNA-based molecular probe for optically reporting cellular traction forces. *Nat Methods* **11**, 1229-1232 (2014).

74. Wang, X. *et al.* Defining single molecular forces required to activate integrin and notch signaling. *Science* **340**, 991-994 (2013).

75. Wang, Y. *et al.* Force-activatable biosensor enables single platelet force mapping directly by fluorescence imaging. *Biosens Bioelectron* **100**, 192-200 (2018).

76. Woodside, M.T. *et al.* Nanomechanical measurements of the sequence-dependent folding landscapes of single nucleic acid hairpins. *Proc Natl Acad Sci U S A* **103**, 6190-6195 (2006).

77. Lin, M.M. *et al.* Unfolding and melting of DNA (RNA) hairpins: the concept of structure-specific 2D dynamic landscapes. *Phys Chem Chem Phys* **10**, 4227-4239 (2008).

78. Bustamante, C. *et al.* Mechanical processes in biochemistry. *Annu Rev Biochem* **73**, 705-748 (2004).

79. Bell, G.I. Models for the specific adhesion of cells to cells. *Science* **200**, 618-627 (1978).

80. Ansari, A. *et al.* Is Hairpin Formation in Single-Stranded Polynucleotide Diffusion-Controlled? *J. Phys. Chem. B* **109**, 12982-12989 (2005).

81. Grunwell, J.R. *et al.* Monitoring the Conformational Fluctuations of DNA Hairpins Using Single-Pair Fluorescence Resonance Energy Transfer. *J Am Chem Soc* **123**, 4295-4303 (2001).

82. Greenleaf, W.J. *et al.*Abbondanzieri, E.A. & Block, S.M. Passive all-optical force clamp for high-resolution laser trapping. *Phys Rev Lett* **95**, 208102 (2005).

83. Bustamante, C. *et al.*The effect of force on thermodynamics and kinetics of single molecule reactions. *Biophysical Chemistry* **101**, 513-533 (2002).

84. Bercy, M. *et al.*Hairpins under tension: RNA versus DNA. *Nucleic Acids Res* **43**, 9928-9936 (2015).

85. Liu, Y. *et al.* DNA-based nanoparticle tension sensors reveal that T-cell receptors transmit defined pN forces to their antigens for enhanced fidelity. *Proc Natl Acad Sci U S A* **113**, 5610-5615 (2016).

86. Liu, Y. *et al.* Tension sensing nanoparticles for mechano-imaging at the living/nonliving interface. *J Am Chem Soc* **135**, 5320-5323 (2013).

87. Ma, V.P. *et al.* The magnitude of LFA-1/ICAM-1 forces fine-tune TCR-triggered T cell activation. *Sci. Adv.* **8**, eabg4485 (2022).

88. Hu, Y. *et al.* DNA-Based Microparticle Tension Sensors (uTS) for Measuring Cell Mechanics in Non-planar Geometries and for High-Throughput Quantification. *Angew Chem Int Ed Engl* **60**, 18044-18050 (2021).

89. Yokosuka, T. *et al.* Newly generated T cell receptor microclusters initiate and sustain T cell activation by recruitment of Zap70 and SLP-76. *Nat Immunol* **6**, 1253-1262 (2005).

90. Varma, R. *et al.* T cell receptor-proximal signals are sustained in peripheral microclusters and terminated in the central supramolecular activation cluster. *Immunity* **25**, 117-127 (2006).

91. Hsu, C.J. *et al.* Ligand mobility modulates immunological synapse formation and T cell activation. *PLoS One* **7**, e32398 (2012).

92. Ma, V.P. *et al.* Ratiometric Tension Probes for Mapping Receptor Forces and Clustering at Intermembrane Junctions. *Nano Lett* **16**, 4552-4559 (2016).

93. Dam, T. *et al.* Supported Lipid Bilayers and the Study of Two-Dimensional Binding Kinetics. *Front Mol Biosci* **9**, 833123 (2022).

94. Nowosad, C.R. *et al.* Germinal center B cells recognize antigen through a specialized immune synapse architecture. *Nat Immunol* **17**, 870-877 (2016).

95. Kwak, K. *et al.* Intrinsic properties of human germinal center B cells setantigen affinity thresholds. *Sci Immunol* **3**, eaau6598 (2018).

96. Zhao, B. *et al.* Visualizing Intercellular Tensile Forces by DNA-Based Membrane Molecular Probes. *J Am Chem Soc* **139**, 18182-18185 (2017).

97. Schodin, B.A. *et al.* Correlation Between the Number of T Cell Receptors Required for T Cell Activation and TCR–Ligand Affinity. *Immunity* **5**, 137-146 (1996).

98. Ma, R. *et al.* DNA probes that store mechanical information reveal transient piconewton forces applied by T cells. *Proc Natl Acad Sci U S A* **116**, 16949-16954 (2019).

99. Glazier, R. *et al.* DNA mechanotechnology reveals that integrin receptors apply pN forces in podosomes on fluid substrates. *Nat Commun* **10**, 4507 (2019).

100. Brockman, J.M. *et al.* Mapping the 3D orientation of piconewton integrin traction forces. *Nat Methods* **15**, 115-118 (2018).

101. Xu, K. *et al.* Dual-objective STORM reveals three-dimensional filament organization in the actin cytoskeleton. **9**, 185-188 (2012).

102. Brockman, J.M. *et al.* Live-cell super-resolved PAINT imaging of piconewton cellular traction forces. *Nat Methods* **17**, 1018-1024 (2020).

103. Jungmann, R. *et al.* Multiplexed 3D cellular super-resolution imaging with DNA-PAINT and Exchange-PAINT. *Nat Methods* **11**, 313-318 (2014).

104. Albrecht, C. *et al.* DNA: A Programmable Force Sensor. *Science* **310**, 367-369 (2003).

105. Mishra, R.K. *et al.*. Effect of shear force on the separation of double-stranded DNA. *Phys Rev E Stat Nonlin Soft Matter Phys* **84**, 032903 (2011).

106. Cocco, S. *et al.* Force and kinetic barriers to unzipping of the DNA double helix. *Proc Natl Acad Sci U S A* **98**, 8608-8613 (2001).

107. Hatch, K. *et al.* Demonstration that the shear force required to separate short double-stranded DNA does not increase significantly with sequence length for sequences longer than 25 base pairs. *Phys Rev E Stat Nonlin Soft Matter Phys* **78**, 011920 (2008).

108. Krautbauer, R. *et al.*. Unzipping DNA Olgimers. *Nano Lett* **3**, 493-496 (2003).

109. Gennes, P.G.D. Maximum pull out force on DNA hybrids. *C. R. Acad. Sci. Paris* **2**, 1505-1508 (2001).

110. Mosayebi, M. *et al.*Force-Induced Rupture of a DNA Duplex: From Fundamentals to Force Sensors. *ACS Nano* **9**, 11993-12003 (2015).

111. Liu, J. *et al.* Tension Gauge Tethers as Tension Threshold and Duration Sensors. *ACS Sens* **8**, 704-711 (2023).

112. Lo, W.L. *et al.* Lck promotes Zap70-dependent LAT phosphorylation by bridging Zap70 to LAT. *Nat Immunol* **19**, 733-741 (2018).

113. Sloas, D.C. *et al.* Tension-tuned receptors for synthetic mechanotransduction and intercellular force detection. *Nat Biotechnol* **41**, 1287-1295 (2023).

114. Wan, Z. *et al.* The activation of IgM- or isotype-switched IgG- and IgE-BCR exhibits distinct mechanical force sensitivity and threshold. *Elife* **4** (2015).

115. Zhao, Y. *et al.* Keratocytes Generate High Integrin Tension at the Trailing Edge to Mediate Rear De-adhesion during Rapid Cell Migration. *iScience* **9**, 502-512 (2018).

116. Sarkar, A. *et al.* Force-activatable coating enables high-resolution cellular force imaging directly on regular cell culture surfaces. *Phys Biol* **15**, 065002 (2018).

117. Pawlak, M.R. *et al.* RAD-TGTs: high-throughput measurement of cellular mechanotype via rupture and delivery of DNA tension probes. *Nat Commun* **14**, 2468 (2023).

118. Rashid, S.A. *et al.* DNA Tension Probes Show that Cardiomyocyte Maturation Is Sensitive to the Piconewton Traction Forces Transmitted by Integrins. *ACS Nano* **16**, 5335-5348 (2022).

119. Zhao, Y. *et al.* Cellular Force Nanoscopy with 50 nm Resolution Based on Integrin Molecular Tension Imaging and Localization. *J Am Chem Soc* **142**, 6930-6934 (2020).

120. Ting, L.H. *et al.* Contractile forces in platelet aggregates under microfluidic shear gradients reflect platelet inhibition and bleeding risk. *Nat Commun* **10**, 1204 (2019).

121. Wang, M.S. *et al.* Mechanically active integrins target lytic secretion at the immune synapse to facilitate cellular cytotoxicity. *Nat Commun* **13**, 3222 (2022).

122. Ma, V.P. *et al.* Mechanically Induced Catalytic Amplification Reaction for Readout of Receptor-Mediated Cellular Forces. *Angew Chem Int Ed Engl* **55**, 5488-5492 (2016).

123. Duan, Y. *et al.* Mechanically Triggered Hybridization Chain Reaction. *Angew Chem Int Ed Engl* **60**, 19974-19981 (2021).

124. Duan, Y. *et al.* Mechano-Cas12a Assisted Tension Sensor (MCATS) for Massively Amplified Cell Traction Force Measurements. *bioRxiv* (2022).

125. Feng, Y. *et al.* A bead-based method for high-throughput mapping of the sequence- and force-dependence of T cell activation. *Nat Methods* **19**, 1295-1305 (2022).

126. Lei, K. *et al.*Mechanical Immunoengineering of T cells for Therapeutic Applications. *Acc Chem Res* **53**, 2777-2790 (2020).

127. Ritter, A.T. *et al.* Actin depletion initiates events leading to granule secretion at the immunological synapse. *Immunity* **42**, 864-876 (2015).

128. Tabdanov, E. *et al.* Micropatterning of TCR and LFA-1 ligands reveals complementary effects on cytoskeleton mechanics in T cells. *Integr Biol (Camb)* **7**, 1272-1284 (2015).

129. Fletcher, D.A. *et al*. Cell mechanics and the cytoskeleton. *Nature* **463**, 485-492 (2010).

130. Murrell, M. *et al.* Forcing cells into shape: the mechanics of actomyosin contractility. *Nat Rev Mol Cell Biol* **16**, 486-498 (2015).

131. Roca-Cusachs, P. *et al.* Quantifying forces in cell biology. *Nat Cell Biol* **19**, 742-751 (2017).

132. Polacheck, W.J. *et al.* Measuring cell-generated forces: a guide to the available tools. *Nat Methods* **13**, 415-423 (2016).

133. Legant, W.R. *et al.* Measurement of mechanical tractions exerted by cells in three-dimensional matrices. *Nature Methods* **7**, 969-971 (2010).

134. Tan, J.L. *et al.* Cells lying on a bed of microneedles: an approach to isolate mechanical force. *Proc Natl Acad Sci U S A* **100**, 1484-1489 (2003).

135. Gupta, M. *et al.* Adaptive rheology and ordering of cell cytoskeleton govern matrix rigidity sensing. *Nat Commun* **6**, 7525 (2015).

136. Champion, J.A. *et al.* Role of target geometry in phagocytosis. *Proc Natl Acad Sci U S A* **103**, 4930-4934 (2006).

137. Richards, D.M. *et al.* Target shape dependence in a simple model of receptor-mediated endocytosis and phagocytosis. *Proc Natl Acad Sci U S A* **113**, 6113-6118 (2016).

138. Lou, H.Y. *et al.* Membrane curvature underlies actin reorganization in response to nanoscale surface topography. *Proc Natl Acad Sci U S A* **116**, 23143-23151 (2019).

139. Mohagheghian, E. *et al.* Quantifying compressive forces between living cell layers and within tissues using elastic round microgels. *Nat Commun* **9**, 1878 (2018).

140. Campàs, O. *et al.* Quantifying cell-generated mechanical forces within living embryonic tissues. *Nat Methods* **11**, 183-189 (2014).

141. Vorselen, D. *et al.* Microparticle traction force microscopy reveals subcellular force exertion patterns in immune cell-target interactions. *Nat Commun* **11**, 20 (2020).

142. Lee, W. *et al.* Dispersible hydrogel force sensors reveal patterns of solid mechanical stress in multicellular spheroid cultures. *Nat Commun* **10**, 144 (2019).

143. Kaizuka, Y. *et al.* Mechanisms for segregating T cell receptor and adhesion molecules during immunological synapse formation in Jurkat T cells. *Proc Natl Acad Sci U S A* **104**, 20296-20301 (2007).

144. Jin, W. *et al.* T cell activation and immune synapse organization respond to the microscale mechanics of structured surfaces. *Proc Natl Acad Sci U S A* **116**, 19835-19840 (2019).

145. Ishizaki, T. *et al.* Pharmacological Properties of Y-27632, a Specific Inhibitor of Rho-Associated Kinases. *Mol Pharmacol* **57**, 976-983 (2000).

146. Paul, B.Z.S. *et al.* Platelet Shape Change Is Mediated by both Calcium-dependent and -independent Signaling Pathways. *J Biol Chem* **274**, 28293-28300 (1999).

147. Zimmermann, J.L. *et al.* Thiol-based, site-specific and covalent immobilization of biomolecules for single-molecule experiments. *Nat Protoc* **5**, 975-985 (2010).

148. Huang, W. *et al.* Maleimide-thiol adducts stabilized through stretching. *Nat Chem* **11**, 310-319 (2019).

149. Wagner, C.L. *et al.* Analysis of GPIIb/IIIa Receptor Number by Quantification of 7E3 Binding to Human Platelets. *Blood* **88**, 907-914 (1996).

150. Qiu, Y. *et al.* Platelet mechanosensing of substrate stiffness during clot formation mediates adhesion, spreading, and activation. *Proc Natl Acad Sci U S A* **111**, 14430-14435 (2014).

151. Wang, J. *et al.* Multiparameter Particle Display (MPPD): A Quantitative Screening Method for the Discovery of Highly Specific Aptamers. *Angew Chem Int Ed Engl* **56**, 744-747 (2017).

152. Ahmed, R. *et al.* A Public BCR Present in a Unique Dual-Receptor-Expressing Lymphocyte from Type 1 Diabetes Patients Encodes a Potent T Cell Autoantigen. *Cell* **177**, 1583-1599 e1516 (2019).

153. Otto, O. *et al.* Real-time deformability cytometry: on-the-fly cell mechanical phenotyping. *Nat Methods* **12**, 199-202, 194 p following 202 (2015).

154. Myers, D.R. *et al.* Single-platelet nanomechanics measured by high-throughput cytometry. *Nat Mater* **16**, 230-235 (2017).

155. Bandyopadhyay, S.K. *et al.* Probing ADP Induced Aggregation Kinetics During Platelet-Nanoparticle Interactions: Functional Dynamics Analysis to Rationalize Safety and Benefits. *Front Bioeng Biotechnol* **7**, 163 (2019).

156. Sun, Z., *et al.* Integrin activation by talin, kindlin and mechanical forces. *Nat Cell Biol* **21**, 25-31 (2019).

157. Barger, S.R. *et al.* Membrane-cytoskeletal crosstalk mediated by myosin-I regulates adhesion turnover during phagocytosis. *Nat Commun* **10**, 1249 (2019).

158. Bakalar, M.H. *et al.* Size-Dependent Segregation Controls Macrophage Phagocytosis of Antibody-Opsonized Targets. *Cell* **174**, 131-142 e113 (2018).

159. Weiss, L.E. *et al.* Three-dimensional localization microscopy in live flowing cells. *Nat Nanotechnol* **15**, 500-506 (2020).

160. Wang, X. *et al.* Comparative analysis of various platelet glycoprotein IIb/IIIa antagonists on shear-induced platelet activation and adhesion. *J Pharmacol Exp Ther* **303**, 1114-1120 (2002).

161. Hui, E. *et al.* T-cell costimulatory receptor C28 is a primary target for PD-1-mediated inhibition. *Science* **355**, 1428-1433 (2017).

162. Lee, M.S. *et al.* A Mechanical Switch Couples T Cell Receptor Triggering to the Cytoplasmic Juxtamembrane Regions of CD3zetazeta. *Immunity* **43**, 227-239 (2015).

163. Sage, P.T. *et al.* Antigen recognition is facilitated by invadosome-like protrusions formed by memory/effector T cells. *J Immunol* **188**, 3686-3699 (2012).

164. Aramesh, M. *et al.* Functionalized Bead Assay to Measure Three-dimensional Traction Forces during T-cell Activation. *Nano Lett* **21**, 507-514 (2021).

165. Hellmeier, J. *et al.* DNA origami demonstrate the unique stimulatory power of single pMHCs as T cell antigens. *Proc Natl Acad Sci U S A* **118** (2021).

166. Dong, R. *et al.* DNA origami patterning of synthetic T cell receptors reveals spatial control of the sensitivity and kinetics of signal activation. *Proc Natl Acad Sci U S A* **118** (2021).

167. Fang, T. *et al.* Spatial Regulation of T-Cell Signaling by Programmed Death-Ligand 1 on Wireframe DNA Origami Flat Sheets. *ACS Nano* **15**, 3441-3452 (2021).

168. Whitton, J.L. *et al.* Functional avidity maturation of CD8+ T-cells without seleaction of higher affinity TCR. *Nat Immunol* **2**, 711-717 (2001).

169. Thauland, T.J. *et al.* Cytoskeletal adaptivity regulates T cell receptor signaling. *Sci Signal* **10** (2017).

170. Su, X. *et al.* Phase separation of signaling molecules promotes T cell receptor signal transduction. *Science* **352**, 595-599 (2016).

171. Cespedes, P.F. *et al.* T-cell trans-synaptic vesicles are distinct and carry greater effector content than constitutive extracellular vesicles. *Nat Commun* **13**, 3460 (2022).

172. Olden, B.R. *et al.* Cell-Templated Silica Microparticles with Supported Lipid Bilayers as Artificial Antigen-Presenting Cells for T Cell Activation. *Adv Healthc Mater* **8**, e1801188 (2019).

173. Zhao, W. *et al.* Cell-surface sensors for real-time probing of cellular environments. *Nat Nanotechnol* **6**, 524-531 (2011).

174. Ge, Z. *et al.* Programming Cell-Cell Communications with Engineered Cell Origami Clusters. *J Am Chem Soc* **142**, 8800-8808 (2020).

175. Liu, Y. *et al.* The effects of overhang placement and multivalency on cell labeling by DNA origami. *Nanoscale* **13**, 6819-6828 (2021).

176. Akbari, E. *et al.* Engineering Cell Surface Function with DNA Origami. *Adv Mater* **29** (2017).

177. Jacobelli, J. *et al.* A single class II myosin modulates T cell motility and stopping, but not synapse formation. *Nat Immunol* **5**, 531-538 (2004).

178. Galush, W.J. *et al.* Quantitative fluorescence microscopy using supported lipid bilayer standards. *Biophys J* **95**, 2512-2519 (2008).

179. Zhang, Y. *et al.* Platelet integrins exhibit anisotropic mechanosensing and harness piconewton forces to mediate platelet aggregation. *Proc Natl Acad Sci U S A* **115**, 325-330 (2018).

180. Alegre, M. *et al.* T-cell regulation by CD28 and CTLA-4. *Nat. Rev. Immuno.* **1**, 220-228 (2001)

181. Bachmann, M.F. *et al.* Distinct Roles for LFA-1 and CD28 during Activation of Naive T Cells: Adhesion versus Costimulation. *Immunity* **7**, 549-557 (1997).

182. Wang, Y. *et al.* LFA-1 decreases the antigen dose for T cell activation in vivo. *Int Immunol* **20**, 1119-1127 (2008).

183. Wang, Y. *et al.* LFA-1 affinity regulation is necessary for the activation and proliferation of naive T cells. *J Biol Chem* **284**, 12645-12653 (2009).

184. Nordenfelt, P. *et al.* Coordinated integrin activation by actin-dependent force during T-cell migration. *Nat Commun* **7**, 13119 (2016).

185. Verma, N.K. *et al.* Not Just an Adhesion Molecule: LFA-1 Contact Tunes the T Lymphocyte Program. *J Immunol* **199**, 1213-1221 (2017).

186. Chigaev, A. *et al.* Aspects of VLA-4 and LFA-1 regulation that may contribute to rolling and firm adhesion. *Front Immunol* **3**, 242 (2012).

187. Krummey, S.M. *et al.* Low-Affinity Memory CD8+ T Cells Mediate Robust Heterologous Immunity. *J Immunol* **196**, 2838-2846 (2016).

188. Zehn, D. *et al.* Complete but curtailed T-cell response to very low-affinity antigen. *Nature* **458**, 211-214 (2009).

189. Kolawole, E.M. *et al.* 2D Kinetic Analysis of TCR and CD8 Coreceptor for LCMV GP33 Epitopes. *Front Immunol* **9**, 2348 (2018).

190. Chen, W. *et al.* Forcing switch from short- to intermediate- and long-lived states of the alphaA domain generates LFA-1/ICAM-1 catch bonds. *J Biol Chem* **285**, 35967-35978 (2010).

191. Comrie, W.A. *et al.* F-actin flow drives affinity maturation and spatial organization of LFA-1 at the immunological synapse. *J Cell Biol* **208**, 475-491 (2015).

192. Kim, C. *et al.* Regulation of integrin activation. *Annu Rev Cell Dev Biol* **27**, 321-345 (2011).

193. Kinashi, T. Intracellular signalling controlling integrin activation in lymphocytes. *Nat Rev Immunol* **5**, 546-559 (2005).

194. Hickey, J.W. *et al.* Engineering an Artificial T-Cell Stimulating Matrix for Immunotherapy. *Adv Mater* **31**, e1807359 (2019).

195. Shi, L. *et al.* Substrate stiffness enhances human regulatory T cell induction and metabolism. *Biomaterials* **292**, 121928 (2023).

196. Adu-Berchie, K. *et al.* Generation of functionally distinct T-cell populations by altering the viscoelasticity of their extracellular matrix. *Nat Biomed Eng* (2023).

197. Cai, H. *et al.* Full control of ligand positioning reveals spatial thresholds for T cell receptor triggering. *Nat Nanotechnol* **13**, 610-617 (2018).

198. Taylor, M.J. *et al.* A DNA-Based T Cell Receptor Reveals a Role for Receptor Clustering in Ligand Discrimination. *Cell* **169**, 108-119 e120 (2017).

199. Deeg, J. *et al.* T cell activation is determined by the number of presented antigens. *Nano Lett* **13**, 5619-5626 (2013).

200. Stejskalova, A. *et al.* Biologically Inspired, Cell-Selective Release of Aptamer-Trapped Growth Factors by Traction Forces. *Adv Mater* **31**, e1806380 (2019).

201. Lei, K. *et al.* T cell force-responsive delivery of anticancer drugs using mesoporous silica microparticles. *Materials Horizons* **7**, 3196-3200 (2020).